

Aristotle University of Thessaloniki
Department of Physics



SpectroGEM: A novel Neutron Spectrometer

Eleni Aza

Ph.D. Thesis

Thessaloniki, Greece
2016

Aristotle University of Thessaloniki
Department of Physics



**SpectroGEM:
A novel Neutron Spectrometer**

PhD Thesis

Eleni Aza

Committee:

1. Dimitrios Sampsonidis, Assoc. Prof. AUTH
2. Charikelia Petridou, Prof. AUTH
3. Theodoros Alexopoulos, Prof. NTUA
4. Spyridon Tzamarias, Prof. AUTH
5. Ilias Savvidis, Prof. AUTH
6. Konstantinos Kordas, Ass. Prof. AUTH
7. Matteo Magistris, Researcher CERN

Thessaloniki, March 2016

Αριστοτέλειο Πανεπιστήμιο Θεσσαλονίκης
Τμήμα Φυσικής



SpectroGEM:
Ένα πρωτότυπο φασματόμετρο νετρονίων

Διδακτορική Διατριβή

Ελένη Αζά

Διπλωματούχου Φυσικού Εφαρμογών ΕΜΠ

Επιτροπή:

1. Δημήτριος Σαμψωνίδης, Αν. Καθ. ΑΠΘ
2. Χαρίκλεια Πετρίδου, Καθ. ΑΠΘ
3. Θεόδωρος Αλεξόπουλος, Καθ. ΕΜΠ
4. Σπυρίδων Τζαμαρίας, Καθ. ΑΠΘ
5. Ηλίας Σαββίδης, Καθ. ΑΠΘ
6. Κωνσταντίνος Κορδάς, Επ. Καθ. ΑΠΘ
7. Matteo Magstris, Ερευνητής CERN

Θεσσαλονίκη, Μάρτιος 2016

Acknowledgements

I would like to explicitly thank Marco Silari, coordinator of the ARDENT Marie Curie ITN, for offering me the opportunity to complete my PhD at CERN. I would also like to thank Matteo Magistris, my supervisor at CERN, for the guiding and support he provided during this work. I am very grateful to Fabrizio Murtas for teaching me everything I know about the GEM detector and helping me in the construction of the SpectroGEM. Colleagues at CERN, without whom this work would not have been completed, are Giacomo Manessi and Nesrine Dinar for the BSS measurements, Silvia Puddu for the GEM measurements, and Christina Weiss, Frank Gunsing and Carlos Guerrero from the nTOF Collaboration.

From the Aristotle University of Thessaloniki I would like to thank Dimitrios Sampsonidis, supervisor of my PhD, Charikleia Petridou and Kostas Kordas as members of the committee and supporters of this work. I am also very grateful to Theodoros Alexopoulos, professor at NTUA, member of the PhD committee, supervisor during my Bachelor and Master thesis and teacher during my studies at NTUA; he was the one who inspired me in engaging with research.

Finally I would like to thank my parents, Popi and Tasos, who supported me with every possible way during my PhD, my studies and my life.

*True understanding
does not come out of knowledge or experience,
but out of a movement of stillness.*

Manuel Schoch

Abstract

In this dissertation a novel gaseous detector for neutron spectrometry is presented. The device, called SpectroGEM, was designed, constructed and tested in order to measure neutron spectra in the energy range from thermal to 100 MeV. Having planar geometry, the main advantages are a response over a wide energy range, reasonable counting efficiency, short irradiation time and low weight.

The read-out of the spectrometer is performed with a triple GEM detector. Its efficiency for neutron detection is demonstrated via experimental activities and simulations using several methods. Experiments on the detection of neutrons consist of applying an innovative detector with borated glass sheets as a stray monitor for low energy neutrons inside an irradiation room, time-of-flight measurements with detectors employing several materials for slow and fast neutrons, on-line beam profile imaging with high resolution and measurement of the counting efficiency as a function of the neutron energy.

The SpectroGEM consists of a neutron conversion board divided in regions, each one being dedicated to a specific energy range, and the neutron spectrum is acquired by unfolding the counts from each region. The same operation principle is found in the Bonner Sphere Spectrometer (BSS), a device widely used in radiation protection. Measurements with the BSS are presented in the stray field around a water phantom in the West German Proton Therapy Centre of Essen (WPE), behind concrete shielding at the CERF facility at CERN and at the pulsed field present at the entrance of the CERN Proton Synchrotron (PS).

The design of the SpectroGEM in terms of geometry and material was performed via Monte Carlo simulations with the FLUKA code. Operational tests and spectra measurements are discussed following the construction of the spectrometer. The operational tests consist of investigating the channel response to neutrons, noise elimination and photon-signal rejection, ensuring optimal performance of the GEM detector. The spectrometer was firstly tested with a $^{241}\text{AmBe}$ source and the neutron energy spectrum measured is presented. Spectra from spallation target acquired in

different positions are discussed and useful conclusions for the measuring capabilities of the spectrometer are drawn. Modifications in the design and response matrix of the spectrometer are suggested, leading to more reliable spectra measurements, and possible applications based on the directional design of the spectrometer are introduced.

Περίληψη

Στην παρούσα διδακτορική διατριβή παρουσιάζεται ένα πρωτότυπο φασματόμετρο νετρονίων αερίου γεμίσματος. Η επονομαζόμενη συσκευή ως SpectroGEM σχεδιάστηκε, κατασκευάστηκε και δοκιμάστηκε για τη μέτρηση φασμάτων νετρονίων από θερμικές ενέργειες μέχρι 100 MeV. Έχοντας επίπεδη γεωμετρία, τα κύρια πλεονεκτήματα που παρουσιάζει είναι απόκριση σε ευρύ ενεργειακό φάσμα, αποδοτικότητα μέτρησης, βραχύς απαιτούμενος χρόνος ακτινοβόλησης και χαμηλό βάρος.

Η ανάγνωση του φασματόμετρου πραγματοποιήθηκε με ένα τριπλό ανιχνευτή GEM. Η αποτελεσματικότητά του για την ανίχνευση νετρονίων αποδεικνύεται μέσω πειραματικών δραστηριοτήτων και προσομοιώσεων χρησιμοποιώντας διάφορες μεθόδους. Πειράματα πραγματοποιήθηκαν για την ανίχνευση νετρονίων χαμηλής ενέργειας με καινοτόμο GEM ανιχνευτή που φέρει φύλλα γυαλιού επικαλυμμένα με Βόριο. Ανιχνευτές με διαφορετικά υλικά χρησιμοποιήθηκαν για τη μέτρηση της ενέργειας νετρονίων μέσω του χρόνου πορείας τους, για την απεικόνιση με υψηλή ανάλυση δέσμεων σε πραγματικό χρόνο και καταγραφή της αποδοτικότητας των συσκευών ως συνάρτηση της ενέργειας νετρονίων.

Το SpectroGEM αποτελείται από έναν μετατροπέα νετρονίων χωρισμένο σε περιοχές, κάθε μία από τις οποίες παρουσιάζει απόκριση σε διαφορετικό εύρος νετρονίων. Το φάσμα νετρονίων μετρείται από την ξεδίπλωση των δεδομένων που αποκτήθηκαν από την κάθε περιοχή. Στην ίδια αρχή λειτουργίας βασίζεται και το φασματόμετρο BSS, μια συσκευή που χρησιμοποιείται ευρέως στον τομέα προστασίας από τη ραδιενέργεια. Μετρήσεις με το BSS λήφθηκαν σε κέντρο θεραπείας πρωτονίων στο Essen (WPE), πίσω από θωράκιση τσιμέντου στις εγκαταστάσεις του πειράματος CERF στο CERN και στο παλμικό φάσμα νετρονίων στην είσοδο του Συγχρότρου Πρωτονίων (PS) στο CERN.

Ο σχεδιασμός του φασματόμετρου διεξήχθη μέσω προσομοιώσεων Monte Carlo με τον κώδικα FLUKA. Η αρχή λειτουργίας του και η ικανότητά του στη μέτρηση φασμάτων διερευνήθηκαν κατόπιν της κατασκευής του. Μετρήσεις πραγματοποιήθηκαν για την απόκριση των καναλιών σε σήμα προερχόμενο από νετρόνια, απόρριψη

του ηλεκτρονικού θορύβου και του πιθανού σήματος από φωτόνια. Η συσκευή αρχικά χρησιμοποιήθηκε για τη μέτρηση του φάσματος προερχόμενο από πηγή $^{241}\text{AmBe}$ και φασμάτων στην οροφή του πειράματος CERF μέσω βομβαρδισμού στόχου σιδήρου με αδρονιακή δέσμη. Τροποποιήσεις στην αρχική γεωμετρία του φασματομέτρου προτείνονται με βάση τα συμπεράσματα που εξήχθησαν από τις πειραματικές δραστηριότητες και πιθανές εφαρμογές του συζητώνται με βάση την κατευθυντική σχεδίασή του.

Contents

Introduction	1
1 Neutron detection	4
1.1 Neutron detection methods	4
1.1.1 Slow neutron detection	5
1.1.1.1 The $^{10}\text{B}(\text{n},\alpha)^7\text{Li}$ reaction	6
1.1.1.2 The $^6\text{Li}(\text{n},\alpha)^3\text{H}$ reaction	7
1.1.1.3 The $^3\text{He}(\text{n},\text{p})^3\text{H}$ reaction	7
1.1.1.4 The Gd neutron capture reaction	8
1.1.1.5 Neutron-Induced fission reactions	8
1.1.1.6 Radiative capture reactions (n, γ)	9
1.1.2 Fast neutron Detection	10
1.1.2.1 Elastic scattering	10
1.1.2.2 Moderation	12
1.2 Neutron detectors	14
1.2.1 The BF_3 tube for slow neutrons	14
1.2.2 The Long Counter for fast neutrons	15
2 The Gas Electron Multiplier (GEM) for neutron detection	17
2.1 The detector	17
2.1.1 The foils	18
2.1.2 The Single GEM	18
2.1.3 The Triple GEM	23
2.2 The acquisition system	25
2.3 Charged particles	26
2.3.1 Monitoring of relativistic hadron beams	26
2.3.2 Quality Assurance of hadron-therapy beams	29
2.4 Neutrons	30

2.4.1	Stray neutron monitoring	30
2.4.1.1	Experimental analysis	33
2.4.1.2	Comparison with FLUKA simulation	35
2.4.1.3	Detector activation	36
2.4.2	Time-of-flight	38
2.4.2.1	Time-of-flight measurements	40
2.4.2.2	Efficiency to neutrons	41
2.4.2.3	Efficiency to photons	44
2.4.3	Beam profile at nTOF	46
2.4.3.1	Profile at EAR1	46
2.4.3.2	Profile at the beam dump	47
2.4.4	Neutron moderation effects	49
2.4.4.1	Effect on time-of-arrival	49
2.4.4.2	Effect on beam spot dimensions	51
2.5	Conclusions	53
3	Neutron spectrometry and dosimetry	54
3.1	Spectra characteristics	54
3.2	Application fields	55
3.2.1	Radiation protection	55
3.2.2	Nuclear physics experiments	58
3.3	Neutron spectrometers	58
3.3.1	Recoil proton telescope	58
3.3.2	Nuclear reaction based spectrometers	59
3.3.3	Time-of-flight methods	60
4	The Bonner Sphere Spectrometer (BSS)	61
4.1	The CERN BSS	61
4.2	The BSS-LUPIN for pulsed fields	65
4.3	Experimental activities	67
4.3.1	The CERN BSS for secondary neutrons inside a proton therapy facility	68
4.3.1.1	Spectrum inside and outside the room	70
4.3.1.2	Global neutron $H^*(10)$ intercomparison	71
4.3.1.3	Conclusions	75
4.3.2	The CERN BSS performance behind concrete shielding	75
4.3.2.1	Neutron spectrum measurements	75
4.3.2.2	Neutron $H^*(10)$ measurement and intercomparison	77

4.3.3	Performance comparison of the CERN BSS and BSS-LUPIN in pulsed fields	78
4.3.3.1	Neutron fluence comparison	79
4.3.3.2	Neutron $H^*(10)$ comparison	81
4.3.3.3	Conclusions	83
4.4	Extensions and improvements	83
4.4.1	Response to high energies	83
4.4.2	Response to thermal energies	84
4.5	Conclusions	86
5	Design and study of the SpectroGEM	88
5.1	Material and methods	88
5.1.1	Thermal neutrons	90
5.1.1.1	Conversion efficiency comparison	91
5.1.1.2	Angular distribution of charged particles	92
5.1.1.3	Energy spectrum of charged particles	93
5.1.2	Epithermal and intermediate neutrons	94
5.1.3	Fast neutrons	96
5.2	Response matrix simulation	97
5.3	The read-out detector	101
5.4	Enhanced design	102
5.5	Study of cross-talk effects	103
5.5.1	Regional irradiation	103
5.5.1.1	Slow neutrons	105
5.5.1.2	Intermediate neutrons	106
5.5.1.3	Fast neutrons	107
5.5.2	Total irradiation	107
5.6	Photon contribution	109
5.7	Conclusions	113
6	Construction and applications of the SpectroGEM	114
6.1	Construction	114
6.2	Operational tests	115
6.2.1	Noise elimination	117
6.2.2	Voltage stability and channel response	118
6.2.3	Photon signal elimination	119
6.2.4	Response to neutrons	122
6.3	Experimental activities	124

6.3.1	Irradiation with photon sources	124
6.3.2	Neutron spectrum of $^{241}\text{AmBe}$	128
6.3.3	Neutron spectra from spallation target	130
6.3.3.1	Experimental set-up	132
6.3.3.2	Spectra measurement	133
6.3.4	Conclusions	140
6.4	Testing the unfolding procedure	142
6.4.1	Shifted $^{241}\text{AmBe}$	142
6.4.2	Modified $^{241}\text{AmBe}$	143
6.4.3	Closure test	144
6.4.4	Conclusions	146
6.5	Future prospects	146
6.5.1	Improvements	146
6.5.2	Applications	152
	Conclusions	153
	Appendix A The FLUKA Monte Carlo code	156
A.1	Low energy neutron transport	156
A.2	Estimation of physical quantities	157
	Appendix B Response matrix of the SpectroGEM	159

Introduction

Neutron spectrometry is commonly performed for radiation protection purposes with a view to protecting people and the environment from the harmful effects of ionizing radiation. The techniques employed are typically based on the detection of prompt energetic charged particles produced from neutron interaction with matter, and were developed soon after the discovery of neutrons by Chadwick (1932). The complexity of measuring neutron energy distributions of wide range is not only intrinsic to the indirect methods required, but also due to the different kinds of neutron reactions which dominate in different energy ranges. Several techniques have been developed and studied over the last decades; time-of-flight and nuclear-reaction-based spectrometers, recoil proton telescopes, foil activation methods etc, with the most widely used being the Bonner Sphere Spectrometer (BSS). Each technique is characterized by a certain energy range measured, isotropic or non-isotropic response, time and energy resolution, counting efficiency, instrumentation weight and transportability, dependence on neutron spectra and on the irradiation time.

In the frame of the present thesis a new Micro-Pattern Gaseous Detector (MPGD) for neutron spectrometry, called SpectroGEM, was designed, constructed and tested in order to combine advantages found in different existing instruments and techniques. It consists of a neutron conversion board divided in regions, each region being dedicated to a specific energy range. The read-out is performed by a triple Gas Electron Multiplier (GEM) detector and the neutron spectrum is acquired by unfolding the counts from each region with common codes, following the operation principle of the BSS but with planar geometry and a single irradiation required. The main advantages of the new device are a response over a wide energy range (from thermal energy to 100 MeV), reasonable counting efficiency, short irradiation time and low weight. The response is non-isotropic due to its planar geometry. This feature can be advantageous when information about the spectrum direction is of interest.

The work presented in this thesis can be divided into three main parts: the first

part discusses the operation principle of the GEM detector and demonstrates its ability to measure neutrons, the second part introduces the BSS and the unfolding methods for obtaining neutron spectra via measurements in different kinds of radiation fields and the third part focuses on the design, construction and testing of the new device for neutron spectrometry. The content of each chapter is listed below.

The main principles of neutron detection are described in Chapter 1. The nuclear reactions of interest and the detection methods for slow and fast neutrons are discussed in detail. Two important type of neutron detectors are briefly presented, namely the BF_3 tube for slow and the Long Counter for fast neutrons.

Chapter 2 consists of two main sections. In the first one the operation principle of the triple GEM detector is described. The second one presents experimental activities and results are presented in order to demonstrate the efficiency of different methods for neutron detection. The GEM detector is first evaluated as a stray neutron monitor for low energy neutrons in the mixed field of the CERN-EU High Energy Reference Field (CERF), showing linear response in high particle rates, high counting efficiency and photon signal rejection. Time-of-flight measurements performed at the neutron Time-of-Flight (nTOF) facility at CERN are presented and the beam spectrum is obtained by means of several detectors with appropriate converters for the entire energy range, measuring at the same time the beam profile and count rate. The efficiency to photons and the counting saturation point of the detector is investigated in the same facility.

An introduction to neutron spectrometry and dosimetry is given in Chapter 3. Typical spectra of secondary particles from spallation reactions are discussed and operational dosimetric quantities in radiation protection are introduced. The importance of neutron spectrometry is then highlighted and a description of common spectrometers is given, in order to introduce the techniques employed.

Chapter 4 is dedicated to the Bonner Sphere Spectrometer. Its operation principles and the calculation of its response matrix with the latest version of the FLUKA Monte Carlo code are described. Improvements in the response of the system are suggested for its employment in pulsed neutron fields, where proportional counters are known to underestimate the true interaction rate. Experimental results are presented in the stray field around a water phantom in the West German Proton Therapy Centre of Essen (WPE), behind concrete shielding at the CERF facility and at the pulsed field present at the entrance of the CERN Proton Synchrotron (PS). Finally, future extensions and improvements are suggested for the system response in the thermal and high energy region.

The design of the SpectroGEM via Monte Carlo simulations with the FLUKA code is presented in Chapter 5. The study for the geometry and material employed

is described in detail, as well as the corresponding response matrix which was simulated. Modifications of the optimal geometry are introduced in order to fit the requirements of the GEM, which is used as the read-out detector. Possible contribution from photons to the signal induced is investigated. In addition, future possible improvements are explored for the optimization of the spectrometer response, leading to more accurate and more reliable results.

In Chapter 6 operational tests and spectra measurements are discussed following the construction of the spectrometer. The acquisition and read-out systems are described in detail. The operational tests consist of investigating the channel response to neutrons, noise elimination and photon-signal rejection, ensuring optimal performance of the GEM detector. The spectrometer is then tested with an $^{241}\text{AmBe}$ source and the neutron energy spectrum measured is presented. Spectra from spallation target acquired in different positions are discussed and useful conclusions for the measuring capabilities of the spectrometer are drawn. Modifications in the design and response matrix of the spectrometer are suggested, leading to more reliable spectra measurements, and possible applications based on the directional design of the spectrometer are introduced.

Chapter 1

Neutron detection

This chapter discusses the main principles of slow and fast neutron detection, based on the material and nuclear interactions of interest. Isotopes with high cross-section for low energy neutrons are introduced, such as ^{10}B , ^6Li , ^3He and Gd, while detection processes for fast neutrons are discussed. In addition, the operation principles of two common neutron detectors are described, the BF_3 tube for slow and the Long Counter for fast neutrons.

1.1 Neutron detection methods

Neutrons are generally detected through nuclear reactions that result in prompt energetic charged particles such as protons and alpha particles. Every type of neutron detector involves the combination of a target material designed to convert neutrons into charged particles, coupled with a radiation detector. Since in most materials the cross section for neutron interactions strongly depends on the neutron energy, different techniques have been developed for neutron detection in different energy regions.

For the purpose of neutron spectrometry, neutrons can be classified in two categories depending on their energy: they are considered either fast neutrons or slow neutrons, where the conventional threshold corresponds to the energy of the abrupt drop in the cadmium absorption cross section, the so-called cadmium cut-off energy. They are also commonly classified on the basis of their kinetic energy E_n and corresponding dominant nuclear reactions (see Table 1.1).

Below 0.1 eV, neutrons reach thermal equilibrium with the surrounding material, exhibiting a Maxwellian energy distribution [1]. The most probable energy for

Table 1.1: Neutron energy ranges

Category	E_n
Thermal	< 0.1 eV
Epithermal	0.1 - 10 eV
Intermediate	10 eV - 100 keV
Fast	100 keV - 100 MeV
High-energy	> 100 MeV

thermal neutrons is given by:

$$E_0 = k_B * T \quad (1.1)$$

where k_B is the Boltzmann constant and T is the medium absolute temperature. At a room temperature (20°C), the most probable energy for thermal neutrons is $E_0 \sim 0.0253$ eV.

In the energy range between 100 keV and 10 MeV, neutrons can interact via elastic scattering (n, n) with low Z materials like hydrogen and carbon, transferring part of their energy to the recoil nuclei. Neutrons with energies above 10 MeV interact mainly through inelastic scattering (n, n') with high Z materials and are able to induce spallation reactions like (n, xn) or (n, np). Neutrons with energies higher than 0.1 eV may slow down through multiple elastic collisions with the nuclei of material and be thermalized with an energy distribution proportional to $1/E_n$. In this energy range, neutron resonance processes, like (n, γ), (n, p), (n, α) and (n , fission) reactions, become important.

Nuclear reactions of interest for slow and fast neutron detection are discussed below, a more detailed description of which can be found in [2].

1.1.1 Slow neutron detection

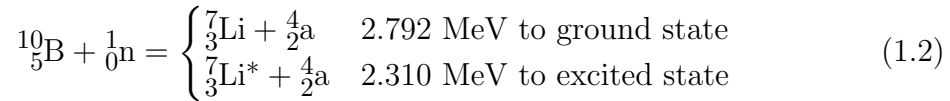
When searching for nuclear reactions which are useful in neutron detection, several factors must be considered. Firstly, the cross section for the reaction must be as large as possible so that efficient detectors can be built with small dimensions. Secondly, intense fields of gamma rays are also produced along with neutrons and the detector should be able to discriminate these particles in the detection process.

The energy liberated in a neutron capture reaction is of great importance and is commonly called Q -value [3]. The higher the Q -value, the greater the energy given to the reaction products, and the easier the task of discriminating against gamma-ray

events using sample amplitude discrimination. All the slow conversion reactions are exothermic so that the kinetic energy of the reaction products is determined only by the Q-value of the reaction. Common reactions for slow neutron detection are listed below.

1.1.1.1 The $^{10}\text{B}(\text{n},\alpha)^7\text{Li}$ reaction

One of the most popular reaction for the conversion of slow neutrons is the $^{10}\text{B}(\text{n},\alpha)^7\text{Li}$ reaction. It may be written:



The branching in the reaction indicates that the product ^7Li may be left either in its ground state or in its first excited state. When thermal neutrons (0.025 eV) are used to induce the reaction, about 94% of all reactions lead to the excited state, emitting a photon with $E = 482 \text{ keV}$, and only 6% directly to the ground state. In both cases, the Q-value of the reaction is very large compared to the slow neutron incoming energy, so that the energy imparted to the reaction products is essentially the Q-value itself and thus it is impossible to extract any information about the original neutron energy. The reaction products must show a net momentum of essentially zero and therefore be emitted in opposite directions. The resulting energies of the alpha particle and the lithium nucleus can be calculated by conservation of energy and momentum as follows:

$$E_{\text{Li}} + E_{\alpha} = 2.31 \text{ MeV} \quad (1.3)$$

$$m_{\text{Li}}v_{\text{Li}} = m_{\alpha}v_{\alpha} \quad (1.4)$$

$$\sqrt{2m_{\text{Li}}v_{\text{Li}}} = \sqrt{2m_{\alpha}v_{\alpha}} \quad (1.5)$$

Solving Equations 1.3, 1.4 and 1.5 simultaneously:

$$E_{\text{Li}} = 0.84 \text{ MeV} \quad \text{and} \quad E_{\alpha} = 1.47 \text{ MeV} \quad (1.6)$$

The cross section for this reaction drops rapidly in increasing neutron energy and is proportional to $1/v$, the reciprocal of the neutron velocity, over most of the range. The thermal neutron cross section is 3840 barns [4].

The natural isotopic abundance of ^{10}B is 19.8%, but for neutron detection purposes materials enriched in ^{10}B up to 95% are employed, in order to increase the intrinsic efficiency. Boron can be used both in the form of a solid coating on the interior walls of a conventional proportional counter, and in the form of BF_3 gas. In the latter case, BF_3 serves both as a target for slow neutrons as well as a proportional gas detector.

1.1.1.2 The $^6\text{Li}(\text{n},\alpha)^3\text{H}$ reaction

Another popular reaction is the (n,α) reaction of ^6Li , leading only to the ground state of the product. The reaction is written:



Calculation of the energy of the reaction products for negligible incoming neutron energy yields the following:

$$E_{3\text{H}} = 2.73 \text{ MeV} \quad \text{and} \quad E_{\alpha} = 2.05 \text{ MeV} \quad (1.8)$$

The alpha particle and the triton produced have to be also oppositely directed.

The thermal neutron cross section for this reaction is 940 barns [4]. It shows a lower cross section as ^{10}B but the higher Q-value results in greater energy given to the reaction products.

1.1.1.3 The $^3\text{He}(\text{n},\text{p})^3\text{H}$ reaction

The gas ^3He is also widely used as a detection medium for neutrons through the reaction:



For reactions induced by low energy neutrons, the Q-value of 764 keV leads to reaction products with energies:

$$E_{\text{p}} = 0.573 \text{ MeV} \quad \text{and} \quad E_{3\text{H}} = 0.191 \text{ MeV} \quad (1.10)$$

The thermal neutron cross section is 5330 barns [4] and its value also falls off with a $1/v$ energy dependence. Although ^3He is commercially available, its relatively high cost and limited supply are important factors to be considered.

The cross sections of ^{10}B , ^6Li and ^3He [4] are summarised in Figure 1.1.

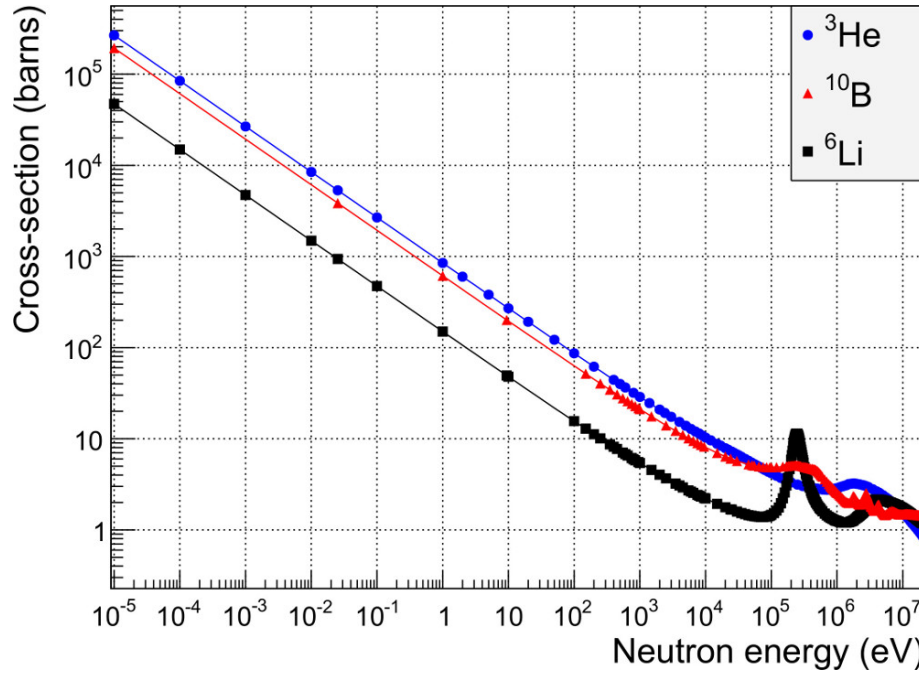


Figure 1.1: Cross-section of ^3He , ^{10}B and ^6Li for increasing neutron energy

1.1.1.4 The Gd neutron capture reaction

The cross section for thermal neutron capture of 255.000 barns [4] in ^{157}Gd is among the highest nuclear cross sections found in any material. The isotope is 15.7% abundant in natural gadolinium and neutron absorption results in reaction products that include gamma rays and conversion electrons. Fast electrons are useful in the application of this reaction for neutron detection, the most significant one is the 72 keV electron, which is emitted in 39% of the capture reactions. The gamma-rays background produced is often problematic for the discrimination of fast electrons and therefore Gd is not yet widely employed.

1.1.1.5 Neutron-Induced fission reactions

The cross sections of ^{233}U , ^{234}U and ^{239}Pu are relatively large at low neutron energies and thus these isotopes can be used as the basis of slow neutron detectors via fission [5]. The ^{233}U reaction is expressed as:



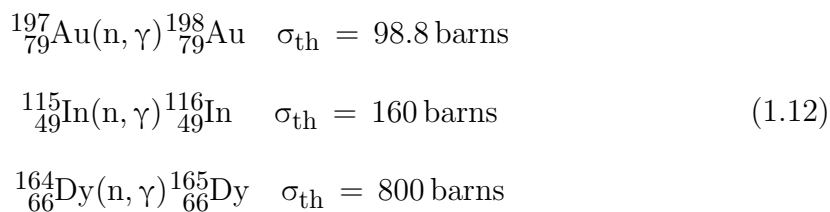
where FF_1 and FF_2 indicate two different fission fragments. The Q-value is equal to 207 MeV, which is extremely large compared with those of the previous reactions. The total energy produced in this reaction is distributed to both neutrons and fission products; in particular, about 168 MeV is the typical kinetic energy of the two fragments. As a result, detectors based on the fission reaction can often give output pulses that are much larger than those induced from other reactions or incident gamma rays.

Almost all fissile nuclides are naturally alpha-emitters and thus detectors containing these isotopes show also an output signal due to alpha particles, whose energy however is lower than the one released in a fission reaction. For this reason, it is sufficient to insert an appropriate threshold in the acquisition system to discard the alpha contribution. The most popular form of fission detector is an ionization chamber with its inner surfaces coated with a fissile material.

1.1.1.6 Radiative capture reactions (n, γ)

Radiative capture reactions [1] are generally exploited to detect thermal and epithermal neutrons due to their large thermal cross section. Neutron measurements are then carried out by measuring the radioactivity induced by neutron interactions. More in detail, a sample is exposed to a neutron flux and then removed. Afterwards, the induced radioactivity is counted generally by employing a Geiger detector for β^- particles and a scintillator, e.g. germanium detector, for γ rays emitted during the decay. In order to achieve a high sensitivity, these activation materials must have large cross sections for a neutron-induced reaction and their thickness has to be kept small not to perturb the neutron flux.

Corrections have to be applied in order to take into account the irradiation time, the post-irradiation decay, and the measurement time. The most widely used capture reactions are:



All of the isotopes produced are β^- -emitters, with half lives of about 2.7 days, 54.1 minutes, and 140 minutes, respectively.

1.1.2 Fast neutron Detection

In principle all reactions for slow neutron detection can be applied to detect fast neutrons as well. However, the probability that the neutron will interact by one of these reactions decreases rapidly with increasing neutron energy and thus fast neutron devices must employ a different detection scheme to yield an instrument with acceptable detection efficiency.

An important distinction in the application of fast neutron detectors is the possibility to measure the energy of the incoming neutron. The energy of the reaction products changes significantly with incoming neutron energies no longer negligible compared to the reaction Q-value. An accurate measurement of the reaction-product energies can then be used to deduce the incoming neutron energy simply by subtracting the reaction Q-value. In elastic scattering the Q-value is zero, so that neutron energies can start being measured by this technique when the resulting recoils have measurable kinetic energy.

However, in some cases the purpose of the measurement is simply to count fast neutrons without a measurement of their energy. Such fast neutron detectors can employ any of the methods discussed to convert neutrons to charged particles and then simply record all the pulses. Detectors of this type show a variation in efficiency with neutron energy.

Two of the most common detection processes are elastic scattering, in which the neutron energy is measured, and moderation in which the energy is not measured.

1.1.2.1 Elastic scattering

In this method neutrons are scattered by light nuclei, transferring some portion of the kinetic energy to the target nucleus, resulting in a recoil nucleus. Common target nuclei are hydrogen, deuterium and helium, which the first one being the most popular. The recoil nuclei resulting from neutron elastic scattering from hydrogen are called recoil protons.

The Q-value of elastic scattering is zero because the total kinetic energy is conserved. For single scattering in hydrogen, the fraction of the incoming neutron energy that is transferred to the recoil proton can range anywhere between zero and the full neutron energy. As a result, the average recoil proton has an energy about half that of the original neutron.

For incoming neutrons with nonrelativistic kinetic energy ($E_n \ll \text{GeV}$), conservation of momentum and energy in the centre-of-mass coordinate system gives the following relation for the energy of the recoil nucleus:

$$E_R = \frac{2A}{(1+A)^2}(1 - \cos\Theta)E_n \quad (1.13)$$

where

A = mass of target nucleus/neutron mass

E_n = incoming neutron energy (laboratory system)

E_R = recoil nucleus kinetic energy (laboratory system)

Θ = scattering angle of the neutron in the centre-of-mass coordinate system

To express Equation 1.13 to the laboratory coordinate system in which the original target nucleus is at rest, the following transformation can be used:

$$\cos\vartheta = \sqrt{\frac{1 - \cos\Theta}{2}} \quad (1.14)$$

where ϑ = scattering angle of the recoil nucleus in the lab coordinate system

Combining Equations 1.13 and 1.14 gives the following relation for the recoil nucleus energy in terms of its own angle of recoil:

$$E_R = \frac{4A}{(1+A)^2}(\cos^2\vartheta)E_n \quad (1.15)$$

From Equation 1.15 it can be seen that the energy given to the recoil nucleus is uniquely determined by the scattering angle. When the neutron is deflected only slightly, the recoil is emitted almost perpendicular to the incoming neutron direction ($\vartheta \simeq 90^\circ$), and Equation 1.15 predicts that the recoil energy is near zero. At the other extreme, a head-on collision of the incoming neutron with the target nucleus will lead to a recoil in the same direction ($\vartheta \simeq 0^\circ$), resulting in the maximum possible energy:

$$E_R|_{\text{MAX}} = \frac{4A}{(1+A)^2}E_n \quad (1.16)$$

The equation is also valid for compounds, such as polyethylene, and the maximum fraction of energy transferred to a recoil nucleus in a single collision is listed in Table 1.2 for common material. As the target nucleus mass increases, the maximum fractional energy transfer decreases and only in collisions with ordinary hydrogen can the neutron transfer all its energy in a single encounter.

Table 1.2: Maximum fractional energy transfer in neutron elastic scattering

Target Nucleus	A or M_r	$\frac{E_R}{E_n} _{MAX}$
^1_1H	1	1
^2_1H	2	0.889
^3_2He	3	0.750
^4_2He	4	0.640
CH_2	10.5	0.314
$^{12}_6\text{C}$	12	0.284
$^{16}_8\text{O}$	16	0.221

1.1.2.2 Moderation

The inherently low detection efficiency for fast neutrons of any slow neutron detector can be improved by surrounding the detector with hydrogen-containing moderating material. The incident fast neutron can then lose a fraction of its initial kinetic energy in the moderator before reaching the detector as a low-energy neutron, for which the detector efficiency is generally higher.

By increasing the thickness of the moderator, the number of collisions will increase, leading to a lower value of the most probable energy when the neutron reaches the detector. One would therefore expect the detection efficiency to increase indefinitely with moderator thickness if this was the only factor under consideration. A second factor, however, tends to decrease the efficiency with increasing moderator thickness: the probability that an incident fast neutron ever reaches the detector will decrease as the moderator is made thicker. The reason lies in the increased probability of a neutron to be thermalized and captured by the moderator, or escape from the surface of the moderator. Both probabilities, absorption and escaping, increase rapidly with increasing moderator thickness.

Effects that can take place during the moderation are summarized in Figure 1.2, taken from Ref. [2]:

As a result of all these factors, the efficiency of a moderated slow neutron detector when used with a monoenergetic fast neutron source will show a maximum at a specific moderator thickness. By careful choice of the dimensions and composition of the moderator-detector system, its overall efficiency versus energy curve can often be shaped and tailored to suit a specific application.

Moderating power A standard basis for comparing moderating abilities of different materials is the moderating power [6]. If one material has a larger moder-

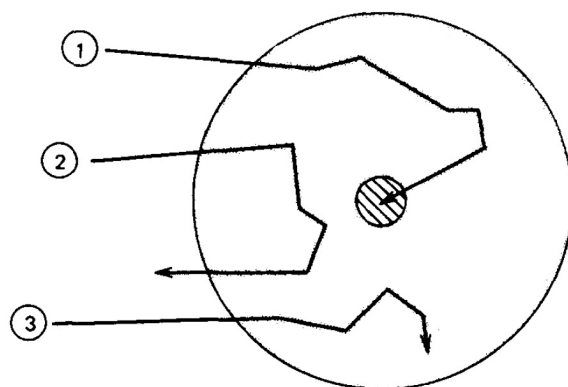


Figure 1.2: Schematic representation of neutron histories in moderated detectors: 1. Fast neutrons are successfully moderated and detected. 2. Partially or fully moderated neutrons escape. 3. Neutrons parasitically captured by the moderator.

ating power than another, less of that material is needed to achieve the same degree of moderation. For an effective moderator, both the interaction probability and the average energy loss in one scatter should be high. The moderating power is defined as $\xi \cdot \Sigma_s$, where Σ_s is the macroscopic scattering cross section and ξ is the average logarithmic energy decrement in a scatter, $\ln(E_{\text{initial}}) - \ln(E_{\text{final}})$. When elastic collisions in an element with atomic weight A dominate the scattering process, the decrement becomes:

$$\xi = 1 - \frac{(A-1)^2}{2A} \ln \frac{A+1}{A-1} \quad (1.17)$$

For $A > 2$, ξ can be approximated by $2/(A + 0.67)$. The moderating power of a compound is given by Eq. 1.18:

$$\xi \cdot \Sigma_s = \frac{\rho N_A}{M} (n_1 \sigma_1 \xi_1 + n_2 \sigma_2 \xi_2 + \dots) \quad (1.18)$$

However, a more comprehensive measure of moderating materials is the ratio $\xi \cdot \Sigma_s / \Sigma_a$, which takes into account the absorption cross section.

Table 1.3 gives the moderating powers and ratios for common moderator materials for neutrons in the energy range 1 eV - 100 keV [7]. Polyethylene is commonly selected because of its high moderating power and ratio.

Table 1.3: Moderating powers and ratios of selected materials.

Moderator	Moderating power (1 eV - 100 keV)	Moderating ratio
Water	1.28	58
Heavy water	0.18	2100
Graphite	0.064	200
Polyethylene	3.26	122

1.2 Neutron detectors

In the following sections a brief description is provided for two common types of neutron detectors, the BF_3 tube for slow neutrons and the Long Counter for fast neutrons.

1.2.1 The BF_3 tube for slow neutrons

A widely used detector for slow neutrons is the BF_3 proportional tube [8]. It consists of a cylindrical aluminum tube filled with BF_3 at a pressure of 0.5 to 1.0 atm. Aluminum is typically used as the detector wall because of its small cross section for neutrons. The anode is almost always a single thin wire running down the axis of the tube. In this device, BF_3 serves both as the target for slow neutron conversion into secondary particles as well as a proportional gas.

When a neutron is absorbed by the ^{10}B component of the gas, an α particle and a recoil ^7Li nucleus are produced, travelling off in opposite directions and creating primary electron-ion pairs in the gas. The size of the resulting pulse depends on whether the lithium nucleus was left in the ground state or an excited state. When it is left in the ground state (about 6% of the time), the pulse is larger than if the nucleus were left in an excited state (about 94% of the time). The reason lies in the larger kinetic energy of the charged particles (2.792 MeV vs 2.310 MeV) that is deposited in the gas and creates electron-ion pairs.

If the detector diameter is sufficiently large, all the kinetic energy of the α particle and recoil ^7Li nucleus is deposited in the detector gas [9]. The pulse height spectrum therefore shows two peaks: a large one at 2.31 MeV, when the lithium nuclei were left in an excited state, and a small one at 2.792 MeV, when they were left in the ground state (see Figure 1.3, taken from Ref[2]).

For typical sized tubes (2-5 cm diameter), smaller pulses are often produced because either the α particle or ^7Li nucleus deposit some of its energy in the detector wall rather than the gas. If the neutron interaction takes place in the gas close

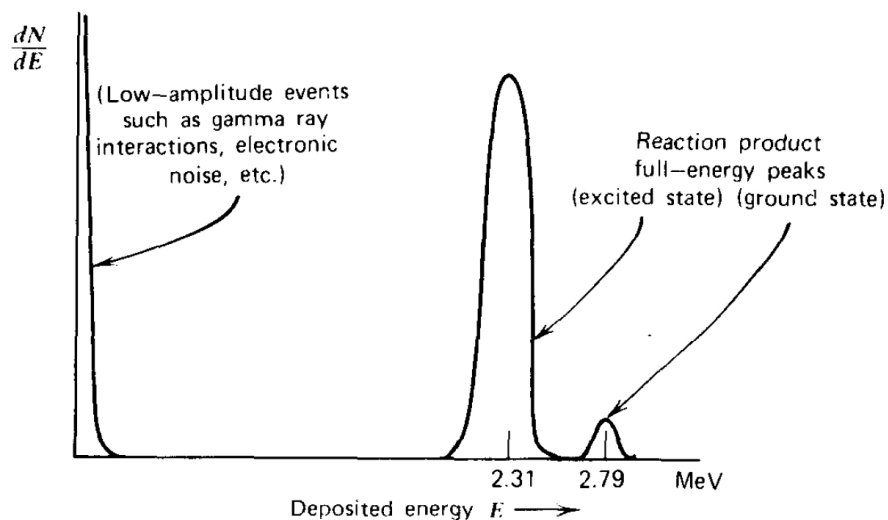


Figure 1.3: Expected spectrum from a large tube in which all reaction products are fully absorbed

enough to one side of the tube for either the α particle or lithium nucleus to strike the wall, the distance to the other side of the tube would be greater than the range of the particle heading towards it. The resulting "wall effect" creates two steps on the left side of the 2.31 MeV peak (see Figure 1.4, taken from Ref [2]).

The lower step on the left is produced as a result of the α particle striking the wall and the ${}^7\text{Li}$ depositing all its energy (0.84 MeV) in the gas. The higher step to the right results from the ${}^7\text{Li}$ nucleus striking the wall and the α particle depositing all its energy (1.47 MeV) in the gas.

Bare BF_3 detectors respond almost exclusively to slow neutrons and they can be surrounded by a suitable moderator in order to be able to detect fast neutrons. The thickness of the moderator can range from 2 to 15 cm, depending on the neutron energy spectrum and other constraints [10].

1.2.2 The Long Counter for fast neutrons

The Long Counter [11], also called "flat response" counter, has a counting efficiency which is nearly energy-independent for neutrons with energy up to 10 MeV. It consists of a neutron detector tube, most frequently a BF_3 tube, placed in the centre of a paraffin cylinder, the latter of which is covered with a layer of B_2O_3 and an additional paraffin layer.

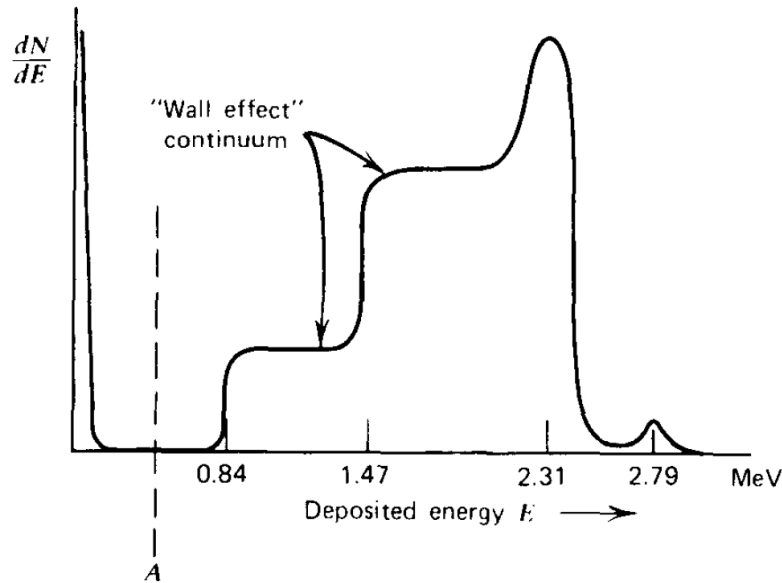


Figure 1.4: Additional Continuum due to the wall effect

The response curve depends on several moderation features. One end of the inner cylinder is not covered by the boron and additional paraffin, so that the device is sensitive only to neutrons coming from the direction of this end. Those from other directions tend to be moderated by the outer paraffin layer and are subsequently captured in the B_2O_3 layer without being detected. Neutrons impinging on the front face will penetrate some distance before undergoing moderation, which increases for increasing neutron energy. The response depends on the diameter and effective length of the moderator and on the length and position of the sensitive volume of the BF_3 tube. The efficiency of common Long Counters is around 1%, while arrangements utilizing multiple gas proportional tubes [12] can reach 11%.

Chapter 2

The Gas Electron Multiplier (GEM) for neutron detection

The Triple Gas Electron Multiplier (GEM) [13], [14] is a detector for charge amplification in gas-filled volumes. The GEM can detect ionizing radiation and thus it can be directly employed for the detection of charged particles and photons. However, applying the methods described in Chapter 1, the indirect detection of neutrons with high efficiency has proved to be possible. A detailed description of the GEM operation principles is given in this chapter, and experimental activities are described for the detection of charged particles and for neutrons. Experiments on the detection of neutrons consist of applying an innovative detector with borated glass sheets as a stray monitor for low energy neutrons inside an irradiation room, time-of-flight measurements with detectors employing several material for slow and fast neutrons, on-line beam profile imaging with high resolution and measurement of the GEM efficiency as a function of the neutron energy.

2.1 The detector

The Triple GEM consists of three thin insulating polymer foils, coated on both sides with thin metal layers which are the two electrodes, a cathode and an anode. The whole structure is perforated with a large number of circular holes, acting as a multiplication channel for electrons released by ionizing radiation in the gas mixture. Applying a suitable voltage difference between the two metal sides of the foils, a high electric field (~ 100 kV/cm) is generated inside the holes and avalanche multiplication occurs if electrons drift into the hole region. With a single multiplier foil a gain of

10^3 can be reached.

2.1.1 The foils

The foils are thin ($\sim 50 \mu\text{m}$) and made of kapton, clad on each side with a thin copper layer ($5 \mu\text{m}$) and chemically perforated with a high density of holes. The holes usually have a bi-conical structure with an external diameter of $70 \mu\text{m}$ and internal of $50 \mu\text{m}$ and a pitch of $140 \mu\text{m}$ (Figure 2.1).

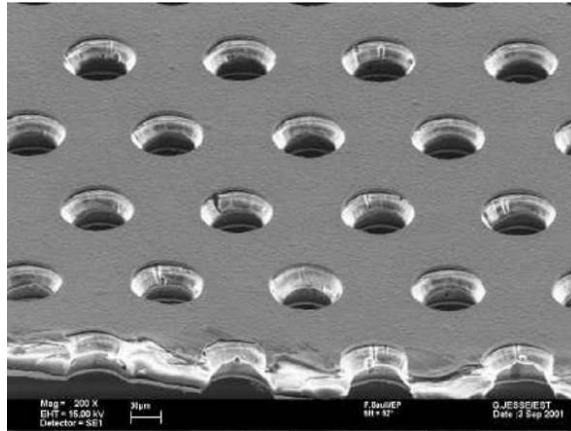


Figure 2.1: Picture of GEM foil taken with an electron microscope

They are manufactured using a double-mask photo-lithography method. Two identical masks are produced, whose pattern is transferred to a photo-resist coated foils by exposure to UV light. The two masks need to be precisely aligned and the patterned copper layer is used as a mask during the chemical process of the kapton etching. The shape of the holes is successively obtained by immersing the patterned foil in a solvent. The chosen geometrical foil parameters affect the electric field lines and therefore the overall efficiency of the detector [15].

2.1.2 The Single GEM

The most simple GEM detector is the single one, where one foil is sandwiched between two flat parallel electrodes. The upper electrode plays the role of cathode and the lower one as an anode, as shown in Figure 2.2.

The drift field E_d is generated by the upper side of the GEM foil and the cathode, and the induction field E_i between the lower side of the foil and the anode. The relative regions are called drift and induction gaps.

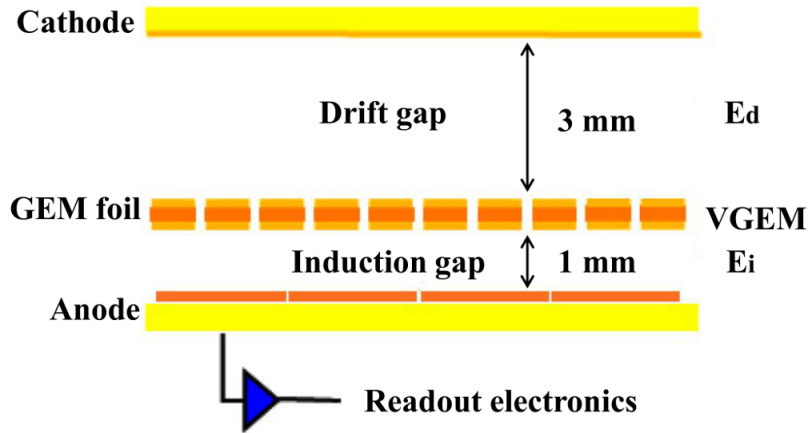


Figure 2.2: The single GEM detector

Ionization electrons produced in the drift gap by charged particles follow the drift lines and move towards the GEM holes, where they are multiplied. The ratio of the number of electrons entering the induction gap over the initial number of electrons in the drift gap is called *Gain*. However, there is a limit for the multiplication process, given by the increase of probability for secondary processes. This limit is called Raether condition [13] and is equal to $G \sim 10^8$. A small number of these electrons are collected on the lower side of the foil without being detected. Most of them however are transferred in the induction region, giving rise to an induced signal on the anode. The fraction of multiplied electrons being transferred depends on the ratio between the two electric fields. The multiplication ions are mainly collected on the upper side of the foil instead of drifting towards the cathode, leaving the GEM hole available for the next multiplication in a relatively short time (few μs).

There are two types of GEM detectors, depending on the direction of the incoming particle with respect to the foil: side-on and head-on. In a side-on detector the particles enter parallel to the foil, while in a head-on enter perpendicular. The configurations are shown in Figure 2.3 and their significance will be explained in Section 2.4.

The characteristics of a single GEM detector that need to be defined are the electric field and the thickness of the gaps, the filling gas and the voltage applied to the foil.

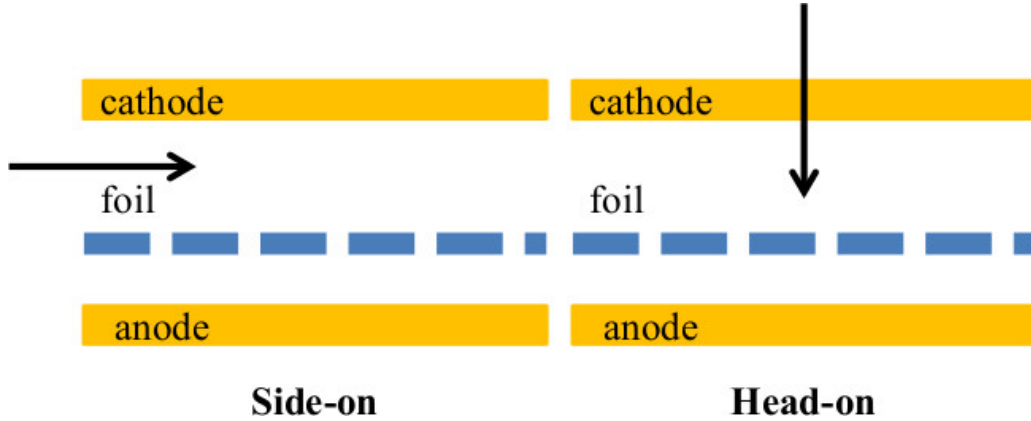


Figure 2.3: Side-on and head-on configuration of the GEM detector

Electric field and thickness of the gaps The geometry of the drift gap needs to provide high particle detection efficiency and for common gases the typical value is 3 mm [14]. The number of electron clusters produced follows the Poisson distribution with an average value \bar{n} , depending on the particle energy and the gas mixture, and is an indicator for the energy deposited. The electron-ion pairs produced need to be separated as quickly as possible, so that their number is not reduced by recombination effects. A fast separation is achieved by applying a high drift field and small drift gaps. In addition, pile-up effects can occur for a wider gap, since the charge integrated by the detector depends on the number of primary electrons released in the gap. The purpose of the drift field is guiding the primary electrons into the GEM holes (Figure 2.4).

Low efficiency can occur for low field values (~ 0.5 kV/cm), due to low electron drift velocity and large diffusion. At intermediate values (1-3 kV/cm), the signal reaches a plateau and decreases again for higher value of drift field [16]. The value of the drift field is chosen in this plateau and depends on the gas mixture for given foil geometry.

The induction gap is typically 1 mm thick in order to maximize the signal fraction integrated by the amplifier. The signal is induced by the electron motion in the gap and therefore the current depends on the time spent by the electrons to cross the induction gap. Assuming that the current signal has rectangular shape, the time equals to the ratio of the drift velocity u_d over the gap thickness x and the current is given by the formula:

$$i = \frac{q \cdot u_d}{x} \quad (2.1)$$

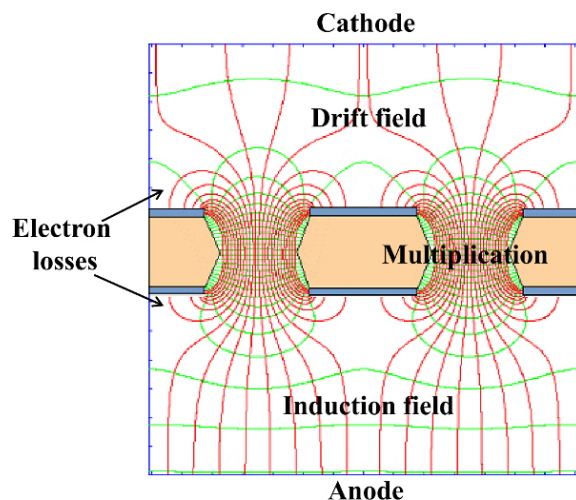


Figure 2.4: The electric field created in the drift and induction gaps

This consideration suggests both the use of a fast gas mixture and small induction gap thickness. However, too small gap can lead to discharges on the anode and gain dis-uniformity.

Voltage applied to the foil The voltage V_{GEM} applied to the foil sides develops a high electric field inside the holes, and the *intrinsic* gain depends directly on the voltage value:

$$G_{\text{intrinsic}} = \propto e^{\langle \alpha \rangle V_{\text{GEM}}} \quad (2.2)$$

where $\langle \alpha \rangle$ is the average of the first Townsend coefficient [17] along the electron path through the hole. This coefficient is gas mixture and field dependent.

The gain is restricted by the extraction and collection efficiencies, namely the probability that an electron enters the induction gap and the signal is collected on the anode. The product of these two efficiencies can be defined as *electron transparency* T . The effective gain of the detector is defined as the product of the intrinsic gain and the electron transparency:

$$G_{\text{eff}} = G_{\text{intr}} \cdot T \quad (2.3)$$

The filling gas In general there are no exclusions on the choice of gas or gas mixture for the operation of any gaseous detector. Since the initiation of gas amplification of a corresponding gas depends on the kinetic energy of the incident particle,

the high voltage limit of the supplying device is theoretically the only constraint. However, a main point in the considerations for a detector is the low working voltage, as it directly affects the design and material constraints.

Noble gases are the best candidates for gas amplification at low electric field due to their shell configuration. A specific minimal amount of ionized gas particle is needed for gas ionization in the drift gap, corresponding to the ionization potential of the gas. Table 2.1 summarizes the excitation (E_x) and ionization energy (E_i) for common noble gases, as well as the average energy (w_i) required to produce one electron-ion pair in the gas [18]. All numbers are for normal temperature and pressure (NTP). Argon was chosen as the main filling gas of the detector.

Table 2.1: Excitation and ionization properties of common noble gases

Gas	E_x (eV)	E_i (eV)	w_i (eV)
He	19.8	24.5	41
Ar	11.6	15.7	26
Ne	16.7	21.6	36
Xe	8.4	12.1	22

Due to primary ionization in the drift region and gas amplification inside the foil, the gas volume is filled with ions and excited atoms, which are not collected by the readout structure. Ions are guided on the field lines to the GEM surface or the cathode, occasionally followed by the emission of a photon. The gas atoms descend to their ground state by either emitting an electron from an inner shell (Auger effect) or by emission of another photon. Taking into account that the minimum energy of these photons is $E_{\text{Ar(g)}} = 11.6$ eV (Table 2.1) and therefore higher than the ionizing potential of copper ($E_{\text{Cu(ion)}} = 7.7$ eV), they may hit metal-clad surfaces in the detector and release new electrons which may undergo amplification processes as well.

To prevent the detection of those undesired electrons, one or more so-called quencher gases can be added to the noble one, creating a mixture. These quencher gases consist of polyatomic molecules, containing more than four atoms, whose large amount of non-radiative excited states allows the absorption of photons in a wide energy range [18]. An additional advantage of quencher gases is decreasing the discharge probability, which will be discussed in Section 2.1.3. Table 2.2 summarizes the properties of common quenching gases.

A gas mixture free of hydrocarbons is non flammable and can withstand high rate environments. Studies have shown [19] that an Ar-CO₂ mixture can provide sufficient drift velocity with relatively low diffusion. Argon has high diffusion, but

Table 2.2: Excitation and ionization properties of common noble gases

Gas	E_x (eV)	E_i (eV)	w_i (eV)
CF ₄	12.5	15.9	54
DME	6.4	10.0	24
CO ₂	5.2	13.7	33
CH ₄	9.8	15.2	28
C ₂ H ₆	8.7	11.7	27
i-C ₄ H ₁₀	6.5	10.6	23

when mixed with CO₂, the effect is reduced and the drift velocity increases. As shown in Figure 2.5 [19], the higher the percentage of CO₂, the higher the velocity for increasing electric field. The gas mixture chosen was Ar 70% - CO₂ 30% and the average energy (w_i) required to produce one electron-ion pair is 30 eV.

2.1.3 The Triple GEM

The use of three GEM foils provides higher gain because each foil acts as preamplifier for the next one. Apart from the drift and induction gap, two transfer gaps are defined between the foils, as shown in Figure 2.6.

The transfer gaps Gas ionization occurs in every gap of the detector when ionizing radiation is present. The main difference between the primary electrons produced in the various gaps is the number of multiplication steps they undergo along their drift towards the anode; electrons produced in the drift gap are multiplied three times, while those generated in the first drift gap cross only two foils. As a result, electrons produced in the first drift gap by background radiation can induce a signal large enough to be discriminated by the front-end electronics. This fact suggests that the gap thickness has to be kept as low as possible and the typical value is 1 mm.

Primary electrons produced in the second transfer gap very rarely give rise to a detectable signal, since they are multiplied only in the last foil. However, the thickness of this gap is correlated with the discharge probability. When the gain exceeds the Raether limit discussed in Section 2.1.2, the electric field is strongly increased near the front of the avalanche and can lead to a spark breakdown. This effect can be reduced using a quencher gas and increasing the thickness of the second transfer gap. In this way the electron diffusion is increased and the electron cloud can be spread over more than a single hole, reducing the probability of reaching the Raether limit. The typical thickness of the second transfer gap is 2 mm.

Voltage applied to the foils For a triple GEM detector the *intrinsic* gain is an exponential function of the total voltage applied to the three foils $V_{\text{GEM}}^{\text{tot}}$. Considering the electron transparency *electron transparency* T_{tot} , the *effective* gain is defined as:

$$G_{\text{eff}} = e^{\langle \alpha \rangle^{\text{tot}} V_{\text{GEM}}^{\text{tot}}} \prod_{i=1}^3 \epsilon_k^{\text{coll}} f_k^{\text{extr}} \quad (2.4)$$

At a fixed $V_{\text{GEM}}^{\text{tot}}$ it is advisable to increase the voltage applied on the first foil and reduce the one applied to the third in order to reduce discharge effects. In this case, the charge reaching the third foil is greater but the diffusion effect spreads the electron cloud over a larger number of holes, reducing the discharge probability. The

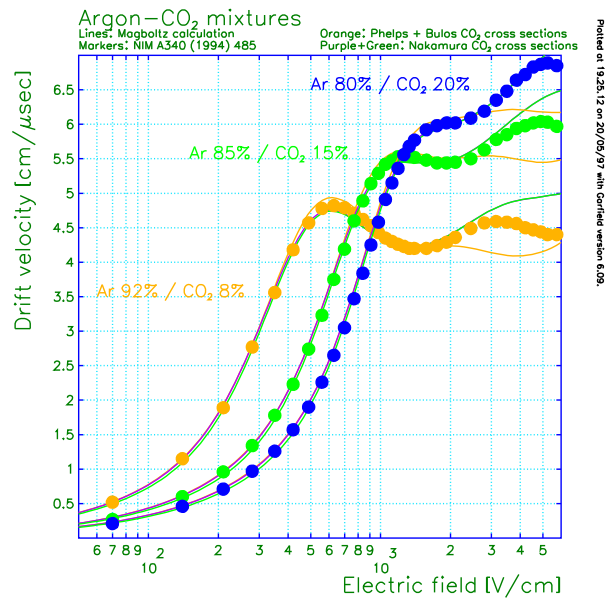


Figure 2.5: Drift velocity in increasing electric field for mixtures of Argon - CO₂. Taken from Ref. [19].

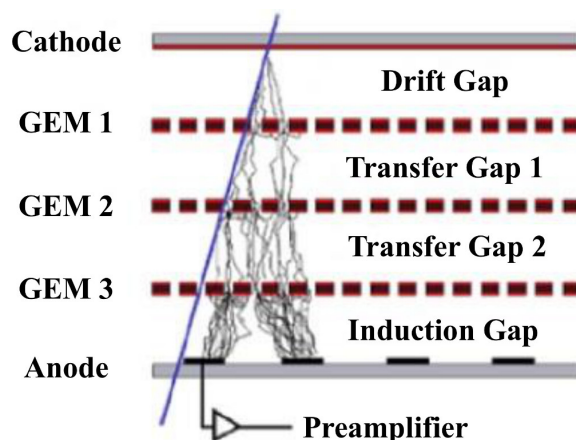


Figure 2.6: The triple GEM detector

optimal configuration of the GEM voltages is:

$$V_{\text{GEM}}^1 \gg V_{\text{GEM}}^2 \geq V_{\text{GEM}}^3 \quad (2.5)$$

The voltage applied to the foils is not uniquely determined. For given gaps and gas mixture, the voltage depends additionally on the kind of particle to be detected and its energy, as will be discussed in Section 2.4.

2.2 The acquisition system

The signal generated by the electron cascade is induced on a padded anode, which consists of a total of 128 pads with different sizes depending on the application. The read-out is kept at ground potential and is connected to the front-end electronics. The front-end chips used to readout the pads are the CARIOCA-GEM digital chips [20] (Figure 2.7), each of which holds 8 identical channels of current-mode Amplifiers, Shapers and Discriminators (ASD). The Discriminator produces an LVDS (low-voltage differential signaling) signal with a threshold defined by the acquisition program.

All the CARIOCA chips are connected to a custom made FPGA Mother Board [21] (Figure 2.8) attached to the back of the detector that analyses the LVDS signal coming from the chips. The FPGA board is able to perform count and time measurements of discriminated signals coming from the 128 channels and can collect multiple gates into memory with negligible dead time, allowing an external or an internal trigger.

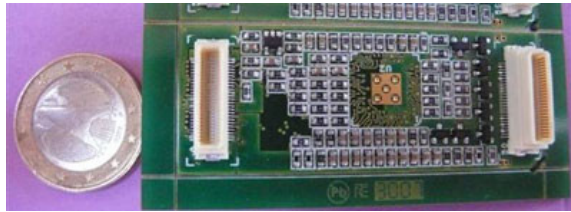


Figure 2.7: The CARIOCA chip



Figure 2.8: The FPGA motherboard

The high voltage system used to power the GEM foils is the HVGEM NIM module [22] (Figure 2.9). It consists of 7 independent HV channels referred to ground, six of which can provide up to 700 V and one up to 1400 V, allowing higher portability of the GEM detector, as well as flexibility in the application of the desired voltage to each foil. In addition, each channel is equipped with a high sensitivity current meter for the detection of possible discharges and the current driven by the detector with 10 nA precision.

2.3 Charged particles

Considering the large active area and the high particle rate ($10^8 \text{ s}^{-1} \cdot \text{cm}^{-2}$) [13] the detector can measure, beam monitoring is one of its main applications. The detector was tested in two hadron beams: one for research at CERF [23] and one for hadron therapy at the National Center for Oncological Hadrontherapy (CNAO) [24] in Italy.

2.3.1 Monitoring of relativistic hadron beams

A triple GEM was used as a beam monitor [25] at the CERN-EU high-energy Reference Field (CERF) [23] facility at CERN during the December 2012 run [26]. The CERF facility is installed in one of the secondary beam lines (H6) from the Super



Figure 2.9: The HVGEM NIM module

Proton Synchrotron (SPS). A 120 GeV/c positively charged hadron beam composed of 61% π^+ , 35% p^+ and 4% K^+ hits a copper target generating a wide spectrum of particles, while the beam extraction time (spill) from the SPS lasts 9.5 s over a 45 s cycle. The beam intensity is approximately constant, producing a constant irradiation field at the exposure locations. The intensity can be adjusted by two collimators in the beam line, which control the horizontal and vertical acceptance. A layout of the experimental area is shown in Figure 2.10.

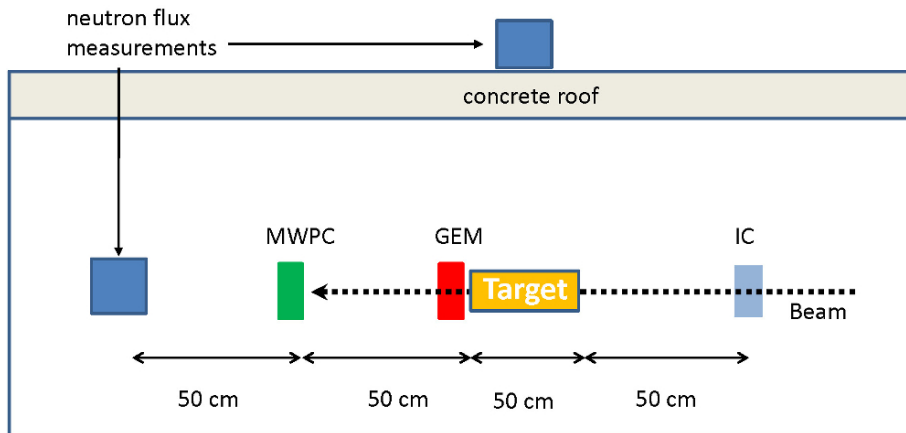


Figure 2.10: CERF facility layout

The profile of the beam is normally measured with a Multi-Wire Proportional Chamber (MWPC) installed in-between the two target positions. The intensity

of the primary beam is monitored by an air-filled ionisation chamber (IC) [27] at atmospheric pressure, placed in the beam just upstream of the copper target. A triple GEM detector with a $1\ \mu\text{m}$ aluminium cathode was used as a beam monitor between the MWPC and the copper target, with a view to replacing the Polaroid films used up to now for the beam set-up on the target. The GEM was mounted on a stand aligned to the centre of an aluminium tube that replaced the target for these measurements (Figure 2.11).



Figure 2.11: Experimental set-up. The GEM detector on the left is aligned to the aluminium tube (target position). The beam is impinging from right to left.

Measurements of beam profile and intensity The detector has an area of $5 \times 5\ \text{cm}^2$, the read-out pad size is $6 \times 3\ \text{mm}^2$ and it was filled with Ar/CO_2 (70/30). The acquisition system was the one described in Section 2.2. The beam profile was measured with both the MWPC and the GEM and compared for different intensities. In addition, good correlation was found between GEM and IC counts during an intensity scan, resulting in 137 ± 2 GEM per IC count with a rather constant efficiency of $0.63 \pm 0.02\%$ in the range from 10^7 to 10^8 particles per spill.

Multi Wire Proportional Chambers (MWPC) are used in many transfer lines and experimental areas at CERN. They can provide reliable X and Y profile measurements but present some limitations, such as saturation at high intensities and limited spatial resolution. In order to overcome these constraints, the beam profile obtained with the MWPC and the GEM was compared. The vertical and horizontal position of the beam and the sigma of the associated Gaussian distributions were determined with the MWPC (Figure 2.12a) and the GEM (Figure 2.12b).

The beam line collimators were adjusted in order to obtain the desired beam

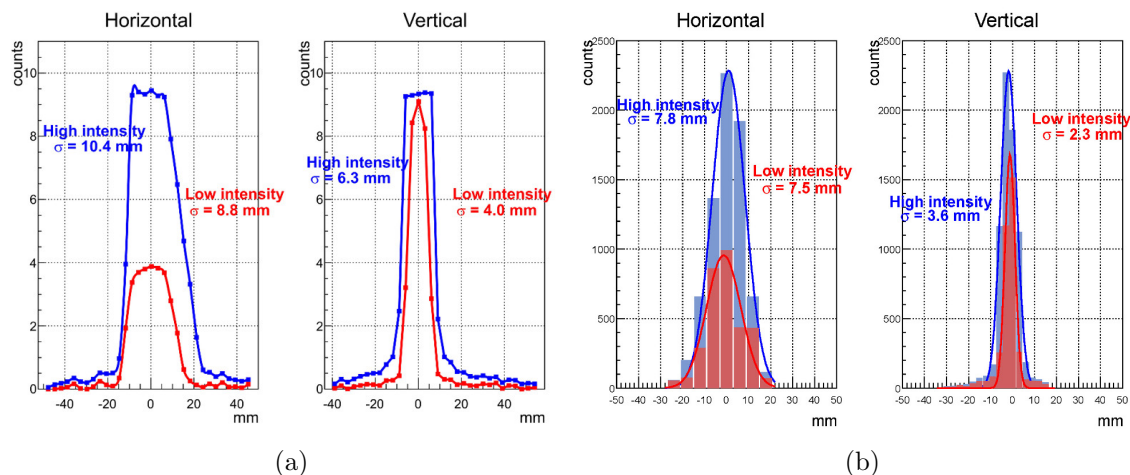


Figure 2.12: Beam profile measured with the MWPC and the GEM for low and high intensity. a) Beam profile from the MWPC. The chamber saturates at high intensity. b) Beam profile from the GEM, well-fitted with a Gaussian curve.

intensity. The flux of beam particles ranged from $8 \cdot 10^4 \text{ s}^{-1}$ to $8 \cdot 10^7 \text{ s}^{-1}$ and a scan was performed in this intensity range. By progressively opening the collimators, the beam remained aligned on the target with increasing intensity, but with a slight diffusion. Figure ?? shows that at high intensity the MWPC saturated, which increases the uncertainty of the sigma of the Gaussian distribution.

2.3.2 Quality Assurance of hadron-therapy beams

The same detector was tested as part of the Quality Assurance (QA) system of the CNAO Center [24] for a pencil carbon ion beam. The detector was irradiated with a scanning beam procedure, delivering a uniform dose distribution on a $4 \times 4 \text{ cm}^2$ area. The beam intensity was 10^6 particles per spot and energy 252 MeV/c, corresponding to a water equivalent depth of 125 mm. The FPGA electronic readout was detached from the detector to avoid electronics damage due to the high dose and the connection was made with 3 m cable (Figure 2.13a). A radiochromic foil was placed in front of the detector and the horizontal profiles acquired with the GEM and the foil are compared in Figure 2.13b. More information can be found in reference [28].

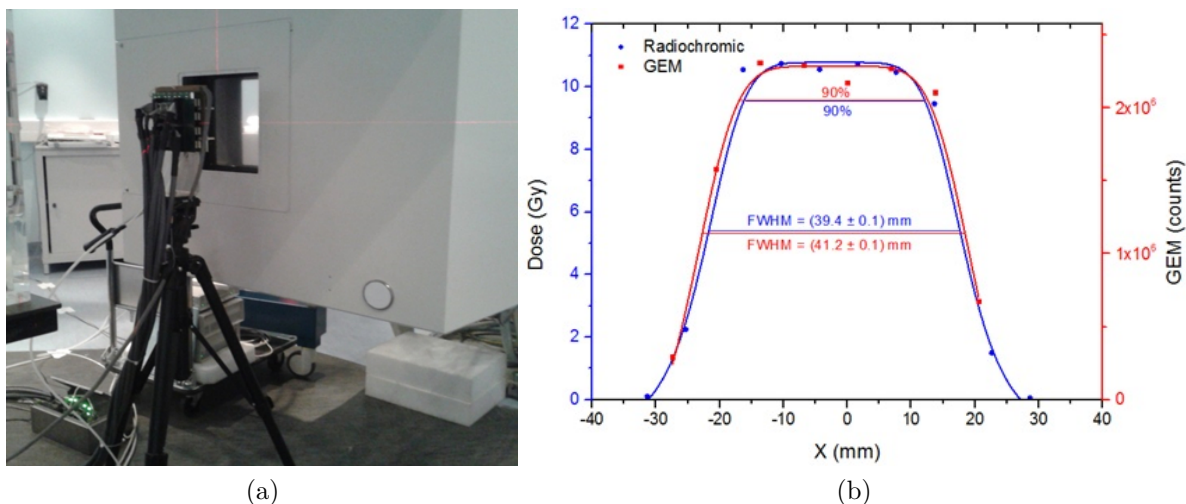


Figure 2.13: a) Experimental set-up at CNAO. b) Horizontal beam profile comparison between GEM and radiochromic film.

2.4 Neutrons

The triple GEM detector was firstly investigated as a stray neutron monitor in mixed fields. Neutron time-of-flight measurements were also performed and the beam spectrum at n_TOF [29] was obtained by means of several detectors with appropriate converters. The operation of the device as a neutron beam monitor was demonstrated, measuring online at the same time the beam profile and the count rate. In addition, the effect of polyethylene to the neutron time-of-flight and beam profile was explored.

2.4.1 Stray neutron monitoring

A triple GEM detector for low energy neutrons and high rejection of gamma background [30] was tested at CERF during the December 2012 run [26] as stray neutron monitor, measuring the low-energy neutron flux scattered from the target inside the cave (Figure 2.14). The measured neutron count rate was correlated with the reference beam monitor IC count rate and compared with previous Monte Carlo simulations of the radiation field around the target.

The device has a side-on configuration (see Section 2.1.2) with a window of 2.25 cm² and filled with Ar/CO₂ (70/30), as schematically shown in Figure 2.15. The charged particles produced from neutron interactions in the borated glass ionize the

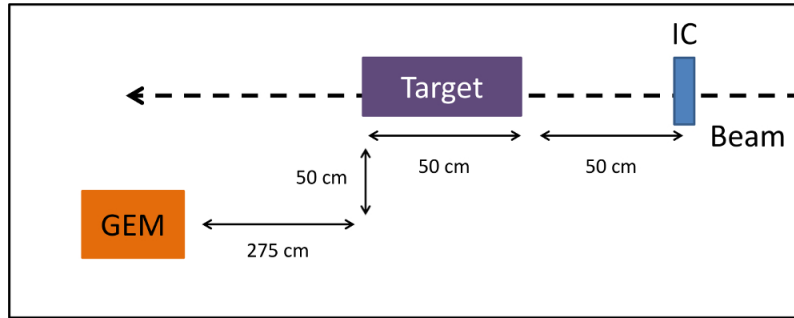


Figure 2.14: CERF experimental layout

gas mixture in the drift region of the detector thus producing secondary electrons. These electrons drift reaching the three GEM foils where they are multiplied and finally induce a detectable signal.

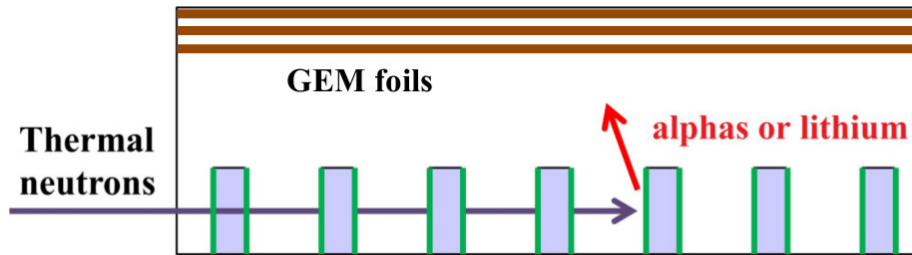


Figure 2.15: Thermal neutron conversion in the borated sheets

Borated glass sheets were used for the detection of slow neutrons. When a neutron is absorbed into the ^{10}B layer, an alpha particle and a ^7Li ion are produced through the reactions described in Section 1.1.1.1. One set of five glass sheets $40 \times 10 \times 1 \text{ mm}^3$ was borated with $300 \text{ nm } ^{10}\text{B}$ on both sides using an electron deposition technique and placed in the same detector with another set of five sheets, which were not borated. By having the two sets placed together it is possible to check the difference in their performance under localized irradiation (Figure 2.16).

The side-on geometry is often preferred than the head-on, because the probability for neutron conversion increases with the number of borated sheets. A simulation with the FLUKA [31], [32] Monte Carlo code was performed in order to investigate this fact. Five borated glass sheets with the same dimensions as for the detector were simulated, with a thermal neutron flat rectangular beam (0.025 eV) impinging on them. The fluence of alpha particles per cm^2 per primary beam particle was simulated with the USRBIN estimator described in Appendix A.2. The results are

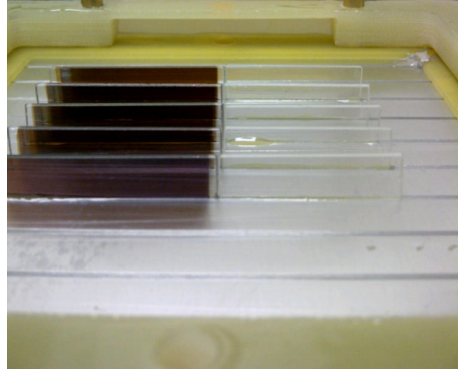


Figure 2.16: View of the cathode with borated glass (left) and simple glass (right)

shown in Figure 2.17 with the beam impinging from left to right.

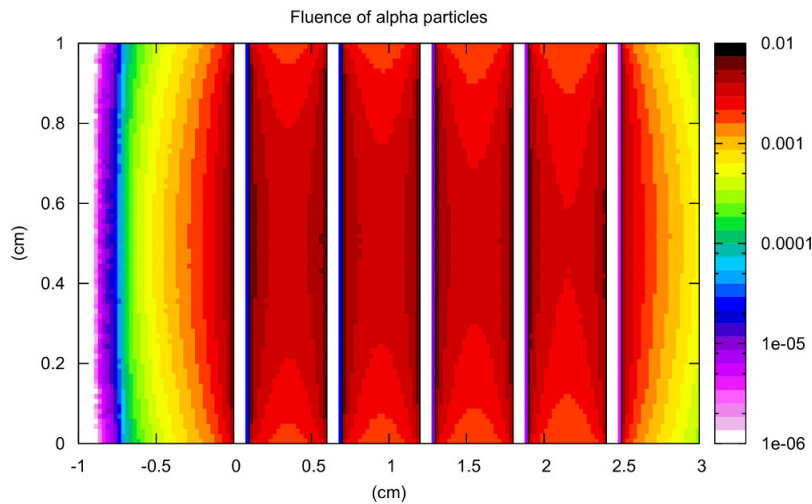


Figure 2.17: Fluence of alpha particles in the drift gap of the detector. The five sheets dimensions are $40 \times 10 \times 1 \text{ mm}^3$. The colour palette on the right indicates the fluence per cm^2 per primary neutron impinging on the sheets.

The alpha particle fluence from neutron conversion decreases slightly from sheet to sheet. This means that the neutron interaction probability is higher in the first sheet and decreases as it moves horizontally inside the drift gap, as demonstrated also in [33]. Alpha particles produced in all sheets will drift to the first foil and initiate the ionization. Therefore the total number of ionizations with 5 converters will be higher than with a single converter. However, the alpha particles produced are not able to cross the glass sheets, as shown in Figure 2.17, since their range is a

few μm for 1.47 MeV. This is a major drawback because it decreases the detection probability.

The signal generated by the electron cascade was induced on a padded anode, which consists of a total of 128 pads, each of area $6 \times 3 \text{ mm}^2$, organized in an 8×16 matrix. The acquisition system was the one described in Section 2.2 and the field values applied were 3, 3, 3, 5 kV/cm from drift to induction gap.

2.4.1.1 Experimental analysis

The detector was first characterized for the pad multiplicity and gain with a view to maximizing the efficiency and photon rejection. The gain of the detector is an exponential function of the total voltage applied to the three foils and depends on the gas mixture. The neutron count rate measured was compared with the one from the IC and was found to have linear response with the number of beam particles on target.

Pad multiplicity Higher multiplication and diffusion takes place with increasing voltage. The electron cluster size is also expected to increase, as it involves more neighbouring pads. The cluster size was measured from the mean number of pad multiplicity by applying a time gate short enough to record only one neutron. The results are shown in Figure 2.18 with a statistical error of 10% and indicate that the multiplicity increases rapidly with increasing voltage.

High voltage working point Since the detector is to be used as a neutron monitor, it is important to distinguish between neutrons and photons, i.e. between charged particles from neutron conversion and electrons from photon interactions. The photon signal is often not detected due to the electronics threshold set to the readout chips. However, if the energy deposited by photons is high enough to generate a detectable signal, such signal cannot be distinguished from the one of alpha particles and ${}^7\text{Li}$ ions, because the detector cannot measure the charge.

A photon rejection technique has been introduced [34], according to which it is possible to discard the photon signal by applying suitable voltage to the foils. For this reason, two HV scans from 750 to 960 V were performed, one with a beam intensity of $5 \cdot 10^5 \text{ s}^{-1}$ particles on target and one with a ${}^{137}\text{Cs}$ source in order to assess the differences in the response. Neutron counts are acquired only from the borated part (Figure 2.16), while background charged particle and photon counts are acquired on both parts. The total number of neutrons is measured by subtracting the counts from the non-borated part and dividing by the pad multiplicity.

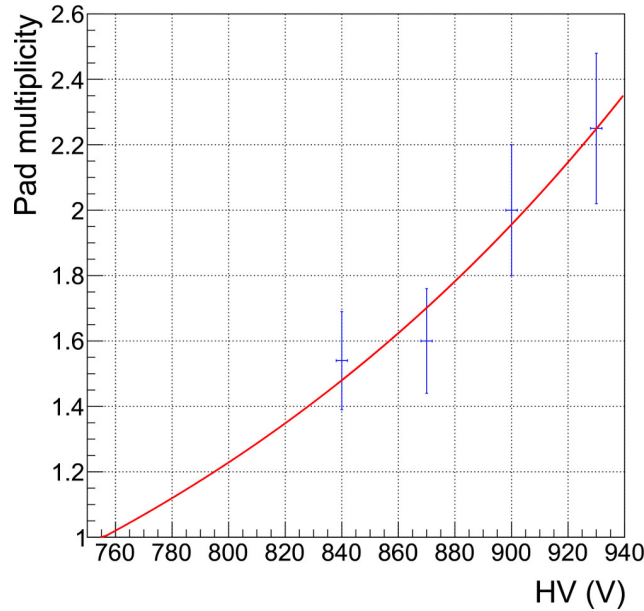


Figure 2.18: Pad multiplicity as a function of increasing HV

The results from the two HV scans are shown in Figure 2.19. Photons start being detected at 870 V, while for lower voltages the signal is derived only from neutrons. The working point was thus determined as 850 V (300-280-270 V for foils 1-2-3, respectively) for highest efficiency and photon rejection. According to past measurements [35], the photon sensitivity is around 10^{-7} .

The distribution of counts on the active area for low gain (820 V) is shown in Figure 2.20a, in which the counts stem mainly from the borated sheets (right section of the detector). However, a few counts are also acquired in the non-borated sheets (left section), due to charged particles emitted by the target. For high gain (900 V, Figure 2.20b) it is possible to see the photon contribution on the non-borated part. When the applied voltage is in the plateau region (820 to 870 V), the contribution from the non-borated part to the total number of counts is 15%.

Detected neutron rate An intensity scan was performed with the flux of beam particles on the target ranging from $8 \cdot 10^4 \text{ s}^{-1}$ to $2 \cdot 10^7 \text{ s}^{-1}$. The time gate was set to 500 ms and the voltage applied to the foils was 850 V, corresponding to a gain of 300 [35]. The IC has a calibration factor of $(2.2 \pm 0.2) \cdot 10^4$ particles per IC count [27]. Good correlation was found between neutron counts and IC counts during the intensity scan resulting in the ratio 0.7 ± 0.1 neutrons per IC count, which is

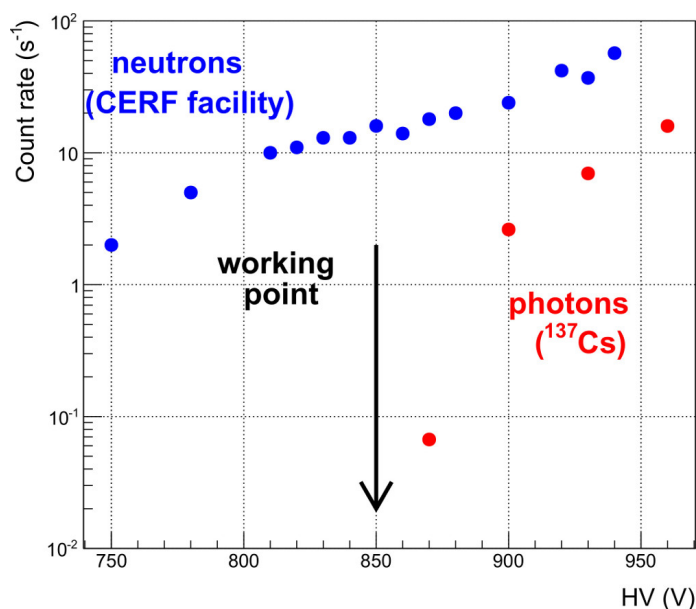


Figure 2.19: Number of counts measured for neutrons and photons with increasing voltage. The photon rejection is below 870 V.

equivalent to $(3.3 \pm 0.1) \cdot 10^{-4}$ neutrons per particle on target per second. The results are shown in Figure 2.21. The neutron flux measured was $(2.9 \pm 0.1) \cdot 10^3 \text{ cm}^{-2} \cdot \text{s}^{-1}$ for the highest beam intensity ($2 \cdot 10^7 \text{ s}^{-1}$).

2.4.1.2 Comparison with FLUKA simulation

The experimental conditions inside the CERF target area were simulated in the past by Vincke et al. [36] with the FLUKA Monte Carlo code (version May 2003), in order to study the response of six air-filled ionization chambers for radiation protection applications. The six detectors were positioned around the target and the particle spectra in each of these positions were simulated. The beam energy and particle composition were the same as those of the present measurements and the estimated particle spectra were computed per primary beam particle and per unit area. For the present measurements the detector was placed in one of these positions (number 6 in ref. [36]). According to the simulations, the neutron energy in this position ranges from 0.025 eV to 20 GeV; the particle spectra are displayed in Figure 2.22. Even though a wide variety of charged particles is present in this position, it is possible to discard their signal by subtracting the counts in the non-borated part from the counts in the borated part (Figures 2.20a and 2.20b). This technique proves to be

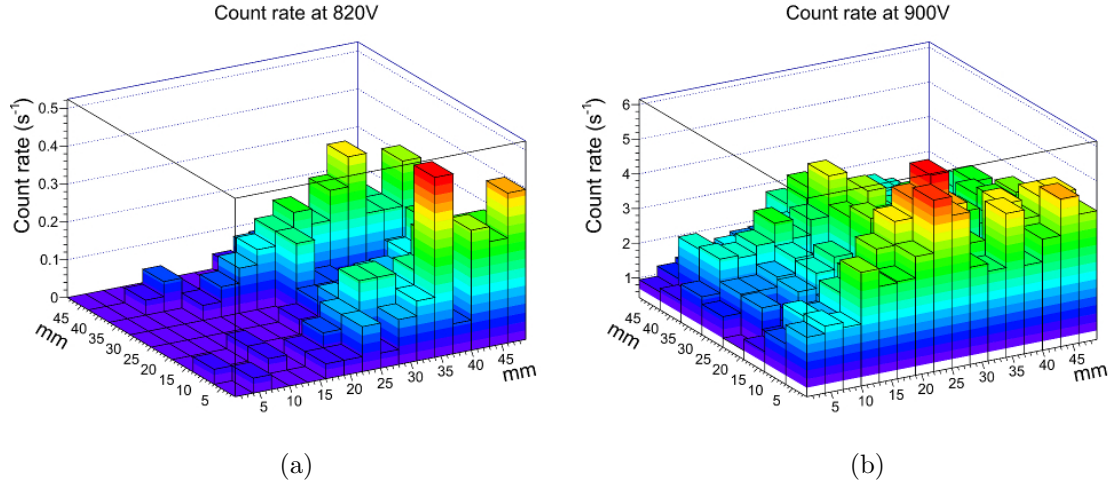


Figure 2.20: Count rate measured for each pad. The left section of the detector corresponds to the non-borated part and the right one to the borated one. a) With HV=820 V neutrons are detected on the right section. b) With HV=900 V the photon signal is detected on both sides.

very useful in mixed fields such as the present case.

The mean efficiency of the detector in the neutron energy range 0.025 eV to 8.5 eV was measured as 4.3% in the TRIGA experimental facility [37], with a neutron spectrum similar to the one at CERF. The total number of neutrons measured at CERF was $(21 \pm 3) \cdot 10^3$. With a detector efficiency of 4.3%, the number of impinging neutrons was estimated at $(49 \pm 8) \cdot 10^4$. The simulated number of neutrons was calculated as $(49 \pm 2) \cdot 10^4$, taking into account that the area of the device window is 2.25 cm^2 . The experimental results are in very good agreement with the simulation and provide a further validation of the simulated neutron field used for instrument tests and workplace calibration.

2.4.1.3 Detector activation

Sensitivity and stability studies have shown that the detector can be activated when irradiated with a high flux of energetic particles [35]. In order to investigate this phenomenon, measurements were performed twenty-four hours after the end of the experiment. The dose rate on the GEM measured with a Geiger-Muller counter was $0.2 \mu\text{Sv/h}$, but no signal was measured with the GEM when the working HV (850 V) was applied. In order to detect such signal, which is probably coming from photons

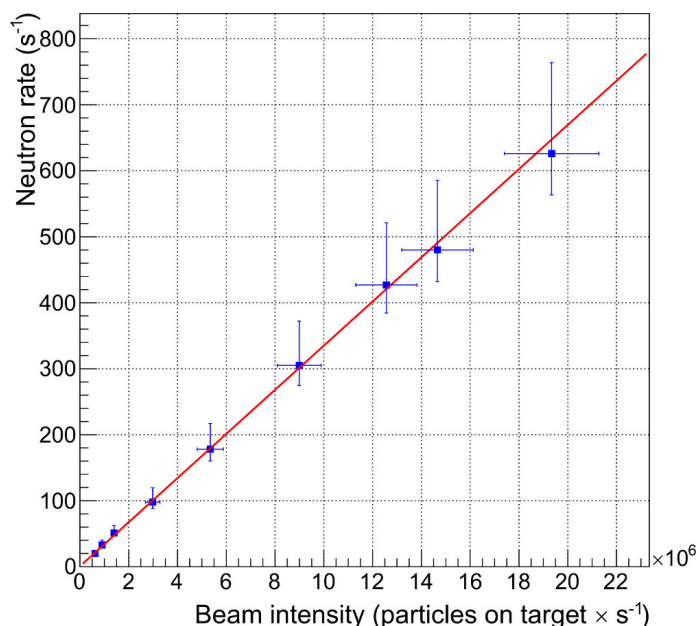


Figure 2.21: Neutrons rate detected per beam particle on target per second.

(gamma rays), the voltage applied to the foils was set to the maximum gain (at 1150 V). The mean counting rate from the total area was 3.2 ± 0.3 counts/s. This effect cannot interfere with the neutron signal during the GEM irradiation because it can only be detected at maximum gain.

Conclusions A Triple GEM detector was previously tested as in-beam monitor of relativistic hadron beams [25]. In this work a version of the device with borated glass sheets has been successfully employed for the detection of scattered low energy neutron radiation. By applying a working HV of 850 V it is possible to reject the photon signal, while the combination of borated and non-borated glass sheets allows the elimination of the signal from background charged particles, thus optimizing the ratio of signal over background. The detector showed linear correlation with the beam intensity, with a ratio equal to $(3.3 \pm 0.1) \cdot 10^{-4}$ neutrons per beam particle impinging on the target, and corresponding to a neutron flux of $(2.9 \pm 0.1) \cdot 10^3 \text{ cm}^{-2} \cdot \text{s}^{-1}$ for the highest intensity. Considering its overall performance as a low energy neutron counter and the negligible activation, the detector can be employed as an online neutron reference counter.

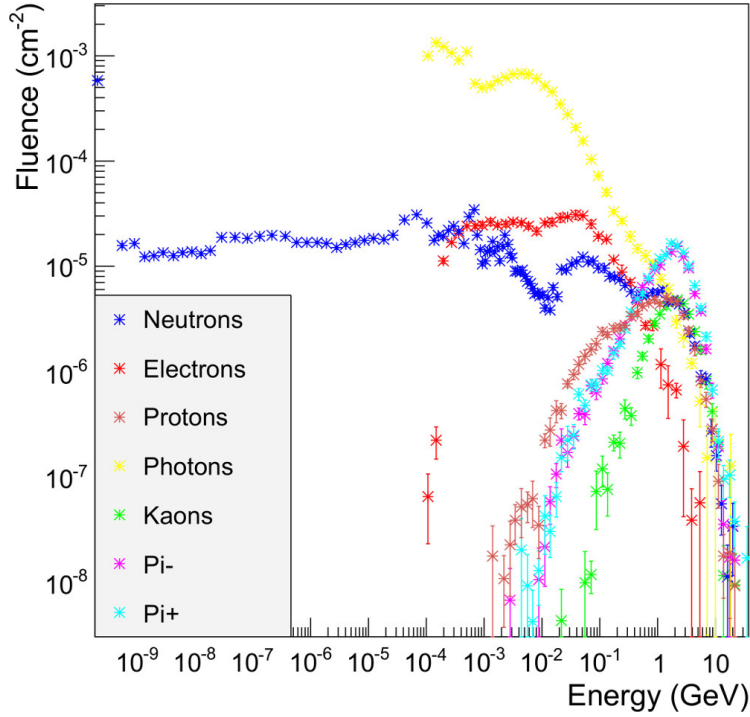


Figure 2.22: Particle spectra calculated with FLUKA (from [36]). Fluence is expressed in particles per cm^2 per primary beam particle. The neutron energy ranges from thermal to 20 GeV.

2.4.2 Time-of-flight

Neutron time-of-flight measurements for both slow and fast neutrons [38], [39] were performed at the nTOF facility [29] at CERN,. This facility features a white neutron source produced by spallation on a lead target through 20 GeV/c protons from the Proton Synchrotron (PS) with a maximum intensity of $7 \cdot 10^{12}$ protons per pulse. Neutrons produced travel inside the beam pipe and arrive at two experimental areas, EAR1 and EAR2 with distances from the target 185 m and 20 m respectively. Measurements can also be performed right before the EAR1 beam dump, located at 200 m from the target. Due to the long flight path and short proton pulse, the neutron time-of-flight defines their kinetic energy and the spectrum produced ranges from 10^{-3} eV to 1 GeV (see Figure 2.23). Using the PS trigger it was possible to synchronize the GEM data acquisition in order to select a given neutron energy window and measure the time-of-flight and detector efficiency as a function of neutron energy.

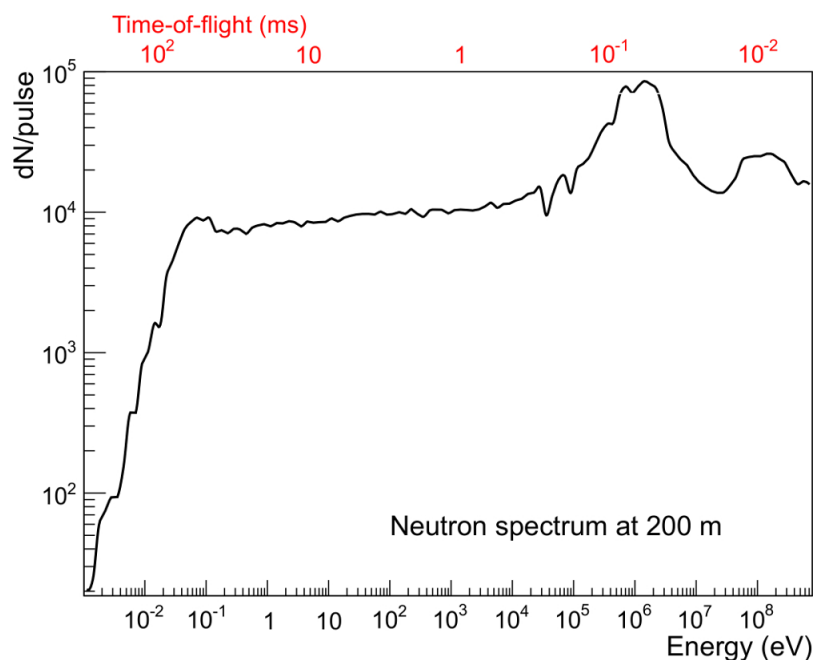


Figure 2.23: Neutron spectrum arriving at 200 m at n-TOF [29].

Detectors and experimental set-up One of the GEM detectors for low energy neutrons, named GEM ^{10}B and described in detail in Section 2.4.1, has an active area of $5 \times 5 \text{ cm}^2$ and glass sheets borated with a thickness of 300 nm on both sides. The second detector for low energy neutrons has an active area of $10 \times 10 \text{ cm}^2$ and a $1 \text{ }\mu\text{m}$ B_4C cathode [37]. The fast neutron GEM detector [40] equipped with $60 \text{ }\mu\text{m}$ polyethylene (PE) and $40 \text{ }\mu\text{m}$ aluminium has an active area of $10 \times 10 \text{ cm}^2$. The detectors were filled with a gas mixture of Ar/CO_2 (70/30), their anodes are composed of 128 pads of different sizes and the acquisition system was the one described in Section 2.2. Their characteristics and measurement positions are summarized in Table 2.3.

Table 2.3: Summary of detector characteristics and positions for beam energy spectrum and imaging measurements.

Detector	Conversion	Area (cm^2)	Pad size (mm^2)	Position
GEM ^{10}B	^{10}B	5×5	3×6	185 m
GEM B_4C	B_4C	10×10	8×8	200 m
GEM PE	PE	10×10	8×8	200 m

The detectors GEM B₄C and GEM PE were placed at a distance of 200 m from the target, between the beam pipe and the dump (Figure 2.24a). They were mounted on a stand and remotely centred by means of a rail, so that the beam impinges vertically to the foils. The FPGA-based motherboard used to analyse the signal coming from the read-out chips was placed off-beam (see Figure 2.24a) in order to avoid possible interruptions due to the high beam flux, discussed later in Section 2.4.2.3. The GEM ¹⁰B was tested inside the experimental area (EAR1) at a distance of 185 m (Figure 2.15). Since it is a side-on detector (see Figure 2.3), the beam impinges parallel to the foils through the window.

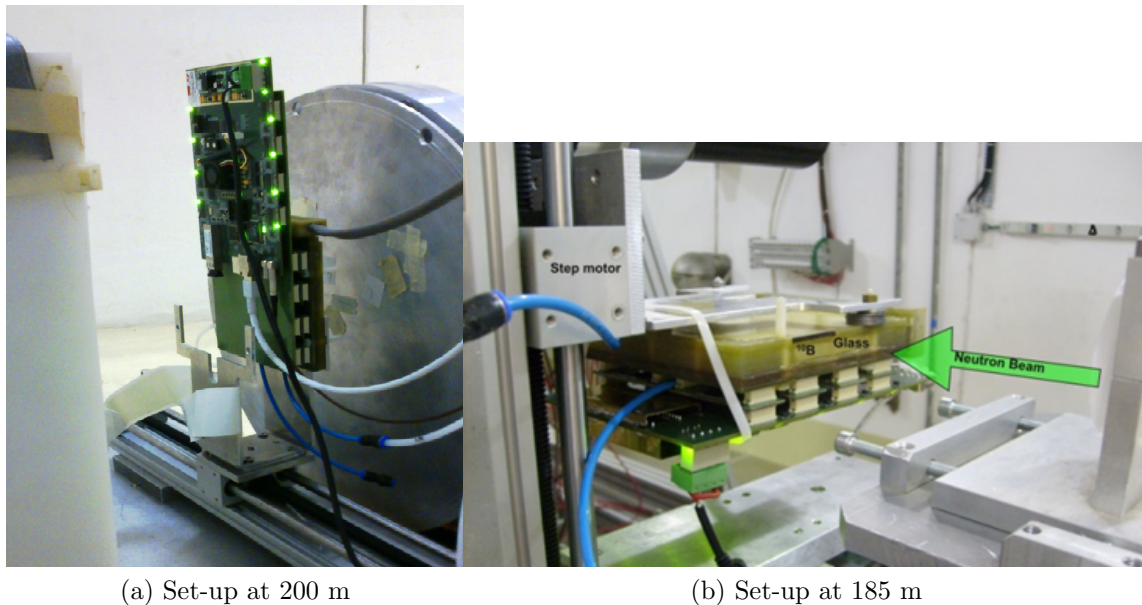


Figure 2.24: Experimental set-up at 200 and 185 m. a) The head-on detectors GEM B₄C and PE were placed at a distance of 200 m, between the beam pipe and the dump. b) The side-on detector GEM ¹⁰B was tested at 185 m, inside the Experimental Area 1 (EAR1).

2.4.2.1 Time-of-flight measurements

Time-of-flight measurements were performed via the FPGA-based motherboard, externally triggered a few μ s before the proton beam hits the target. The beam energy spectrum was measured from the neutron time-of-flight, using the classical kinetic energy formula for energy less than 1 MeV (Equation 2.6) and the relativistic one

for more than 1 MeV (Equation 2.7). Thus the time-of-flight ranged from 700 ns for 1 GeV to 150 ms for thermal neutrons.

$$E_n = \frac{1}{2} m \cdot v^2, \quad E_n < 1 \text{ MeV} \quad (2.6)$$

$$E_n = m c^2 (\gamma - 1), \quad \gamma = \left(1 - \frac{v^2}{c^2}\right)^{-\frac{1}{2}}, \quad E_n > 1 \text{ MeV} \quad (2.7)$$

where c is the speed of light and v the neutron velocity ($v=L/t$ with L being the distance from the target and t the time-of-flight).

Two different acquisition methods were employed by means of the FPGA: the multi-slide and the delay scan methods for slow and fast neutrons respectively. The multi-slide method allowed measurement of up to 250 successive gates of the same width in once, without any dead time between them and with a minimum width of 30 μs each. The delay scan method was performed by increasing the delay by a specific time-window and applying a gate of the same width with a minimum of 20 ns.

The data acquisition for GEM ^{10}B (185 m) was organized in 150 slices for a gate of 1 ms width for each slice. A delay of 10 ms was applied, so that the measured energy ranged from thermal energy to 2 eV. Measurements with GEM B_4C (200 m) were performed in two stages: 200 slices of 0.05 ms each were acquired in the range 2 eV to 10 keV and 400 slices from thermal energy to 2 eV with a gate of 0.5 ms. A delay scan of 100 ns gate was performed for fast neutron measurements with GEM PE (200 m), resulting in 154 steps for the energy range 1 MeV to 1 GeV.

The number of counts measured per spill for increasing neutron energy is shown in Figure 2.25a for GEM ^{10}B , GEM B_4C and GEM PE. The average number of protons impinging on the target for this acquisition was $(6.5 \pm 0.3) \cdot 10^{12}$ per pulse.

Good correlation was found between the total number of counts measured with GEM B_4C and proton intensity on target varying from $2 \cdot 10^{12}$ to $7 \cdot 10^{12}$ per spill. The detector showed linear response, as shown in Figure 2.25b, with a ratio of $(8.0 \pm 0.4) \cdot 10^{-13}$ counts per proton on target per pulse. The total number of counts acquired for the highest proton intensity was 5.0 ± 0.3 per pulse for thermal up to 10 keV neutrons.

2.4.2.2 Efficiency to neutrons

The efficiency to neutrons was measured as the ratio of the detected counts normalized with the pad multiplicity to the impinging neutrons [29].

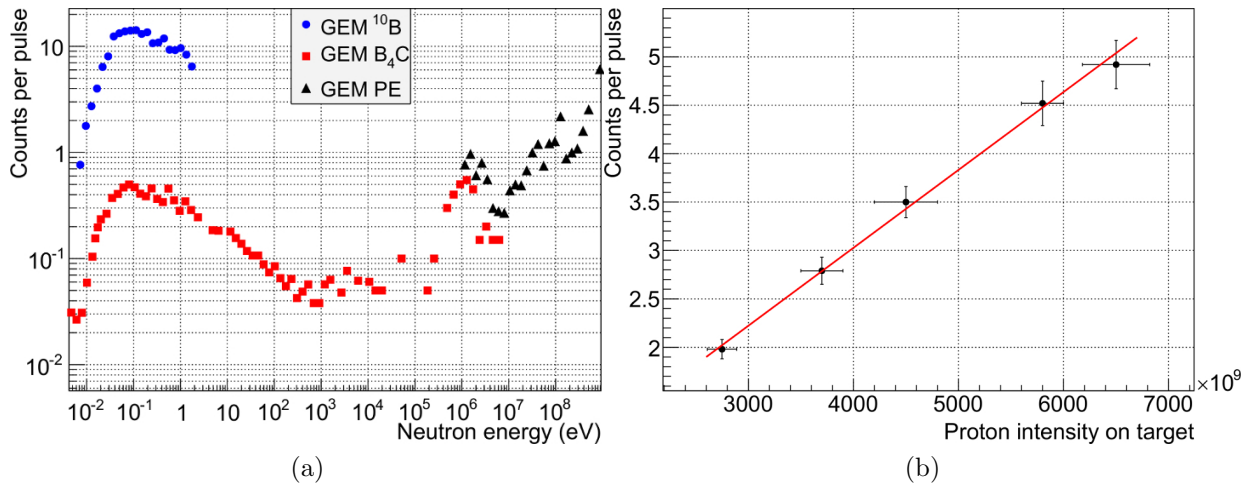


Figure 2.25: a) Number of counts per pulse measured with the detectors GEM ^{10}B , B_4C and PE for increasing energy. b) Correlation plot between measured counts and proton intensity for GEM B_4C .

Pad multiplicity The pad multiplicity, introduced in Section 2.4.1.1, was measured for the GEM B_4C and the results are shown in Figure 2.26.

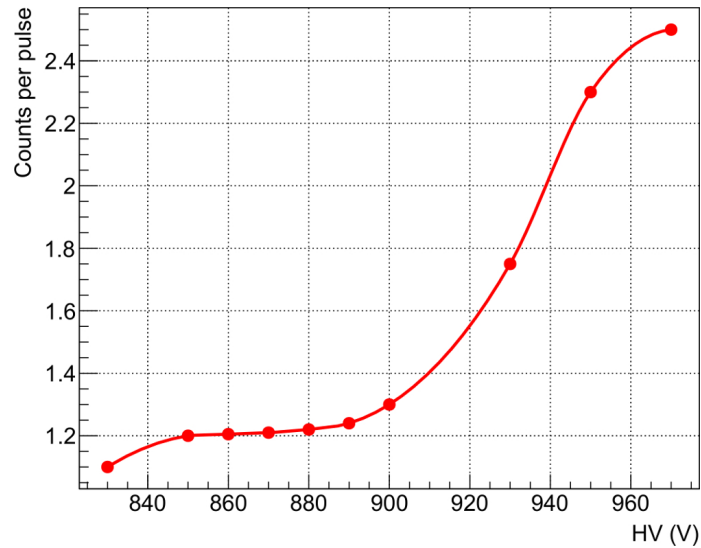


Figure 2.26: Pad multiplicity measured with the GEM B_4C for increasing high voltage (HV) applied to the foils.

The mean number of pads hit per neutron is lower for this device than the one for GEM ^{10}B for the same high voltage applied (see Figure 2.18) and the reason lies mostly in the larger pad size of GEM B_4C ($8 \times 8 \text{ mm}^2$) compared to the one of ^{10}B ($3 \times 6 \text{ mm}^2$). In addition, the electron cloud size for the GEM B_4C is smaller, because the charged particles produced inside $1 \mu\text{m}$ B_4C enter the drift gap with lower energy than those produced inside 300 nm ^{10}B , since they need to cross a larger amount of material before ionizing the gas. As a result, the induced signal is collected from a smaller number of pads. For 880 V the pad multiplicity for B_4C is 1.22 while for ^{10}B is 1.5 from the fitted function (see Figure 2.18).

Efficiency measurements The efficiency of GEM ^{10}B was measured in the past [33] as $4.3 \cdot 10^{-2}$ for thermal neutrons. The present time-of-flight measurements have given the opportunity to measure the efficiency in short energy ranges (Figure 2.27a) with a value of $(4.2 \pm 0.2) \cdot 10^{-2}$ for thermal neutrons. The efficiency decreases for increasing neutron energy because this is the trend of the reaction cross section of $^{10}\text{B}(n,\alpha)^7\text{Li}$. The detector was operated at low gain (300) in order to reject the gamma background, as discussed in Section 2.4.1.1.

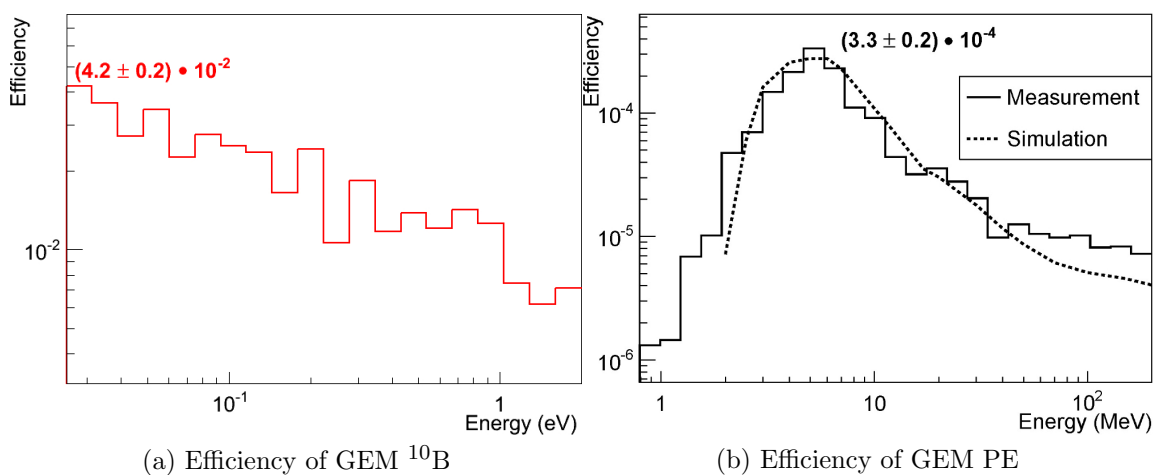


Figure 2.27: Efficiency of GEM ^{10}B and PE measured in the corresponding energy ranges. a) The efficiency of GEM ^{10}B decreases for increasing neutron energy. b) The efficiency of GEM PE increases, reaching a maximum at 6 MeV. A simulation with FLUKA is shown for comparison.

The GEM PE efficiency was measured [40] at the Frascati Neutron Generator (FNG, ENEA-Frascati) [41] as $3.8 \cdot 10^{-5}$ for 2.5 MeV neutrons. At nTOF it was mea-

sured as $(4.8 \pm 0.3) \cdot 10^{-5}$ for the same energy and further extended up to 200 MeV. The average efficiency in the range 2 - 20 MeV was measured as $(1.3 \pm 0.1) \cdot 10^{-4}$, while it was simulated as $1.2 \cdot 10^{-4}$ [40] using the GEANT4 tool [42] and in the present study $(1.3 \pm 0.1) \cdot 10^{-4}$ with FLUKA, using the USRBDX estimator A.2. The results shown in Figure 2.27b are in good agreement with both previous [40] and current measurements.

2.4.2.3 Efficiency to photons

A detailed simulation of the particle spectrum arriving at the nTOF beam dump was performed in the past [43] with FLUKA. Apart from neutrons and charged particles, a high flux of prompt and delayed photons with a spectrum ranging from several keV to several GeV arrives at 200 m. This spectrum was measured with the GEM B₄C applying the working HV of 880 V and employing a delay scan of 50 ns width (Figure 2.28).

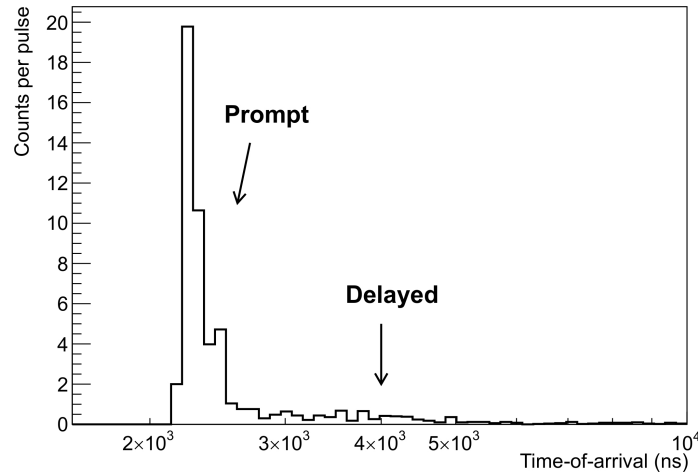


Figure 2.28: Time-of-arrival of the prompt and delayed photon flash measured with the GEM B₄C at 880 V.

The time-window of prompt photons is 300 ns (2100 to 2400 ns arrival time), after which delayed photons are detected. This time window overlaps with the neutron time-of-arrival up to 300 MeV and therefore the neutron spectrum cannot be measured above this energy without photon contribution. According to the simulation, the total number of prompt photons per pulse arriving at the dump was $2.38 \cdot 10^5$ and 30 counts per pulse were measured. Thus the resulting efficiency to photons is $1.3 \cdot 10^{-4}$ and comparable with the GEM PE efficiency to fast neutrons. However, the

neutron flux is always at least 20 times higher than the photon one, so that photons do not contribute to the detected signal.

Saturation point The prompt photon rate of $10^{11} \text{ cm}^{-2} \cdot \text{s}^{-1}$ exceeds the maximum rate of $10^8 \text{ cm}^{-2} \cdot \text{s}^{-1}$ [13] that can be measured with the GEM detector when operated at a high voltage of 1050 V. The number of counts per pulse of the prompt flash was measured with the GEM B₄C for increasing proton intensity on target for an applied voltage of 900 V and 1050 V and the results are shown in Figure 2.29. The detector saturates for 1050 V (2nd order polynomial fit) but shows linear response for 900 V. The saturation point appears at 600 counts for 1050 V, corresponding to $2 \cdot 10^7$ counts $\text{cm}^{-2} \cdot \text{s}^{-1}$ in the 300 ns time-window. Since the device is constantly irradiated by such high photon flux, independently from its counting capability, possible electronics damage can occur and this is the reason why the FPGA Motherboard was placed off-beam, as shown in Figure 2.24a.

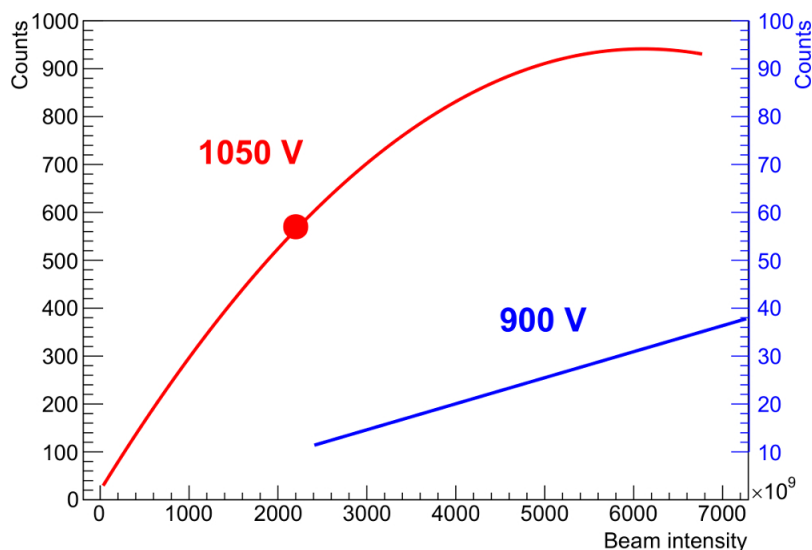


Figure 2.29: Number of counts for increasing beam intensity measured with the GEM B₄C for 1050 V and 900 V voltage applied. The detector saturates for 1050 V, while its response is linear for 900 V.

The saturation effect was observed during the measurement and a snapshot of the beam spot in the acquisition system was taken for these two voltages (see Figure 2.30). The photon flash at 900 V (2.30a) is a Gaussian, while at 1050 V (2.30b) it is an annular distribution, which is flat at the region where the beam spot should

appear. The colour scale on the right of the figures indicates the total number of counts per pad for a number of events, which is not the same for the two acquisitions.

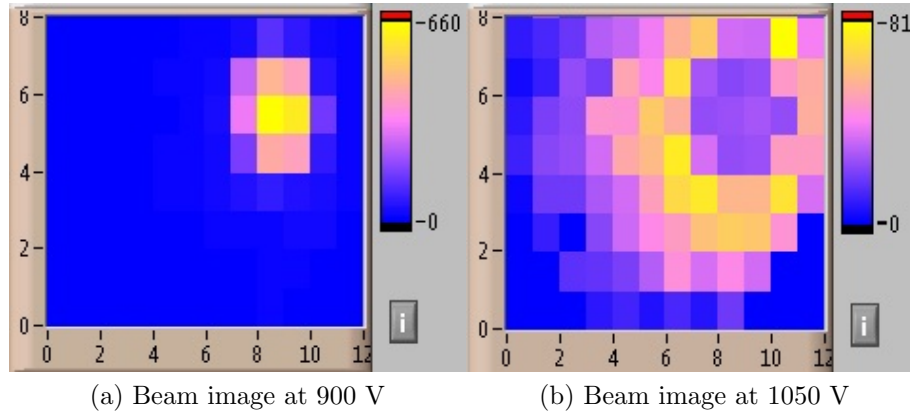


Figure 2.30: Snapshot of the on-line acquisition system measuring the photon flash for 900 V and 1050 V voltage applied respectively.

2.4.3 Beam profile at nTOF

The beam profile was measured with the three GEM detectors, see Table 2.3, at EAR1 (185 m) and the beam dump (200 m) of the nTOF facility. Even though the neutron energy spectrum in Figure 2.23 arriving at these positions should not differ significantly, the beam dimensions are expected to increase for the additional 15 m flight path due to higher diffusion of slow neutrons.

2.4.3.1 Profile at EAR1

The GEM ^{10}B for low energy neutrons was employed for beam imaging at EAR1 (185 m). Since it is a side-on detector and the beam is larger than the detector window, a horizontal and a vertical scan were performed with a step motor in order to reconstruct the entire image. The GEM was fixed on a step motor (Figure 2.24b) and the two scans were performed with 15 steps, each one displaced 3 mm from the previous one.

The following procedure was used in order to reconstruct the beam image:

1. Two matrices, V_{ij} for the vertical and H_{ij} for the horizontal scan, were created and the peak of each count distribution was centred to position (20, 20) cm of each matrix.

2. The two matrices were summed to obtain the matrix $S_{ij} = V_{ij} + H_{ij}$.
3. The matrix S_{ij} was weighted by the entries of another matrix D , composed of numbers 0.5 and 1. Number 0.5 was placed in the bins where there was overlapping of the matrices V_{ij} and H_{ij} , while number 1 was placed at the rest of the bins. Applying this method, it was possible to obtain the arithmetic mean from counts of overlapping bins and the sum from non-overlapping bins.

The reconstructed beam image, following the Gaussian distribution, is shown in Figure 2.31.

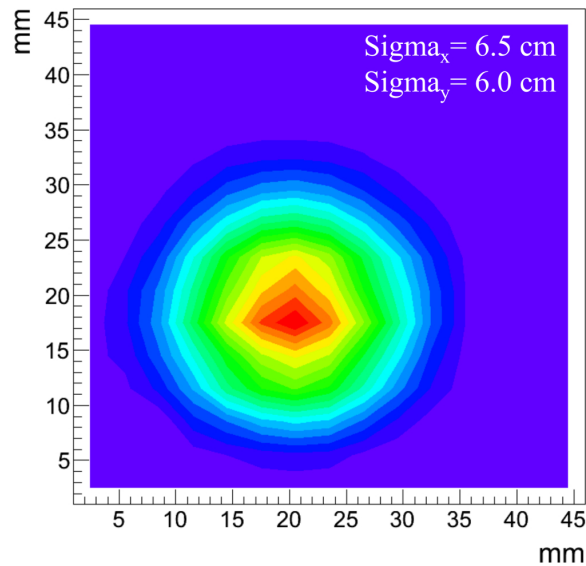


Figure 2.31: Beam profile measured with the GEM ^{10}B at 185 m. The distribution is fitted with the Gaussian function and the sigma in x and y directions is 6.5 cm and 6.0 cm respectively.

2.4.3.2 Profile at the beam dump

The beam image was measured at distance 200 m (beam dump) with the GEM B_4C and the GEM PE. Both detectors are head-on with a $10 \times 10 \text{ cm}^2$ active area and therefore it was possible to acquire the image at once, as shown in Figures 2.32a and 2.32b. The beam spot for low energy neutrons (Figure 2.32a) was found larger than the one for fast neutrons (Figure 2.32b), due to higher diffusion of the slow neutrons while they travel inside the beam pipe.

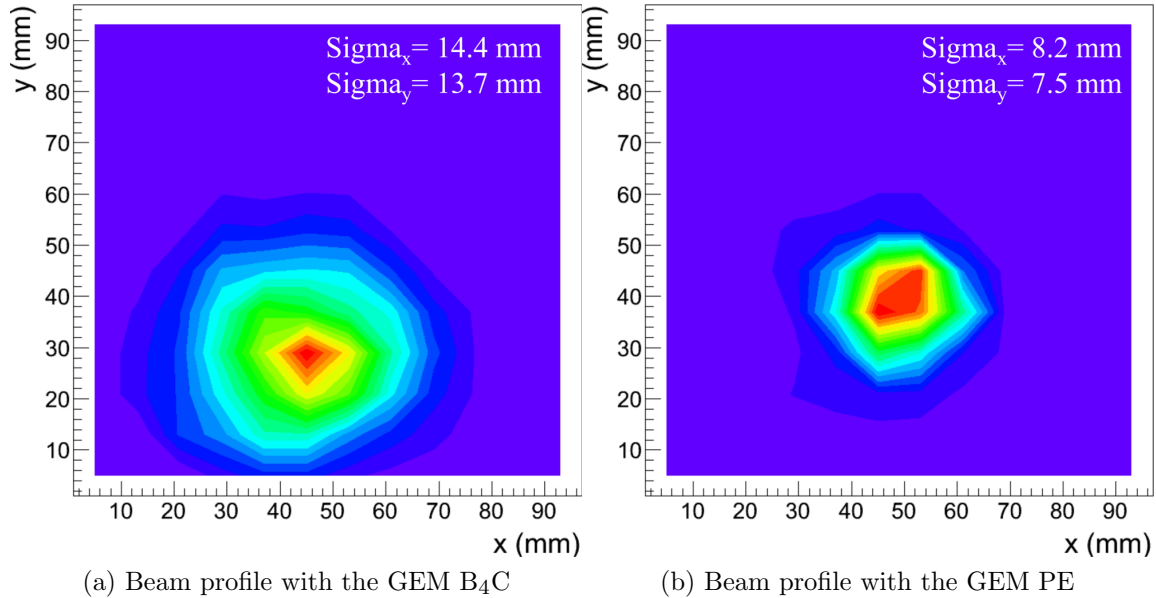


Figure 2.32: Beam profile measured with the GEM B₄C and PE at 200 m. The beam spot is larger for the slow neutron component and the mean of the distribution is shifted vertically.

A significant increase in the beam dimensions of the low energy component is also evident for an additional flight path of 15 m. According to simulations performed for the beam dimensions at 185 m and 200 m [44], the spot diameter was simulated as 4.8 ± 0.2 cm and 10.6 ± 0.2 cm, and it was measured as 4.0 ± 1.2 cm and 8.7 ± 1.6 cm. The results are in fair agreement, given the large measurement uncertainty stemming from the pad size. The fast component of the beam spot at 200 m was measured in the past [45] with another GEM PE (6x12 mm² pad size) and was found to have the same dimensions.

It should be noted that the mean position of the beam spot is not the same for slow and fast neutrons (Figure 2.32), but is shifted vertically by a few cm for slow neutrons. This effect is due to the gravitational force [29], which has a measurable impact on the spatial profile of slow neutrons, while for fast neutrons the profile remains virtually unaffected.

Beam distribution in different energy ranges The energy distribution of the neutron beam was measured by means of the FPGA-based acquisition system, described in Section 2.2. This system allows an off-line analysis of the beam image

in specific energy ranges, in order to measure possible differences in shape. The sigma of the fitted beam distribution measured with the GEM B₄C in horizontal (x) and vertical (y) direction is shown in Table 2.4 for different energy ranges. It is evident that the size of the beam increases significantly in the thermal region (0.01 to 0.05 eV), an effect which mostly concerns the x direction.

Table 2.4: Sigma in x and y direction of the fitted beam distribution for different energy ranges, measured with the GEM B₄C.

Range (eV)	Sigma x	Sigma y
0.01 - 0.05	16.1 ± 0.3	13.9 ± 0.2
0.05 - 2	14.8 ± 0.2	13.8 ± 0.2
2 - 8	14.4 ± 0.2	13.7 ± 0.2
8 - 100	14.3 ± 0.1	13.6 ± 0.2

2.4.4 Neutron moderation effects

The effect of neutron moderation using polyethylene was investigated by placing 1 cm and 3.5 cm thickness on the GEM B₄C which was installed in front of the beam dump at nTOF. The polyethylene pieces were manufactured in such a way as to perfectly fit on the detector, without leaving any gap when placed in front of it. The experimental set-up is shown in Figure 2.33. The new neutron time-of-flight and beam dimensions were measured in order to explore the moderation effect, discussed in Section 1.1.2.2.

2.4.4.1 Effect on time-of-arrival

The nTOF spectrum (see Figure 2.23) shows a high neutron fluence at 1 MeV and is approximately flat for lower energies. By placing polyethylene in front of the B₄C detector, the following interactions take place:

1. Recoil proton production from fast neutrons contribute to the signal detected, as described in Section 1.1.2.1.
2. Moderated fast and intermediate neutrons have higher probability of conversion to alpha particles and lithium ions, according to the conversion reaction described in Section 1.1.1.1.



Figure 2.33: Experimental set-up at 200 m. Pieces of polyethylene are placed in front of the GEM B₄C.

It should be noted that the correlation between time-of-flight and energy is lost when such an amount of polyethylene is used, because neutrons are delayed while scattered inside the material. The time-of-flight spectrum was measured by employing a delay scan procedure for the fast neutron part and a multi-slide for the slow part, as described in Section 2.4.2.1. The spectra acquired with and without polyethylene are compared in Figure 2.34.

The peak at 11 μs , corresponding to 1 MeV when measured with B₄C, is shifted to 40 μs with B₄C + 1 cm PE due to the mechanisms described above, and especially due to recoil proton production. The maximum transferrable energy from polyethylene is 31.4%, see Table 1.2, which means that 1 MeV neutron can transfer up to 300 keV energy to the recoil proton. The peak at 40 μs corresponds to these 300 keV protons. Adding 3.5 cm polyethylene, the peak is higher and further shifted to 100 μs , both due to recoil proton production and moderation of fast neutrons.

A high peak appears at 11 ms with B₄C + 1 cm PE due to fast and intermediate neutron moderation. The detector response both for 1 and 3.5 cm polyethylene increases in the region 10 - 1000 eV compared to plain B₄C, but for 1 cm the response is higher. This effects indicates that low energy neutrons have higher probability of being absorbed in 3.5 cm polyethylene, thus never reaching the B₄C layer for

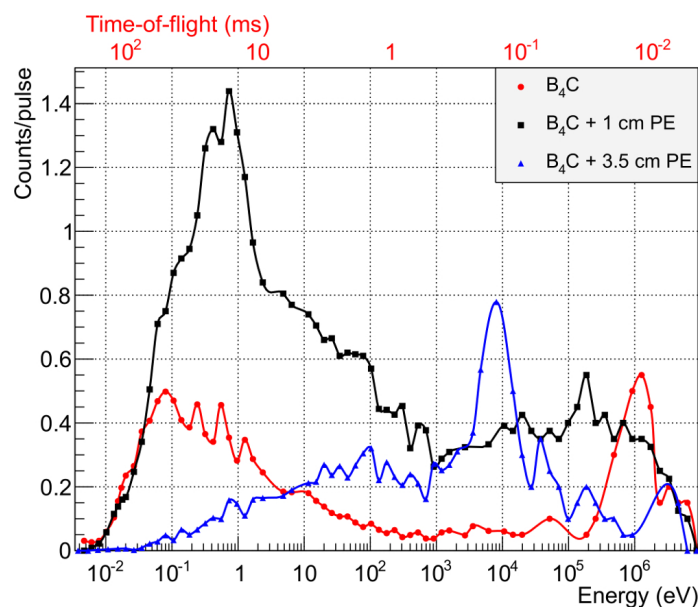


Figure 2.34: Time-of-flight spectra measured with plain B_4C and the addition of two polyethylene pieces, 1 cm and 3.5 cm.

conversion.

The probability of neutron interaction with one of the two mechanisms is described by the corresponding cross-section. The cross-sections [4] for the reactions (n,a) from B_4C and (n,p) from polyethylene are shown in Figure 2.35.

For ~ 1 MeV the cross-section is approximately the same. For energies less than 100 keV, the (n,a) cross section is larger, which means that neutrons are more probable to be converted to alpha particles than recoil protons. Even though the cross-section for (n,p) is not negligible for energies less than 100 keV, the signal induced in the detector for these energies is hardly measurable. The reason lies in the fact that recoil protons produced from 100 keV neutrons have a maximum energy of 30 keV, resulting in average proton energy of 15 keV, while the electronics detection threshold is 20 keV.

2.4.4.2 Effect on beam spot dimensions

The addition of polyethylene causes neutron diffusion and therefore the beam spot dimensions are expected to increase. The sigma of the fitted beam distribution in x and y direction is shown in Table 2.5 for two neutron energy ranges for plain B_4C , $B_4C + 1$ cm PE and $B_4C + 3.5$ cm PE. The beam dimensions increase for increasing

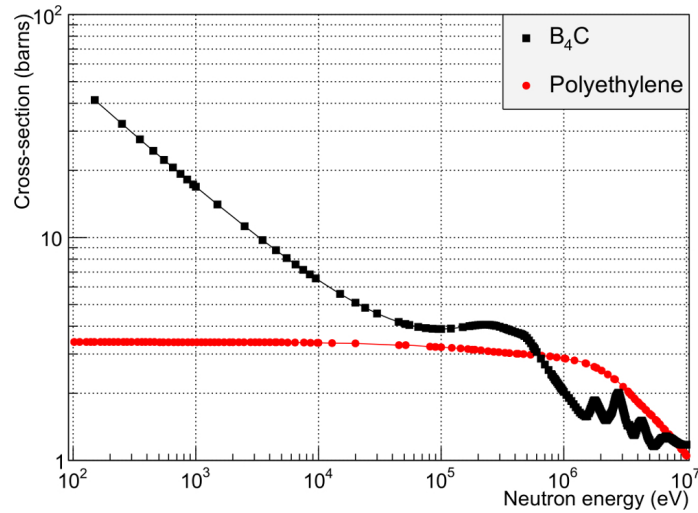


Figure 2.35: Cross-section of the reactions (n,a) in B_4C and (n,p) in polyethylene.

polyethylene thickness, which is more significant for low energy neutrons.

Table 2.5: Sigma in x and y direction of the fitted beam distributions for plain B_4C , $B_4C + 1$ cm PE and $B_4C + 3.5$ cm PE.

Range	Polyethylene (cm)	Sigma x	Sigma y
fast to 10 eV	0.0	14.0	13.8
10eV to thermal	0.0	15.0	14.3
fast to 10 eV	1.0	16.7	16.4
10eV to thermal	1.0	17.3	16.5
fast to 10 eV	3.5	18.4	17.8
10eV to thermal	3.5	25.2	22.1

Neutrons inside polyethylene will undergo elastic and non-elastic scattering. After each collision they travel a mean free path and are deflected by a scattering angle in all directions with equal probability, so that the original motion direction is lost after a succession of collisions. The larger the amount of polyethylene, the higher the number of collisions neutrons undergo before they reach the B_4C layer and are either converted to detectable charged particles, or they deposit all their energy and are absorbed. As a result, a too large amount of polyethylene would completely distort the initial beam spot and the detected neutron distribution would not follow a Gaussian distribution any more.

2.5 Conclusions

The GEM was successfully employed for the detection of charged particles and neutrons. The efficiency was measured as $4.2 \cdot 10^{-2}$ for thermal neutrons with the GEM ^{10}B and $1.3 \cdot 10^{-4}$ for fast neutrons with the GEM PE. The devices were characterized for the pad multiplicity and the HV working point. A photon rejection technique was implemented by applying suitable voltage to the foils. In addition, the GEM detector was proved to be effective in measuring neutron beam profiles (see Section 2.4.3) in different energy ranges via the time-of-flight technique described in Section 2.4.2.1, with a resolution which depends on the read-out pad size.

The GEM detector shows a number of characteristics, which make it suitable as read-out device of the new spectrometer. These characteristics include a large active area, count information in two dimensions, simple data analysis, acceptable efficiency and low-cost material. However, it cannot be used directly for neutron spectrometry because it does not provide energy information. In the two following chapters, the principles of neutron spectrometry and techniques for measuring neutron spectra are presented. This information will then be used to describe the design of SpectroGEM.

Chapter 3

Neutron spectrometry and dosimetry

The collection of instruments and techniques for measuring the energy distribution of neutrons is known as *neutron spectrometry*, the necessity of which is highlighted in this chapter. Spectra characteristics from spallation reactions are firstly discussed and dosimetric quantities in radiation protection are introduced. A description of common spectrometers follows as a preface to the techniques employed for neutron spectrometry.

3.1 Spectra characteristics

Among the possible neutron spectra which are typically produced from various nuclear reactions, the one from spallation is the most common. Spallation [46] refers to nuclear inelastic reactions that occur when energetic subatomic particles interact with a target nucleus. The kinetic energy of the particles needs to be higher than 100 - 150 MeV, so that the deBroglie wavelength λ is smaller than the size of the nucleus. Otherwise, the nucleon does not interact with individual nucleons, but with the whole nucleus. The deBroglie wavelength is given by the formula:

$$\lambda = \frac{h}{\sqrt{2 \cdot m \cdot E}} \quad (3.1)$$

where h stands for the Planck constant and m , E for the particle mass and energy respectively.

Protons are the most common incident particles used for spallation processes and the wavelength for energies of 100 - 150 MeV is $2.8 - 2.3 \cdot 10^{-13}$ cm, which is shorter than the typical size of the nucleus (10^{-12} cm).

The initial collision between the incident particle and the target nucleus leads to a series of direct reactions, called intranuclear cascade, where individual nucleons or small groups of nucleons are ejected from the nucleus. During the first stage of this process, the so-called cascade stage, the incident particle undergoes a series of direct reactions with nucleons of the target, where high energy secondary particles with energy from 20 MeV to the incident particle energy are created. In the second stage, evaporation, the excited nucleus relaxes by emitting low energy (<20 MeV) neutrons, protons and residuals. After the evaporation, the nucleus that remains may be radioactive and emit gamma rays.

The neutron spectrum produced will show three characteristic peaks (the thermal, evaporation and cascade (high energy) peaks), but also a continuum in the epithermal region. The thermal peak is always present in a neutron spectrum and corresponds to particles reaching thermal equilibrium, discussed in Section 1.1, after several collisions with the nuclei of the target and the surrounding material, while the epithermal continuum corresponds to moderated fast neutrons. The evaporation and cascade peaks correspond to the respective stages of the intranuclear cascade. These neutron spectra characteristics are found at nTOF [29] and on the roof of the CERF [23] facility.

3.2 Application fields

Neutron spectrum information is not only useful for nuclear physics experiments, but is also essential for radiation protection purposes, since neutrons are typically the major component of stray radiation around accelerators and nuclear reactors and need to be monitored for safety reasons.

3.2.1 Radiation protection

Neutron dosimetry is commonly performed in radiation protection with a view to protect people and the environment from the harmful effects of ionizing radiation. Internationally accepted quantities and units for radiation and radioactivity are developed by the International Commission on Radiation Units and Measurements (ICRU) and the International Commission on Radiological Protection (ICRP), which also provide recommendations and procedures for measuring and applying these quantities.

The basic physical dose quantity for all types of ionizing radiation and any irradiation geometry is the absorbed dose D , defined as the mean energy $d\bar{\varepsilon}$ imparted to matter of mass dm and measured in $\text{J}\cdot\text{kg}^{-1}$ or Gray (Gy):

$$D = \frac{d\bar{\varepsilon}}{dm} \quad (3.2)$$

Radiation protection quantities have been introduced by ICRP [47], whose definition is based on the average absorbed dose, $D_{T,R}$ in the volume of a specific organ or tissue T , due to radiation of type R (see Table 3.1). The radiation R is given by the type and energy of radiation either incident on the body or emitted by radionuclides residing within it. The protection quantity *equivalent dose* in an organ or tissue, H_T , is then defined by:

$$H_T = \sum_R w_R D_{T,R} \quad (3.3)$$

where w_R is the radiation weighting factor for radiation R . The sum is performed over all types of radiations involved while the unit of equivalent dose is $\text{J}\cdot\text{kg}^{-1}$ and has the special name Sievert (Sv).

Table 3.1: Recommended radiation weighting factors by ICRP Publication 103.

Radiation type R	Weighting factor w_R
Photons	0.12
Electrons and muons	0.08
Protons and charged particles	0.04
Alpha particles and heavy ions	0.01
Neutrons	Continuous function of energy

However, this body-related protection quantity cannot be measured in practice and therefore operational quantities are used for the assessment of equivalent doses in tissues or organs. These quantities aim to provide a conservative estimate for the value of the protection quantities related to an exposure of persons under most irradiation conditions. They are often used in practical regulations or guidance.

One of the most common quantities for area monitoring is the *ambient dose equivalent*, $H^*(10)$. It is the equivalent dose which would be generated in the associated oriented and expanded radiation field at a depth of 10 mm on the radius of the ICRU sphere, which is oriented opposite to the direction of incident radiation.

The relation between the measurable and operational quantities is established by fluence-to-dose equivalent conversion coefficients [48] for continuous neutron spectra. Therefore the $H^*(10)$ is determined from Equation 3.4:

$$H^*(10) = \int h_{\Phi}(E)\Phi_E dE \quad (3.4)$$

where $h_{\Phi}(E)$ is the corresponding energy dependent fluence-to-dose equivalent conversion coefficient and Φ_E (cm^{-2}) is the energy distribution of the neutron fluence. The energy deposited and thus the dose equivalent produced by neutrons comes largely from their kinetic energy via hydrogen elastic scattering. The fluence-to-dose coefficients for increasing neutron energy are shown in Figure 3.1 from 1 meV to 10 GeV.

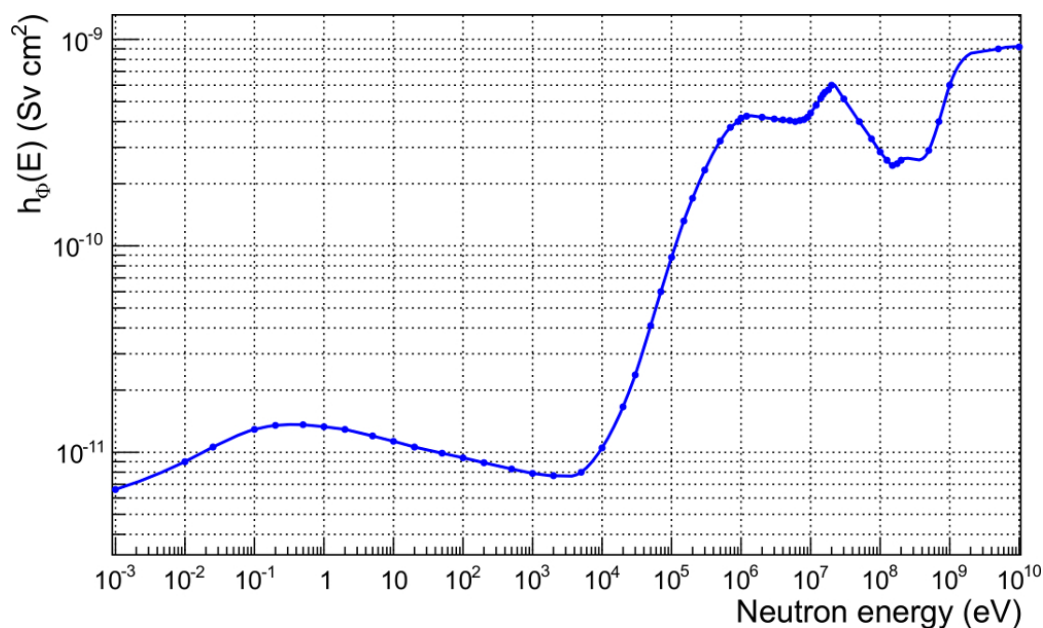


Figure 3.1: Fluence-to-dose equivalent conversion coefficient for neutron energies from 1 meV to 10 GeV, provided by ICRP 74 [48]

Shielding studies for accelerators [49] and nuclear reactors [50] require knowledge of the neutron spectrum and the dose equivalent rate. The fast neutron component from the source and the thermal originated in the shielding by fast neutron thermalization need to be determined in order to calculate the amount of shielding demanded to absorb the radiation produced. Since the secondary gamma radiation due to thermal neutron capture in the shielding is a major contributor to the dose equivalent

rate outside the shielding, measurements of the neutron spectrum are fundamental to radiation protection.

3.2.2 Nuclear physics experiments

Neutron fluence measurements are essential for instrument calibration [23] in terms of dose equivalent. The primary reference quantity used for the calibration of neutron measuring devices, e.g. area monitors, personal dosimeters, spectrometers etc., is the neutron fluence. This quantity is determined by appropriate experimental methods whereas dosimetric quantities are derived by applying the recommended fluence-to-dose conversion coefficients.

The radiative environment during present nuclear physics experiments requires neutron spectrum evaluation due to the neutron-induced damage to materials. Structural material such as semiconductor crystals can undergo permanent physical damages [51], the most common of which is the so-called displacement effect. This effect leads to transistor conductivity reduction, electrical field distortions and noise increase. A priori knowledge of the neutron spectrum and the subsequent dose can ensure the optimal operation of semiconductors and electronic components.

3.3 Neutron spectrometers

Since the discovery of neutrons, many methods for measuring their energy distribution have been developed. Before 1960 the main spectrometers were proportional counters, cloud chambers, organic scintillators, recoil telescopes, time-of-flight and activation foils techniques. Since 1960, the Bonner Sphere Spectrometer (BSS) [52] is the most employed instrument for neutron spectrometry, showing a number of advantages when compared to other methods. Beside the BSS, which are extensively discussed in Chapter 4, other widely used techniques for neutron spectrometry are described below.

3.3.1 Recoil proton telescope

Recoil proton telescopes [53] are devices measuring the neutron energy from the recoil proton energy via (n,p) reactions. This method requires prior knowledge of the incident neutron direction, as demonstrated in Equation 1.15, and thus these devices are based on a narrow selection of recoil directions by collimation or other means. From Equation 1.15, the energy of recoil protons observed at an angle ϑ with respect to the incoming neutron direction is given by:

$$E_p = E_n \cos^2 \theta \quad (3.5)$$

A schematic diagram of a common form of recoil telescope is shown in Figure 3.2. Neutrons are incident on a thin film, usually made from an organic polymer, whose thickness is kept small compared to the range of the lowest energy recoil proton to be measured. A very thin ΔE detector is placed in front of a thicker E detector. The first one serves to reduce backgrounds from competing reactions and other unwanted events, while the second one fully stops the recoil protons. By operating the two detectors in coincidence, only particles incident from the direction of the radiator are recorded.

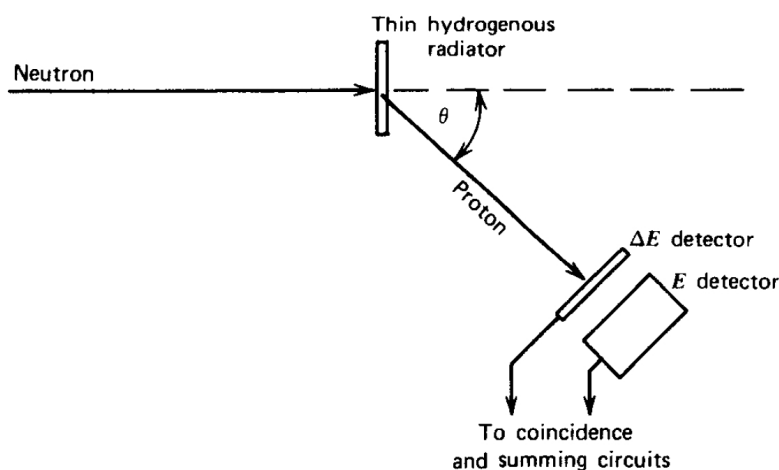


Figure 3.2: A proton recoil telescope

The dominant disadvantage of the proton recoil telescope is its very low detection efficiency [54] (typically 10^{-5}) and the narrow energy range measured (a few MeV).

3.3.2 Nuclear reaction based spectrometers

These spectrometers rely on the measurement of the pulse height spectrum of the charged particles produced by neutron induced reactions. The reactions are the same as for slow neutron detection, described in 1.1.1, ${}^3\text{He}(n,p){}^3\text{H}$ ($Q=0.764$ MeV), ${}^6\text{Li}(n,\alpha){}^3\text{H}$ ($Q=4.786$ MeV) and ${}^{10}\text{B}(n,\alpha){}^7\text{Li}$ ($Q=2.792$ MeV), but they are employed for fast neutron spectrometry [55].

As shown in Figure 1.1, the fast neutron cross section for all reactions falls off continuously with increasing neutron energy, with ${}^3\text{He}(n,p){}^3\text{H}$ having the highest

cross section and thus being the most popular. The pulse height spectrum from a detector based on this reaction will give the full energy peak at E_n+Q , corresponding to all the (n,p) reactions induced directly by the incident neutron. A continuum will also be present due to partial energy transfer to a recoiling helium nucleus, and corresponds to 75% of the incoming neutron energy according to Equation 1.16. At last, an epithermal peak appears at the Q-value 0.764 MeV due to the detection of incident neutrons moderated in external materials. The measured energy range is 0.05 - 10 MeV.

3.3.3 Time-of-flight methods

The neutron energy distribution can be acquired by measuring their time-of-flight over a known distance. Facilities dedicated to this method, such as nTOF [29] and LANSCE [56], deliver neutron beams in the full energy range and provide flight-paths at which the neutron spectrum can be measured. An example of the measurement procedure was given in Section 2.4.2 with the Triple GEM detector.

Chapter 4

The Bonner Sphere Spectrometer (BSS)

The Bonner Sphere Spectrometer (BSS) [52] is one of the most employed instruments for neutron spectrometry. In this chapter the CERN BSS and the recalculation of its response matrix with the newest version of the FLUKA code are described. In addition, improvements performed in the response of the system are presented for its employment in pulsed neutron fields, where proportional counters underestimate the true interaction rate. Experimental results are discussed in the stray field around a water phantom in the West German Proton Therapy Centre of Essen (WPE), behind concrete shielding at the CERF [23] facility and at the pulsed field present at the entrance of the CERN PS. Finally, future extensions and improvements are suggested for the system response in the thermal and high energy region.

4.1 The CERN BSS

The CERN BSS consists of seven spheres (see Figure 4.1): five polyethylene spheres with outer diameter of 81, 108, 133, 178 and 233 mm, complemented by two other spheres, nicknamed Ollio and Stanlio, where cadmium and lead inserts were introduced in order to reduce the sensitivity to thermal neutrons and increase it for high energies, up to the GeV range.

The system design, its calibration in the energy range from 144 keV to 19 MeV and the applications at high-energy accelerators are described in [57]. The geometry of the 81 mm sphere is shown in Figure 4.2; for the other four polyethylene spheres the diameter is obviously different.

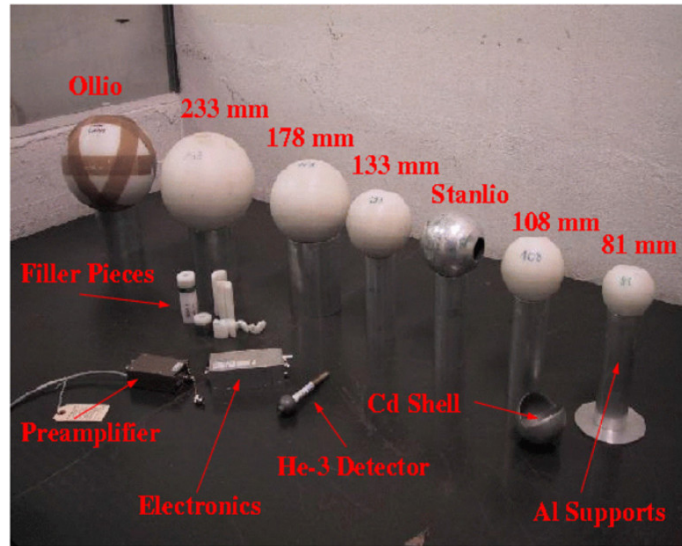


Figure 4.1: The CERN BSS

For simplicity the moderating material is represented as a single uniform piece of polyethylene surrounding the ^3He counter, but it is composed by several pieces: a hollow sphere and four plugs. The sphere is partially hollow (34 mm diameter cavity) in order to host at its centre the counter and its stem, which hosts the cable for providing the high voltage to the counter and for transporting the output signal to the preamplifier. The residual voids are filled with plugs in which the counter is enclosed before being inserted in the sphere. Two plugs enclose the spherical part and two plugs enclose the stem and have variable length depending on the sphere diameter. The stem plugs have been slightly modified compared to the past, in order to accommodate an additional rubber layer which is present in the new version of the counter.

The geometries of Ollio and Stanlio are given in Figure 4.3. The plugs used for Ollio and Stanlio are composed by polyethylene, cadmium and lead and are designed in order to create uniform shells of materials once the counter is inserted in the sphere.

The polyethylene and lead densities were measured via the water displacement technique: four out of the five polyethylene spheres (the 81 mm sphere was too small to allow a substantial water displacement) were first weighed and then introduced in a graduated container filled with water in order to measure their volume (Table 4.1). The average density of polyethylene was found to be $0.96 \pm 0.01 \text{ g/cm}^3$, consistent with the value used in past simulations.

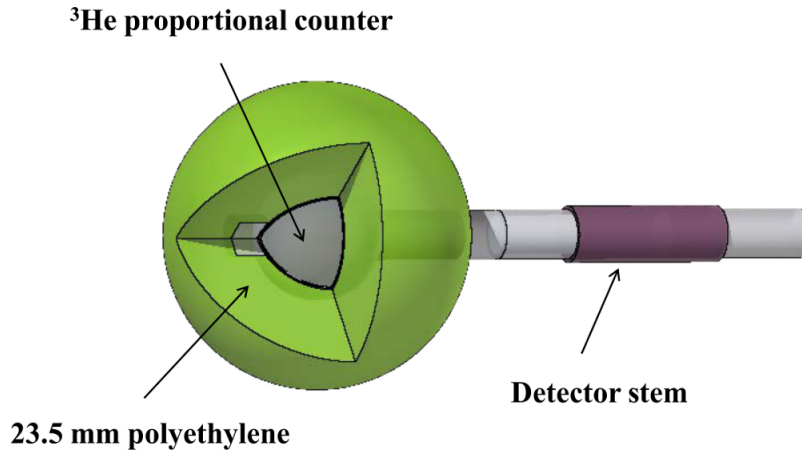


Figure 4.2: Geometry of the 81 mm sphere.

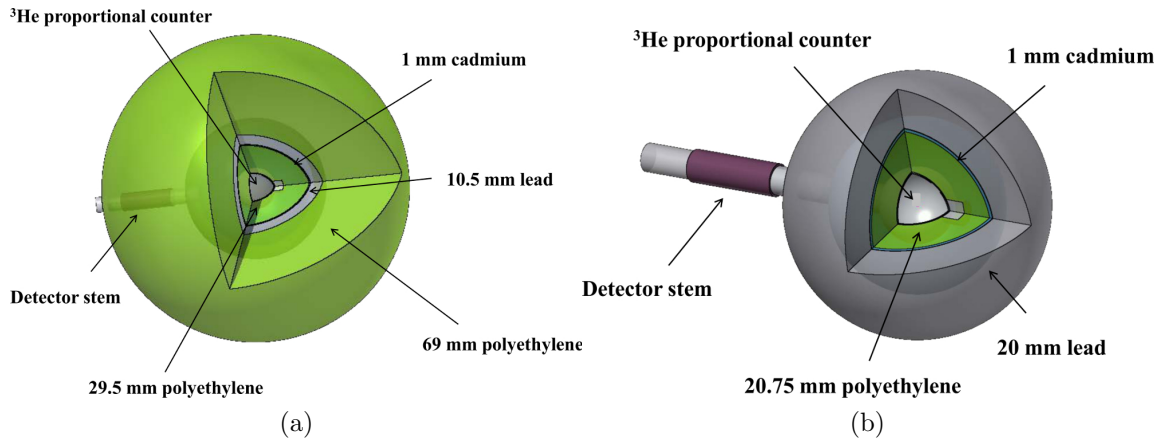


Figure 4.3: Geometry of Ollio (a) and Stanlio (b)

The lead purity has been checked via measurements performed with a portable optical emission spectrometer, PMI-MASTER Pro by Oxford Instruments, which provided a composition averaged over five samples of 99.8% Pb, 0.05% Sn and negligible fractions of other materials. A lead purity of 100% can be therefore assumed for this study, as this introduces negligible uncertainties.

The counter is a spherical Centronic SP9 filled with 2.3 atm (233,047 Pa) of ^3He and 1.2 atm (121,590 Pa) of krypton. These values have been provided by the supplier [58] and slightly differ from the nominal values, which were the ones used in the past. An air gap of 0.5 mm exists between the counter and the filler, intended as the average difference between the external radius of the counter and the internal

Table 4.1: Densities obtained via the water displacement measurements.

Sphere	Volume (cm ³)	Weight (kg)	Density (g/cm ³)
108 mm	575	544.26	0.95 ± 0.01
133 mm	1170	1096.05	0.94 ± 0.01
178 mm	2850	2753.54	0.97 ± 0.02
233 mm	6350	6192.25	0.97 ± 0.01

radius of the filler. This gap was carefully measured and differs significantly from the 3.5 mm given in ref. [57], a value taken as a conservative upper limit of the real geometry.

The response matrix of the CERN BSS was calculated in the past with the 1998 version of FLUKA. The results showed limitations in terms of relatively high statistical uncertainties and reduced number of energy bins below 20 MeV. These issues are due to the limited computing power of the time and to the specificities of that version of FLUKA, whose libraries had only 72 values of cross sections for neutron energies below 20 MeV, whereas the latest version has 260 values of approximately equal logarithmic width, 31 of which are thermal. Dedicated simulations were performed in order to recalculate the response matrix, by following the same methodology explained in [57], with the 2011.2b version of FLUKA and the USRTRACK estimator (see Appendix A.2). In brief, the response of a sphere is defined for each energy E_i of the impinging neutrons as:

$$R(E_i) = \frac{N_{\text{atom}} \cdot \sum_{E_j=0(\text{eV})}^{E_j=\infty} \Delta x(E_j) \sigma(E_j)}{F_u} \quad (4.1)$$

where N_{atom} is the ^3He atomic density (cm⁻³), $\Delta x(E_j)$ is the track length of the neutrons in the counter (cm), calculated by FLUKA for each energy E_j of the neutrons entering the active volume, $\sigma(E_j)$ is the cross section of the reaction $^3\text{He}(n,p)^3\text{H}$ (cm²), and F_u is the normalisation quantity, i.e. the fluence of neutrons impinging on a surface perpendicular to the sphere (cm⁻²): $F_u = 1/4 \cdot r^2$, where r is the sphere radius. Thanks to a FLUKA routine, the user directly obtains the result of Equation 4.1 for the 260 energies by running one simulation. For energies above 20 MeV each additional energy E_i needs a dedicated simulation to be run.

The polyethylene, lead and cadmium densities were 0.96 g/cm³, 8.64 g/cm³ and 11.35 g/cm³, respectively. The gas mixture density was 0.004369 g/cm³. The cross section applied to hydrogen in polyethylene was the default one for CH₂, as defined by the code, and free gas natural carbon for carbon. Two PHYSICS cards were used,

one for coalescence and one for the new evaporation model. The response functions have been calculated for neutron energies up to 2 GeV and are showed in Figure 4.4. The Monte Carlo statistical uncertainties are not shown for clarity, even if in most cases they are lower than the marker size.

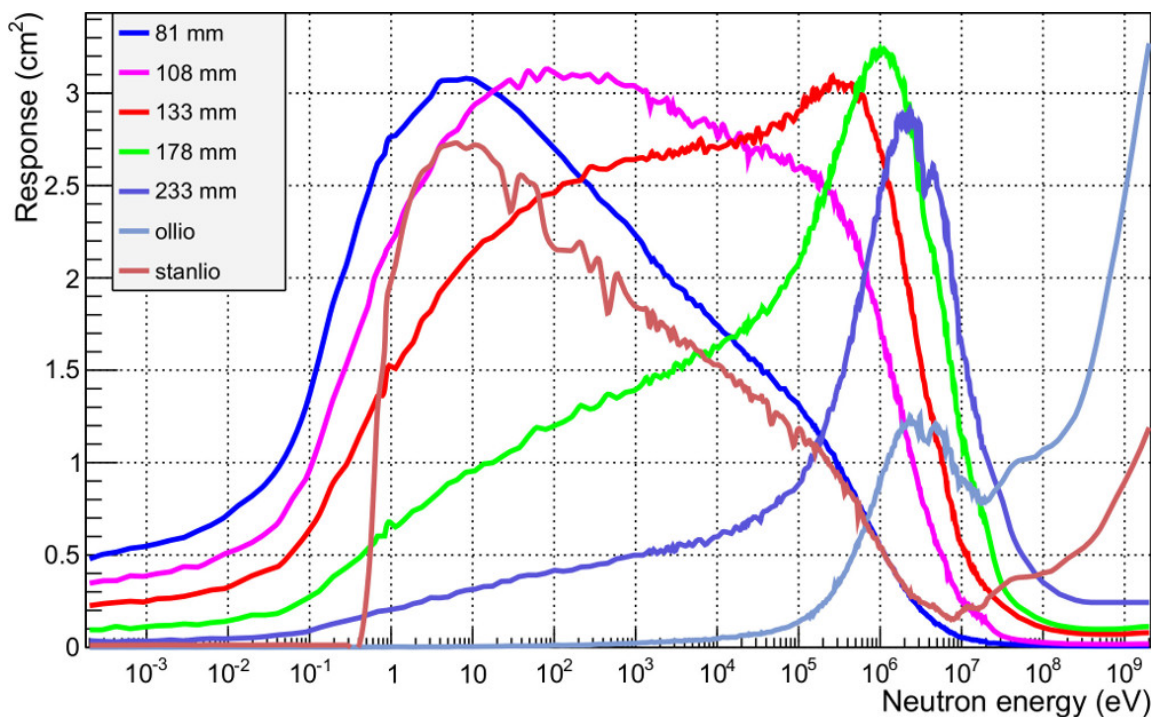


Figure 4.4: The CERN BSS response matrix as a function of the impinging neutron energy, calculated via FLUKA simulations.

The new simulations did not significantly change neither the shape nor the values of the response functions obtained in the past [57], but improved the energy resolution and consistently reduced the statistical uncertainties over the entire energy range.

4.2 The BSS-LUPIN for pulsed fields

When measuring in pulsed neutron fields (PNF), proportional counters suffer from dead time effects and show severe underestimations of the true interaction rate, which result in strong limitations of their applications, especially around particle accelerators, where PNF are a common radiation environment. The same limitations concern the CERN BSS, employing a proportional counter as the thermal neutron detector.

These dead time losses are common of all systems working in pulse mode and can be correctly compensated with correction algorithms only in case of steady-state sources of constant intensity, but not in the case of PNF [2]. A promising approach that overcomes these limitations is described in [59], [60], with the development of a new instrument, called LUPIN, whose front-end electronics is based on a current-to-voltage logarithmic amplifier, permitting the reconstruction of the time profile of the neutron interactions. The signal is digitally handled and the charge produced in the gas is calculated by integrating the current over a user settable time base. This allows measuring the generated charge even if the neutron interactions pile up. The total charge divided by the average charge expected by a single interaction represents the number of interactions occurring during the integration time.

In order to extend the applications of the CERN BSS to radiation environments characterised by PNF, the LUPIN electronics could be employed to analyse the signal obtained from the ^3He and then derive the integrated number of counts from each sphere without being affected by saturation losses. Since this innovative working principle needs an electrostatic shielding in order to avoid noise pick up, the BSS geometry must be slightly modified in order to host in the sphere an aluminium cylinder of 1 mm thickness to surround the ^3He counter and the polyethylene fillers. The system with this modified geometry will be called BSS-LUPIN. Figure 4.5 shows the geometry of the 81 mm sphere.

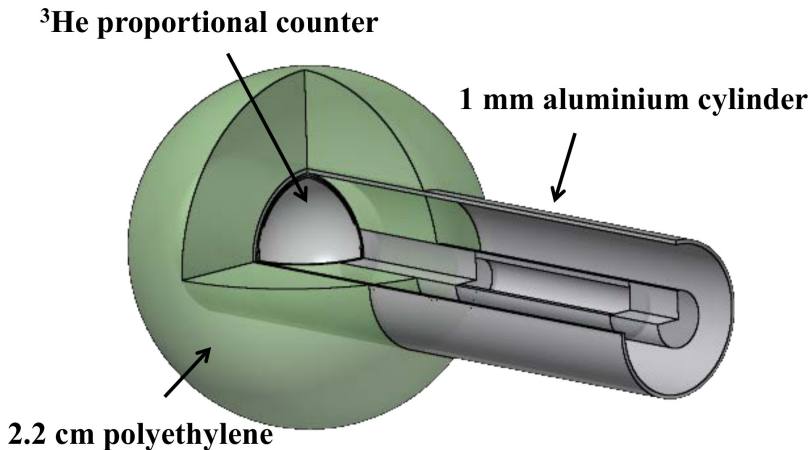


Figure 4.5: Geometry of the 81 mm sphere of the BSS-LUPIN.

FLUKA simulations showed that the insertion of the aluminium cylinder in the spheres does not significantly change the response matrix. Figure 4.6 shows the BSS-LUPIN response matrix.

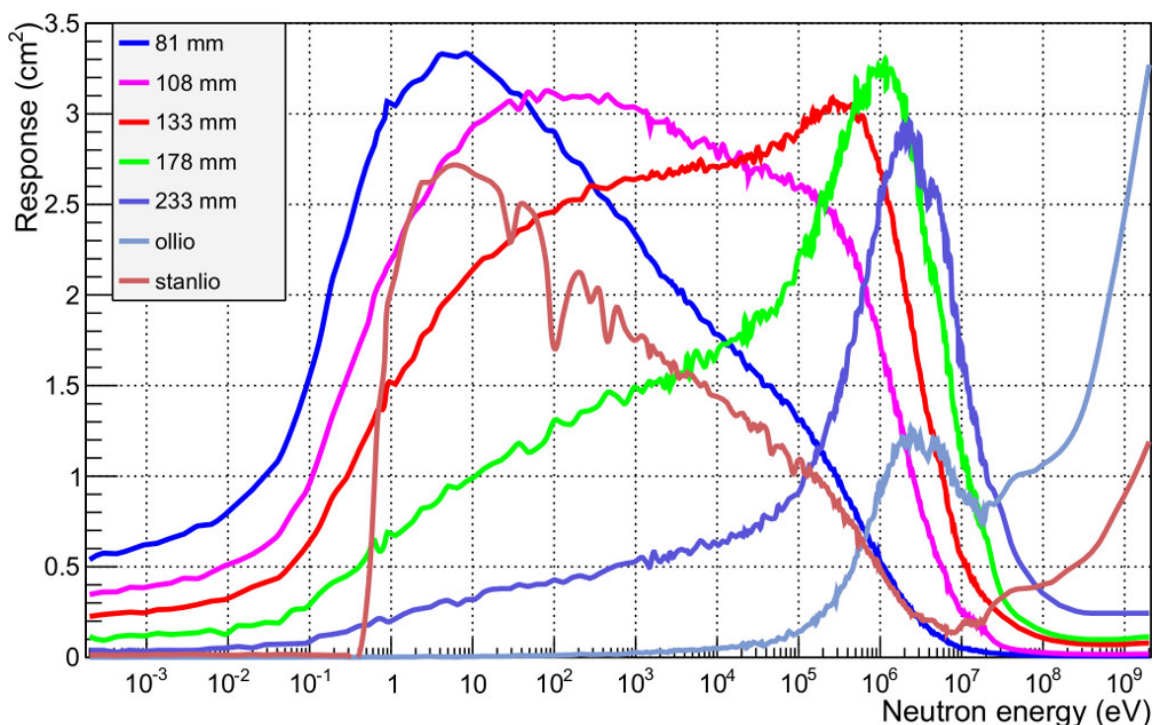


Figure 4.6: The BSS-LUPIN response matrix as a function of the impinging neutron energy, calculated via FLUKA simulations.

The insertion of the aluminium tube in the sphere introduces negligible changes in the response function, except for the 81 mm sphere, whose sensitivity is slightly increased for energies of few eV. This is due to the fact that aluminium has a high neutron transmission factor, in spite of reduced cross-section below 200 keV, and the geometry in which the neutrons traverse the biggest relative fraction of aluminium thickness on the overall path needed to reach the ^3He counter is the 81 mm sphere.

4.3 Experimental activities

The neutron spectrum is derived by unfolding the counts obtained from the spheres, normalised to a reference quantity, with their response matrix shown in Figure 4.4. Obtaining accurate results from a BSS is strictly related to a good estimation of the measuring uncertainty and to the availability of a well-established response matrix, calculated on a consistent number of energy bins and verified in reference neutron fields. In addition, attention must be paid to the correct use of the unfolding code

[61].

The neutron spectrum was calculated by unfolding the experimental data with three unfolding codes: MAXimum Entropy Deconvolution (MAXED) [62], GRAVEL [63] and FRascati Unfolding Interactive Tool (FRUIT) Six [64]. The first two codes, available in the PTB U.M.G. package [65], require an a priori estimation of the neutron spectrum, called guess spectrum, typically derived via Monte Carlo simulations, which should be as close as possible to the true spectrum. On the other hand, FRUIT employs a parametric approach which requires only qualitative information on the type of radiation environment where the measurements have been performed. Nevertheless, FRUIT can also be used with a numerical approach which requires the knowledge of the guess spectrum.

The uncertainties for MAXED have been obtained via the IQU_FC33 program implemented in the PTB U.M.G. package. IQU_FC33 considers variations in the measured data and in the guess spectrum and uses standard methods in order to perform a sensitivity analysis and derive the uncertainty values on the calculated spectrum via the propagation techniques.

A series of measurements were performed with the CERN BSS in the stray field around a water phantom, outside the concrete shielding of a reference facility and at the pulsed field in the beginning of the access tunnel to a proton synchrotron. The BSS-LUPIN was also used for neutron spectrometry in the latter, in order to compare their performance to pulsed fields.

A high voltage scan of the ^3He proportional counter was firstly performed in the CERN calibration laboratory, in order to determine the appropriate voltage applied during the measurements. The 233 mm sphere was irradiated with a $^{238}\text{PuBe}$ source with an activity of 1.85 TBq for 5 min, increasing the voltage by 100 V from 100 to 1200 V. The results are shown in Figure 4.7. A count plateau is present from 800 to 1100 V and therefore the working point was chosen as 800 V.

4.3.1 The CERN BSS for secondary neutrons inside a proton therapy facility

Neutron spectrometry measurements with the CERN BSS [66], [67] were performed inside and around the Fixed-Beam Treatment Room (FBTR) at the Proton Therapy Facility of Essen (WPE), in Germany, along with neutron $H^*(10)$ measurements, which were compared with the extended-range rem meter WENDI-2 [68], the conventional rem meter LB 6411 [69] a TEPC [70] and a ^3He proportional counter.

A $64 \times 64 \times 45 \text{ cm}^3$ water phantom was irradiated by a 226.7 MeV proton beam delivered in Uniform Scanning (US), an active beam delivery mode in which the

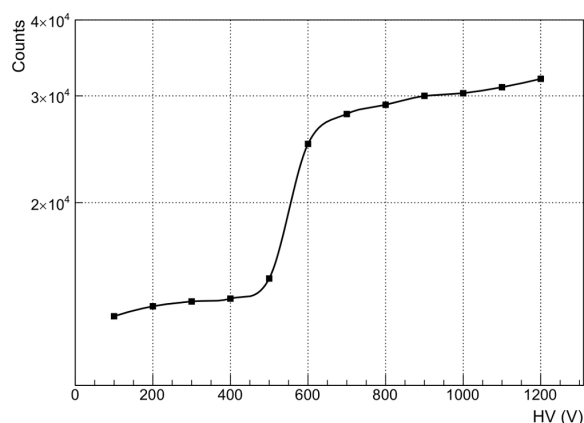


Figure 4.7: High voltage scan of the ^3He proportional counter with the 233 mm sphere. A count plateau is visible in the range from 800 to 1000 V.

beam spot is continuously scanned over a predefined area of 19 cm x 22 cm. No beam scatterer was used inside the treatment nozzle, so that the main neutron production arose from the water phantom only. During the neutron measurements, the delivered Monitor Units (MUs) from the IC23 ionization chamber inside the treatment nozzle were recorded. The relationship between these MUs and the number of protons delivered to the water phantom was established through a preliminary current measurement using a Bragg Peak Chamber Type 34070 placed at the isocenter. A global uncertainty of 5% is associated with the measurement of the number of delivered protons, taking into account the following uncertainties: 4% on the mass stopping power of the protons, 3% on the gap of the Bragg Peak Chamber, 1.4% on the air density, 1% on the collected charge in the Bragg Peak Chamber and 0.5% on the number of Monitor Units.

An overview of the considered neutron measurement positions inside and around the FBTR is given in Figure 4.8. Two positions were located inside the treatment room (1a and 1b), at respectively ~ 94 and ~ 7 degrees from the proton beam axis, as seen from the center of the water phantom. One position (2a) was located inside the technical room, which is separated from the FBTR by a 2 meter thick concrete shielding wall and another one (1g) in the entrance of the access maze. In general no staff is present in this room but it was chosen as representative for an operator room since it is separated from the FBTR by a 2 meters-thick concrete wall.

The full FBTR was simulated using MCNPX 2.7.0 [71] and more information can be found in [66]. The particle source was defined in front of the water phantom as a 19 cm x 22 cm rectangle producing a parallel and uniform beam of 226.7 MeV

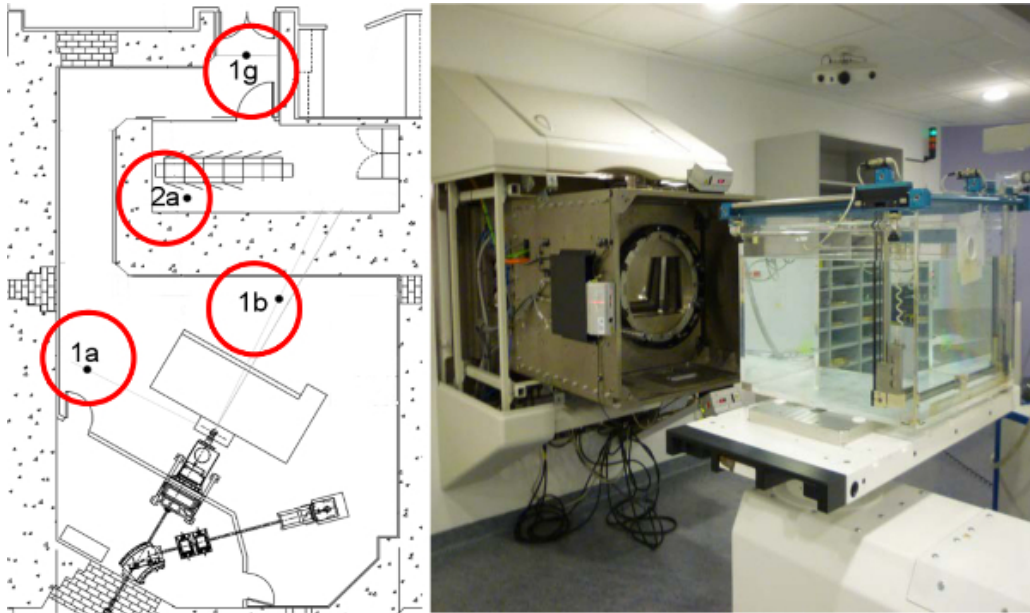


Figure 4.8: Measurement positions and experimental set-up.

protons and the neutron spectra were calculated inside air spheres of 15 cm diameter located in the reference positions.

4.3.1.1 Spectrum inside and outside the room

For positions 1a, 1b, 2a and 1g, the Figures from 4.9 to 4.12 show the BSS unfolded spectra with MAXED and GRAVEL, compared with the simulated neutron spectra, called guess spectra. The uncertainties associated to the spectra unfolded with MAXED are those calculated with the IQU code, except for energies above 20 MeV where 20% relative uncertainties have been considered. For the positions 1a, 1b and 2a, the spectra unfolded with GRAVEL agree with the MAXED results within the uncertainties of the latter. It is not fully the case for position 1g, where the GRAVEL spectrum is larger than the MAXED spectrum by 20-40% in the thermal and high energy peaks.

In Position 1a (Figure 4.9), the guess spectrum matches the unfolded spectra very well for neutrons with energies larger than 5 MeV. In the intermediate energy range and in the evaporation peak up to 5 MeV, the guess spectrum is smaller than the unfolded spectra by 25%.

For Position 1b, the simulated and measured spectra are compared in Figure 4.10. The guess spectrum agrees very well with the unfolded spectra at all energies except

in the high energy peak, where an overestimation appears above 150 MeV.

In Position 2a (Figure 4.11), the unfolded spectra are lower than the simulated spectra by a factor 2.4 that remains relatively constant on the entire energy range. The results are similar to those of Satoh et al. [72], obtained with the simulation code PHITS and the DARWIN spectrometer at the Fukui Proton Therapy Center.

The neutron spectrum in position 1g (Figure 4.12) is mainly characterized by a large thermal peak as well as a relatively small high energy peak. The simulated spectra are larger than the average BSS results on the whole energy range, but the overestimation factor is larger on the high energy peak than the thermal one. The main contribution to the high energy peak are neutrons directly transmitted through the technical room while to the thermal one are neutrons scattered inside the access maze.

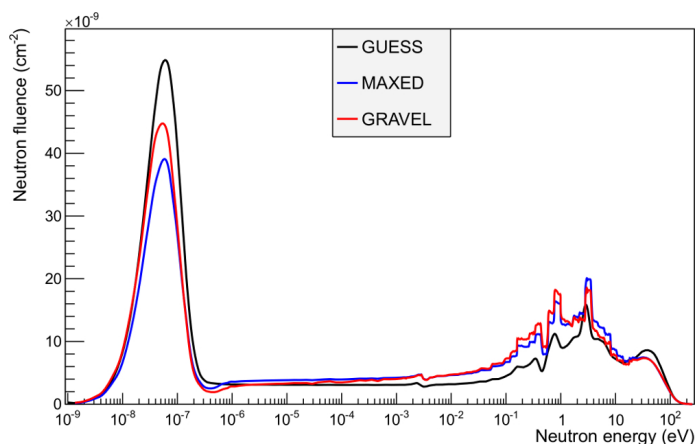


Figure 4.9: Neutron spectra obtained with MAXED and GRAVEL for position 1a, compared with the guess spectrum.

4.3.1.2 Global neutron $H^*(10)$ intercomparison

The neutron $H^*(10)$ rates obtained from the unfolding analysis of the BSS data performed with MAXED and GRAVEL and expressed in $\mu\text{Sv}/(\text{nA}\cdot\text{h})$ are in good agreement with each other in every considered position (Figure 4.13). The WENDI-2 measurements agree very well with the $H^*(10)$ rates of the BSS data in the four types of neutron fields considered (positions 1a, 1b, 1g, 2a). In these cases it is not necessary to introduce position-specific calibration correction factors, based on the local neutron spectrum, in order to further improve the accuracy of the $H^*(10)$ measurements performed with the WENDI-2 detector.

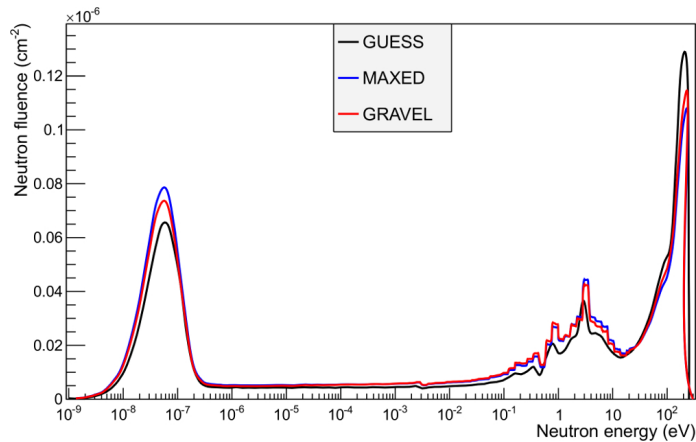


Figure 4.10: Neutron spectra obtained with MAXED and GRAVEL for position 1b, compared with the guess spectrum.

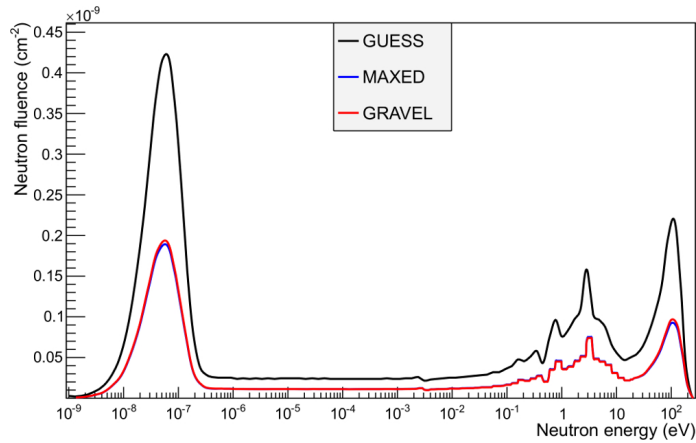


Figure 4.11: Neutron spectra obtained with MAXED and GRAVEL for position 2a, compared with the guess spectrum.

Compared to the WENDI-2 detector, the conventional REM counter LB 6411 measures values lower by 40% in position 1b (Figure 4.13) and by 27% in positions located behind the shielding (position 2a). The low response to high energy neutrons of the LB 6411 thus causes a small underestimation of the measured $H^*(10)$ rates in these positions in which the proportion of neutrons with more than 20 MeV lies between 15% and 30%, according to the MCNPX simulations. In position 1a, however, better agreement was found between the LB 6411 measurement and the WENDI-2 and BSS data. According to the MCNPX simulations [?], the neutrons with more

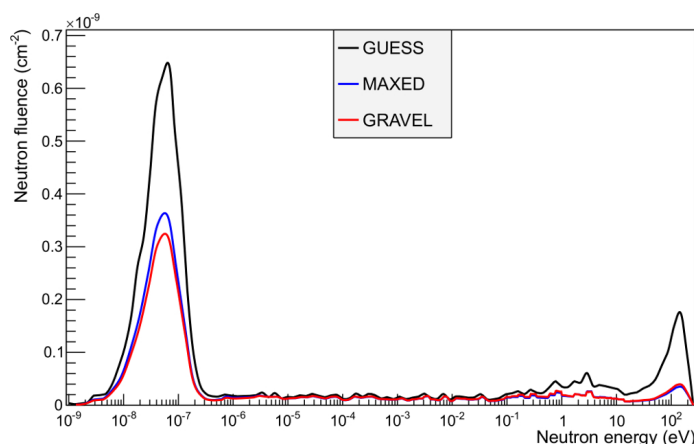


Figure 4.12: Neutron spectra obtained with MAXED and GRAVEL for position 1g, compared with the guess spectrum.

than 20 MeV constitute only 5% of the total neutron flux in this position. It seems that the LB 6411 can be used for area monitoring of neutrons inside proton therapy facilities, although accurate neutron $H^*(10)$ measurements behind the shielding and in forward positions inside the treatment room would actually require the calculation of a position-specific calibration correction factor. The TEPC results are affected by rather large counting uncertainties, but they are globally consistent with the other measurements.

For the positions 1a, 1b and 2a the contribution of thermal neutrons to the total neutron $H^*(10)$ rate was calculated by folding the neutron spectra from the MCNPX simulations and the unfolded BSS spectra with the fluence-to-dose coefficients up to $2 \cdot 10^{-7}$ MeV. The thermal $H^*(10)$ contributions calculated using the MCNPX spectra and the average of the thermal $H^*(10)$ contributions derived from the unfolded BSS spectra are compared to the ^3He counter measurements in Table 4.2.

Table 4.2: Thermal contribution to the neutron $H^*(10)$ rate, from the MCNPX simulation, the unfolded BSS spectra (average result) and the measurement with the ^3He counter, all expressed in $\mu\text{Sv}/(\text{nA}\cdot\text{h})$.

Position	MCNPX	BSS	^3He counter
1a	25.90 ± 0.04	25 ± 2	12 ± 3
1b	33.95 ± 0.04	38 ± 3	17 ± 4
2a	0.244 ± 0.002	0.099 ± 0.008	0.04 ± 0.01

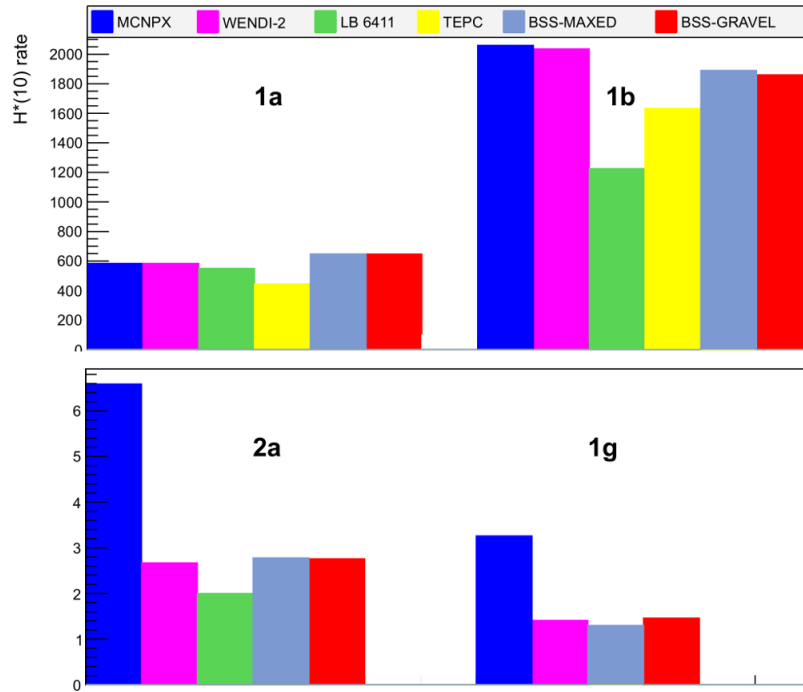


Figure 4.13: Total $H^*(10)$ intercomparison between the BSS, WENDI-2, LB 6411 and TEPC, expressed in $\mu\text{Sv}/(\text{nA}\cdot\text{h})$.

It appears that, on average, the simulated thermal $H^*(10)$ contributions overestimate the ^3He counter measurements by a factor of 2 inside and a factor of 6 outside the treatment room. The causes of these overestimations, especially inside the treatment room, are not well understood. However, in the considered positions this problem is not significant because the thermal contributions only represent a few percent of the total neutron $H^*(10)$ rates. Moreover, inside the access maze where the neutron flux is largely thermal, the contribution of the thermal neutrons to $H^*(10)$ also remains relatively small compared to the contribution of neutrons with more than 0.1 MeV.

As for the results derived from the unfolded BSS spectra, the thermal contributions to $H^*(10)$ are also larger than the ^3He counter measurements by a factor 2 both inside and outside the treatment room. The BSS does not include a thermal neutron counter, which causes poor energy resolution in the thermal region. Therefore, the shape of the guess spectrum has a strong influence on the thermal peak of the unfolded spectra.

4.3.1.3 Conclusions

The CERN BSS was successfully employed for neutron spectrometry inside (positions 1a and 1b) and outside a FBTR (positions 2a and 1g). The unfolded spectra with MAXED and GRAVEL were found in agreement with each other in absolute values and total $H^*(10)$ in all positions. This agreement was also present with the guess spectrum in positions inside the FBTR, but not outside, where the unfolded absolute fluence appeared to be uniformly underestimated by a factor ~ 2 with respect to the guess fluence. The $H^*(10)$ in these positions was also measured with the CERN BSS and compared with the values estimated with the guess spectrum and obtained with REM counters and was found to be closer to the experimental rather than the simulated values.

4.3.2 The CERN BSS performance behind concrete shielding

A series of measurements were performed with the CERN-BSS behind the 80 cm thick concrete side shielding of the CERF facility during the December 2014 run [73], in the area indicated in Figure 4.14 and with the beam impinging from right to left. The neutron spectrum was measured in the so-called positions CS2 and CS4, with CS2 being closer to the shielding corner and CS4 closer to the target. The SPS supercycle had three beam extractions to the North Area per minute, with duration of about 5 s and intensity on the T4 target of about $2 \cdot 10^{12}$ particles.

The spectra were obtained by unfolding the experimental data with MAXED and GRAVEL and the guess spectrum was obtained by FLUKA for both positions. The $H^*(10)$ in these positions was also measured and compared with the values obtained with REM counters.

4.3.2.1 Neutron spectrum measurements

Each sphere was installed on an aluminium support in order to be at the same height of the target, and was exposed for about 10 minutes. The number of integrated counts was corrected for dead time losses and normalised to the number of particles impinging on the target. The total uncertainty includes the one on the beam monitoring (10%) and on the positioning (5%), whereas the statistical uncertainty on the number of counts was negligible. The spectra for position CS2 and CS4 are shown per unit of lethargy and per particle on target in Figures 4.15 and 4.16, respectively, employing the same guess spectrum for both positions.

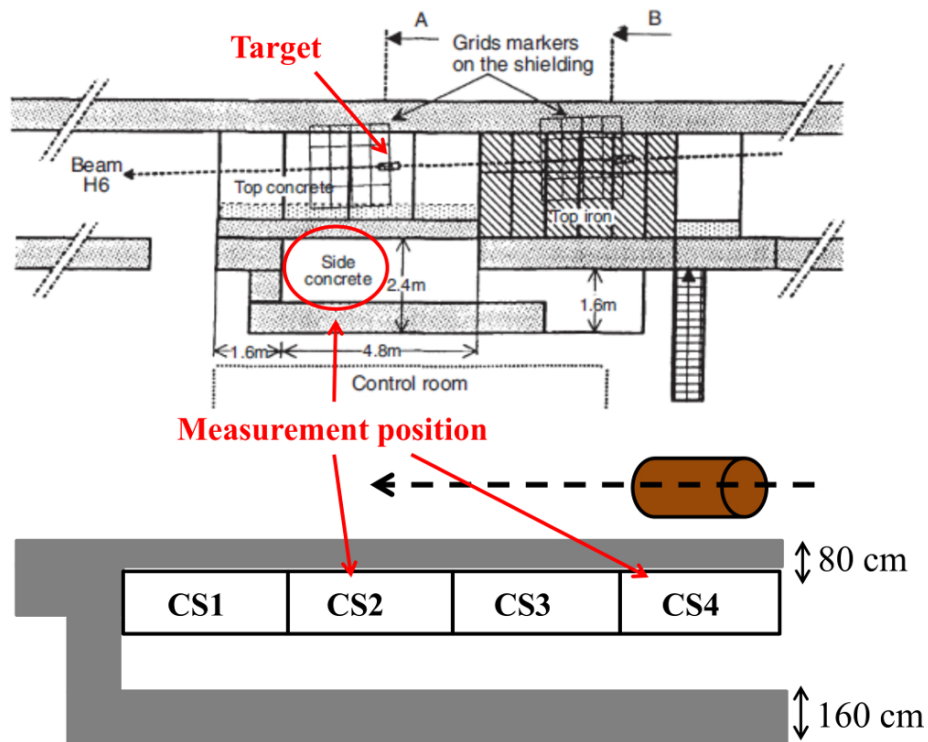


Figure 4.14: Experimental set-up. The spectrum was measured in positions CS2 and CS4 behind the concrete shielding and at the same height of the target.

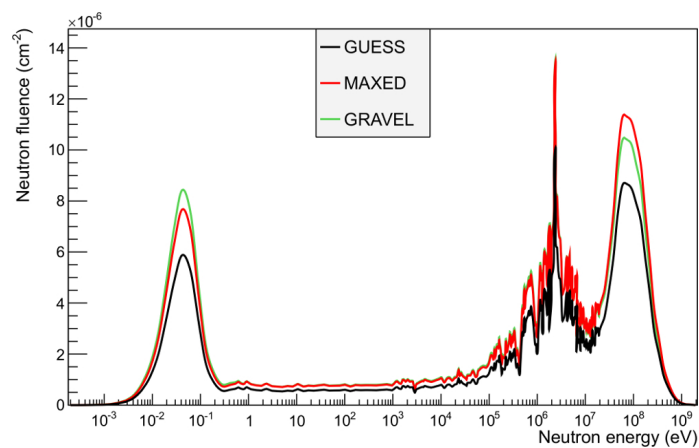


Figure 4.15: Neutron spectra obtained for position CS2, compared with the guess spectrum.

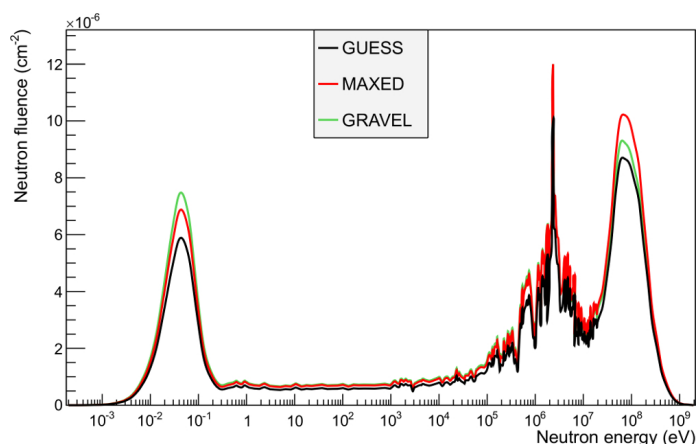


Figure 4.16: Neutron spectra obtained for position CS4, compared with the guess spectrum.

The spectra calculated with the two codes for the same position are in good agreement both in shape and absolute value of the neutron fluence. The thermal, evaporation and high energy peaks are well visible, with the last two emerging at the same energy as those at the concrete roof spectrum [23]. The magnitude of the thermal peak is slightly higher for position CS2 ($8.4 \pm 1.0 \cdot 10^{-6}$ with GRAVEL) than CS4 ($7.5 \pm 0.9 \cdot 10^{-6}$ with GRAVEL), because the first is closer to the shielding corner and the contribution of moderated scattered neutrons is higher. In addition, the absolute values of the neutron fluence is higher for CS2 in the total spectrum, even though CS4 is closer to the target, and the reason lies on the forward direction at which neutrons are scattered from the target.

4.3.2.2 Neutron $H^*(10)$ measurement and intercomparison

Measurements of the $H^*(10)$ were performed in several reference positions with WENDI-2. Table 4.3 compares the $H^*(10)$ values in position CS2 and CS4, obtained from the calculated spectra folded with the ICRP 74 fluence-to-dose conversion coefficients and measured with the WENDI-2 in the December 2014 run and with two other detectors in the past, the LINUS [74] and the HANDI TEPC [75].

All values are in good agreement within their range of uncertainties. Only the values obtained with LINUS in 2002 are slightly lower, but this could be due to a variety of causes, including a slight different position of the target at that time. Moreover, as observed in the comparison of the calculated neutron spectra, the $H^*(10)$ in position CS2 is slightly higher than in CS4.

Table 4.3: $H^*(10)$ values obtained from the unfolded spectra and measured with different neutron detectors. The values are normalised to IC counts [27].

Pos.	MAXED	GRAVEL	WENDI-2	LINUS	HANDI
CS2	0.42 ± 0.05	0.40 ± 0.05	0.42 ± 0.04	0.35 ± 0.03	0.43 ± 0.03
CS4	0.37 ± 0.04	0.36 ± 0.04	0.34 ± 0.03	0.29 ± 0.02	0.30 ± 0.03

4.3.3 Performance comparison of the CERN BSS and BSS-LUPIN in pulsed fields

In order to compare the performance of the BSS-LUPIN with the conventional CERN BSS, a series of measurements were performed with both systems [76] at the beginning of the access tunnel to the beam extraction area of the CERN Proton Synchrotron (PS).

During the measurements the proton beam was extracted from the PS at 14 GeV using the continuous transfer technique [77]. In the extraction phase, comparatively large losses are observed all around the accelerator. These are due to particles scattered by the electrostatic septum used to slice the beam. At the beginning of the access tunnel to the beam extraction area the typical duration of the losses is 2.1 s, with a fraction of lost beam of about 1%. The stray radiation field in the area is therefore ideal to test the performance of the BSS-LUPIN in PNF. The area is located at the accelerator level, just before an interlocked door. The pulse repetition rate is 0.83 Hz, i.e. one pulse every 1.2 s.

The measurements were performed by exposing each sphere in the reference position. Each measurement lasted for about 30 minutes, in order to reduce the statistical uncertainty on the integrated number of counts to a minimum. For the CERN BSS the integrated counts were corrected for dead time losses. The results obtained with both systems, given in Table 4.4, are expressed in number of counts normalised to the protons accelerated in the PS, as derived from TIMBER [78], an interface that allows obtaining data on the operation of the CERN accelerators in terms of settings, particle fluence and beam intensity. The global uncertainty takes into account the statistical one (which is always below 1% except for Ollio) the uncertainty on the positioning and on the reproducibility of the stray field and the uncertainty on the data of the integrated fluence derived from TIMBER (which is equal to 5%).

Table 4.4: Results obtained with the CERN BSS and the BSS-LUPIN during the measurements at PS, together with the statistical and systematic uncertainties.

Sphere	CERN BSS	BSS-LUPIN
81 mm	$2.39 \pm 0.13 \cdot 10^{-11}$	$2.20 \pm 0.12 \cdot 10^{-11}$
108 mm	$1.69 \pm 0.10 \cdot 10^{-11}$	$2.38 \pm 0.13 \cdot 10^{-11}$
133 mm	$1.25 \pm 0.07 \cdot 10^{-11}$	$2.79 \pm 0.15 \cdot 10^{-11}$
178 mm	$8.91 \pm 0.55 \cdot 10^{-12}$	$4.23 \pm 0.31 \cdot 10^{-11}$
233 mm	$5.00 \pm 0.32 \cdot 10^{-12}$	$9.39 \pm 0.54 \cdot 10^{-12}$
Stanlio	$5.61 \pm 0.35 \cdot 10^{-12}$	$7.49 \pm 0.45 \cdot 10^{-12}$
Ollio	$9.38 \pm 0.76 \cdot 10^{-13}$	$1.96 \pm 0.40 \cdot 10^{-12}$

4.3.3.1 Neutron fluence comparison

The neutron spectrum was calculated by unfolding the experimental data with MAXED, GRAVEL and FRUIT, while the guess spectrum was obtained via FLUKA simulations performed for a position close to the measuring area, taken from [79]. Since the guess spectrum is given as a function of the number of lost protons and the counts are normalised to the protons accelerated in the PS, a beam loss of 1% was assumed in order to relate the two quantities. This assumption does not introduce significant uncertainties as for the guess spectrum the main information needed is the spectral shape. Figures 4.17 and 4.18 show the spectra obtained by the unfolding performed with MAXED, GRAVEL and FRUIT for the data obtained with the CERN BSS and the LUPIN-BSS, respectively. The spectra are given in neutron fluence per unit of lethargy, normalised to the number of protons accelerated in the PS. The guess spectrum is also shown for comparison, whereas the uncertainties are not given for clarity.

The MAXED and GRAVEL spectra in Figure 4.17 are characterised by a large peak at thermal energies and by smaller peaks in the MeV region, which is particularly jagged due to the high uncertainty of the guess spectrum, which depends on the poor statistics of the Monte Carlo simulations when the expected fluence is extremely low. The fluence integrated in the intermediate region, from 1 eV to few hundred keV, is negligible for all spectra. The intense thermal peak and the limited fluence above 1 eV are due to the fact that the stray field at the beginning of the PS tunnel, which is a 50 m long bent tunnel, is characterised by neutrons that underwent many scattering events along the concrete walls, substantially reducing their energy. Similarly, the probability of detecting high energy neutrons is very limited and thus the presence of fluence above 20 MeV is questionable. The solution spectra obtained

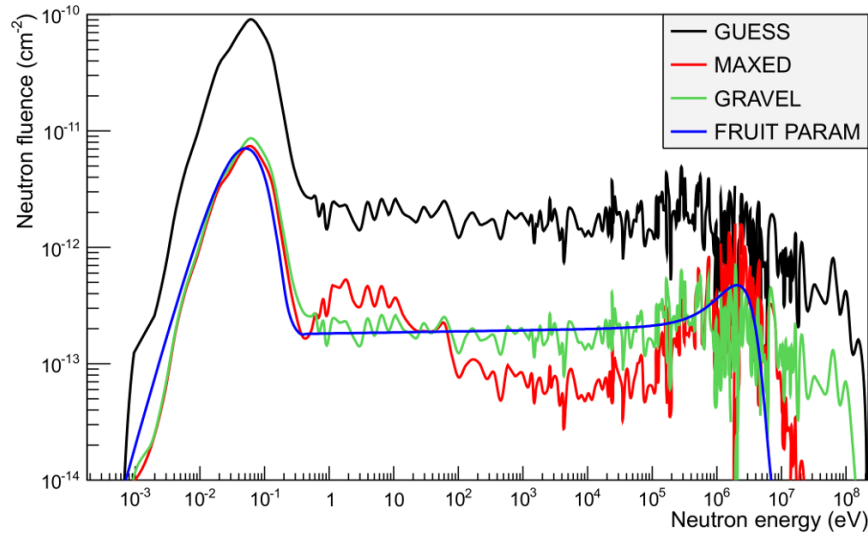


Figure 4.17: Solution spectra obtained from the CERN BSS (guess spectrum shown for comparison).

with MAXED and GRAVEL strongly depend on the guess spectrum and the peaks at 20 and 100 MeV do not have physical meaning but derive from the guess spectrum shape. The latter was in fact calculated in a position at a few meter distance from the measurement position, where the gradient of the ambient dose equivalent, $H^*(10)$, rate is very high [79]. The uncertainties calculated for MAXED are 8% for the thermal peak, 15-20% for the intermediate region, 10% around the 2 MeV peak and more than 50% for energies higher than 5 MeV. On the other hand the FRUIT spectrum is characterised by a smoother shape, without the many resonances present in the MeV region, and it is limited to 5 MeV, being the superposition of elementary spectra described by a set of physically meaningful parameters [64]. The uncertainties given by FRUIT are 7% for the thermal peak, 9% in the intermediate region and 10% around the 2 MeV peak. The fluence of the solution spectra is lower than the guess over the entire energy range, especially in the thermal region.

The spectra obtained from the same code have similar shape for both the CERN BSS and the BSS-LUPIN, whereas the absolute intensity, especially in the thermal and in the MeV region, is different. The uncertainties obtained for MAXED and FRUIT for the BSS-LUPIN were slightly lower than for the CERN BSS, due to the higher measured fluence. The spectra have a thermal peak whose maximum reaches $8 \cdot 10^{-12} \text{ cm}^{-2}$ for the CERN BSS, consistently lower than that of the BSS-LUPIN, whose maximum is $2 \cdot 10^{-11} \text{ cm}^{-2}$. The intermediate region has an average

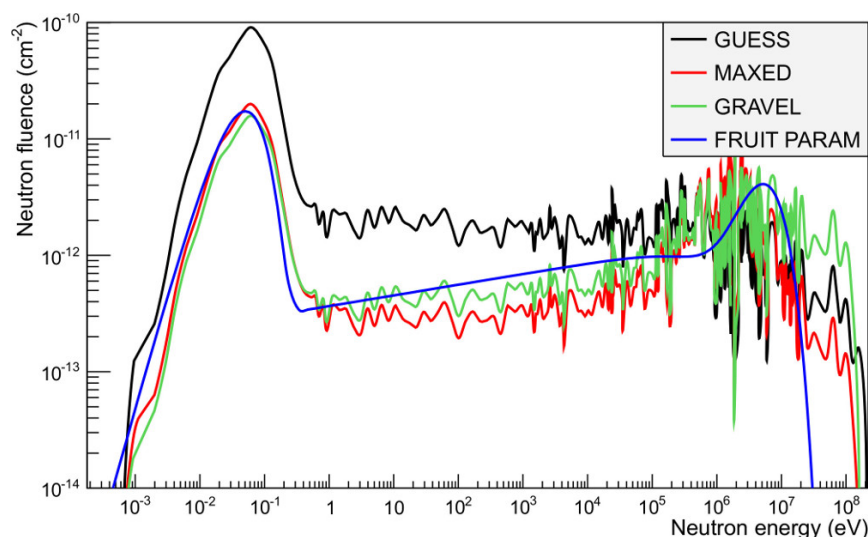


Figure 4.18: Solution spectra obtained from the BSS-LUPIN (guess spectrum shown for comparison).

value of $2 \cdot 10^{-13} \text{ cm}^{-2}$ for the CERN BSS and $6 \cdot 10^{-13} \text{ cm}^{-2}$ for the BSS-LUPIN. For the MeV region it is more difficult to define an average value, but the BSS-LUPIN spectrum shows an intensity approximately double than the CERN BSS. The same conclusion can be drawn from all codes: the fluence obtained from the CERN BSS is lower compared to the BSS-LUPIN. This confirms that the pulsed structure of the stray field leads to underestimation of the number of counts for a system using a proportional counter coupled with conventional NIM electronics. The underestimation is more significant for higher neutron interaction rate, i.e. for the spheres which show high sensitivity in the thermal or the MeV region. As a consequence the CERN BSS solution spectra underestimate the total fluence. This fact is better recognized in Figure 4.19, which compares the spectra unfolded by MAXED: the fluence is substantially higher for the BSS-LUPIN in the entire energy range, except for the eV region.

4.3.3.2 Neutron $H^*(10)$ comparison

The $H^*(10)$ values, normalised to the PS proton fluence, were calculated by folding the solution spectra and their uncertainties with the ICRP fluence-to-dose coefficients [48] and shown for the two systems in Table 4.5. The uncertainties on the $H^*(10)$ were obtained by folding the upper and the lower values of the energy bins of the final spectra with the corresponding ICRP coefficient, using the uncertainties obtained

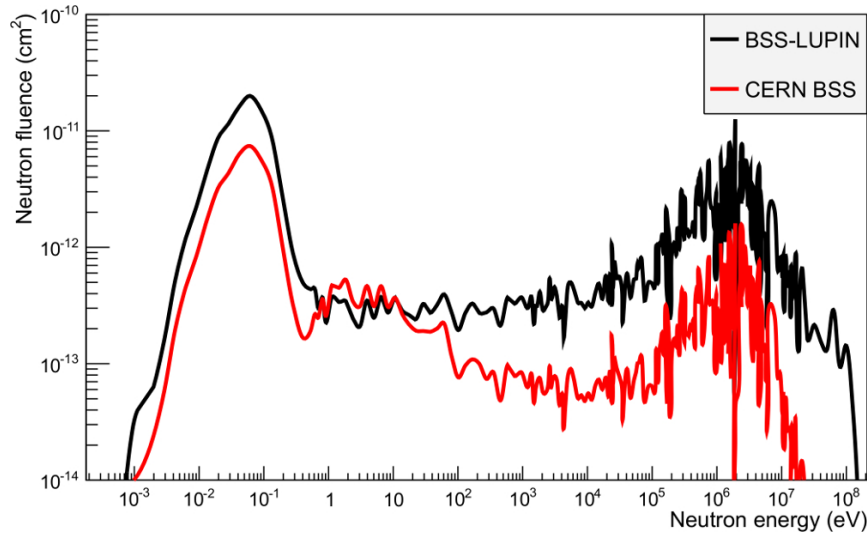


Figure 4.19: Comparison of solution spectra obtained with MAXED from the CERN BSS and the BSS-LUPIN.

with MAXED and FRUIT. The same uncertainties were assumed for MAXED and GRAVEL, due to the similarities in the unfolding algorithms.

Table 4.5: Calculated $H^*(10)$, normalized to the PS proton fluence and expressed in Sv per proton.

System	MAXED	GRAVEL	FRUIT
CERN BSS	$6.3 \pm 1.0 \cdot 10^{-13}$	$6.0 \pm 0.9 \cdot 10^{-13}$	$6.1 \pm 0.3 \cdot 10^{-13}$
BSS-LUPIN	$38.1 \pm 6.4 \cdot 10^{-13}$	$47.5 \pm 7.8 \cdot 10^{-13}$	$41.8 \pm 3.5 \cdot 10^{-13}$

The $H^*(10)$ values obtained with the different unfolding codes for the same system are compatible within their uncertainties. On the other hand, the CERN-BSS underestimates the $H^*(10)$ as compared with the BSS-LUPIN by a factor of 7 on average. As observed in the comparison of the solution spectra above, it is clear that the CERN-BSS heavily underestimates the neutron interaction rate, which results in underestimating the $H^*(10)$. The reliability of the $H^*(10)$ value obtained from the LUPIN-BSS solution spectra is confirmed by measurements performed with neutron rem counters in the same area [80], which showed $H^*(10)$ values in the range 2.2 to $4.4 \cdot 10^{-12}$ Sv per accelerated proton. Given the strong $H^*(10)$ gradient in this area as explained above, these values are in agreement with the BSS-LUPIN measurements.

4.3.3.3 Conclusions

The CERN BSS was upgraded for its use in PNF by employing innovative electronics specifically conceived for this purpose. The upgraded system, called BSS-LUPIN, was employed in a measurement campaign at the CERN PS in an area characterised by the presence of PNF and showed to be able to correctly estimate the neutron spectrum and the $H^*(10)$, avoiding underestimations induced by count losses. Additional measurement campaigns are planned in order to further test the performance of the upgraded system.

4.4 Extensions and improvements

In order to increase the number of applications in which the BSS could be efficiently employed and to improve its sensitivity in specific energy ranges, some modifications to the existing BSS have been evaluated.

4.4.1 Response to high energies

In order to enhance the sensitivity of the BSS above 20 MeV, a new configuration of Stanlio has been investigated. The idea which originally brought to the development of Stanlio was to build a sphere whose response function was extended above 20 MeV but suppressed as much as possible at few MeV, i.e. where the 233 mm sphere and Ollio show their sensitivity peak [81], in order to keep the response functions of the three spheres as independent as possible. This requirement imposed to limit the polyethylene thickness to 20 mm, otherwise a higher thickness would have increased the sensitivity at about few MeV. On the other hand, this forced the response function to be relatively low, if compared to Ollio, at high energies. However, in the view of better defining the details of the neutron spectrum in this region, it could be desirable to increase the high energy part of the response function, even if this results in a slightly higher response at few MeV.

Stanlio is composed (from the ^3He counter outwards) of 20.75 mm polyethylene, 1 mm cadmium and 20 mm lead as shown in Figure 4.3b. A modified configuration, nicknamed Stanlio-2, was investigated: Stanlio-2 has a polyethylene thickness of 30 mm. The corresponding response function obtained from FLUKA simulations are shown in Figure 4.20.

The thicker layer of polyethylene in Stanlio-2 significantly increases the sensitivity for energies above 1 keV, and in particular above 20 MeV, where the sensitivity is three times higher than for Stanlio, whereas for lower energies the response function is

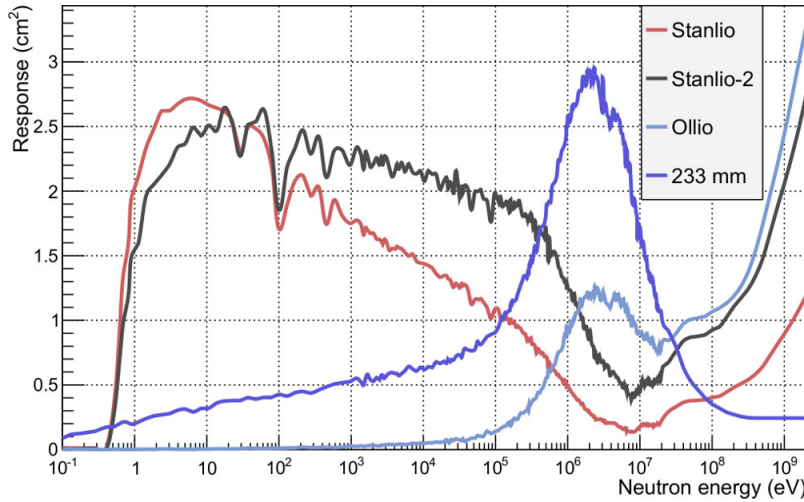


Figure 4.20: Response functions of Stanlio and Stanlio-2, as calculated via FLUKA. The response functions of Ollio and the 233 mm sphere are also plotted for comparison.

substantially unchanged. The minimum at few MeV is still present but the sensitivity in that region approximately doubled.

Given that the main interest is in having a second sphere with a good sensitivity at high energies, such as Ollio, but with a depressed response at few MeV, in order to have response functions as independent as possible, the replacement of Stanlio with Stanlio-2 could be useful. The modified geometry would result in a reasonable additional weight of 3 kg: 9.5 kg for Stanlio-2 instead of the 6.5 kg for Stanlio.

4.4.2 Response to thermal energies

The CERN BSS is lacking a sphere with a sensitivity peak in the thermal region. In fact there are at present only two spheres with a non-negligible response for thermal neutrons, i.e. the 81 mm and 108 mm spheres. An innovative sphere, nicknamed Calimero, has been studied for this purpose, the geometry of which is shown in Figure 4.21.

The sphere is constituted by graphite only and has a diameter of 130 mm. Graphite has been used instead of polyethylene due to its reduced moderation properties, discussed in Section 1.1.2.2. This limited moderation allows to closely reproduce the response function of a bare ^3He counter, but without the issues usually related to its use, i.e. electrical noise, fragility, signal instability and high sensitivity to vibra-

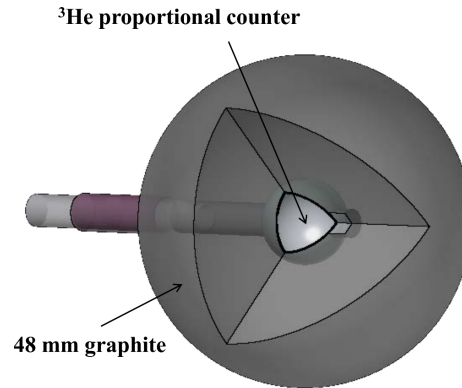


Figure 4.21: Geometry of Calimero.

tions. Figure 4.22 shows the response function calculated via FLUKA for Calimero and, for comparison, the response function of the bare counter.

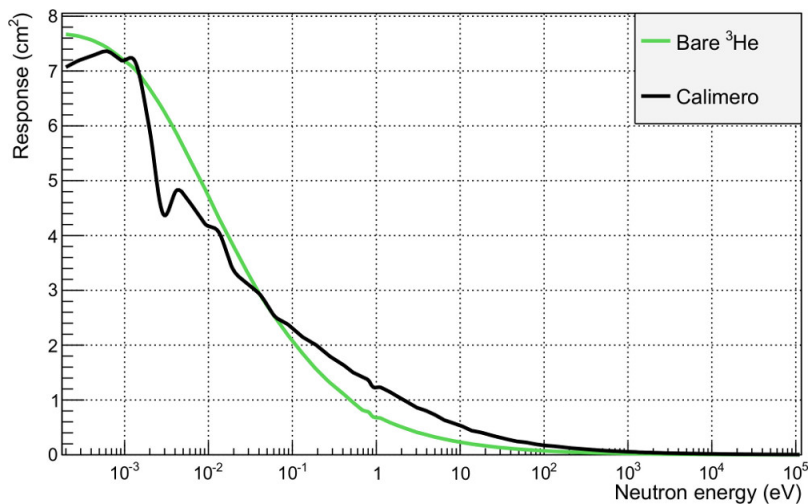


Figure 4.22: Response function of Calimero, as calculated via FLUKA. The response function of the bare detector is also shown for comparison.

The sensitivity resembles the behaviour of the reaction cross section of the neutrons in the counter. The slight deviations are due to the neutron absorption cross section in graphite, which reduces the sensitivity below 0.1 eV, and to the slight moderation effects of graphite, which enhance the response above 0.1 eV. The response is essentially negligible above 100 eV.

The introduction of Calimero in the CERN BSS would allow having a sphere with

a sensitivity peak in the thermal region. As a consequence one could also suppress the sensitivity of the 81 mm and 108 mm spheres in this region in order to increase the level of independence of the response functions. This can be done by covering the spheres with an external shell of cadmium, which has a high neutron absorption cross section below 0.4 eV. The 81 mm sphere can already be employed with an external 1 mm thick cadmium shell, whereas a dedicated shell should be built for the 108 mm sphere. Figure 4.23 shows a comparison between the response functions of the bare detector and Calimero with the response functions of the 81 mm and 108 mm sphere surrounded by the cadmium shell, as calculated via FLUKA.

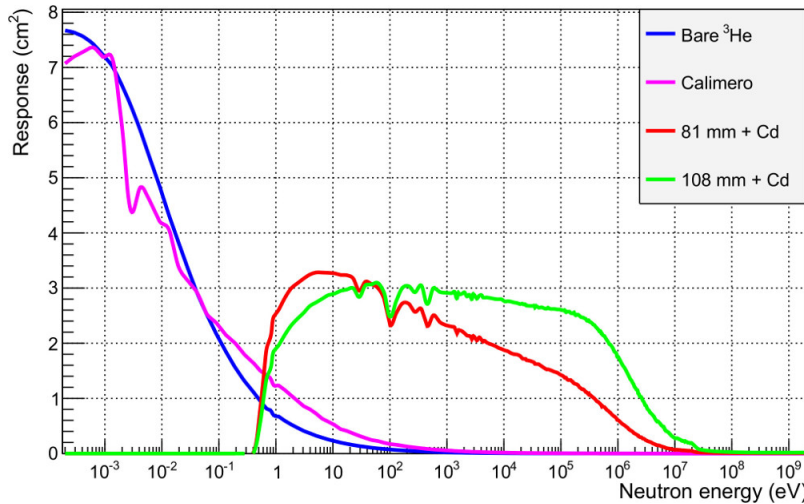


Figure 4.23: Comparison of the response functions calculated via FLUKA for the bare detector, Calimero and the 81 mm and 108 mm spheres surrounded by the cadmium shell.

The response functions of the spheres surrounded by the cadmium shell are suppressed below 0.4 eV, whereas the sensitivity of Calimero is extremely high in the thermal region. The overlap between the sensitivity of the different spheres is very limited and included in the energy range between 0.4 eV and 100 eV.

4.5 Conclusions

The BSS is currently the only device able to measure a neutron spectrum from thermal to energies in the GeV region. However, there is a number of inconveniences related to the experimental set-up. These are the weight of the total system, approximately 40 kg for the spheres and the crate with components, and the acquisition time

for measuring separately with each sphere. In addition, ^3He proportional counters are extremely expensive due to the ^3He shortage in the recent years.

The new spectrometer described in the present study was designed with view to overcoming these inconveniences while employing the same operation principles of the BSS, but with a different geometry and read-out detector. The design, construction and test of the SpectroGEM are discussed in Chapters 5 and 6 respectively.

Chapter 5

Design and study of the SpectroGEM

In this chapter the study for the spectrometer geometry and material simulated with FLUKA is described in detail. Modifications to this geometry are introduced in order to fit the requirements of the read-out GEM characteristics. Additional phenomena induced by ionizing radiation are investigated, such as possible contribution from photons to the total signal and cross-talk effects.

5.1 Material and methods

The spectrometer is composed by a neutron conversion board where different regions are implemented, each one dedicated to a specific neutron energy range. The charged particles produced are read-out by a triple GEM detector, while the neutron spectrum is acquired by unfolding the data from different regions, resembling the operation principle of the BSS but with planar geometry.

The device employs the following detection methods:

1. Thermal neutron conversion into charged particles using an appropriate converter.
2. Epithermal and intermediate neutron moderation to thermal energies and conversion to charged particles.
3. Fast neutron elastic scattering from light nuclei, followed by the production of recoil protons.

Each of these detection regions can be used as a separate detector measuring in a different energy range. When all of them are assembled together in the same system, they can serve as a spectrometer. Counts from each region will correspond to a specific energy range and the neutron spectrum can be inferred via common unfolding codes, discussed in Section 4.3. The geometry was designed as planar (see Figure 5.1): neutrons impinging on each region produce charged particles, measured by a read-out detector chosen for this purpose.

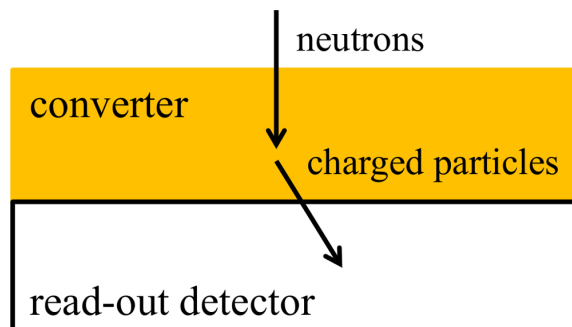


Figure 5.1: Schematic side view of a detection region in planar geometry. Charged particles produced from neutron conversion emerge from the converter and enter the read-out detector.

Three factors need to be considered when defining the converter dimensions, i.e. thickness and area:

1. The converter thickness should be large enough to maximize the probability of neutron conversion.
2. Charged particles produced from neutron conversion should have enough energy to cross the converter and enter the read-out detector.
3. The converter area should be optimized as to minimize low energy neutron escaping and absorption.

A region was assigned to each predefined energy range, resulting in several regions which are read-out by the same detector. Each of these was simulated with FLUKA to find the best material and dimensions, and to study the efficiency and response function. The area and thickness of the converter for each of the resulting six regions was determined for maximum efficiency, i.e. the number of charged particles emerging from the converter per impinging neutron, using the USRDBX estimator

(see Appendix A.2). The simulation consisted of a flat monoenergetic neutron beam of rectangular shape and dimensions of the respective region, impinging vertically on each region. The energy ranges were defined as thermal, epithermal, intermediate and fast, in the ranges listed in Chapter 1, and the detection methods are described as follows.

5.1.1 Thermal neutrons

In search for a solid thermal neutron converter with high cross section, ^{10}B and LiF were investigated for their high conversion efficiency. Boron has a cross-section of 3840 barns for thermal neutrons with the conversion reaction $^{10}\text{B}(n,\alpha)^7\text{Li}$, see Section 1.1.1.1, while ^6Li in LiF has 940 barns with the reaction $^6\text{Li}(n,\alpha)^3\text{H}$, see Section 1.1.1.2. The range of charged particles produced was calculated with SRIM [82] for different densities for the two materials and are shown in Figures 5.2a and 5.2b respectively.

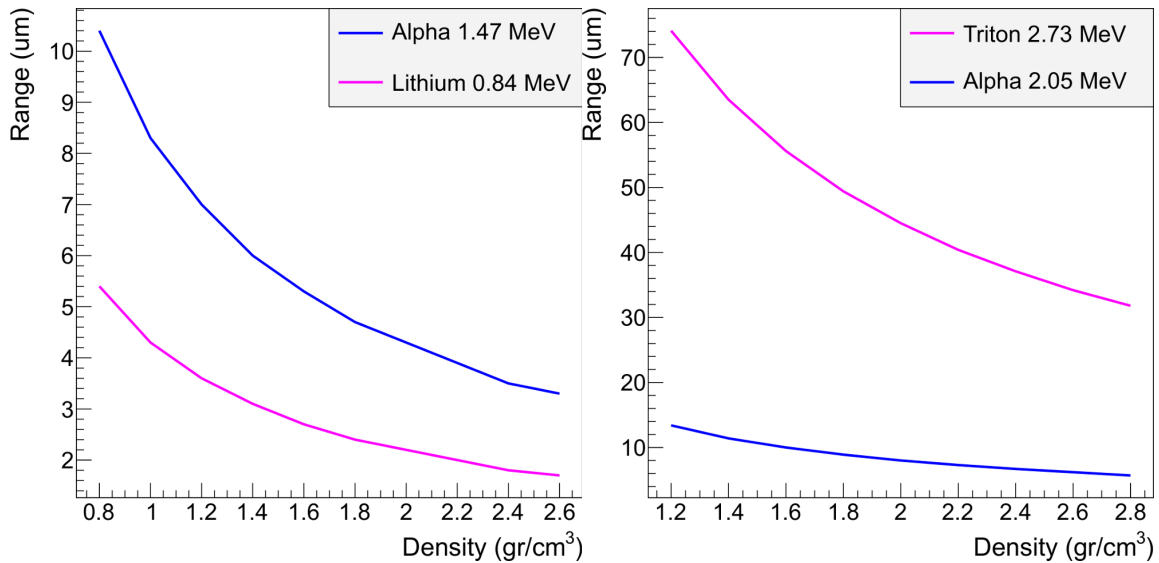


Figure 5.2: Range of charged particles from neutron conversion inside ^{10}B (left) and LiF (right).

5.1.1.1 Conversion efficiency comparison

The estimated quantity with FLUKA was fluence, which is defined as the number of charged particles emerging from each region per cm^2 per impinging neutron and described in detail in Appendix A.2. When fluence is integrated over the total area, it is equivalent to the efficiency and it was estimated for different material thicknesses. For material density 2.35 g/cm^3 for ^{10}B and 2.63 g/cm^3 for LiF, the range of charged particles for ^{10}B are $R_{\text{Li}} = 2 \text{ }\mu\text{m}$ and $R_{\text{alpha}} = 3.7 \text{ }\mu\text{m}$, while for LiF are $R_{\text{alpha}} = 6 \text{ }\mu\text{m}$ and $R_{\text{triton}} = 34 \text{ }\mu\text{m}$. The conversion efficiency for increasing material thickness is shown in Figure 5.3 for both ^{10}B and LiF. It should be noted that no energy threshold was applied for the charged particles emerging from the converter.

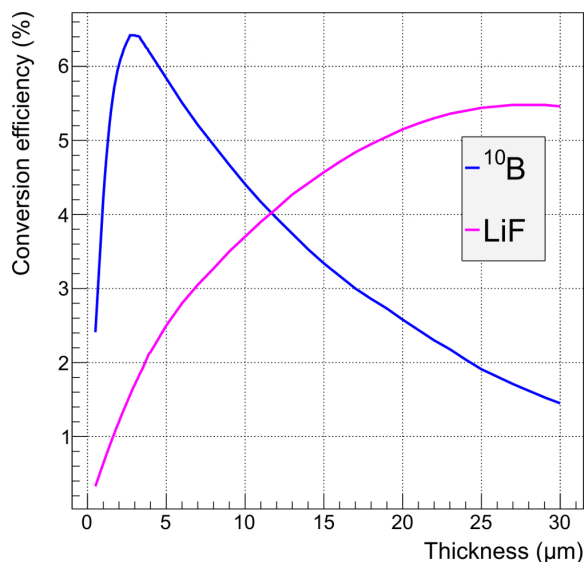


Figure 5.3: Comparison of neutron conversion efficiency in percentage for increasing thickness of ^{10}B and LiF.

The conversion efficiency for ^{10}B increases with increasing thickness, reaching a plateau in the range $2.7 - 3.3 \text{ }\mu\text{m}$ at 6.42% , after which it decreases. For LiF the efficiency reaches a plateau at $27 \text{ }\mu\text{m}$ with 5.48% . According to these results, the efficiency of LiF is comparable to the one of ^{10}B despite the fact that its conversion cross-section is four times lower. The reason lies in the higher energies at which the charged particles are emitted, as discussed in Section 1.1.1.2.

A comparison can be drawn with previous studies for the same converters; McGregor et al. [83] calculated analytically the neutron efficiency of a semiconductor-based

foil detector and Park et al. [84] simulated the efficiency of a boron-coated neutron GEM detector with MCNP [71]. A cut-off energy was set at 300 keV for the charged particles emerging from the converter when irradiated by thermal neutrons, and the results are displayed in Table 5.1. An additional comparison was conducted for pure ${}^6\text{Li}$ in the present study .

Table 5.1: Optimum thickness and maximum neutron efficiencies of LiF, ${}^{10}\text{B}$ and ${}^6\text{Li}$ converters for thermal neutron irradiation. The results are compared with previous studies for a cut-off energy for charged particles equal to 300 keV.

	Optimum thickness			Maximum Efficiency		
	LiF	${}^{10}\text{B}$	${}^6\text{Li}$	LiF	${}^{10}\text{B}$	${}^6\text{Li}$
Ref. [83]	26 μm	2.4 μm	120 μm	4.4%	4%	11.6%
Ref. [84]	28 μm	2.5 μm	-	4.7%	4.1%	-
present	27 μm	2.3 μm	110 μm	4.9%	4.2%	11.2%

The results are in reasonable agreement, considering that one of them is calculated analytically and the other two simulated with different codes (MCNP and FLUKA). For an applied threshold of 300 keV, the conversion efficiency of LiF is higher than ${}^{10}\text{B}$. However, experience has shown that such a thick layer (27 μm) of LiF cannot be produced.

Since no threshold constraints appear in the present case, ${}^{10}\text{B}$ can be chosen as the neutron converter of the spectrometer and a layer of 2.7 μm can be employed for the detection of thermal neutrons, serving as Region 1. According to previous experience [33] though, the deposition of more than 1 μm of ${}^{10}\text{B}$ is challenging with common techniques and therefore this is the thickness chosen for thermal neutron conversion, showing an efficiency of 4.2%. As a result, the first region of the spectrometer employs only a ${}^{10}\text{B}$ foil with 1 μm thickness and $2 \times 2 \text{ cm}^2$ area. The area was decided based on the need for comparable absolute response of all regions at the range they show maximum response, which will be discussed in Section 5.2.

5.1.1.2 Angular distribution of charged particles

Charged particles from slow neutron conversion in ${}^{10}\text{B}$ will be emitted at opposite directions, as explained in Section 1.1.1.1. Integration over the total number of angles results in isotropic emission of alpha particles and ${}^7\text{Li}$ ions inside the converter. However, charged particles travelling in a solid angle larger than a certain ϑ_L depending on the ${}^{10}\text{B}$ thickness, have higher probability to be absorbed inside the converter.

The angular distribution of charged particles emerging from different thickness was simulated with the USRYIELD estimator (see Appendix A.2) and shown in Figure 5.4. The spatial distribution is quite uniform over the solid angle for very thin layers (<400 nm), while increasing the thickness, two regions can be distinguished: a central zone inside the ϑ_L angle, where the particle density is uniform, and an external one where the density decreases almost linearly with ϑ . The rejection angle for 1 μm thickness of ^{10}B is 60° .

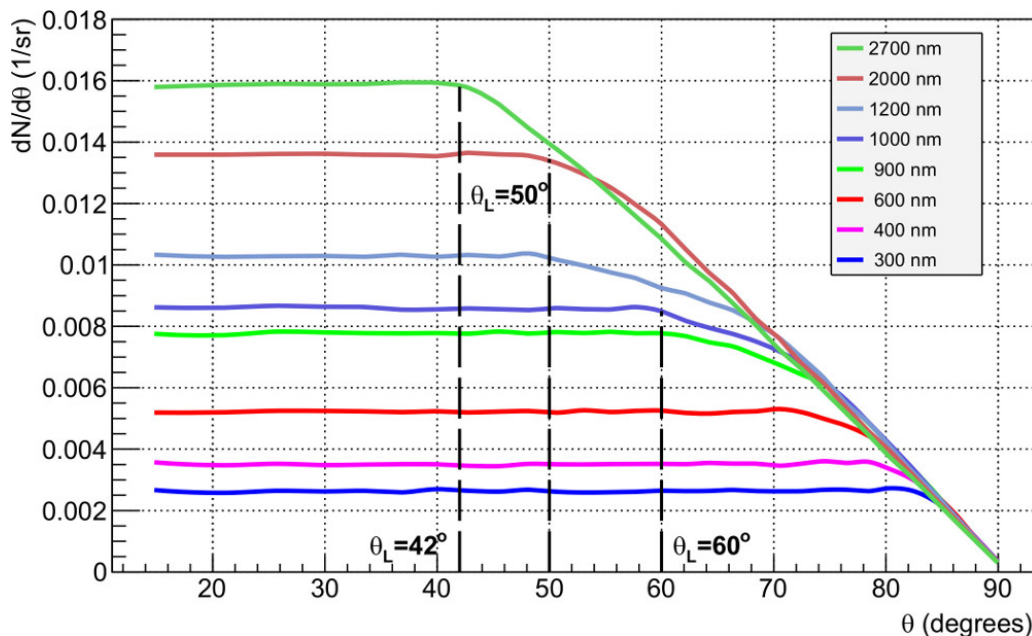


Figure 5.4: Angular distribution of charge particles emerging from different thickness of ^{10}B , each one showing a rejection angle ϑ_L . For 1 μm thickness of ^{10}B , this angle corresponds to 60° .

5.1.1.3 Energy spectrum of charged particles

Every device has a detection threshold, i.e. a cut-off energy for inducing a detectable signal. Useful information can be acquired from the particle spectrum entering the detector, concerning the energy deposited in its active volume. Charged particles from the $^{10}\text{B}(n,\alpha)^7\text{Li}$ reaction are always emitted at the same energies (see 1.6) independently from the incoming neutron energy, but a spectrum emerges from the converter due to their stopping power in ^{10}B . The spectrum emerging from 1 μm ^{10}B is shown in Figure 5.5, expressed in fluence per impinging thermal neutron.

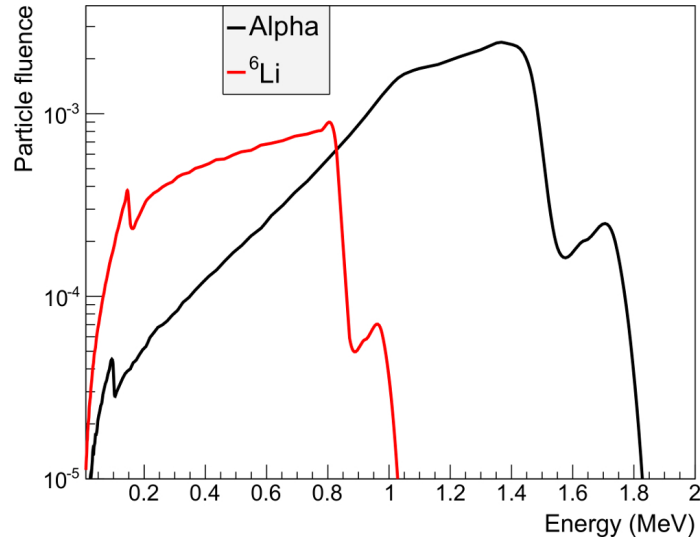


Figure 5.5: Particle spectrum emerging from 1 μm of ${}^{10}\text{B}$ per impinging thermal neutron.

It can be noted that the spectra are peaked at $E_{\text{Li}}=0.84$ MeV and $E_{\alpha}=1.47$ MeV, but there are two additional peaks around 1 MeV and 1.7 MeV respectively. These correspond to the different branching ratios of the radiative and non-radiative channels of the ${}^{10}\text{B}(n,\alpha){}^7\text{Li}$ reaction (see branching in 1.2). The additional peaks and tails at lower energies, as well as the broadened peaks in the spectra, are due to the energy straggling that particles experience in passing through different thickness of boron reaching the detector; indeed, particles emitted at large angles travel over longer tracks inside the material, losing more energy than others.

5.1.2 Epithermal and intermediate neutrons

Epithermal and intermediate neutrons can be detected via the ${}^{10}\text{B}(n,\alpha){}^7\text{Li}$ reaction with higher efficiency once moderated with polyethylene to lower energies. The polyethylene layer thickness needs to be large enough to thermalize the neutrons without absorbing them, as shown in Table 1.3. The response functions of these regions resemble those of the BSS [76], in which each sphere shows maximum response for a specific neutron energy depending on the amount of polyethylene employed.

The response of different regions was investigated for polyethylene thickness in the range 1 - 10 cm and area 1 - 100 cm^2 . For the detection of epithermal neutrons the desired response peak should appear for 1 eV neutron energy. This can be achieved

with 2 cm polyethylene thickness of 0.94 g/cm^3 density and $4 \times 4 \text{ cm}^2$ area (Region 2). An intermediate neutron peak at 100 eV can be produced with 5 cm polyethylene thickness and $6 \times 8 \text{ cm}^2$ area (Region 3). Increasing the amount of polyethylene and area, the detection of 1 MeV neutrons is possible with 8 cm polyethylene and $9 \times 9 \text{ cm}^2$ area (Region 4), while showing significant response also to intermediate neutrons.

The shape of the charged particle spectrum entering the read-out detector is the same for all regions, since the alpha particle and the lithium ion are always emitted at the same energies. However, the absolute fluence is different between regions due to the different efficiency they show. The charged particle spectra per impinging neutron entering the detector for Regions 2, 3 and 4 are shown in Figure 5.6, estimated with USRBDX (see Appendix A.2). The regions were irradiated with the neutron energy at which they show the highest response and dimensions equal to the respective region area.

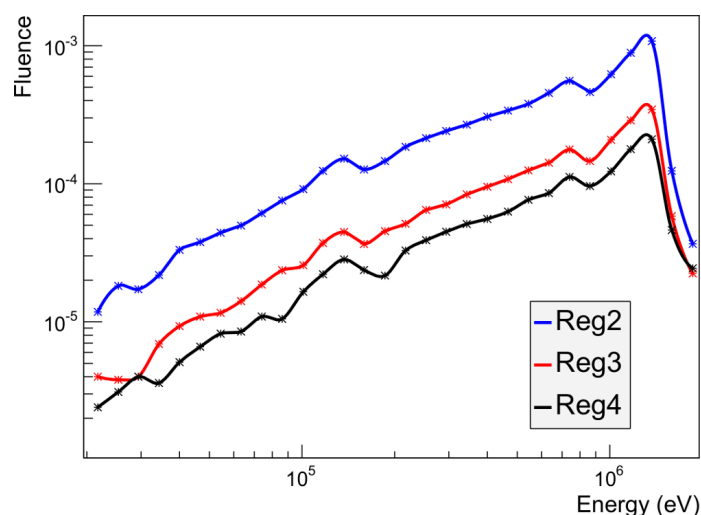


Figure 5.6: Charged particle spectra per impinging neutron, entering the detector from Regions 2, 3 and 4, when irradiated with 1 eV, 100 eV and 400 keV neutrons respectively.

The detection efficiency decreases with increasing neutron energy for the $^{10}\text{B}(n,\alpha)^7\text{Li}$ reaction, as shown in Figure 1.1. When epithermal or intermediate neutrons impinge on polyethylene, only a fraction of them reach the thermal state and have higher probability of being converted, despite the amount of polyethylene employed. As a result, the region efficiency decreases with increasing amount of polyethylene and this fact can be explained with the simulated neutron spectrum entering the boron foil for each region (Figure 5.7).

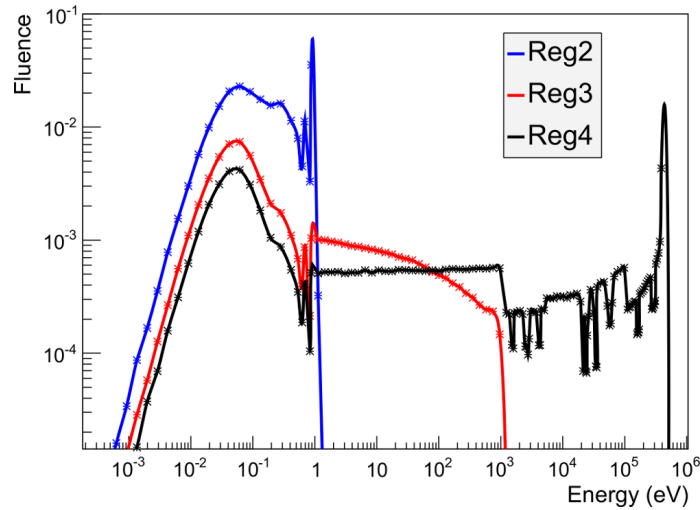


Figure 5.7: Neutron spectra entering the detector per impinging neutron from Regions 2, 3 and 4, when irradiated with 1 eV, 100 eV and 400 keV respectively.

5.1.3 Fast neutrons

Fast neutrons can be detected via elastic scattering by light nuclei, as described in Section 1.1.2.1. Polyethylene is a common material used for this purpose and the maximum transferable energy to the recoil proton is 31.4%, as displayed in Table 1.2. The conversion efficiency, i.e. number of protons produced per impinging neutron, was simulated for thickness and neutron energy in the range 0.1 - 4 mm and 1 - 20 MeV respectively for a 20 keV threshold. The results are shown in Figure 5.8.

The stopping power of protons in matter decreases for increasing proton energy, so that the conversion efficiency should decrease after a specific neutron energy, depending on the material and the detection threshold of the read-out device. For 0.1 mm thickness the maximum efficiency appears at 4 MeV, for 0.5 mm at 7 MeV and for higher thickness at 9 MeV. It should be noted that the efficiency reaches a plateau at 2 mm polyethylene and does not increase for higher thickness, suggesting that this is the optimal amount for fast neutron conversion.

Two regions were designed for the detection of fast neutrons: one with 700 μm polyethylene and one with 2 mm polyethylene and 1 mm aluminium (Figure 5.9). The first shows an efficiency peak at 8 MeV, while the second one at 20 MeV. The addition of 1 mm aluminium stops a few MeV protons, so that the two regions show response in relatively well separated energy regions. However, the efficiency for the

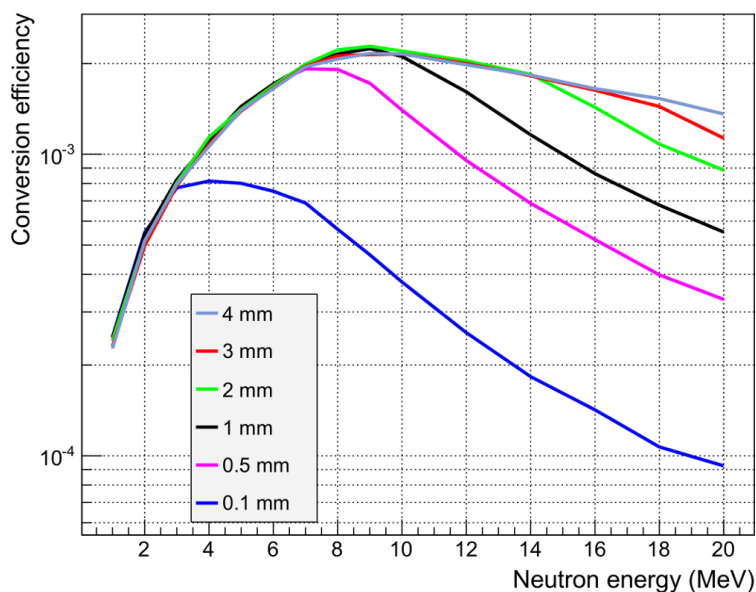


Figure 5.8: Conversion efficiency of fast neutrons with varying energy in different thickness of polyethylene. The efficiency reaches a plateau of $2.25 \cdot 10^{-3}$ at 2 mm.

second significantly decreases by rejecting the protons produced, as measured and simulated previously (see 2.27b). In order to obtain comparable absolute response, the area of Region 6 (2 mm PLE + 1 mm Al), was determined as 100 cm^2 and for Region 5 (700 μm PE) 50 cm^2 .

Fast neutrons impinging on 2 mm polyethylene are hardly moderated and therefore protons produced enter the read-out detector at high energies. The proton fluence from Regions 5 and 6 is shown in Figure 5.10 for neutron energies of 8 and 20 MeV respectively. The efficiency of each region was simulated as the total number of protons entering the detector per impinging neutron and Region 5 shows higher efficiency ($2.24 \cdot 10^{-3}$) than Region 6 ($1.49 \cdot 10^{-3}$).

5.2 Response matrix simulation

The characteristics of all regions are summarized in Table 5.2. These consist in the thickness of ^{10}B , polyethylene (PE) and aluminium (Al) from the read-out detector outwards, the area and the energy peak for each region.

The response matrix of the spectrometer was simulated with a different formula than the one used for the BSS (see Equation 4.1). The reason lies in the fact that

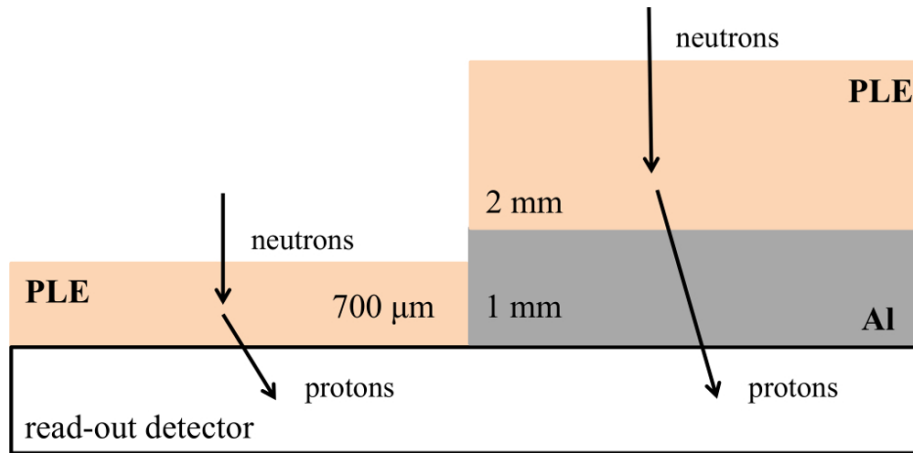


Figure 5.9: Side view of Regions 5 (left) and 6 (right). Aluminium added to Region 6 stops a few MeV protons for better response separation.

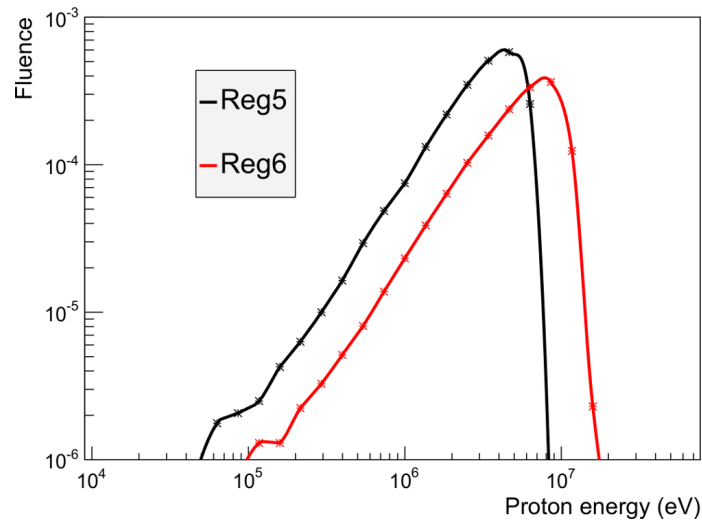


Figure 5.10: Protons spectra entering the detector per impinging neutron from Regions 5 and 6, when irradiated with 8 and 20 MeV respectively.

Table 5.2: Material, thickness and peak energy for each region from the read-out detector outwards.

Region	^{10}B (μm)	Al (cm)	PE (cm)	Area (cm^2)	Peak (eV)
Reg1	1	0.0	0.00	2 x 2	0.025
Reg2	1	0.0	2.00	4 x 4	1
Reg3	1	0.0	5.00	6 x 8	10^2
Reg4	1	0.0	8.00	9 x 9	$4 \cdot 10^5$
Reg5	0	0.0	0.07	5 x 10	$8 \cdot 10^6$
Reg6	0	0.1	0.20	10 x 10	$2 \cdot 10^7$

the products of the $^3\text{He}(n,p)^3\text{H}$ reaction are not transported by the FLUKA code when the incoming neutron energy is less than 20 MeV (see Appendix A), while for the $^{10}\text{B}(n,\alpha)^7\text{Li}$ reaction they are transported. Therefore the response matrix was simulated employing the USBDX estimator as the number of charged particles per incoming neutron entering the read-out detector, divided by the normalisation quantity F_u , i.e. the fluence of neutrons impinging on a surface perpendicular to the area A (cm^{-2}): $F_u = 1/A$ for each region. The number of charged particles is the sum of alpha particles, ^7Li ions and protons and the formula is given by Equation 5.1.

$$R(E_i) = \frac{\text{Nr of charged particles}}{F_u} \text{ cm}^2 \quad (5.1)$$

The response matrix was simulated in the range from thermal to 100 MeV neutrons and it is shown in Figure 5.11. When compared to the BSS matrix (see Figure 4.4), it is evident that the response of the new spectrometer is lower. This is mostly due to the smaller area of the regions. Another reason is the fact that the efficiency for planar geometry is lower than for spherical, because only one particle from the $^{10}\text{B}(n,\alpha)^7\text{Li}$ reaction can be detected. Taking into account also the rejection angle depending on the amount of boron, as shown in Figure 5.4, the efficiency ratio between planar and spherical geometry is less than 0.5. However, the total time needed for measuring with the new spectrometer should not differ from the time needed for a single sphere with low efficiency, e.g. Ollio or 233 mm, and thus the acquisition can be performed in a faster and more simple way.

This neutron conversion board can be used with any detector able to measure counts individually from each region. A triple GEM was decided to be employed as the read-out detector, designed to fit specific requirements discussed in the following section.

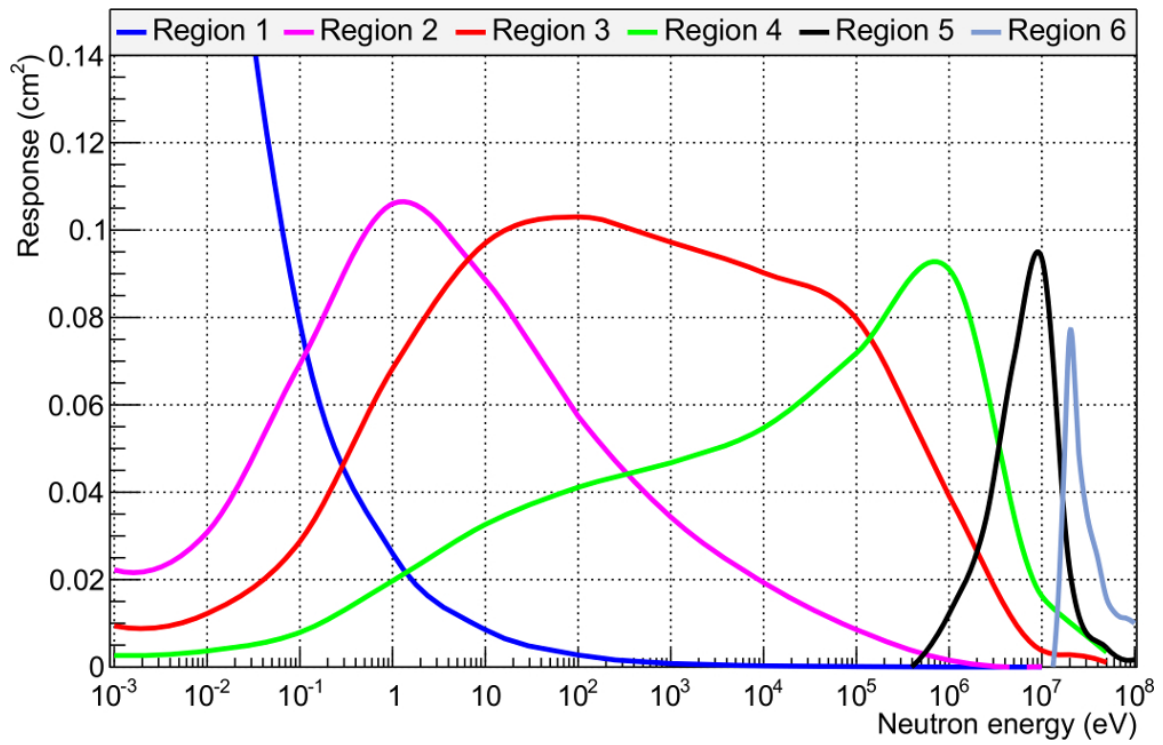


Figure 5.11: Response matrix of the spectrometer.

5.3 The read-out detector

The detector was designed with an active area of $35.2 \times 20.8 \text{ cm}^2$ and 256 read-out pads of $2.2 \times 1.3 \text{ cm}^2$ each. The cathode is composed of $50 \text{ }\mu\text{m}$ aluminium and 2.2 mm polyethylene. A layer of $^{10}\text{B}_4\text{C}$ ($1 \text{ }\mu\text{m}$ thickness) is used for low energy neutron conversion and placed on a $500 \text{ }\mu\text{m}$ aluminium foil, as shown in Figure 5.12. The $500 \text{ }\mu\text{m}$ aluminium and $1 \text{ }\mu\text{m}$ $^{10}\text{B}_4\text{C}$ are present only in Regions 1 to 4, while for Region 6 an additional aluminium foil of 1 mm was placed under the $50 \text{ }\mu\text{m}$ foil. For Region 5 no extra material was needed, as the cathode itself serves for fast neutron conversion.

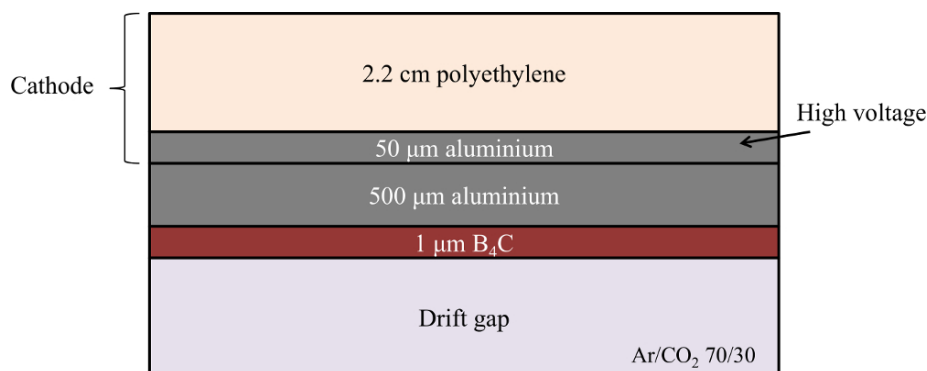


Figure 5.12: Cathode configuration of the GEM detector and additional material for neutron conversion. The $500 \text{ }\mu\text{m}$ aluminium and $1 \text{ }\mu\text{m}$ $^{10}\text{B}_4\text{C}$ are present only in Regions 1 to 4.

The typical drift gap of 3 mm (see Section 2.1.2) is not suitable for neutron detection, because charged particles from neutron conversion need a longer path in $\text{Ar}/\text{CO}_2 \text{ 70}/30$ in order to deposit their full energy. This is the reason why the GEM ^{10}B detector was assembled with a 10 mm drift gap, as discussed in 2.4.1. As a result, the drift gap thickness has to be large enough to allow the charged particles to deposit enough energy to induce a detectable signal. The induced charge is recorded by the CARIOCA chips [20], posing a threshold of 40 fC that corresponds to a minimum energy of 25 keV deposited in the drift gap.

Considering the stopping power of alpha particles, lithium ions and protons in $\text{Ar}/\text{CO}_2 \text{ 70}/30$, the thickness of the drift gap was chosen as 5 mm . Lithium ions of 0.84 MeV have a range of 4 mm in this gas mixture, depositing all of their energy, while alpha particles of 1.47 MeV have a range of 7 mm , which means that they will deposit a great portion of their energy. However, protons from elastic scattering are not emitted at a fixed energy and their stopping power in $\text{Ar}/\text{CO}_2 \text{ 70}/30$ depends on

their energy. Figure 5.13 shows the energy in keV deposited by protons in a 5 mm drift gap, calculated with SRIM. According to these results, the stopping power of protons decreases with increasing energy and only those entering the drift gap with energy less than 14 MeV will deposit more than the threshold of 25 keV.

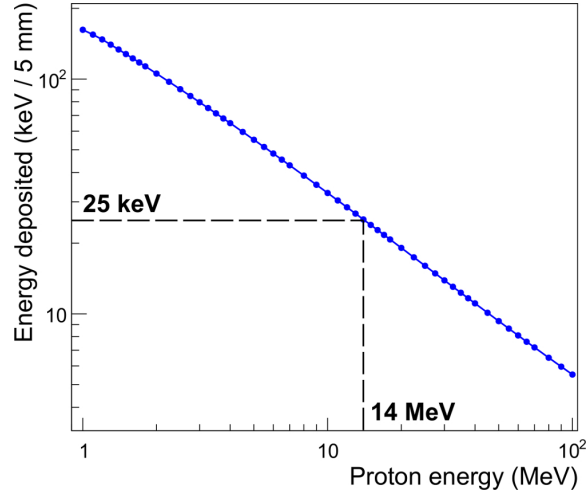


Figure 5.13: Energy deposited by protons of increasing energy in 5 mm drift gap. Only protons with less than 14 MeV will deposit more than the threshold of 25 keV in order to be detected.

Each transfer and induction gap is 2 mm thick (see Figure 2.6). The acquisition system is the same as the one used for previous measurements with the only difference that two FPGAs are needed instead of one due to the large active area .

5.4 Enhanced design

The conversion board was firstly designed with the purpose to define the material and number of regions to be employed. An enhanced design was then introduced, so that the area of each region corresponds to an integer number of read-out pads ($2.2 \times 1.3 \text{ cm}^2$) and the detector cathode material is taken into account. The additional material (50 μm aluminium and 2.2 mm polyethylene) and converter change ($^{10}\text{B}_4\text{C}$ instead of ^{10}B) resulted in response decrease of Regions 1 to 4 and slight modification of Regions 5 and 6. $^{10}\text{B}_4\text{C}$ consists of 78% ^{10}B , which means that its maximum efficiency is 78% of ^{10}B .

The new characteristics, including the cathode material and the number of read-out pads for each region, are summarized in Table 5.3 and the board designed with

Autodesk Inventor Professional 2014 is shown in Figure 5.14.

Table 5.3: Material and modified geometrical characteristics for each region from the detector outwards. The number of corresponding read-out pads is given for each of them.

Region	$^{10}\text{B}_4\text{C}$ (μm)	Al (cm)	PLE (cm)	New area (cm^2)	Pads
Reg1	1	0.055	0.22	2.2 x 2.6	2
Reg2	1	0.055	2.22	6.6 x 2.6	6
Reg3	1	0.055	5.72	6.6 x 7.8	18
Reg4	1	0.055	8.22	8.8 x 9.1	28
Reg5	0	0.005	0.22	6.6 x 5.2	12
Reg6	0	0.100	0.42	6.6 x 7.8	18

5.5 Study of cross-talk effects

The regions are separated by at least two read-out pads, in order to avoid cross-talk effects between neighbouring regions. This separation can be effective for charged particles but not for neutrons, which do not have continuous energy deposition in material and can travel long distances without interacting. A simulation with FLUKA was performed in order to investigate this effect; regions were irradiated individually with a neutron beam of different energies and their response was compared to the one obtained from total irradiation of the board with the same energy.

5.5.1 Regional irradiation

Three regions were irradiated in FLUKA with a flat rectangular beam, with beam size matching the region area and beam energy corresponding to the maximum region response. The fluence of neutrons and charged particles was estimated with the USRBIN card (see Appendix A.2), with a binning that corresponds to the read-out pad dimensions. Neutron fluence was estimated in the board volume above the detector cathode and charged particle fluence, i.e. alpha particles, lithium ions and protons, in the drift gap. The regions were surrounded by air and the drift gap was composed of Ar/CO₂ 70/30.

5.5.1.1 Slow neutrons

Region 2 was irradiated with 1 eV neutrons, at which energy it shows the highest response according to the matrix shown in Figure 5.11. The results for neutrons and charged particle fluence are shown in Figure 5.15 as viewed from top.

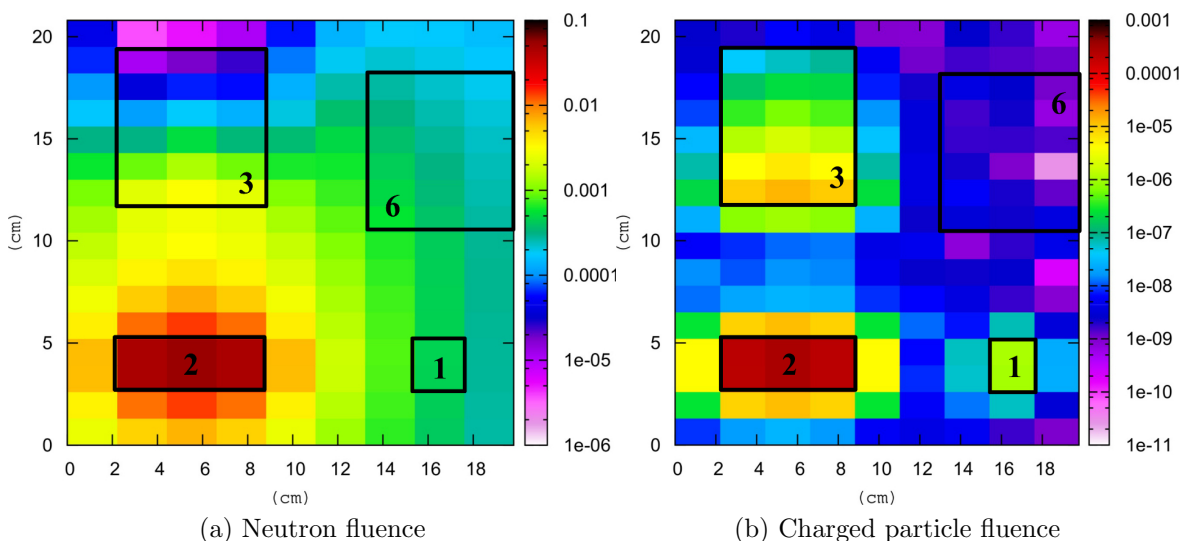


Figure 5.15: Top view of neutron (a) and charged particle fluence (cm^{-2}) (b) on the left part of the detector when Region 2 is irradiated with a neutron beam of 1 eV. The histogram binning corresponds to the read-out pad dimensions.

According to the neutron fluence results in Figure 5.15a, a small fraction of neutrons is stopped inside the 2.22 cm polyethylene and another fraction reaches the boron foil, but many of them are scattered from the top and the sides of the polyethylene block, reaching Regions 1, 3 and 6. The lower part of Region 3 is mostly affected, where the neutron fluence is 10 times lower than the one inside Region 2, while Region 6 remains mostly uninfluenced. This fact is demonstrated in Figure 5.15b, where the fluence of charged particles is estimated. The irradiation of Region 2 will induce signal in the two neighbouring regions, 1 and 3, due to scattered neutrons from Region 2 when converted to charged particles in Regions 1 and 3. Region 6 remains unaffected because it does not employ a boron foil. Therefore the cross-talk effect is due to scattered neutrons and not charged particles, since the latter deposit their energy in the gas before reaching neighbouring regions.

5.5.1.2 Intermediate neutrons

The same study was performed for Region 4, which was irradiated with a neutron beam of 400 keV. The neutron fluence in the right part of the converter board is shown in Figure 5.16a, while the one of charged particles in 5.16b

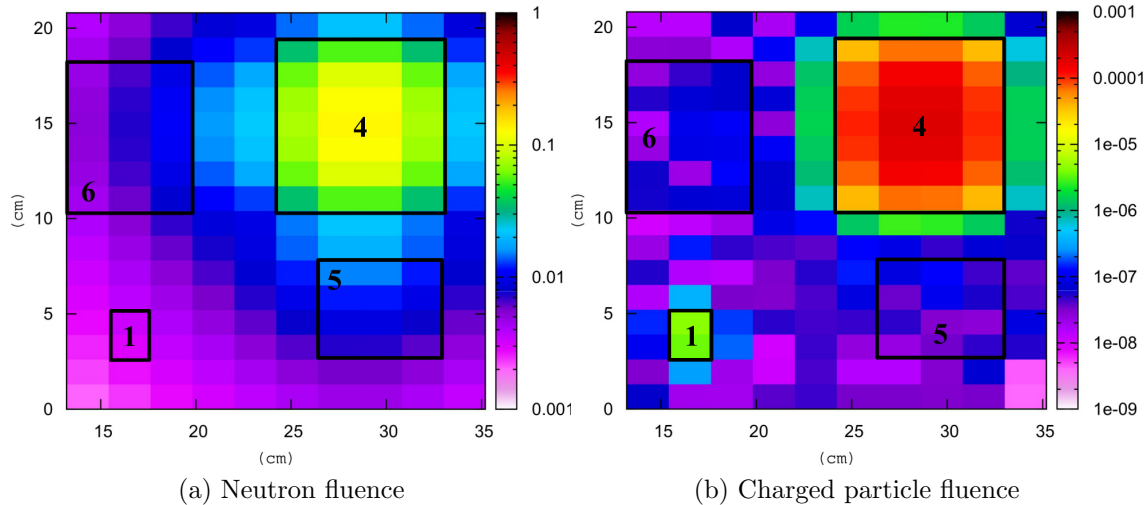


Figure 5.16: Top view of neutron (a) and charged particle fluence (cm^{-2}) (b) on the right part of the detector when Region 4 is irradiated with a neutron beam of 400 keV.

A fraction of neutrons impinging on Region 4 escape isotropically from the sides of the polyethylene piece, reaching Regions 1, 5 and 6, as shown in Figure 5.16a. The neutron fluence in all of them is significantly low, especially in Region 1, but this is not the case for the charged particle fluence. As shown in Figure 5.16b, neutrons are converted in Region 1 but not in Regions 5 and 6, where there is no boron. Even though the response of Region 1 to 400 keV neutrons is negligible, some of the neutrons arriving to this region have been moderated along their path and have energy which is low enough to make interactions with boron very likely. Regions 5 and 6 will remain mostly unaffected by the irradiation of Region 4, since they can only detect neutrons with energy higher than 1 MeV and charged particles escaping from Region 4.

5.5.1.3 Fast neutrons

The study of cross-talk effects when irradiating Region 6 is of great importance, because it is placed in the middle of the board and neighbouring with all regions. Region 6 was irradiated with a 25 MeV neutron beam and the results are shown in Figure 5.17.

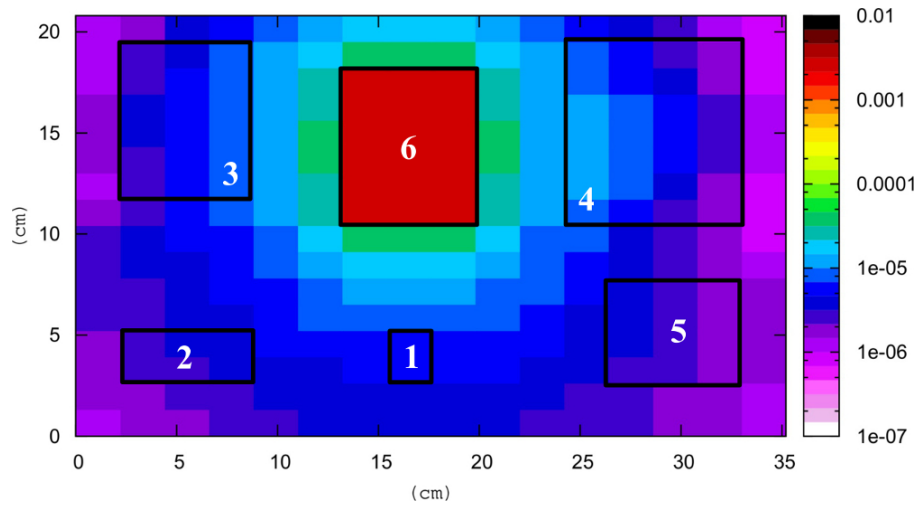


Figure 5.17: Top view of neutron fluence (cm^{-2}) on the total area when Region 6 is irradiated with a neutron beam of 25 MeV.

Neutrons escape isotropically from Region 6 and can reach any region. However, these neutrons are not moderated substantially in the 4.2 mm polyethylene. As a result, no neutron conversion will take place in the boron foils of Regions 1 to 4, but signal can be induced from the recoil protons. This fact is outlined in Figure 5.18, which shows that protons are generated inside Region 6 and cross a distance of several centimetres in the drift gap before reaching the neighbouring regions. Nevertheless, the proton fluence in all regions is low and cross-talk effects will show negligible impact on the response of Regions 1 to 5 to fast neutrons, thanks to the large distance between regions.

5.5.2 Total irradiation

The existence of cross-talk phenomena was proved with the partial irradiation of regions with different neutron energies and the charged particle fluence induced to neighbouring regions. The aftermath can be estimated by comparing the response

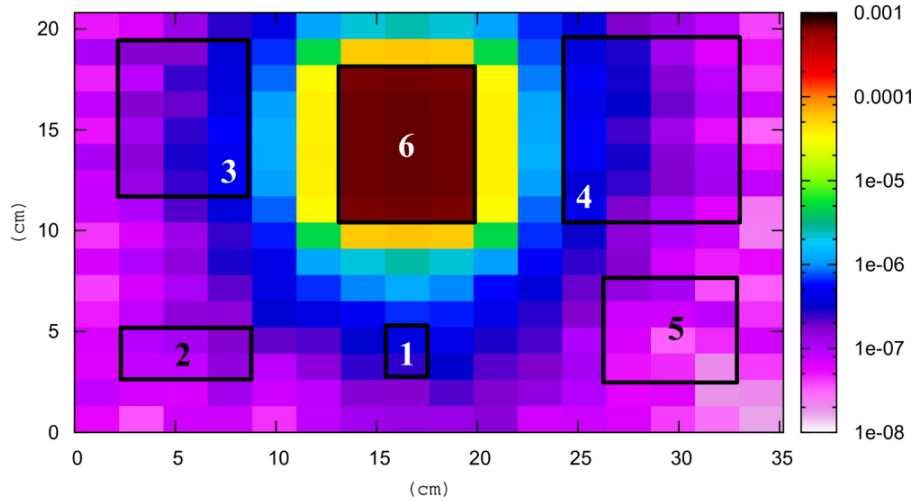


Figure 5.18: Top view of charged particle fluence (cm^{-2}) on the total area when Region 6 is irradiated with a neutron beam of 25 MeV.

of each region for partial and total irradiation, i.e. when all regions are irradiated at the same time with the same neutron energy. A flat rectangular neutron beam of dimensions $35.2 \times 20.8 \text{ cm}^2$ and 13 different energies impinging on the board was simulated with FLUKA. The ratio between responses for total and partial irradiation of each region is shown in Table 5.4, providing a quantitative estimation of the cross-talk effect.

It is evident that this effect is significant for regions when they are irradiated with energies to which they are designed to show low response. Region 1 is mostly affected in the keV - MeV region, due to scattered neutrons from neighbouring regions that arrive moderated, while Region 2 shows relatively constant response increase in the entire range, except for neutrons with energy less than 1 eV. The same trend can be seen for Regions 3 and 4, showing higher response for low energies, at which their response is negligible when partially irradiated. A decisive factor for their response increase is the thickness of the polyethylene pieces (5.72 and 8.22 cm respectively), increasing the probability that scattered neutrons from neighbouring regions enter from the sides. Regions 5 and 6 are not influenced by scattered neutrons with energy less than 5 MeV, because in these regions only recoil protons with a maximum energy of 1.5 MeV can be produced, which are stopped in the aluminium cathode.

In conclusion, all regions employing boron are sensitive to scattered neutrons with energy less than 1 MeV and this effect must be considered in their response functions. Taking into account the modified geometry and the non-negligible cross-talk effects,

Table 5.4: Ratio of response between total and partial irradiation for all regions and different energies. Values higher than 1 suggest count contribution from cross-talk effects.

E_n (eV)	Reg1	Reg2	Reg3	Reg4	Reg5	Reg6
$1.2 \cdot 10^{-2}$	1.1	4.5	14.7	35.8	-	-
$1.1 \cdot 10^{-1}$	1.2	2.2	6.3	17.0	-	-
$1.0 \cdot 10^0$	1.2	1.3	2.1	4.2	-	-
$1.2 \cdot 10^1$	1.2	1.2	1.4	2.1	-	-
$1.2 \cdot 10^2$	1.5	1.2	1.3	1.6	-	-
$1.1 \cdot 10^3$	1.3	1.3	1.2	1.5	-	-
$1.0 \cdot 10^4$	2.3	1.3	1.2	1.2	-	-
$1.2 \cdot 10^5$	2.1	1.4	1.1	1.1	-	-
$4.0 \cdot 10^5$	3.2	1.4	1.0	1.1	-	-
$1.0 \cdot 10^6$	3.8	1.3	1.1	1.1	-	-
$5.0 \cdot 10^6$	1.0	1.3	1.2	1.1	1.1	-
$1.5 \cdot 10^7$	1.0	1.1	1.2	1.2	1.0	2.6
$2.5 \cdot 10^7$	1.0	1.1	1.1	1.1	1.0	1.0
$1.0 \cdot 10^8$	1.0	1.1	1.1	1.1	1.0	1.0

the new response functions are listed in Appendix B.

5.6 Photon contribution

Previous measurements with the GEM have shown non-negligible photon detection efficiency (see Section 2.4.2.3), which can be eliminated when applying appropriate high voltage to the foils, as shown in Figure 2.4.1.1. Neutrons in Regions 1 to 4 are detected via the $^{10}\text{B}(n,\alpha)^7\text{Li}$ reaction, 94% of which lead to photon emission with 482 keV energy. Photons can be also produced inside polyethylene and the aluminium cathode via inelastic scattering. The detection efficiency depends on the photon energy and attenuation length in the material being crossed and therefore the photon spectrum entering the read-out detector from each region need to be investigated for different neutron energies.

Region 2 was irradiated with a 1 eV neutron beam and the fluence of photons crossing three surfaces was estimated with USRBDX; 1) photons emerging from polyethylene and entering the aluminium cathode, 2) from the cathode to the boron foil and 3) from the foil to the drift gap (see cathode structure in Figure 5.12).

The scoring region was only Region 2, without taking into account the neighbouring areas, and the photon fluence per impinging neutron is shown in Figure 5.19 for all surfaces.

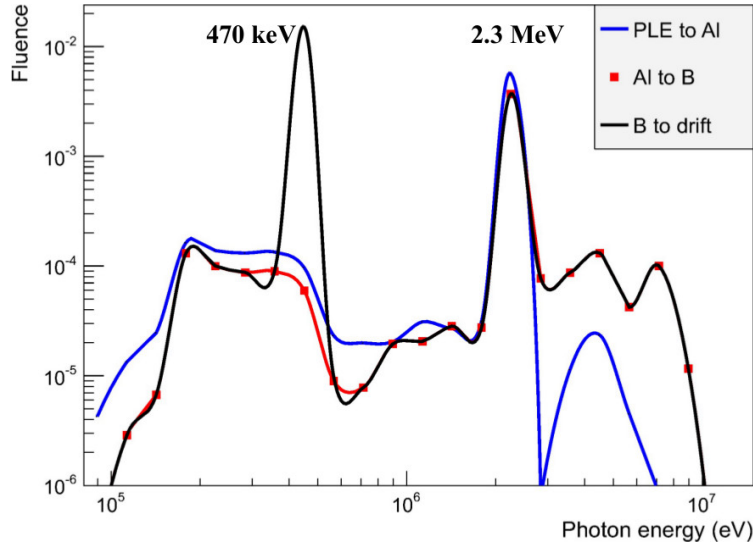


Figure 5.19: Photon fluence (cm^{-2}) crossing three surfaces: polyethylene to aluminium, aluminium to boron and boron to drift gap. The 470 keV peak stems directly from the neutron reaction with boron and the 2.3 MeV peak from inelastic scattering in polyethylene and aluminium.

Two distinct peaks are visible; one in the energy bin 400 - 500 keV (470 keV), and one in the bin 2 - 2.5 MeV (2.3 MeV). According to the results of the study, the 470 keV peak emerges only after the boron foil and therefore corresponds to the 482 keV photon. The 2.3 MeV peak is already present after the polyethylene layer and stems from the de-excitation of hydrogen and carbon atoms. The photon fluence exiting the aluminium cathode is identical with the one exiting polyethylene, except for two smaller peaks around 4.5 MeV and 7 MeV, which are due to neutron interactions inside aluminium.

The 2.3 MeV energy peak shows comparable fluence to the 470 keV, implying that both polyethylene and boron act as source of photons for the read-out detector. The photon fluence produced inside Region 2 is shown in Figure 5.20 as a function of distance, when the beam impinges on the region from right to left.

Photons are mainly produced at a distance of 8 mm inside polyethylene and the fluence at point 0 in the figure corresponds to photons which have not been absorbed in polyethylene. These photons are added to the ones produced inside boron via the

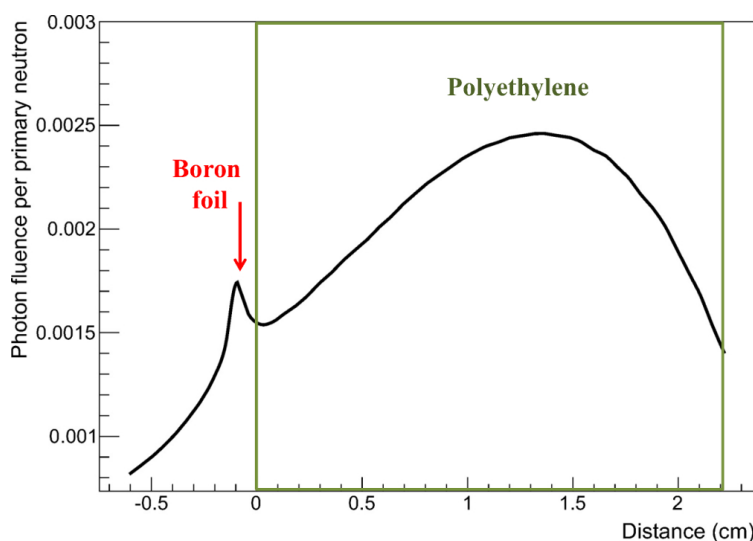


Figure 5.20: Photon fluence (cm^{-2}) projected to the distance travelled inside Region 2 (2.28 cm in total), with the beam impinging from right to left. Photons are firstly produced in polyethylene and secondly in the boron foil.

$^{10}\text{B}(n,\alpha)^7\text{Li}$ reaction, as the peak at -0.1 cm indicates in Figure 5.20. and the total number of photons enters the drift gap.

The same study was performed with all regions, when irradiated with the neutron energy at which they show maximum response: 0.025 eV, 1 eV, 1 keV and 400 keV for Regions 1, 2, 3 and 4 respectively. The photon fluence entering the drift gap for Regions 1 to 4 is shown in Figure 5.21. The 470 keV and 2.3 MeV peaks are present in the photon spectrum for all regions and the different absolute fluence for each region is due to their efficiency, as discussed in Section 5.1.2.

The photon fluence entering the drift gap for Regions 5 and 6 is shown in Figure 5.22, when irradiated with 15 MeV and 25 MeV respectively. Several distinct peaks appear for 250 and 450 keV, 1, 2 and 4.5 MeV. In these regions all neutron interactions take place in polyethylene and aluminium, especially in Region 6 which employs 1 mm of the latter. Region 5 shows the same photon peaks, although the one at 4.5 MeV is dominant.

The interaction of 25 MeV neutrons with aluminium results in the production of secondary neutrons, alpha particles, gamma radiation and residual nuclei. According to the simulation performed, the percentage of particles generated in inelastic interactions per impinging neutron is: 37% ^4He , 9% protons, 24% photons and 30% neutrons. A large number of aluminium isotopes produced are gamma emitters, in-

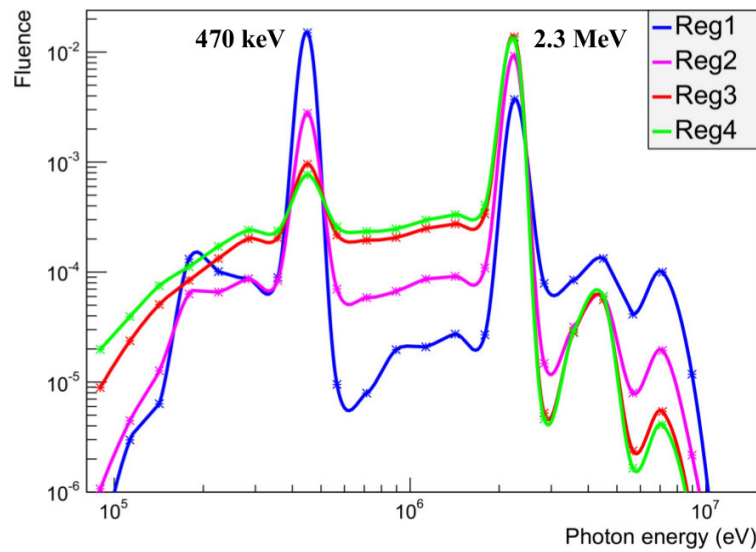


Figure 5.21: Photon spectra entering the drift gap from Regions 1 to 4, when irradiated with 0.025 eV, 1 eV, 1 keV and 400 keV respectively. The spectra shapes are similar and the absolute fluence is varying with each region characteristics.

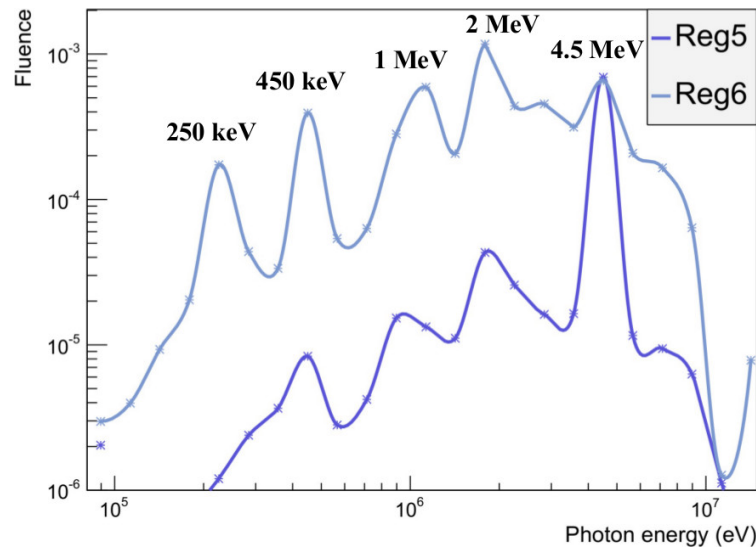


Figure 5.22: Photon spectra entering the drift gap from Regions 5 and 6, when irradiated with 15 and 25 MeV respectively. The peaks stem mostly from interactions in aluminium for Region 6, while for Region 5 from the detector cathode itself.

cluding ^{24}Al . The total cross-section of the reaction $^{27}\text{Al}(n,\gamma)$ is a few barns for this neutron energy.

5.7 Conclusions

A neutron conversion board was designed, able to serve as a spectrometer. The optimal geometry simulated with FLUKA was modified in order to use a triple GEM as the read-out detector, designed specifically for this application. The response function of each region was simulated in the energy range 0.001 eV to 100 MeV, taking into account cross-talk effects when all regions are irradiated simultaneously. Photon contribution from each region in the read-out detector was also investigated, resulting in peaks of several energies which need to be eliminated during the acquisition. The construction and test of the spectrometer are described in the following chapter.

Chapter 6

Construction and applications of the SpectroGEM

This chapter discusses operational tests and spectra measurements performed after the construction of the SpectroGEM. The operational tests consist of investigating the channel response to neutrons, noise elimination and methods for photon signal rejection, as well as ensuring optimal performance of the GEM detector. The spectrometer is then tested with an $^{241}\text{AmBe}$ source and the neutron energy spectrum is measured. Spectra acquired in different positions near a spallation target are discussed and conclusions about the measuring capabilities of the spectrometer are drawn. Improvements in the design and response matrix of the spectrometer are also suggested, which would lead to more reliable spectra measurements. Possible applications of the spectrometer are introduced, which rely on its directional response.

6.1 Construction

The detector was assembled in the National Laboratory of Frascati (INFN-LNF) using the manufacturing method described in [85]. The cathode was built with 2.2 cm polyethylene and 50 μm aluminium, as shown in Figure 5.12, and the boron and aluminium foils were glued on the inner surface, as indicated in Figure 5.14. A picture of the cathode and the anode is shown in Figure 6.1, where five out of six regions are visible. No extra material was needed for Region 5, as the cathode itself serves for fast neutron detection in the required energy range (see Table 5.3 for region characteristics).

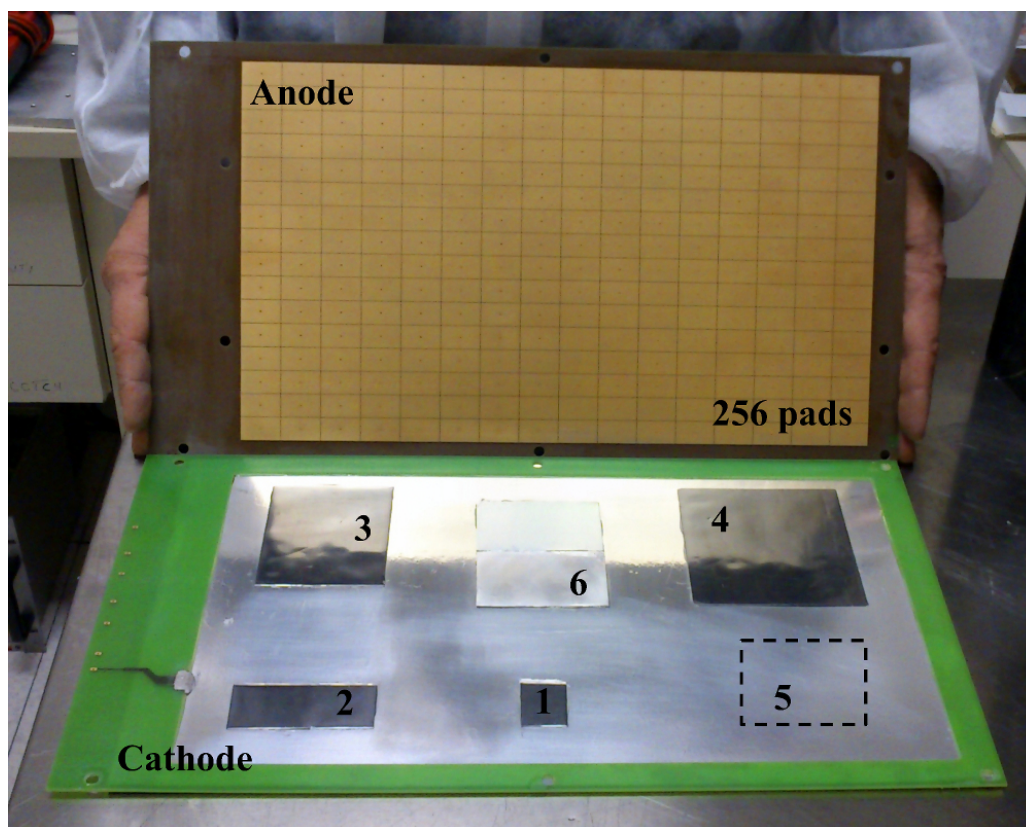


Figure 6.1: Picture of the anode and cathode before the detector is sealed. Regions 1 to 4 employ boron foils, Region 6 employs aluminium and Region 5 is composed by the cathode itself. All regions are designed to fit the read-out pad dimensions.

6.2 Operational tests

The acquisition system is the one described in Section 2.2. The 256 pads are read by 16 CARIOCA chips, each one holding 8 identical channels. The chips are connected to a custom made FPGA Motherboard, which analyses the signal coming from them, while the GEM foils are powered by the HVGEM NIM module. Both the FPGA and the voltage module are operated on-line via two Labview-based programs. The total area is read-out by two FPGAs, controlling 128 pads each.

All of the detector components were tested in the laboratory before placing the polyethylene pieces on top. The tests included the elimination of electronic noise, high voltage stability, response of all channels and photon signal rejection.

A Labview-based was specifically developed and a screenshot is shown in Figure

6.2. In the upper left part, indicated as number 1, the 16 thresholds (THR1 - 16) can be set, as well as the overall detection threshold. Acquisition parameters can be set below the threshold panel, such as the gate width (internal or triggered), possible time delay and the multi-slice mode discussed previously in 2.4.2.

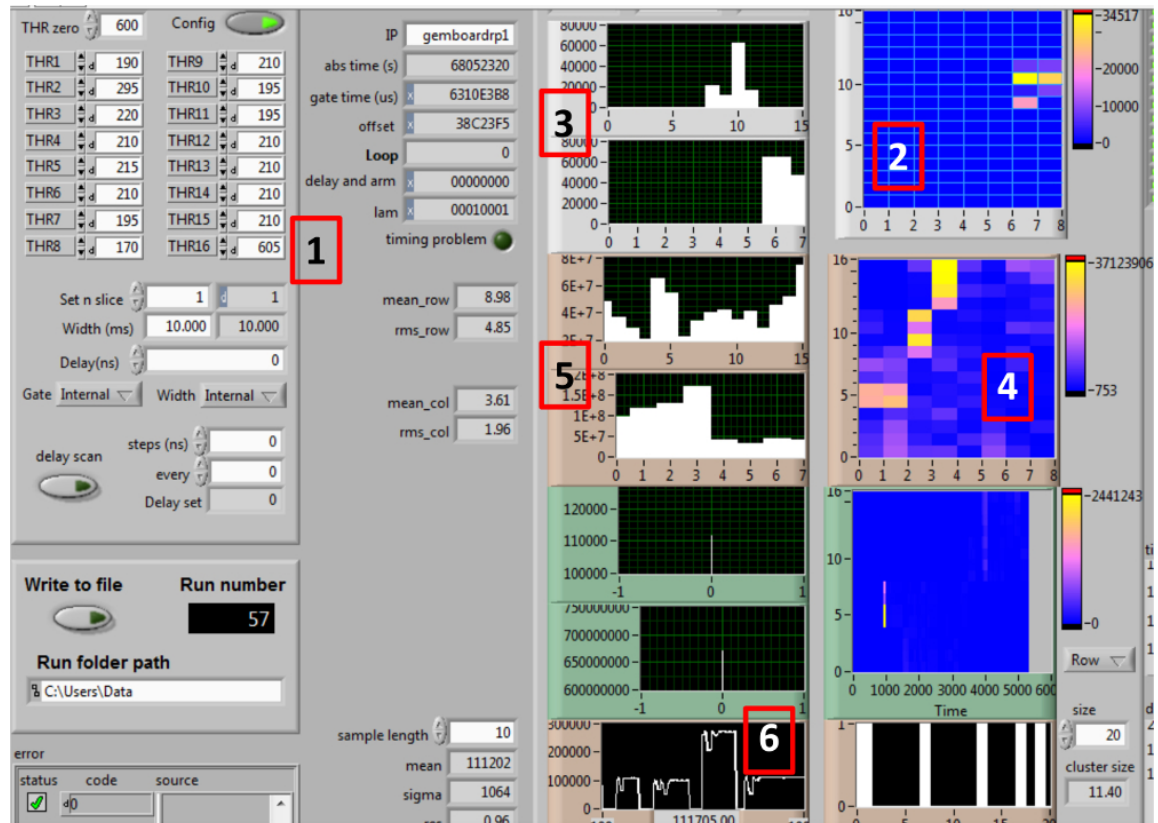


Figure 6.2: The Labview-based program managing the FPGA. The instantaneous and accumulated counts per pad are displayed on-line in the panels indicated with numbers 2 and 4, as well as their distribution on both directions in panels 3 and 5.

In the right part, indicated as number 2, the instantaneous counts on the 128 pads are displayed, consisting of 8 pads (2.2 cm^2) in the horizontal and 16 pads (1.3 cm^2) in the vertical direction. The count distribution in these directions is shown in the panels indicated as number 3. The counts over the total acquisition time are shown in number 4 and their distribution over the pads in both directions is shown in number 5.

The electronic noise can also be monitored on-line in panel number 6 and its elimination procedure is described below.

6.2.1 Noise elimination

The electronic noise takes place in the chips and the threshold is managed by the FPGA and set via the Labview-based program. Each chip provides two thresholds, the latter of which corresponds to eight channels, hence 16 thresholds for the 128 pads. The tests were performed separately for the left and right part of the detector, as shown in Figure 6.3, and the FPGA was attached on the chips via an intermediate board in order to further eliminate the noise.

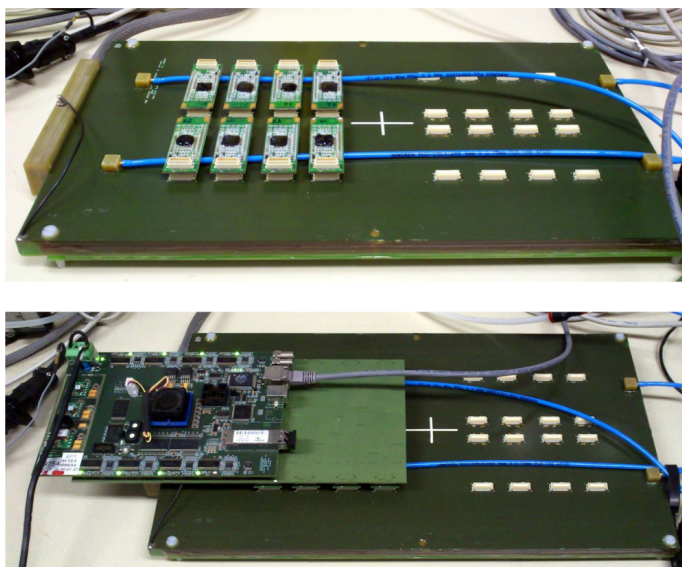


Figure 6.3: The detector read-out system. Eight CARIOCA chips are managed by an FPGA, which is displaced via an extension board to avoid electronic noise from the FPGA power supply.

The thresholds (THR1 - 16) are equalized by applying a different value to each of them, so that their noise is eliminated when applying the overall threshold, indicated as THR zero in the upper left part of the program. The maximum noise of each threshold (THR1 - 16) can be found by varying its value and finding the peak in the panel indicated with number 6 in Figure 6.2. Once the maximum of each threshold is found, the overall threshold (THR zero) is set at a higher value in order to further reject signal from the background, depending on the kind of particles the detector is designed to measure.

6.2.2 Voltage stability and channel response

The Labview-based program for controlling the voltage applied to the foils is shown in Figure 6.4. The total voltage and the one applied to each foil are shown on the upper left part of the control panel, indicated with number 1. Possible variations of the values in time are shown in the panel indicated with number 2 and it can be seen in the figure that the voltage remains constant, a fact which is of great importance during the acquisition because it defines the detector gain, as discussed in 2.4.

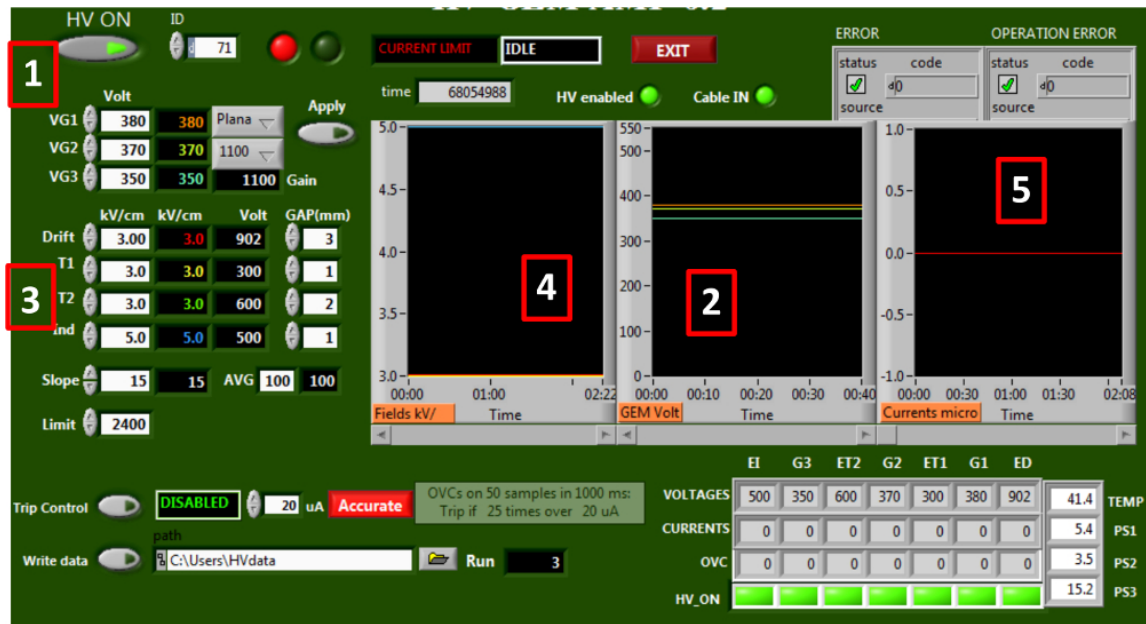


Figure 6.4: The Labview-based program managing the HVGEM NIM. The three panels show on-line the field values, voltage applied to each foil and currents driven by them.

The field values (drift, transfer 1 and 2 and induction) are recorded in the panel number 3 and can be visualized in time in number 4. Panel number 5 records the current driven in the foils during the acquisition and should be zero when the detector is not triggered by radiation.

Both parts of the detector were irradiated with a ^{137}Cs source in order to verify the noise elimination and proper operation of the channels. The detector was filled with Ar/CO₂ 70/30 and the total voltage was set to 1100 V. The source spot can be seen in Figure 6.5a for 20 events with the count distribution in both directions visible on the left side. The source was subsequently moved along the detector active

area (Figure 6.5b) (right), in order to verify that all channels respond to radiation. The same procedure was followed for the right part of the detector and no electronic noise or gain instability was detected in either part.

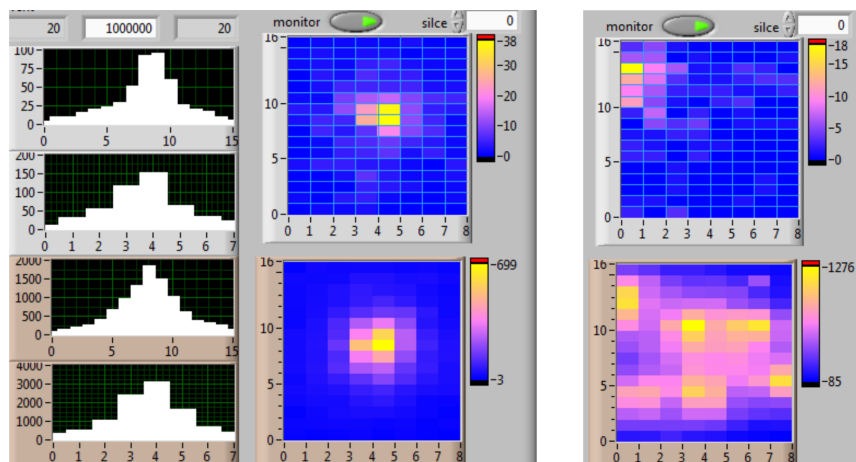


Figure 6.5: On-line image of the ^{137}Cs source over a number of events (instantaneous and accumulated) and the count distribution in both directions (left). Irradiation of all channels to test their response to ionising radiation (right).

6.2.3 Photon signal elimination

According to previous measurements discussed in 2.4.1.1, the photon signal can be eliminated by applying suitable voltage, which was determined as 870 V (sum in three foils). High voltage scans were performed in the laboratory with gamma emitting sources to investigate whether the device shows the same performance as the neutron detectors discussed in Section 2.4.

The sources used were ^{137}Cs (153 kBq), ^{60}Co (3.5 kBq), ^{106}Ru (45 kBq) and ^{241}Am (40 kBq) and the detector was tested before placing the polyethylene pieces, so that the response is uniform in the total area. Photons of 662 keV are emitted by ^{137}Cs and two peaks at 1.17 and 1.33 MeV emitted by ^{60}Co . ^{106}Ru is a beta emitter but the daughter nucleus ^{106}Rh emits two photon peaks at 512 and 622 keV, while ^{241}Am is an alpha emitter with a photon peak at 60 keV. It should be noted that photons are also produced in the detector cathode, composed of polyethylene and aluminium, as simulated in Section 5.6. Thus the signal detected is a combination of primary and secondary photons. The voltage range investigated was 850 to 1100 V

with a time gate of 1 s and the efficiency of the detector to these photon energies for increasing voltage was measured at the same time.

The number of particles impinging on the detector per emitted particle was calculated via the solid angle on a rectangular detector [86]. The projected surface area was calculated knowing the distance from the source (d) and the active width (w) and height (h) of the corresponding area, while the ratio of impinging over emitted particles was calculated by dividing the area with 4π , which is the maximum collection efficiency. The formula for calculating the emission solid angle for a rectangular area is given by Equation 6.1.

$$\Omega = 4 \cdot \arcsin(\sin\alpha \cdot \sin\beta) \quad (6.1)$$

where $\alpha = \arctan(\frac{w}{2d})$ and $\beta = \arctan(\frac{h}{2d})$

The measurement was performed at the right part of the detector and the sources were placed at a distance of 0.5 cm from the centre of the active area, measuring the counts from the total area, which consists of Region 4 (only the boron foil), Region 5 and Region 6 without the extra 2 mm polyethylene on top of the cathode. The parameters used were $d = 0.5$ cm, $w = 18$ cm and $h = 20.8$ cm, resulting in a collection efficiency of 0.475. Considering an isotropic particle emission and the planar geometry of the detector, it is expected that the maximum value is 0.5 when the source is attached to the detector. The detection efficiency for increasing voltage is shown in Figure 6.6 for the sources and it is defined as the number of detected over impinging particles.

Photons of 512, 622 and 662 keV are more probable to interact with the gas molecules via Compton Scattering and those with energy 1.17 and 1.33 MeV via the same mechanism and especially via Pair Production. In both cases electrons are produced, which can ionise the gas and induce detectable signal. This signal is amplified for increasing voltage applied and thus the detector efficiency increases as well. From Figure 6.6 it is evident that the efficiency to all photon energies is negligible ($\sim 10^{-7}$) at 870 V and therefore no photons are detected during the acquisition if the voltage is substantially low. The photon efficiency value is in good agreement with previous measurements [35].

It can be seen in Figure 6.6 that the efficiency functions for ^{106}Ru and ^{137}Cs are different in absolute value and shape despite the fact that they emit photons with similar energy. The main reason lies in the geometry of the sources, since each one is collimated at a different extend and therefore the number of particles impinging on the detector is different for each geometry. As a result, this number is disproportionally overestimated for all sources due to the incapability of measuring

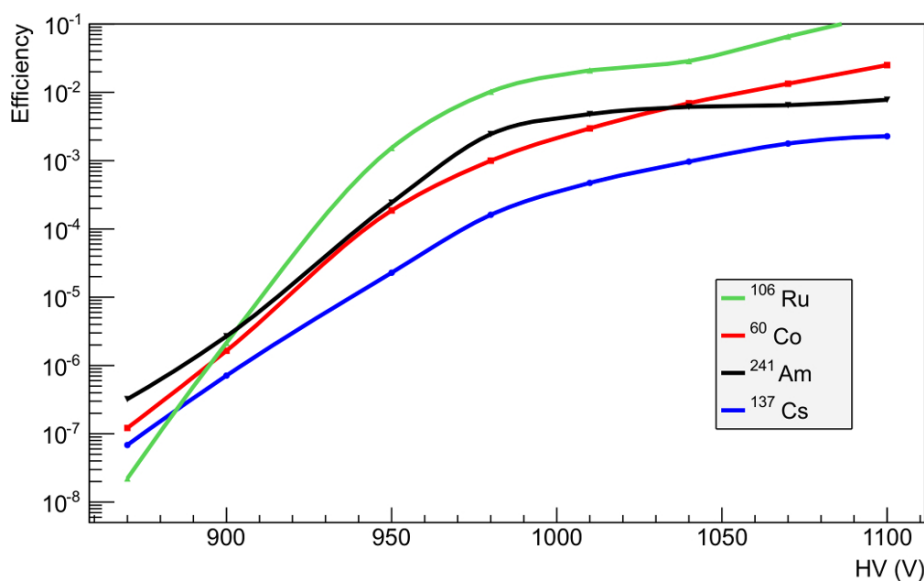


Figure 6.6: Efficiency to photon emitting sources for increasing voltage applied, with a value of $\sim 10^{-7}$ for 850 V.

the collimation impact. The spot images measured for ^{106}Ru and ^{137}Cs are shown in Figure 6.7, while the Gaussian fit information is given in Table 6.1, verifying the different collimation impact. The position uncertainties correspond to the pad size (2.2 cm in the x and 1.3 cm in the y direction), while the sigma uncertainties are given by the data analysis code [87]. From the different values of the sigma in Table 6.1 it can be seen that ^{106}Ru is collimated at a larger extend than ^{137}Cs , while the mean position of both distributions remains the same within uncertainties.

Table 6.1: Source spot characteristics for ^{106}Ru and ^{137}Cs , fitted with a Gaussian function on both directions.

Source	Mean X	Mean Y	Sigma X	Sigma Y
^{106}Ru	86.9 ± 22.0	102.0 ± 13.0	20.2 ± 0.8	18.1 ± 0.8
^{137}Cs	79.7 ± 22.0	104.9 ± 13.0	30.6 ± 0.7	30.0 ± 0.7

The main objective of this measurement was to investigate whether the photon signal can be eliminated by applying common voltage values to the new detector, i.e. in the range 850 - 900 V where triple GEM neutron detectors are usually operated. This study confirms that the photon rejection technique as for other GEM (see Section 2.4) can be employed to the new detector.

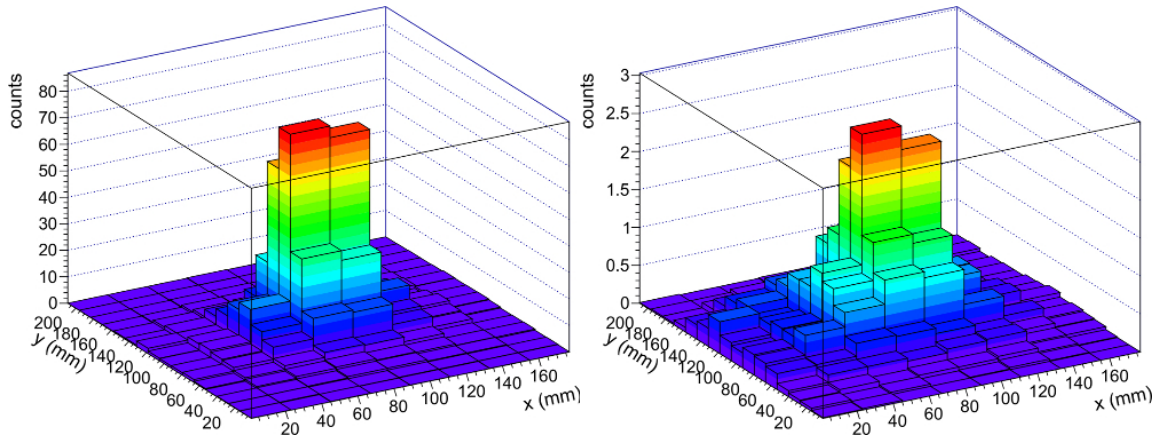


Figure 6.7: Spot images measured for ^{106}Ru (left) and ^{137}Cs (right) for the same voltage (1010 V) and number of counts per second.

6.2.4 Response to neutrons

A ^{252}Cf source (723 kBq) was used in order to investigate the detector response to neutrons. The neutron energy spectrum ranges from 200 keV to 8 MeV, with a peak at 1 MeV, while the isotope emits also alpha particles of 5 - 6 MeV and photons of 100 - 200 keV. The alpha particles are absorbed in the detector cathode (2.2 mm polyethylene), while photons can induce detectable signal when suitable voltage is applied (see 6.2.3).

The measurement was performed at the right part of the detector with the voltage ranging from 750 to 1020 V, applying a time gate of 1 s and acquiring the total number of counts from this area. The right part of the detector consists of Region 4 (boron foil), Region 5 (only cathode) and Region 6 (cathode plus 1 mm aluminium), so that the total number of counts stems from alpha particles, lithium ions and protons. It should be noted that the test was performed before placing the polyethylene piece on Region 4. The pad multiplicity, discussed in 2.4.1.1, was measured at the same time for every voltage value and with varying time gate in order to record charged particles from a single neutron. This fact was ensured by acquiring only one event per fifteen triggers with the time gate ranging from 1 to 200 ms for this specific source (neutron energy and activity). The results for the HV scan and the pad multiplicity are shown in Figure 6.8.

A count plateau is visible in the range 830 to 870 V, after which the rate increases for increasing voltage. The signal up to this plateau stems only from neutrons, while the increase after 870 V is due to photons (see also Figures 6.6 and 2.19). Thus

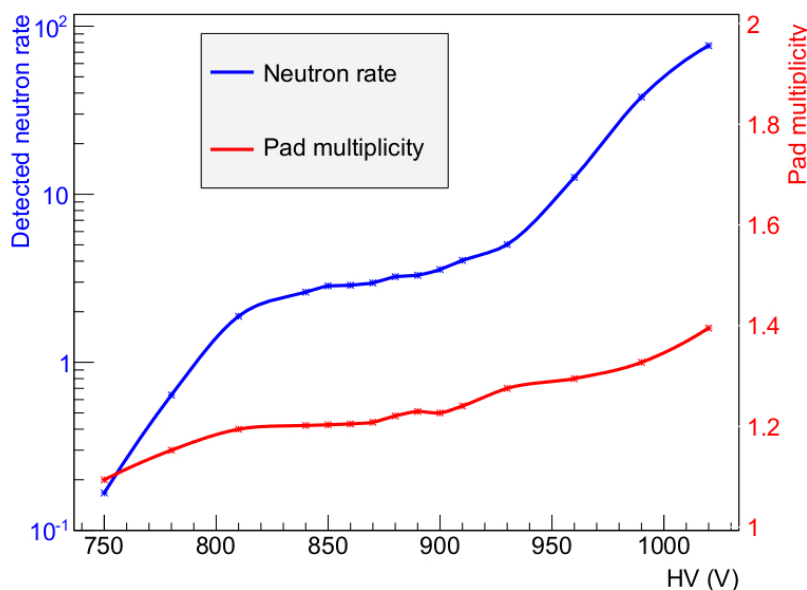


Figure 6.8: Detected neutron rate with a ^{252}Cf source and pad multiplicity for increasing voltage applied. The count plateau starts at 850 V, corresponding to a pad multiplicity of ~ 1.2 .

the operating voltage of the detector was determined as 850 V, ensuring maximum counting efficiency and photon signal elimination.

The pad multiplicity increases for increasing voltage applied, but not at the same extend as for detectors with smaller read-out pad size (see Figures 2.18 and 2.26); up to 900 V it is ~ 1.2 and reaches the value of 1.4 at the highest voltage applied. The electron cloud produced extends in size for increasing voltage but the pads are large enough for the charge to be collected from the same number of pads, regardless of the electron cloud size.

A rough estimation of the efficiency of the right part of the detector before placing the polyethylene piece on Region 4 was performed. The source was placed at a distance of 7 cm from the centre of the part, yielding a ratio of impinging neutrons over emitted equal to 0.226 ± 0.012 and total counting efficiency estimated as $1.2 \pm 0.1 \cdot 10^{-5}$ by folding the source spectrum with the response functions. Region 4 covers 50% of the total area, with a mean efficiency in the peak emission energy range equal to $1.5 \pm 0.3 \cdot 10^{-5}$ and the rest of the area corresponds to Regions 5 and 6, with a mean efficiency of $5.0 \pm 1.0 \cdot 10^{-6}$. In the region around 1 MeV neither boron nor polyethylene yield high neutron cross-section, but only Region 4 with the appropriate polyethylene piece placed on top of it can have acceptable response (see

response matrix in 5.11). The total efficiency was measured as $1 \pm 0.2 \cdot 10^{-5}$, which is in good agreement with the expected one.

6.3 Experimental activities

After placing the polyethylene pieces on top of the cathode (see Figure 6.9), the SpectroGEM was tested again with photon sources in order to investigate whether the extra material can further eliminate the photon signal from each region. The spectrometer was subsequently tested at the CERN Calibration Laboratory with an $^{241}\text{AmBe}$ source and the neutron energy spectrum was successfully measured. Spectra from spallation target were also acquired in different positions and useful conclusions for the measuring capabilities of the spectrometer were drawn.

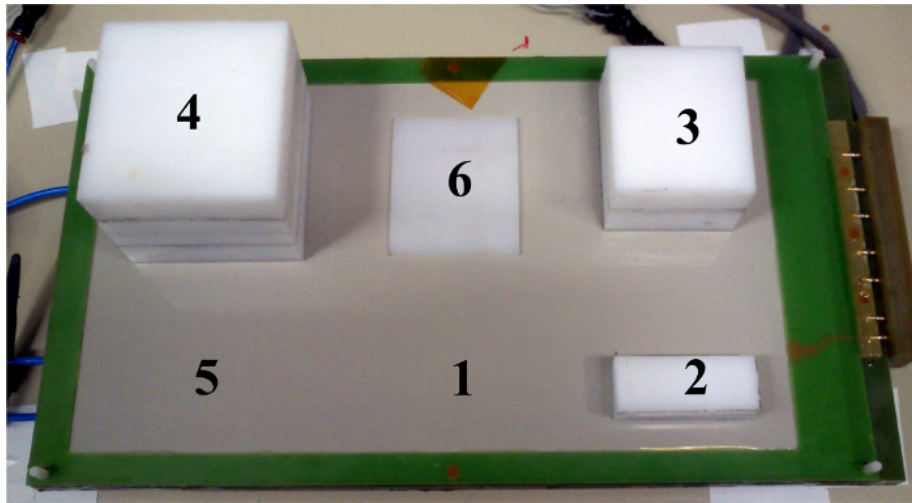


Figure 6.9: Polyethylene pieces of thickness 2, 5, 8 and 0.2 cm were placed on Regions 2, 3, 4 and 6 respectively.

The data acquisition was performed with two FPGAs (Figure 6.10), each one reading 128 channels and managed by a single Labview-based program at the same time (Figure 6.11). The FPGAs were attached indirectly on the spectrometer in order to avoid noise induced to the pads due to their large size.

6.3.1 Irradiation with photon sources

The sources employed were ^{55}Fe (5.9 keV), ^{106}Ru (512 and 622 keV) and ^{60}Co (1.17 and 1.33 MeV), placed at a distance sufficient for uniform irradiation of the active

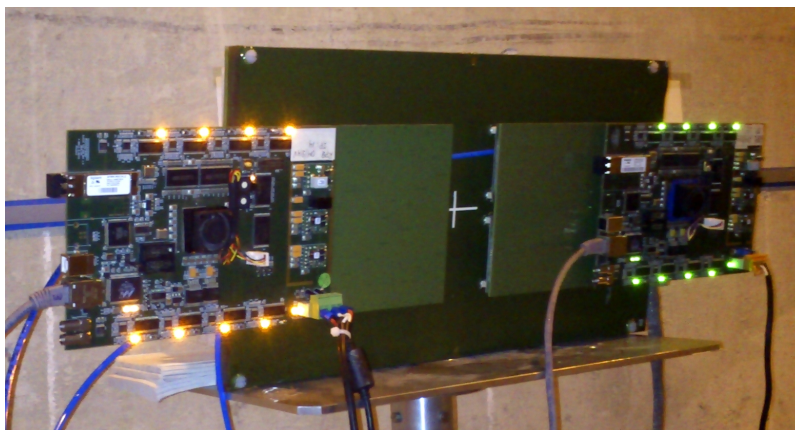


Figure 6.10: Picture of the SpectroGEM. The 256 pads are read-out by two FPGAs attached indirectly to the back of the device.

area; the voltage was set to 1100 V for higher efficiency, as shown in Figure 6.6. The number of counts acquired from each region per pad and per event for the three sources are given in Table 6.2. However, the values can not be compared between sources, due to the different size and shape of the latter, but only between regions for the same source.

Table 6.2: Number of counts measured per pad for the six regions when the spectrometer was irradiated with sources of different photon energies.

Source	Reg1	Reg2	Reg3	Reg4	Reg5	Reg6
^{55}Fe	$5.4 \cdot 10^{-1}$	$3.6 \cdot 10^{-2}$	$5.6 \cdot 10^{-3}$	$1.1 \cdot 10^{-3}$	$8.4 \cdot 10^0$	$8.3 \cdot 10^{-3}$
^{106}Ru	$2.1 \cdot 10^{-1}$	$1.8 \cdot 10^{-2}$	$1.6 \cdot 10^{-2}$	$1.2 \cdot 10^{-2}$	$7.4 \cdot 10^0$	$1.5 \cdot 10^{-2}$
^{60}Co	$4.8 \cdot 10^{-1}$	$8.5 \cdot 10^{-2}$	$7.1 \cdot 10^{-2}$	$5.7 \cdot 10^{-2}$	$1.2 \cdot 10^1$	$5.0 \cdot 10^{-2}$

It can be seen that the number of counts decreased for increasing amount of polyethylene for all sources, because photons have higher absorption probability inside larger amount of material. In addition, the extra 1 mm aluminium layer of Region 6 decreased significantly the photon detection when compared to Region 5 and this effect was mostly observed for the low energy photons of ^{55}Fe (5.9 keV). The number of counts acquired by every pad when the spectrometer was irradiated with ^{55}Fe for a given number of events is shown in Figure 6.12. Regions 2, 3, 4 and 6 are clearly visible due to the reduced counts in these pads. The most vulnerable regions to photon signal are 1 and 5, because the latter consists only of the cathode

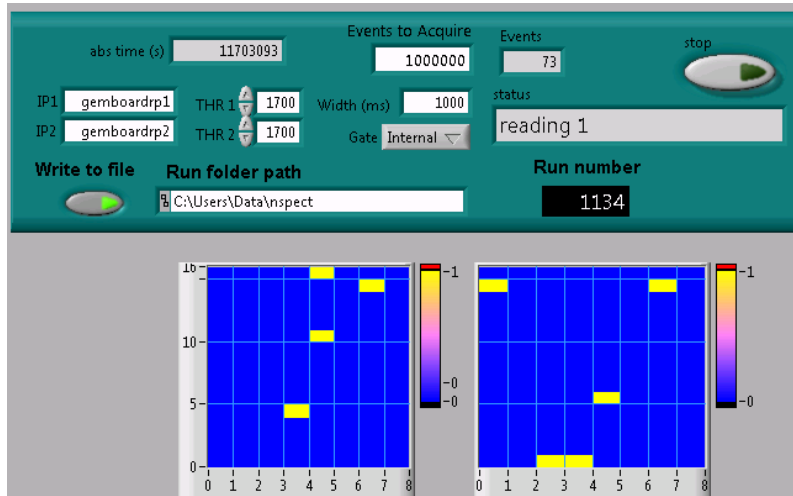


Figure 6.11: Snapshot of the Labview-based program managing the two FPGAs. The number of counts per pad and per event is shown in two panels, each one corresponding to an FPGA.

itself, and the first employs only a boron foil in addition to the cathode.

When the spectrometer was irradiated with ^{106}Ru , this effect was not as significant due to the higher energy of the photons emitted (512 and 622 keV). As shown in Figure 6.13, only regions employing large amount of polyethylene are clearly visible (3 and 4) and yet the number of counts per pad is at maximum 5 times lower than the rest of the regions. For irradiation with ^{60}Co (1.17 and 1.33 MeV) there are no distinct areas where the photon detection efficiency is lower; the number of counts per pad is on average the same for all regions.

These findings are in agreement with the simulation performed and described in Section 5.6. The photon spectrum emerging in the detector from neutron interaction (Figure 5.21) has two distinct peaks, at 500 keV and 2 MeV. The detector response to the 500 keV peak, resembling the one of ^{106}Ru , varies between regions and the fluence entering the drift gap is lower for the regions employing large amount of polyethylene, while the response to 2 MeV photons, close to the emission peak of ^{60}Co , is approximately the same for all regions and thus photons with this energy can penetrate the regions at the same extend.

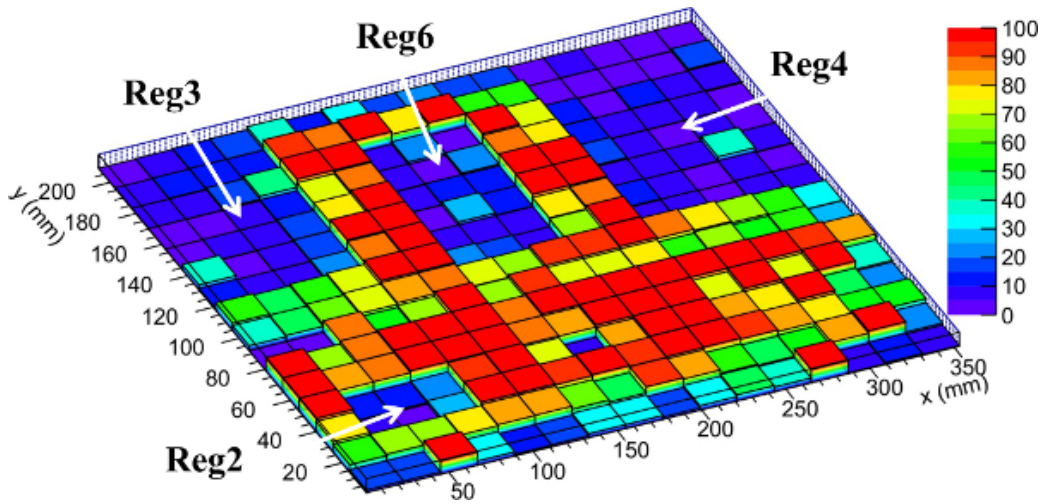


Figure 6.12: Number of counts per pad measured during irradiation with ^{55}Fe . Regions 2, 3, 4 and 6 are clearly visible due to the reduced counts from photons.

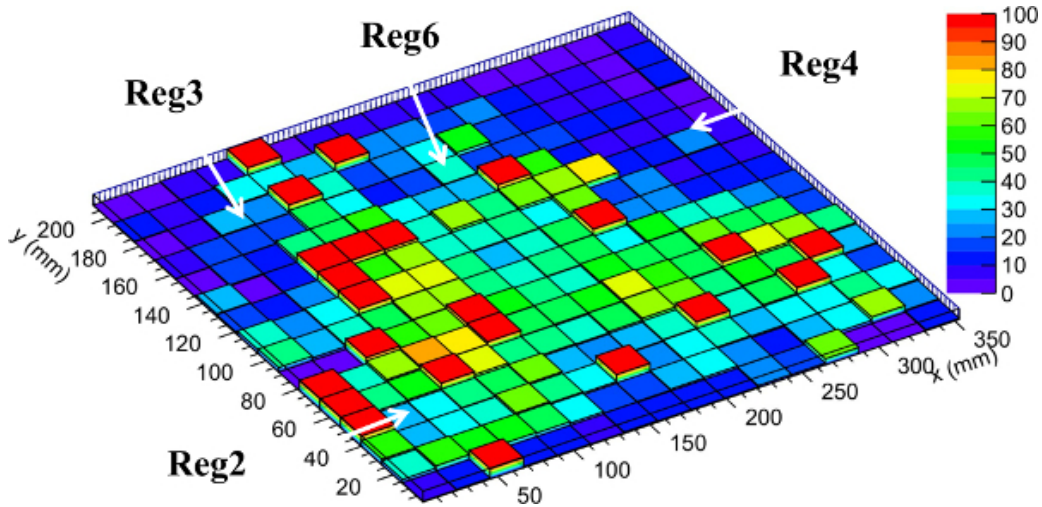


Figure 6.13: Number of counts per pad measured during irradiation with ^{106}Ru . Regions 3, 4 and 6 are clearly visible due to the reduced counts from photons.

6.3.2 Neutron spectrum of $^{241}\text{AmBe}$

The SpectroGEM was tested at the CERN Calibration Laboratory with a $^{241}\text{AmBe}$ source (888 GBq), whose neutron spectrum shows peaks in the region from 3 to 7.5 MeV. The device was placed at a distance of 226 cm from the source, ensuring uniform irradiation of the active area. This factor is of great importance because the response matrix is simulated with a neutron beam impinging vertically on the regions and having the total area dimensions.

The spectrometer was filled with Ar/CO₂ 70/30 and the voltage applied was 850 V (see Figure 6.8) with a gate of 1 sec. The device was irradiated for 25 min and the number of counts from the pads corresponding to each region per emitted neutron was recorded and shown in Table 6.3.

Table 6.3: Number of counts acquired from each region per emitted neutron.

Reg1	Reg2	Reg3	Reg4	Reg5	Reg6
$2.1 \cdot 10^{-11}$	$1.6 \cdot 10^{-10}$	$2.5 \cdot 10^{-9}$	$5.2 \cdot 10^{-9}$	$2.9 \cdot 10^{-9}$	$6.1 \cdot 10^{-10}$

Most of the counts on the active area correspond to Region 4, a large fraction was acquired from Regions 3 and 5, while the contribution from 1, 2 and 6 is almost negligible. This fact suggests that the neutron spectrum is peaked at the range where Region 4 shows the highest response (200 keV to 5 MeV). The number of counts from Region 3, when compared to counts from Region 4, suggests that the spectrum only slightly extends in the keV region, because there is large overlapping between Regions 3 and 4 in the range 10 keV - 1 MeV. Counts from Region 5 correspond to neutrons with energy higher than 2.5 MeV and peaked at 14 MeV without significant overlapping with Region 4; thus the spectrum measured is expected to extend further in the MeV region. Region 6 does not contribute to the spectrum due to the very low number of counts and its response overlapping with Region 5 up to 20 MeV. The number of counts acquired from Regions 1 and 2 is very small when compared to 3, 4 and 5. Nevertheless, such signal is of interest because it could be due to the detection of scattered neutrons inside the irradiation hall, giving rise to signal from the thermal and epithermal regions.

The counts corresponding to each region were used for the data unfolding with MAXED and GRAVEL and the guess spectrum employed was the one of $^{241}\text{AmBe}$, ranging from 0.11 to 11 MeV. No possible contribution from low energy neutrons was taken into account and thus only counts from Regions 3, 4 and 5 were necessary for the reproduction of the spectrum. The uncertainty related to the measurement ranged from 2 to 10% depending on the region and the one related to the $^{241}\text{AmBe}$

spectrum was estimated as 5%. The uncertainties of the final spectrum were obtained for MAXED via the IQU_FC33 program implemented in the U.M.G. package with an average of 5%, except for the keV region where it ranged from 6 to 18%. The spectra obtained with MAXED and GRAVEL are shown in Figure 6.14 in neutron fluence per unit of lethargy, normalised to the number of emitted neutrons, and the $^{241}\text{AmBe}$ spectrum is also shown for comparison.

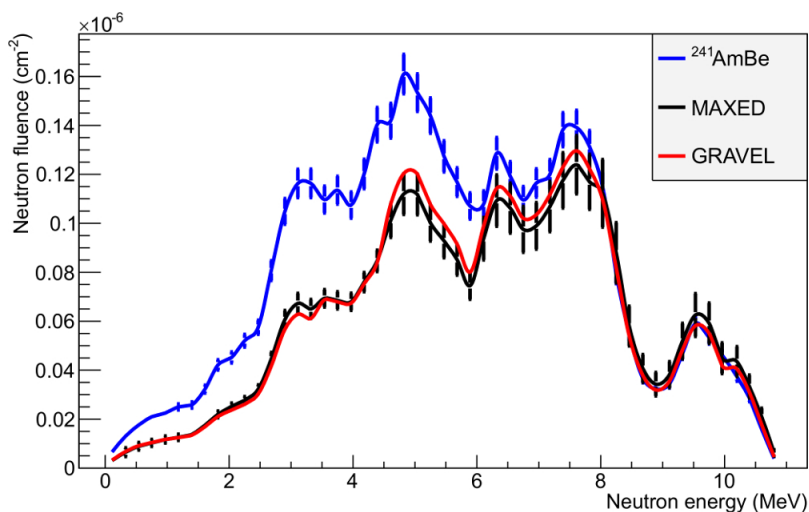


Figure 6.14: Solution spectra obtained with MAXED and GRAVEL. Guess spectrum of $^{241}\text{AmBe}$ is shown for comparison.

The spectra obtained with MAXED and GRAVEL are the same between the uncertainties and their shape follows the one of the $^{241}\text{AmBe}$ spectrum but with lower absolute intensity below 8 MeV. This discrepancy could stem from the fact that the guess spectrum used for the unfolding procedure was not simulated for that specific position inside the irradiation room and thus no low energy neutron component was taken into account, resulting in higher fluence in the MeV region than the measured ones.

The number of counts per region and per emitted neutron was estimated by folding the response matrix of the three regions (3, 4 and 5) with the $^{241}\text{AmBe}$ spectrum and is compared to the measured counts in Table 6.4. The values are in relatively good agreement, with the estimated being higher than the measured. This fact is demonstrated in the solution spectra displayed in Figure 6.14.

The new device is therefore able to measure the neutron spectrum emitted from a radioactive source with reasonable statistical uncertainty in a single irradiation of 25 min. For this kind of spectrum no isotropic instrument response is needed, since

Table 6.4: Comparison between measured and estimated number of counts per region and per emitted neutron.

	Reg3	Reg4	Reg5
Measured	$2.5 \pm 0.3 \cdot 10^{-9}$	$5.2 \pm 0.5 \cdot 10^{-9}$	$2.9 \pm 0.3 \cdot 10^{-9}$
Estimated	$3.0 \pm 0.2 \cdot 10^{-9}$	$6.1 \pm 0.3 \cdot 10^{-9}$	$4.0 \pm 0.2 \cdot 10^{-9}$

the emitted neutron direction is known and the spectrometer is placed at a large distance from material where neutrons are scattered. As a result, the device can be considered as a suitable alternative to existing fast neutron spectrometers, described in 3.3.

6.3.3 Neutron spectra from spallation target

The SpectroGEM was tested at the CERF facility, which provides a broad neutron reference field well characterized and ranging from thermal to several hundreds of MeV. Two fixed positions are defined inside the irradiation room, in which an iron and a lead target can be placed, giving rise to neutron fields on the iron and concrete roofs situated above the targets respectively. Exposure positions are defined on both roofs (16 for each), at which the neutron spectrum is estimated via Monte Carlo simulations with the FLUKA code and serves as reference for instrument calibration and testing. The positions defined, target and beam direction are shown in Figure 6.15.

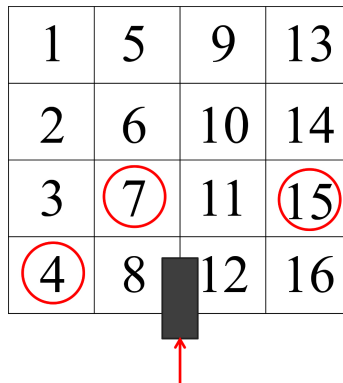


Figure 6.15: Reference positions on the CERF roof. The target is located inside the irradiation room between positions 8 and 12.

The spectrometer was placed at positions 4, 7 and 15 on the concrete roof and at

number 4 on the iron roof. The hadron beam of 120 GeV/c (61% π^+ , 35% p^+ and 4% K^+) was extracted with a spill of 5 s, monitored by the reference detector IC [27], one count from which corresponds to $2.2 \pm 0.2 \cdot 10^4$ particles impinging on the target. The neutron spectra simulated with the FLUKA code in positions 4, 7 and 15 on the concrete roof, named CT4, CT7 and CT15 respectively, are shown in Figure 6.16 per unit of lethargy and per particle impinging on the target [36].

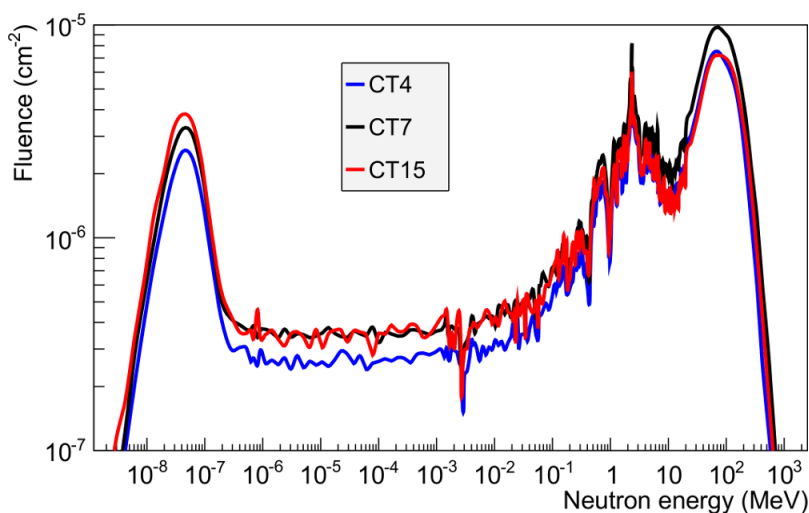


Figure 6.16: Neutron spectra in positions CT4, CT7 and CT15 simulated with FLUKA, taken from [36].

Three distinct peaks are visible for all positions; the thermal, the evaporation at around 2 MeV and the high energy peak at 70 MeV. The shape of the spectra appears to be the same for all positions but the absolute fluence differs according to the distance from the target (see Figure 6.15). The fluence in position CT4 is lower over the entire energy range, mostly due to the fact that neutrons are produced in the forward direction when the beam impinges on the target and thus CT4 is the one at largest distance from the interaction area. Position CT15 is located approximately at the same distance from the target as CT4, but its position is more in the forward direction, inducing higher fluence than CT4 over the entire range. The difference is more significant in the thermal and epithermal region, while the fluence in the high energy peak is identical. Position CT7 is the one closest to the target, hence the higher fluence in the epithermal region and the evaporation and high energy peaks. However, the thermal peak at CT7 is lower than the one at CT15, because neutrons are scattered to a lower extent before reaching CT7.

6.3.3.1 Experimental set-up

The spectrometer was placed in the reference positions with the polyethylene pieces facing the roof, as shown in Figure 6.17. The neutron spectra were simulated with the FLUKA code at a distance of approximately 20 cm above the roof and thus detectors are commonly placed in the middle of the reference positions and mounted on a plastic stand, so that their centre lays at the distance defined.



Figure 6.17: Experimental set-up. The SpectroGEM is placed with the polyethylene pieces facing the roof.

In the case of such a large planar detector the neutron spectrum impinging on each region of the active area is not identical due to the large distance between them and from the centre of the reference position. Given the difference in fluence between positions CT4 and CT7, this fact can play an important role when measuring the spectrum, as it is acquired by unfolding the counts from each region. Another factor possibly leading to measurement discrepancies is the distance of each region from the roof; even though all of them are read-out at the same distance, Regions 3 and 4 employing large amounts of polyethylene are more vulnerable to scattered neutrons from the roof, possibly inducing a larger number of counts than expected.

The acquisition gate of the spectrometer was set to 1 s for both FPGAs, while it was filled with Ar/CO₂ 70/30. The time evolution of counts per spill obtained from the total area was measured at position 4 on the iron roof at 1050 V for higher efficiency and is shown in Figure 6.18. It can be seen that the number of counts for each spill is rather constant and is mostly acquired in 5 gates (corresponding to 5 s)

but they can also be split to 6 gates, since the device is not triggered by the IC. Counts stemming from background and cosmic events are observed between spills in Figure 6.18 but without contributing significantly to the neutron signal.

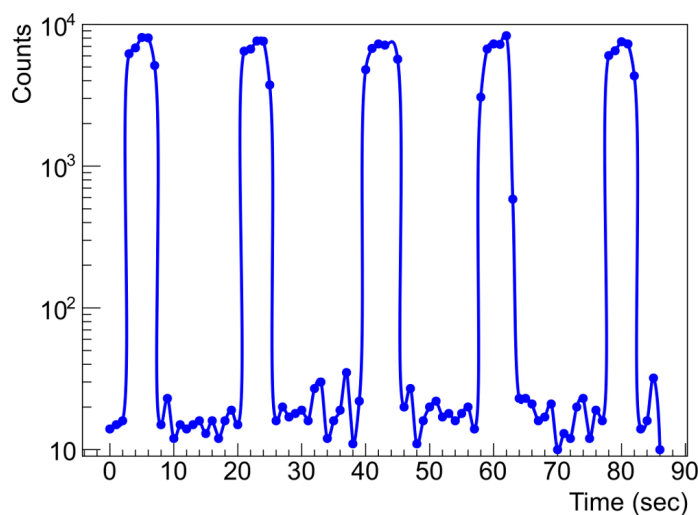


Figure 6.18: Time evolution of counts for 5 spills, acquired with a gate of 1 s.

The appropriate voltage applied was determined via a scan while the spectrometer was placed at the same position on the iron roof with an approximately constant beam intensity of 10^7 particles on target per spill. The total counts per spill from the six regions are plotted in Figure 6.19 for voltage ranging from 750 to 960 V and applying the pad multiplicity for each value. A count plateau is visible from 830 to 870 V, as already demonstrated in Figure 6.8 with a ^{252}Cf source, and thus the working voltage is verified to be 850 V.

6.3.3.2 Spectra measurement

The spectrometer was irradiated with a beam intensity of $(6.2 \pm 0.6) \cdot 10^7$ particles impinging on the target per spill for positions CT4, CT7 and CT15 and the average number of counts per spill acquired from each pad at position CT4 is shown in Figure 6.20; Regions 1 to 4 employing boron are clearly visible due to higher efficiency than Regions 5 and 6. However, a small displacement of the polyethylene piece on Region 2 is noted, as the counts are acquired from 7 pads instead of 6.

Counts per particle impinging on the target were summed from the pads corresponding to each region and were used for the unfolding procedure at position CT4. The statistical uncertainty varied for each region from 3 to 10% due to their differ-

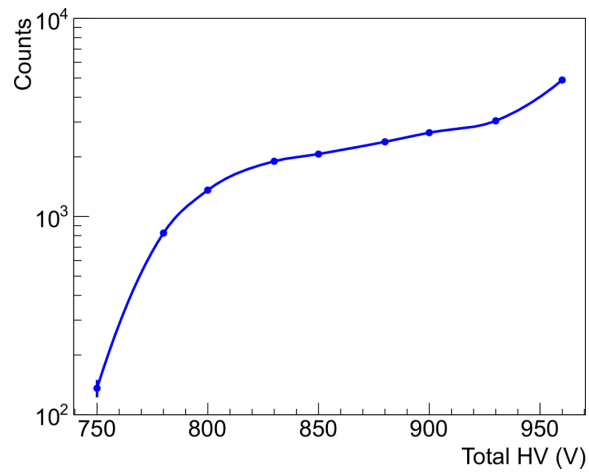


Figure 6.19: Total count per spill acquired from the six regions with varying voltage. The counts plateau is visible in the range 830 to 870 V.

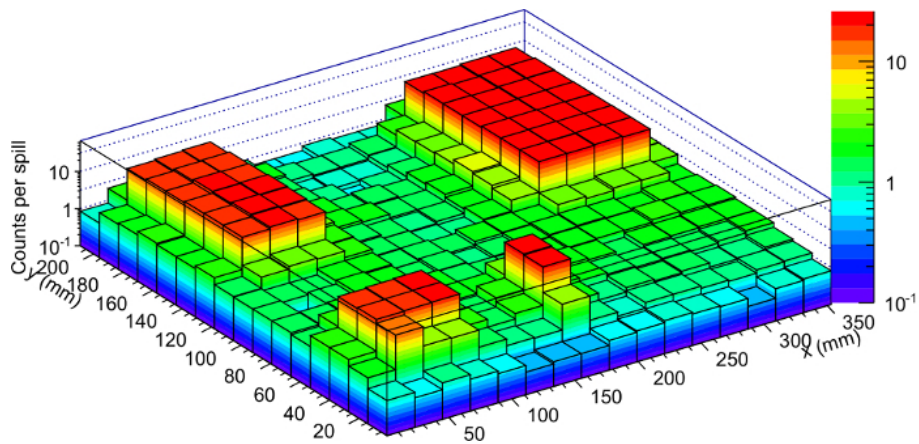


Figure 6.20: Counts per pad acquired for the total active area at position CT4 and beam intensity of $6.2 \cdot 10^7$ particles on target per spill. Regions 1 to 4 employing boron are clearly visible.

ent efficiency, while the uncertainty in the beam intensity, stemming from the IC monitor, was 10%. The unfolded spectra with MAXED and GRAVEL and the guess spectrum are shown in Figure 6.21 for comparison. Due to the low response of the spectrometer for energies higher than 50 MeV [5.11], the high energy peak at 70 MeV was not possible to be obtained and thus counts from Region 6 were not used for the unfolding procedure.

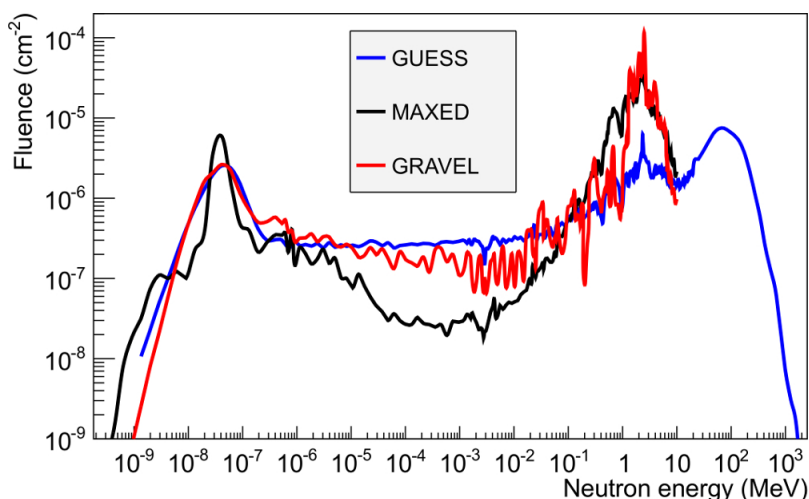


Figure 6.21: Solution spectra with MAXED and GRAVEL acquired at position CT4. The guess spectrum is shown for comparison.

The unfolded spectra with MAXED and GRAVEL in Figure 6.21 are characterised by the thermal and evaporation peaks and their shape is very similar to the guess one. However, both show an intense peak 10 times higher than expected at around 2 MeV, implying count overestimation from Region 4 due to its higher sensitivity to scattered neutrons from the roof. The GRAVEL spectrum has a smoother shape than MAXED in the entire energy range and especially in the thermal region, where the intensity is identical to the guess one. The MAXED spectrum appears to be rather distorted in the thermal and intermediate region from 1 eV to 100 keV, a fact observed also in previous measurements (see Figure 4.17). Nonetheless, the shape and intensity of the evaporation peak is closer to the guess spectrum for MAXED rather than GRAVEL, as it can be seen in Figure 6.22, where the only range from 100 keV to 10 MeV is displayed. The shape of the MAXED spectrum is identical to the guess, while the GRAVEL spectrum is barely correlated.

The data acquired from positions CT4, CT7 and CT15 were unfolded with GRAVEL and MAXED and the results are shown up to 10 MeV in Figures 6.23

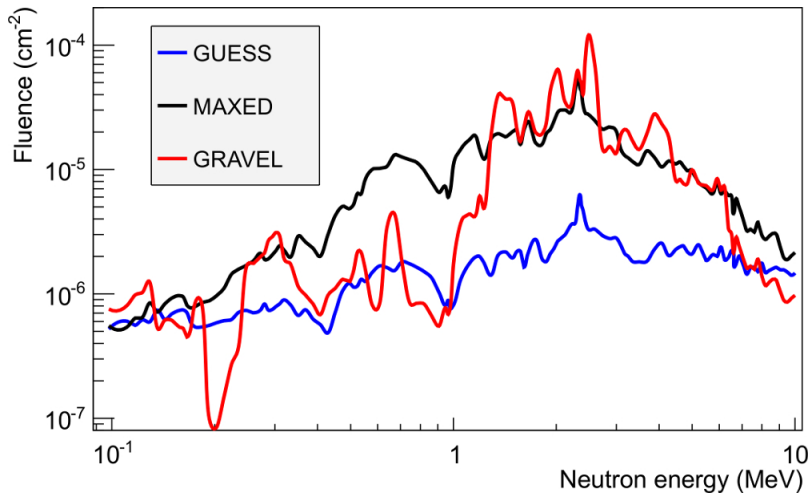


Figure 6.22: Solution spectra with MAXED and GRAVEL at position CT4 displayed in the range 100 keV to 10 MeV. MAXED follows the shape of the guess spectrum in the evaporation region closer than GRAVEL.

and 6.25 respectively. The thermal peak at CT15 is slightly higher than the other positions and in the intermediate region the intensity at CT7 and CT15 is higher than CT4, as expected from the simulated spectrum shown in Figure 6.16, while the evaporation peak at 2 MeV is identical for all positions.

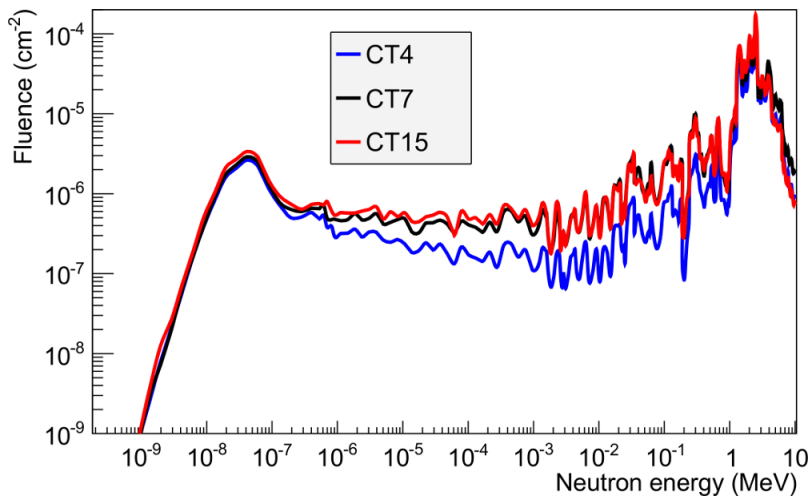


Figure 6.23: Solution spectra with GRAVEL at positions CT4, CT7 and CT15.

According to previous findings, GRAVEL is able to reproduce smoothly the ther-

mal peak, while MAXED is more efficient in the evaporation peak. An enlargement of the thermal peak from 6.23 at all three positions is shown in Figure 6.24, where the difference between intensities can be seen more clearly.

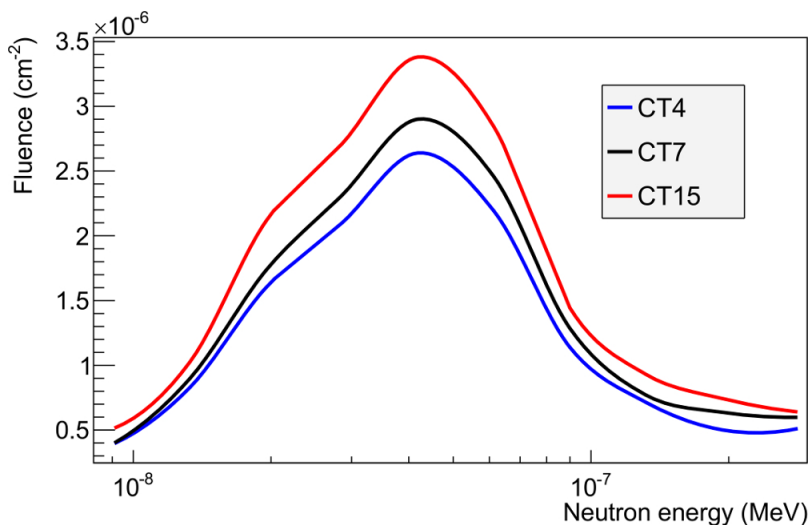


Figure 6.24: Solution spectra with GRAVEL at positions CT4, CT7 and CT15, displayed in the thermal energy region.

The spectra unfolded with MAXED and shown in Figure 6.25 have similar shape, with the intensity at CT7 being higher than CT4 and CT15 for energies more than 1 keV. The intensity at the thermal peak appears to be higher for CT15, but the absolute values can be considered equal between the uncertainty. An enlargement of the evaporation peak is shown in Figure 6.26, with the intensity of CT7 being 2 times higher than CT4 at the peak energy.

The spectrometer was also placed in position 4 on the iron roof, called IT4, where higher neutron intensity and a different spectrum shape are expected. The guess spectrum used was simulated [36] with an older version of FLUKA, whose library had only 72 values of cross-sections for neutron energies below 20 MeV and only one for the thermal component, resulting in the absence of the thermal peak in the spectrum. However, the unfolding code is able to reproduce the Maxwellian energy distribution via an internal algorithm, since the peak always appears at the same energy; during the unfolding procedure it is possible to obtain the solution either in the guess-default spectrum (DS) or the response function (RF) binning.

The solution spectra with MAXED and GRAVEL up to 10 MeV are shown in Figure 6.27 using the DS binning and the guess spectrum at this position is also shown for comparison. The uncertainties related to the measurement statistics were

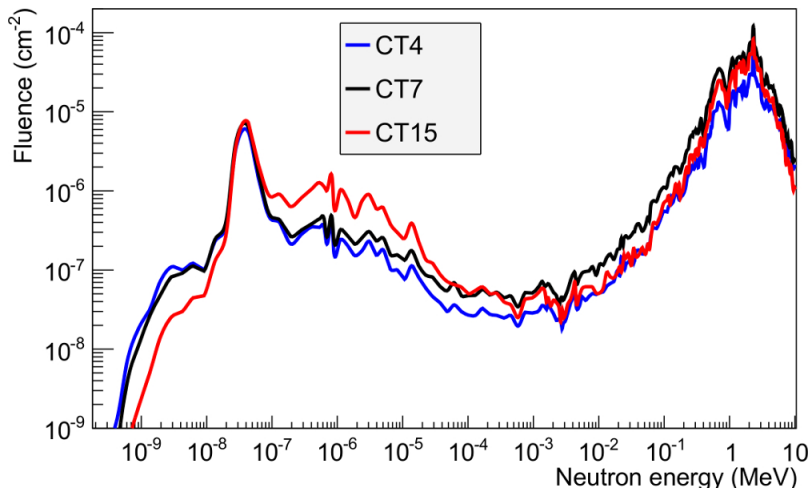


Figure 6.25: Solution spectra with MAXED at positions CT4, CT7 and CT15.

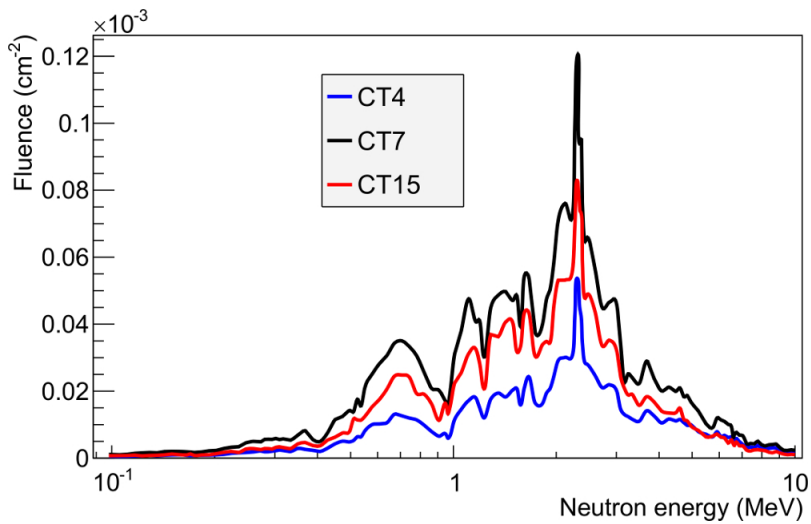


Figure 6.26: Solution spectra with MAXED at positions CT4, CT7 and CT15, displayed in the evaporation region.

negligible for 30 min irradiation time, while a 10% uncertainty was introduced due to the IC monitor. The uncertainties of the solution spectrum were calculated for MAXED with the IQU code, varying from $\sim 30\text{-}50\%$ below and $\sim 10\text{-}15\%$ above 1 keV.

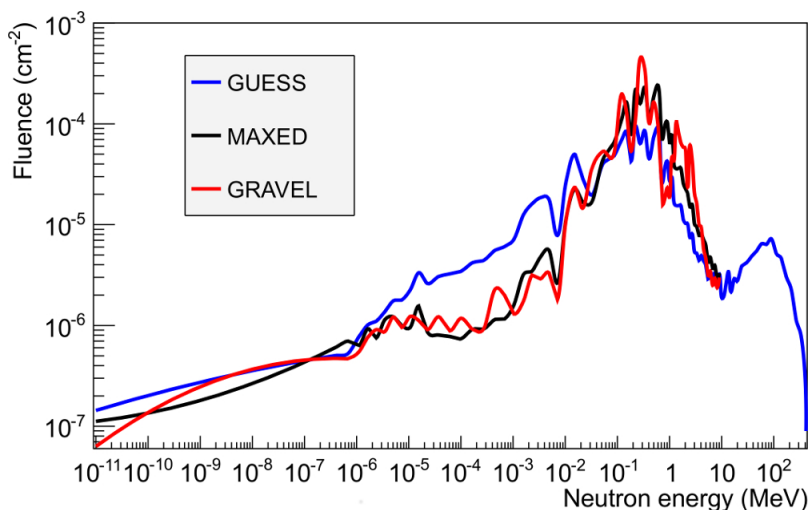


Figure 6.27: Solution spectra using the DS binning with MAXED and GRAVEL at position IT4. The guess spectrum is shown for comparison.

The spectrum on the iron roof shows an intense evaporation peak at ~ 300 keV and a high energy at 90 MeV, while the thermal peak is not visible due to the poor binning of the default spectrum. The MAXED and GRAVEL spectra are very similar, with the first following closer the shape of the guess spectrum over the entire energy range. Both solutions though underestimate the fluence in the intermediate region and overestimate it at the evaporation peak, an effect also observed for the spectrum measured at position CT4 on the concrete roof (see Figure 6.21).

The number of counts per region and per impinging particle on target was estimated by folding the response matrix of the six regions with the guess spectrum and is compared to the measured counts in Figure 6.28. The uncertainties of the guess spectrum were less than 5% and thus not visible in the graph. According to the results, the measured values are always larger than the expected ones and especially for Region 4, which is more vulnerable to scattered neutrons from the roof. Counts acquired from Regions 2, 3 and 5 match well the estimated values within the uncertainties, while those from Regions 1 and 6 deviate by 30% and 50% respectively from the estimated values. As shown in Figure 6.27, the fluence is underestimated in the intermediate part of the solution spectra when compared to the guess but the

number of counts acquired from Regions 2, 3 and 4 is higher than the estimated (see Figure 6.28). This fact is related to the minimization algorithms used by the unfolding codes, which redistributed the counts in such a way that one part of the spectrum is underestimated and the other one overestimated.

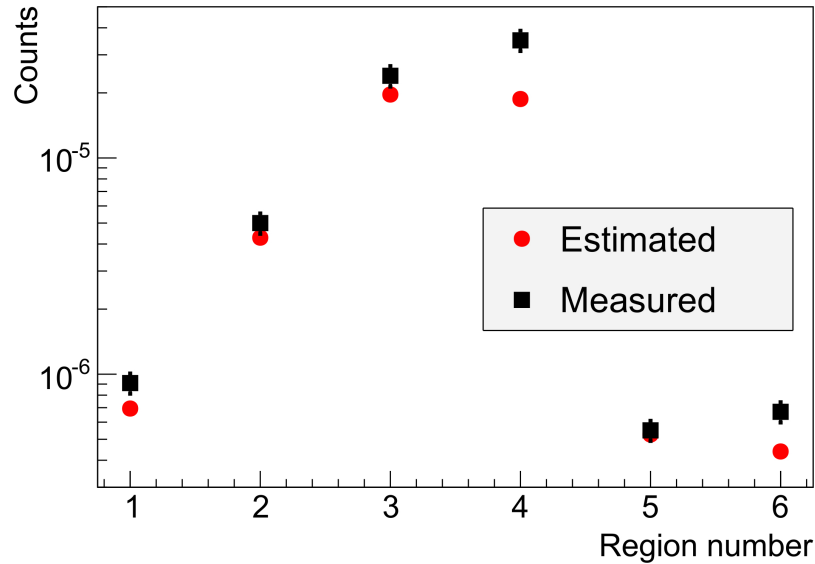


Figure 6.28: Comparison between estimated and measured number of counts per region, normalised per particle on target.

The thermal peak, absent in the spectra in Figure 6.27, was obtained with MAXED using the RF binning and the comparison between the two spectra, DS and RF binning, is shown in Figure 6.29, with the uncertainties of the DS solution displayed in the same graph. The two spectra are very similar for energies above 1 eV, with the intensity of the DS binning being a little higher than the RF in the intermediate region. Since the same counts were used for the two solutions, the algorithm distributed the counts in the RF case in order to generate the thermal peak, resulting in reduced intensity in the rest of the spectrum.

6.3.4 Conclusions

The SpectroGEM was tested in two kinds of neutron fields; an isotropic stemming from a $^{241}\text{AmBe}$ source and stray fields from a spallation target. In both cases the device was able to measure the neutron spectrum within a short-time irradiation (~ 30 min), avoiding the time and energy consuming sequential irradiation of the

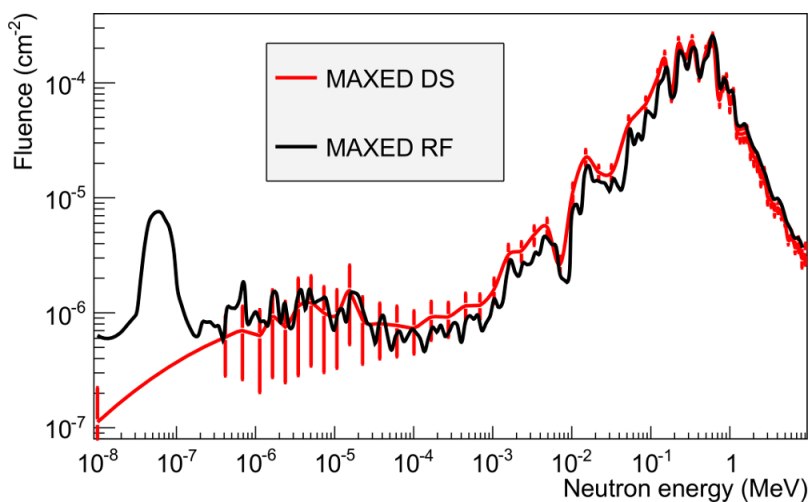


Figure 6.29: Solution spectra with MAXED using the DS and RF binning at position IT4.

BSS. The solutions acquired with MAXED and GRAVEL from the isotropic source were in good agreement between them and with the estimated $^{241}\text{AmBe}$ spectrum, shown in Figure 6.14. Deviations for the stray fields were observed between the two unfolding algorithms, with MAXED reproducing better the evaporation (see Figure 6.26) and GRAVEL the thermal peak (Figure 6.24). In all positions measured the solution spectra underestimated the neutron intensity in the intermediate region and overestimated it in the evaporation peak.

The deviations observed for the stray fields in the measured number of counts per region when compared to the estimated ones (see Figure 6.28) are mostly localised in Region 4, which employs the largest amount of polyethylene. Scattered neutrons from closely surrounding material, the concrete and iron roofs in the present case, appear to induce additional number of counts especially in this region, due to its closest distance to the roof. It is highly unlikely that the additional counts are induced by photons, because previous measurements have shown that Region 4 is not vulnerable to photon detection, as discussed in Section 6.3.1. The excessive number of counts is also related to the planar geometry of the spectrometer and can be resolved only by placing the device at a larger distance from neutron scattering material.

6.4 Testing the unfolding procedure

The solution taken with the unfolding codes is strongly dependent on the guess spectrum used and specifically on the position of the peaks and their absolute fluence. Tests were performed in order to investigate this effect by modifying the $^{241}\text{AmBe}$ spectrum and unfolding the experimental data with MAXED. In the first one the fluence of the $^{241}\text{AmBe}$ spectrum was shifted to a different energy range than the original and in the second test the absolute fluence of two peaks of the original $^{241}\text{AmBe}$ spectrum was changed. In addition, a closure test was performed by unfolding a spectrum with counts derived from a FLUKA simulation.

6.4.1 Shifted $^{241}\text{AmBe}$

Originally the $^{241}\text{AmBe}$ spectrum ranges from 100 keV to 11 MeV. For the needs of this test it was shifted in the range from 2 to 13 MeV keeping the same fluence per bin and the data were unfolded with the shifted spectrum. The initial and the shifted $^{241}\text{AmBe}$ spectra and the solution obtained with MAXED are shown in Figure 6.30.

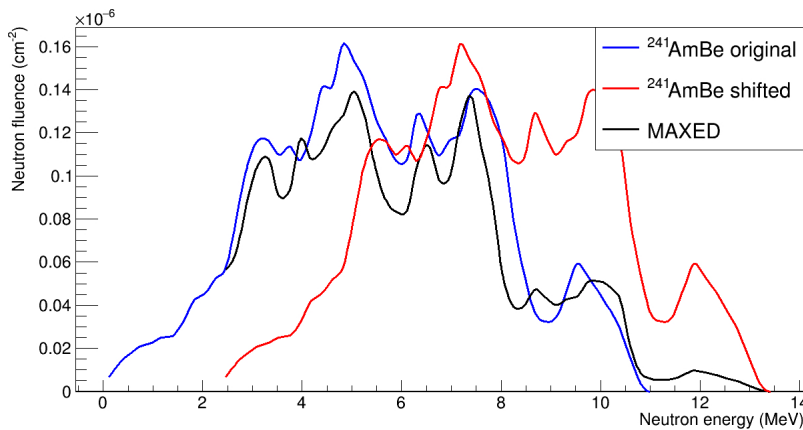


Figure 6.30: Original and shifted $^{241}\text{AmBe}$ spectra and solution obtained with MAXED for the shifted spectrum.

The solution appears to follow the trend of the shifted $^{241}\text{AmBe}$ in the range from 6.5 to 13 MeV, which means that it is strongly dependent on the information provided by the guess spectrum. However, in the range from 100 keV to 6 MeV it follows the shape of the original $^{241}\text{AmBe}$, because in that region the fluence of the shifted one is not high enough to influence the solution. As a conclusion, the

MAXED solution depends on the guess spectrum at a certain degree but it is not following blindly the guess spectrum used for the unfolding procedure.

6.4.2 Modified $^{241}\text{AmBe}$

The absolute fluence of the peaks located at 5 and 9.5 MeV from the original $^{241}\text{AmBe}$ spectrum was modified in order to test the influence of this increase on the unfolded spectrum with MAXED. The fluence around the peak of 5 MeV was increased by 30% and around 9.5 MeV by 50%, as shown in Figure 6.31. The MAXED solution obtained with this modified $^{241}\text{AmBe}$ spectrum is shown in Figure 6.32 and in comparison the spectrum unfolded with the initial $^{241}\text{AmBe}$ spectrum is displayed.

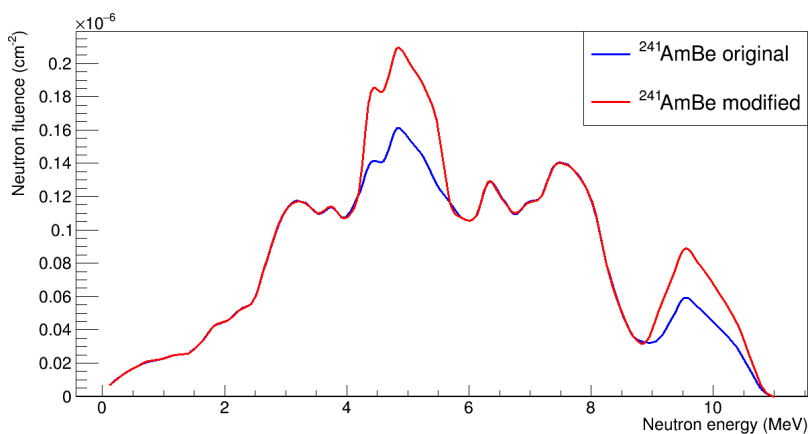


Figure 6.31: Original and modified $^{241}\text{AmBe}$ spectra with increased fluence around the 5 and 9.5 MeV peaks.

The solution with the modified spectrum deviates from the solution with the original one, since the same number of counts were used to unfold both spectra. The fluence at the 5 and 9.5 MeV peaks is increased by reducing the fluence in the other parts of the spectrum. However the fluence increase in the solution spectrum is not proportional to the increase of the modified spectrum used for the unfolding procedure: the peak at 5 MeV is only increased by 16% and at 9.5 MeV by 30%, in contrast to the modifications to the guess spectrum of 30% and 50% respectively. This means that the absolute fluence of the solution follows the trend of the guess spectrum but it is not totally independent. The magnitude of this influence defines also the robustness of the solution acquired, i.e. up to which change percentage of the guess spectrum the solution remains unaffected. This can depend on the number

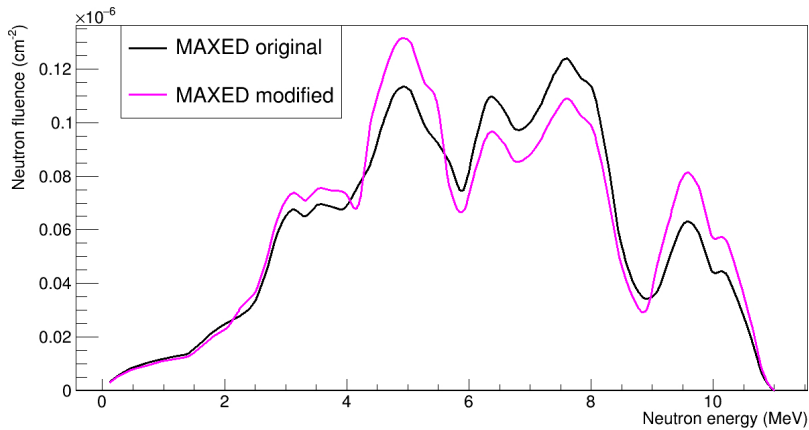


Figure 6.32: MAXED solutions obtained for the original and the modified guess spectra.

of channels used for the unfolding, 3 regions in this case, and on the number of bins of the guess spectrum and the response functions.

6.4.3 Closure test

Another test performed consists in unfolding a spectrum with counts derived from a FLUKA simulation, in order to test at the same time the validity of the response functions and the solution obtained with the unfolding code. The active area of the spectrometer was irradiated with a neutron spectrum produced from a 20 MeV flat rectangular neutron beam impinging on a lead block of 15 cm. The spectrum produced showed a thermal and a 1 MeV peak, as well as a percentage of impinging 20 MeV neutrons that did not interact with the target. The number of counts for each region was estimated via USRBDX A by summing the number of charged particles entering the area from which the signal for each region is acquired.

The unfolding procedure was performed with a guess spectrum equal to the neutron spectrum emerging from the lead target. However, it was found that the actual neutron spectrum on each region deviates from the global spectrum emerging from the target. The simulation set-up and the global and partial spectra for regions 2, 3 and 4 are shown in Figure 6.33.

It can be seen that the partial spectra impinging on the individual regions show higher fluence than the global spectrum over the entire energy range. In fact, the total fluence on regions 2, 3 and 4 are 5%, 16% and 45% respectively higher than the total fluence of the global spectrum. The reason lies in the cross-talk effects: neutrons can

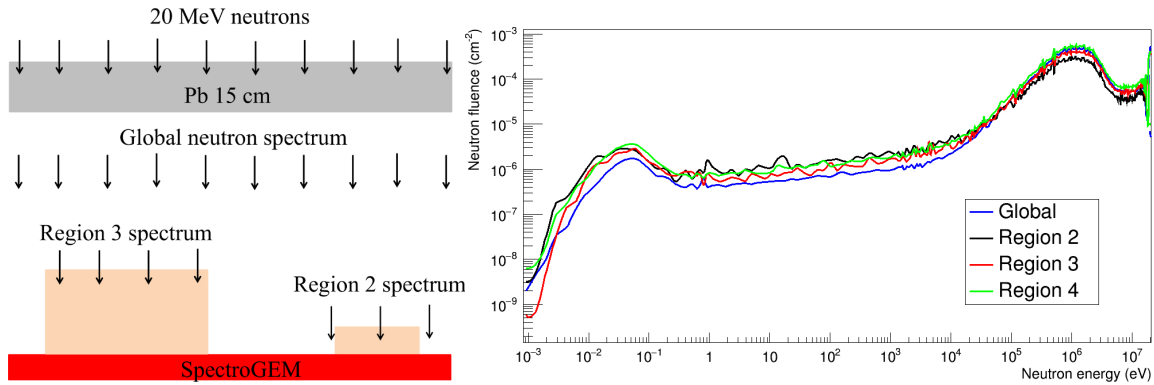


Figure 6.33: Simulation set-up for the closure test (left) and global and partial neutron spectra impinging on the total active area and on individual regions respectively (right).

be moderated inside the polyethylene pieces and after escaping those pieces they can induce a signal to the neighbouring regions. However, for the unfolding procedure only one spectrum can be used as a guess spectrum and in this case it is the global one. The guess and the solution spectrum with MAXED are shown in Figure 6.34. The solution obtained with MAXED follows the shape of the guess spectrum, but the absolute fluence is higher than the one of the guess spectrum over the entire energy range. This increased fluence varies from 20% to 100% and it is more visible at the thermal peak.

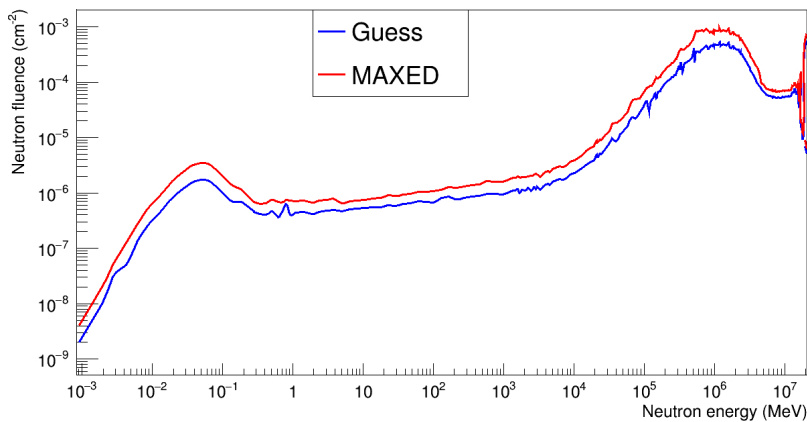


Figure 6.34: MAXED solution and guess spectrum used for the closure test.

6.4.4 Conclusions

This study made clear in the role of the guess spectrum during the unfolding procedure. It appears that both the position of the peaks and the absolute fluence of the guess spectrum have a strong influence on the solution obtained. This influence is inevitable because the unfolding algorithms cannot converge to a solution without prior information of the true spectrum. However, the solution obtained does not follow blindly the guess spectrum but depends strongly also on the response matrix and the counts per region.

The role of the input counts was made clear during the closure test: the solution obtained showed higher fluence than the guess spectrum but its shape was identical to the guess. Another conclusion derived from the closure test is the complexity of choosing the right guess spectrum for the unfolding procedure. It was seen that even in the case of such a simple experimental set-up, the neutron fluence on each region was not identical and thus large deviations can occur between the guess and the solution spectra. When the guess spectrum is estimated via simulations, it could be useful to estimate the individual spectra impinging on each region and using an average fluence as a guess spectrum. Another way of eliminating this complexity derived from cross-talk phenomena is improving the geometry of the spectrometer. This modification is discussed in the following section.

6.5 Future prospects

In this section possible improvements in the design and response matrix of the spectrometer are discussed, which would lead to more accurate and reliable spectra. The advantages and disadvantages of the new device are subsequently discussed in comparison with existing spectrometers, while possible applications based on its directional geometry are introduced.

6.5.1 Improvements

A major improvement that needs to be achieved is shielding the polyethylene pieces from scattered radiation. According to measurements performed and discussed in Section 6.3.3.2, regions employing large pieces of polyethylene are vulnerable to scattered neutrons from surrounding material, resulting in a relatively high number of counts and creating considerable deviations during the unfolding procedure. This effect can be reduced by shielding the polyethylene pieces with material with high neutron absorption, so that the number of neutrons scattered from surrounding ma-

terial and neighbouring regions is reduced. An element which is widely used for this purpose is cadmium, as for the BSS described in Section 4.1, but studies have shown [88] that it is a metal of considerable toxicity. Alternatives have been explored [89] and the suggested material for neutron absorption are natural gadolinium for its high cross-section and flex-boron for its low cost. Flex-boron is a flexible sheet of silicone elastomer which contains 25% of natural boron, commercially available and supplied in 3 mm thick sheets.

In order to obtain a quantitative comparison between different material, the neutron fluence induced by cross-talk effects was simulated with the USRBIN estimator from the irradiation of Region 2 with 1 eV neutrons, shielding Regions 2, 3 and 4 with 3 mm thickness of the three different material, i.e. cadmium, flex-boron and natural gadolinium, only from the sides facing the centre. The fluence from top is shown in Figure 6.35 with and without gadolinium shielding for comparison, expressed in particles per cm^2 in the binning matching the pad area. The addition of 3 mm shielding significantly reduces the neutron cross-talk effect in Regions 1, 3 and 4 when Region 2 is irradiated, as the neutron fluence induced in them is significantly lower. Neutron fluence is induced also in Regions 5 and 6 but no charged particles are produced, according to the results in Table 5.4.

The response from charged particles was estimated in Regions 1, 3 and 4 with the USRBDX estimator with and without shielding (free case). The ratio of responses between free and shielded cases are shown in Table 6.5 for the three material of 3 mm thickness. It is evident that the response from cross-talk effects is reduced at least 10 times and varies for different regions and shielding material; Region 3 is very well shielded in all cases. Flex-boron appears as the most suitable for 1 eV neutrons impinging on Region 2.

Table 6.5: Cross-talk response ratio of free over shielded case for cadmium, gadolinium and flex-boron for Regions 1, 3 and 4. Region 3 appears to be best shielded, while flex-boron is the most suitable for 1 eV neutrons impinging on Region 2.

Regions	Cadmium	Gadolinium	Flex-boron
Reg1	$2.17 \cdot 10^{-1}$	$1.79 \cdot 10^{-1}$	$7.32 \cdot 10^{-2}$
Reg3	$8.43 \cdot 10^{-2}$	$8.07 \cdot 10^{-2}$	$2.02 \cdot 10^{-2}$
Reg4	$1.11 \cdot 10^{-1}$	$1.01 \cdot 10^{-1}$	$2.47 \cdot 10^{-2}$

The cross-talk effect on Regions 1, 3 and 4 also depends on the impinging neutron energy on Region 2, as the response of each one is strongly energy dependent (see response matrix 5.11). A study was conducted for energies varying from 0.1 eV to 10 MeV impinging on Region 2 and the response of Regions 1, 3 and 4 was estimated

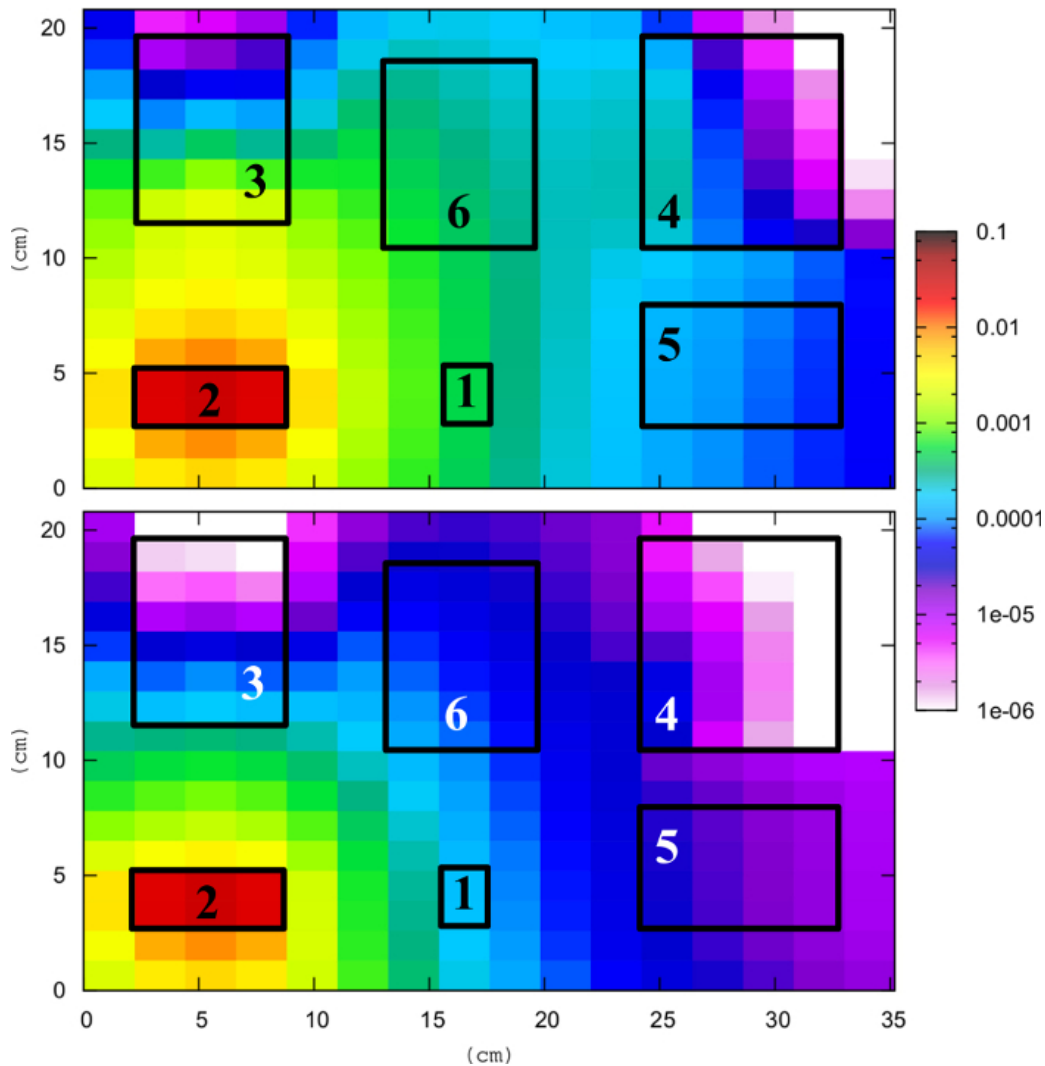


Figure 6.35: Neutron fluence (cm^{-2}) induced to Regions 1, 3, 4, 5 and 6 when Region 2 is irradiated with 1 eV neutrons with and without shielding (bottom and top respectively). The cross-talk effect is reduced when the polyethylene blocks are shielded with 3 mm of gadolinium, allowing better separation of the region response.

for 3 mm of gadolinium shielding. The results are shown in Figure 6.36 for the three regions. Region 3 is the one showing the highest response over the entire energy range, even though it is the best shielded according to the results in Table 6.5, suggesting that it is the one mostly affected by cross-talk effects from Region 2. Region 1 is hardly influenced, as already demonstrated in Table 5.4 even without shielding, while

Region 4 shows significant response despite the fact that it is located 15 cm away from Region 2 and is shielded.

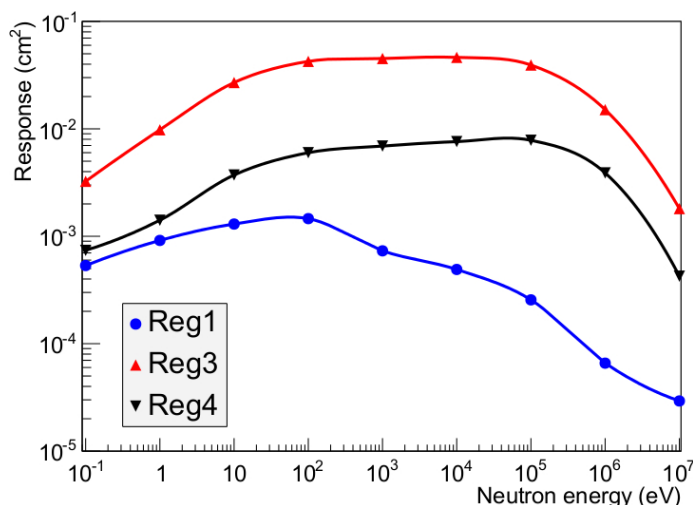


Figure 6.36: Cross-talk response of Regions 1, 3 and 4 for increasing neutron energy impinging on Region 2. Region 3 is the one most affected by induced counts.

The shielding can be more effective by optimizing the material thickness placed on the sides of each region. An additional study was conducted for different thickness of gadolinium, estimating the region response in the range 1 to 5 mm shielding for 1 eV neutrons impinging on Region 2. The results are shown in Figure 6.37 and it is evident that the response of all regions decreases on average by a factor of 2.6 for increasing gadolinium thickness in the range investigated.

Attention needs to be paid to the photon production from neutron interaction with the shielding material, since the detector cannot distinguish the signal from charged particles and photons, as discussed in Section 2.4.2.3. Neutron capture from gadolinium leads to gamma ray emission and therefore the photon fluence was simulated with and without gadolinium shielding, in order to investigate this effect. The photon fluence on the detector can be seen in Figure 6.38, where the absolute values is 10 times higher in the shielded case. Photons are produced in the 3 mm gadolinium layer placed on the sides of Region 2, indicated with arrows in Figure 6.38, inducing higher photon fluence in the neighbouring regions than the case without shielding.

As a result, the shielding chosen must be a material with high neutron absorption probability and low photon emission, ideally with a different thickness for each region due to their different response to varying neutron energy and with reasonable

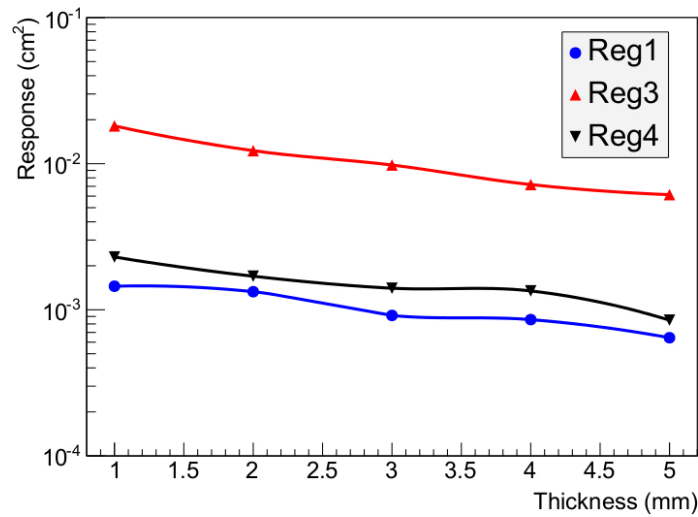


Figure 6.37: Cross-talk response of Regions 1, 3 and 4 for increasing gadolinium thickness, when Region 2 is irradiated with 1 eV neutrons.

cost. It is an improvement that needs to be accomplished in the future, because the region response separation can lead to a more stable spectrum solution obtained from the unfolded data and to lower uncertainties related to the minimization process employed by the unfolding codes.

Another advancement that could lead to more accurate results is simulating response matrices for different irradiation cases. The response matrix simulated and used for the unfolding procedure consists of a flat rectangular beam impinging vertically on the active area and is only an approximation of a real neutron field. It has proved to be adequate for the spectrum (see Section 6.3.2) where the particle direction is vertical with the device placed at a large distance from the source but it is probably not sufficient for the fields measured from spallation targets (see Section 6.3.3). In the latter case the spectrometer was placed on the roof of the irradiation room where particles are mostly directed from the target to the roof, resembling the impinging beam simulated. However, the scattered neutron radiation between the device and the roof could not be taken into account in the response matrix, resulting in the count deviations observed. A new response matrix can be simulated with an isotropic rather than a flat beam impinging on the spectrometer and the difference in the region response between the two matrices can shed light on the extend of the cross-talk effect between neighbouring sections with respect to the impinging particle direction; this simulation could be a good approximation of the scattered neutron radiation from surrounding material.

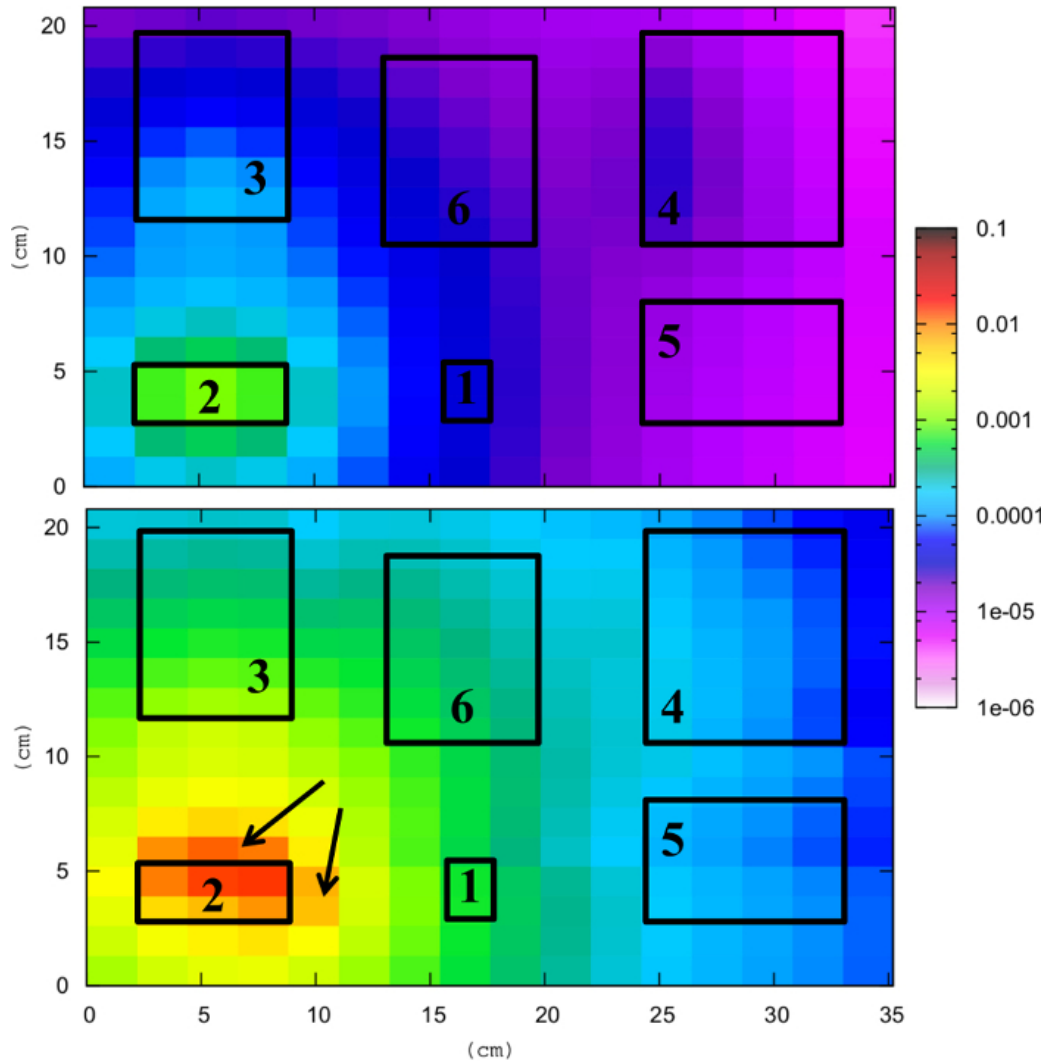


Figure 6.38: Photon fluence (cm^{-2}) induced to Regions 1, 3, 4, 5 and 6 when Region 2 is irradiated with 1 eV neutrons with and without gadolinium shielding (bottom and top respectively). Photons are produced in the sides of Region 2, bottom figure indicated with arrows, inducing higher fluence in the neighbouring regions than the unshielded case (top figure).

Apart from improvements in the existing prototype, new region geometries can be explored in order to extend the measurable energy range. The response of Region 6 is simulated up to 100 MeV (see Figure 5.11) but according to experimental results discussed in 6.3.3 the counts from this region could be correctly unfolded only below

50 MeV, due to its low response in this range. New material combinations can be investigated for increased response at the high energy region.

6.5.2 Applications

The SpectroGEM shows a number of advantages compared to the existing devices described in Section 3.3. It is able to measure a wide energy range of the neutron spectrum in a short single acquisition and it is easily transportable. For comparison, devices which are able to obtain the spectrum in a single acquisition are typically dedicated to fast neutrons, e.g. nuclear-reaction based spectrometers measure in the range 0.05 - 10 MeV and recoil proton telescopes in an even narrower range of a few MeV. In addition, the latter has very low efficiency (typically $\sim 10^{-5}$), resulting in long irradiation times.

When compared to the BSS, the new spectrometer has a directional response and a measurable energy range, which is more narrow. It has the advantage of requiring one short, single irradiation. At the same time it could be preferred to the BSS in cases where the spectrum direction is known.

An interesting application of the SpectroGEM could be its employment for investigating the direction of the neutron spectrum in work fields for radiation protection purposes. By placing the spectrometer on a movable base at a point of interest, it can be externally controlled to rotate and measure the spectrum in different angles, covering all directions around this point without entering inside the area. Apart from measuring the neutron spectrum, the ambient dose equivalent $H^*(10)$ can be estimated for every direction of the field by folding the solution spectrum from MAXED or GRAVEL with the fluence-to-dose coefficients (see Section 3.2.1). Insufficiently shielded areas can be recognized and fixed using such a directional device, which could not be possible with dosimeters that show isotropic response.

Conclusions

Neutron spectrometry is widely performed for radiation protection purposes and nuclear physics experiments. Several techniques in measuring neutron energy distributions were developed over the last decades, mostly characterized by a certain energy measured, isotropic or non-isotropic response, transportability and irradiation time.

In the frame of the present thesis a new Micro-Pattern Gaseous Detector (MPGD) for neutron spectrometry, called SpectroGEM, was designed, constructed and tested, combining the advantages of various existing instruments and techniques. It consists of a neutron conversion board with planar geometry and the read-out is performed with a triple Gas Electron Multiplier (GEM). Regions are identified on this board, each one being dedicated to a specific energy range. The neutron spectrum is inferred by measuring the number of counts per region and unfolding the data with dedicated algorithmic codes.

The design of the board was performed with the FLUKA Monte Carlo code, in order to find the appropriate material and dimensions for each region. The area and thickness of the converter was optimized for maximum neutron interaction probability and efficiency in the detection of charged particles produced. Between common material for neutron conversion, boron was found as the most appropriate due to its high cross-section in a thin layer, showing a maximum efficiency of 6.4% for 2.7 μm of ^{10}B .

The complexity in neutron spectrometry stems mostly from the fact that different kinds of neutron interactions dominate in different energy ranges and thus the majority of instruments respond to either slow or fast neutrons. The SpectroGEM combines two detection methods in the same device: moderation and absorption for energies from thermal to 3 MeV and elastic scattering from 3 MeV to 100 MeV. Six regions were defined on the board: four employing boron and polyethylene for neutron absorption and moderation and two polyethylene and aluminium for elastic scattering. The response of the spectrometer was simulated by estimating the

number of charged particles entering the read-out detector per impinging neutron and depositing energy that corresponds to charge exceeding the GEM electronics threshold, divided by a normalization quantity related to the area of each region.

The GEM detector used for the read-out was designed with an area large enough to host the six regions and several pads spacing between them, in order to reduce cross-talk effects. A study was performed with FLUKA by comparing the region response when the board was irradiated regionally and totally. The outcome showed that regions employing boron are vulnerable to scattered radiation and especially to low energy neutrons up to 10 eV.

Possible photon contribution to the induced signal was also investigated via simulations. Two photon peaks were found dominant in the regions employing boron: a 470 keV peak stemming directly from the neutron reaction with boron and a 2.3 MeV peak from the de-excitation of hydrogen and carbon atoms inside polyethylene. In the regions detecting neutrons with energy higher than 3 MeV, several distinct peaks were present from the interaction with polyethylene and aluminium, ranging from 250 keV to 4.5 MeV. A technique for eliminating the photon signal was introduced after the construction of the spectrometer. By setting suitable values of threshold and voltage, a good compromise between photon rejection and neutron efficiency could be obtained. At the working high voltage the photon efficiency was measured as 10^{-7} for energies higher than 600 keV.

The SpectroGEM was tested in two kinds of fields; an isotropic stemming from a $^{241}\text{AmBe}$ source and stray neutron fields from a spallation target. In both cases the device was able to measure the neutron spectrum within a short-time irradiation (~ 30 min).

When irradiated with a $^{241}\text{AmBe}$ source, the spectrometer was placed at a distance large enough so that neutrons impinged homogeneously on its active area. The spectrum was measured in the range 0.11 to 11 MeV using the data acquired from only three regions, i.e. those that showed high response in this energy range. The uncertainty on the spectrum was calculated on average as 5% and the measured counts were in good agreement with the expected ones, estimated by folding the response functions with the $^{241}\text{AmBe}$ spectrum in the measurement position.

The spectra in different positions on the concrete and iron roofs of the CERF facility were measured quite accurately up to the evaporation peaks (2 MeV and 300 keV for concrete and iron respectively). The high energy peaks at 70 MeV for both spectra were not possible to be obtained due to the low response of the device for energies higher than 50 MeV. The solution spectra obtained with the unfolding codes MAXED and GRAVEL were very similar in all positions, with MAXED reproducing in a smoother way the evaporation peak and GRAVEL the thermal peak. Deviations

were observed in the measured number of counts per region when compared to the estimated ones, mostly localised in regions employing large amount of polyethylene. The reason lies in scattered neutrons from closely surrounding material, the concrete and iron roofs, inducing additional number of counts.

Improvements in the instrument response were investigated via simulations and the suggested method is shielding the polyethylene pieces from the sides with material with high neutron absorption. By applying this method, existing cross-talk effects can be reduced by a factor of 10, leading to more accurate and reliable measurements. The material recommended are gadolinium for its significantly high cross-section and flex-boron for its low cost.

Based on its directional geometry, the SpectroGEM can be employed for investigating the direction of a neutron spectrum in work fields for radiation protection purposes. The device can be rotated and measure the spectrum in different angles, covering all directions around a point of interest. In this way insufficiently shielded areas can be recognized and fixed, which could not be possible with devices that show isotropic response. The main advantages of the new SpectroGEM are wide energy range response (measured from thermal to 11 MeV), short irradiation time and high transportability.

Appendix A

The FLUKA Monte Carlo code

The Monte Carlo FLUKA code is an intrinsically analogue code, which is capable of handling the interactions and the transport of electromagnetic and hadronic particles in any material over a wide range of energy. FLUKA is a continuously evolving code and model implementations are always guided and checked against experimental data. A brief description of the physical model of neutron transport used in the FLUKA version (2011) and the quantities are presented in this appendix.

A.1 Low energy neutron transport

Transport of low-energy neutrons (<20 MeV) is performed by a multigroup algorithm. This technique consists in dividing the energy range of interest into a given number of intervals, the energy groups, the number of which is currently 260 of approximately equal logarithmic width in the energy range 10^{-5} eV to 20 MeV, 31 of which are thermal. Elastic and inelastic reactions are simulated not as exclusive processes, but by group-to-group transfer probabilities forming a so-called "down-scattering matrix".

For a few isotopes only, neutron transport can be done also using continuous cross sections. For ^1H , ^6Li and ^{10}B it is applied as a user option and for the reaction $^{14}\text{N}(n,p)^{14}\text{C}$ pointwise transport is always applied. All other charged secondaries, including fission fragments, are not transported and their energy is deposited at the point of interaction (kerma approximation).

The default FLUKA neutron cross section library contains more than 250 different materials, natural elements or compounds. Hydrogen cross sections, which have a particular importance in neutron moderation, are available also for different types

of molecular binding, such as water and polyethylene. The library is continuously enriched and updated on the basis of the most recent evaluations (ENDF/B, JEF, JENDL etc.).

In the multigroup transport scheme, the production of secondary neutrons via (n, xn) reactions is taken into account implicitly by the so-called "non-absorption probability", a group-dependent factor by which the weight of a neutron is multiplied after exiting a collision. If the only possible reactions are capture and scattering, the non-absorption probability is <1 , but at energies above the threshold for (n, 2n) reaction it can take values larger than 1.

A.2 Estimation of physical quantities

The Monte Carlo equivalent of the result in a real experiment is called an estimator, which is obtained by sampling from a statistical distribution and has a statistical and a systematic error. There are different kinds of estimators used to calculate the same physical quantity and FLUKA offers numerous. These estimators are often called "scoring" capabilities.

One of the most useful physical quantities scored is the fluence and it is defined as the average number of particles crossing a surface per area unit. Given a surface with infinitesimal thickness dt , an incident particle with an angle ϑ with respect to the normal of the surface S will travel a segment $dt/\cos\vartheta$. Therefore, the average surface fluence can be calculated by adding $dt/\cos\vartheta$ for each particle crossing the surface and dividing by the volume $S dt$:

$$\Phi = \lim_{dt \rightarrow 0} \frac{\sum_i \frac{dt}{\cos\vartheta_i}}{S dt}$$

The most widely used scoring commands are the following:

1. USRTRACK: Scores the average differential fluence $d\Phi/dE$ of a given type or family of particles in a given region.
2. USRBDX: Scores the average double-differential fluence $d^2\Phi/dEd\Omega$ of a given type or family of particles on a given surface.
3. USRBIN: Scores the spatial distribution of energy deposited, or total fluence in a regular mesh (cylindrical, Cartesian or per region) described by the user.

4. USRYIELD: Scores a double differential yield of particles escaping a surface. The distribution can be with respect to energy and angle, but also other quantities.

The results are always normalised per primary beam particle.

Appendix B

Response matrix of the SpectroGEM

The response matrix of the spectrometer is presented in this appendix, listed in the format required by the UMG package [65] for the unfolding procedure. The numbers follow the exponential format code "E", e.g. 1.127E-10 corresponds to $1.127 \cdot 10^{-10}$. The first matrix defines the energy bins in MeV (251 in total) and the next six matrices the region response in cm^2 for these energy bins.

MARCH-23-2015 *** Energy bins in MeV

Response Matrix with 251 energy bins, units: cm^2

251	1								
1.000E-10	1.127E-10	1.271E-10	1.432E-10	1.614E-10	1.820E-10	2.051E-10	2.312E-10		
2.606E-10	2.938E-10	3.311E-10	3.733E-10	4.207E-10	4.742E-10	5.346E-10	6.026E-10		
6.792E-10	7.656E-10	8.630E-10	9.727E-10	1.096E-09	1.236E-09	1.393E-09	1.570E-09		
1.770E-09	1.995E-09	2.249E-09	2.535E-09	2.858E-09	3.221E-09	3.631E-09	4.093E-09		
4.613E-09	5.200E-09	5.861E-09	6.607E-09	7.447E-09	8.395E-09	9.462E-09	1.067E-08		
1.202E-08	1.355E-08	1.528E-08	1.722E-08	1.941E-08	2.188E-08	2.466E-08	2.780E-08		
3.133E-08	3.532E-08	3.981E-08	4.487E-08	5.058E-08	5.702E-08	6.427E-08	7.244E-08		
8.166E-08	9.204E-08	1.038E-07	1.169E-07	1.318E-07	1.486E-07	1.675E-07	1.888E-07		
2.128E-07	2.399E-07	2.704E-07	3.048E-07	3.436E-07	3.873E-07	4.365E-07	4.920E-07		
5.546E-07	6.252E-07	7.047E-07	7.943E-07	8.954E-07	1.009E-06	1.138E-06	1.282E-06		
1.445E-06	1.629E-06	1.837E-06	2.070E-06	2.333E-06	2.630E-06	2.965E-06	3.342E-06		
3.767E-06	4.246E-06	4.786E-06	5.395E-06	6.081E-06	6.855E-06	7.727E-06	8.710E-06		
9.817E-06	1.107E-05	1.247E-05	1.406E-05	1.585E-05	1.786E-05	2.014E-05	2.270E-05		
2.559E-05	2.884E-05	3.251E-05	3.664E-05	4.130E-05	4.656E-05	5.248E-05	5.916E-05		
6.668E-05	7.516E-05	8.472E-05	9.550E-05	1.076E-04	1.213E-04	1.368E-04	1.542E-04		

```

1.738E-04 1.959E-04 2.208E-04 2.489E-04 2.805E-04 3.162E-04 3.565E-04 4.018E-04
4.529E-04 5.105E-04 5.754E-04 6.486E-04 7.311E-04 8.241E-04 9.290E-04 1.047E-03
1.180E-03 1.330E-03 1.500E-03 1.690E-03 1.905E-03 2.148E-03 2.421E-03 2.729E-03
3.076E-03 3.467E-03 3.908E-03 4.406E-03 4.966E-03 5.598E-03 6.310E-03 7.112E-03
8.017E-03 9.036E-03 1.019E-02 1.148E-02 1.294E-02 1.459E-02 1.644E-02 1.854E-02
2.089E-02 2.355E-02 2.655E-02 2.992E-02 3.373E-02 3.802E-02 4.285E-02 4.831E-02
5.445E-02 6.138E-02 6.918E-02 7.798E-02 8.790E-02 9.908E-02 1.117E-01 1.259E-01
1.419E-01 1.600E-01 1.803E-01 2.032E-01 2.291E-01 2.582E-01 2.911E-01 3.281E-01
3.698E-01 4.169E-01 4.699E-01 5.297E-01 5.970E-01 6.730E-01 7.586E-01 8.551E-01
9.638E-01 1.086E+00 1.225E+00 1.380E+00 1.556E+00 1.754E+00 1.977E+00 2.228E+00
2.512E+00 2.831E+00 3.192E+00 3.597E+00 4.055E+00 4.571E+00 5.152E+00 5.808E+00
6.546E+00 7.379E+00 8.318E+00 9.376E+00 1.057E+01 1.191E+01 1.343E+01 1.514E+01
1.706E+01 1.923E+01 2.168E+01 2.443E+01 2.754E+01 3.105E+01 3.499E+01 3.945E+01
4.446E+01 5.012E+01 5.649E+01 6.368E+01 7.178E+01 8.091E+01 9.120E+01 1.028E+02
1.159E+02 1.306E+02 1.472E+02 1.660E+02 1.871E+02 2.109E+02 2.377E+02 2.679E+02
3.020E+02 3.404E+02 3.837E+02 4.325E+02 4.875E+02 5.495E+02 6.194E+02 6.982E+02
7.870E+02 8.872E+02 1.000E+03
0
6
Reg1      reg_1
1.000E+00      cm^2      0      0      3      1      1      0
2.006E-01 2.006E-01 2.006E-01 2.006E-01 2.006E-01 2.006E-01 2.497E-01 2.497E-01
2.497E-01 2.687E-01 2.680E-01 2.680E-01 2.680E-01 2.819E-01 2.819E-01 2.819E-01
2.833E-01 2.833E-01 2.833E-01 2.841E-01 2.841E-01 2.841E-01 2.753E-01 2.753E-01
2.753E-01 2.650E-01 2.650E-01 2.650E-01 2.650E-01 2.541E-01 2.541E-01 2.541E-01
2.284E-01 2.284E-01 2.284E-01 2.087E-01 2.087E-01 2.087E-01 1.933E-01 1.933E-01
1.933E-01 1.750E-01 1.750E-01 1.750E-01 1.750E-01 1.581E-01 1.581E-01 1.581E-01
1.450E-01 1.450E-01 1.450E-01 1.384E-01 1.384E-01 1.384E-01 1.340E-01 1.340E-01
1.340E-01 1.179E-01 1.179E-01 1.179E-01 9.884E-02 9.884E-02 9.884E-02 9.884E-02
8.786E-02 8.786E-02 8.786E-02 7.307E-02 7.307E-02 7.307E-02 6.663E-02 6.663E-02
6.663E-02 6.392E-02 6.392E-02 5.396E-02 4.964E-02 4.964E-02 4.371E-02 4.371E-02
4.056E-02 4.056E-02 4.056E-02 3.602E-02 3.602E-02 3.405E-02 3.405E-02 2.995E-02
3.024E-02 2.863E-02 2.863E-02 2.775E-02 2.533E-02 2.262E-02 2.314E-02 2.094E-02
2.006E-02 1.977E-02 1.845E-02 1.823E-02 1.633E-02 1.538E-02 1.442E-02 1.340E-02
1.318E-02 1.354E-02 1.252E-02 1.186E-02 1.142E-02 1.142E-02 1.003E-02 1.018E-02
9.152E-03 8.786E-03 7.688E-03 7.688E-03 8.859E-03 7.322E-03 6.846E-03 6.772E-03
5.894E-03 6.333E-03 6.077E-03 4.686E-03 5.345E-03 5.308E-03 4.649E-03 4.247E-03
4.613E-03 4.649E-03 4.649E-03 4.100E-03 3.405E-03 3.441E-03 3.807E-03 3.295E-03
2.599E-03 2.819E-03 2.965E-03 2.892E-03 1.940E-03 1.757E-03 2.380E-03 1.940E-03
1.940E-03 1.464E-03 1.757E-03 1.904E-03 1.574E-03 1.391E-03 1.501E-03 1.721E-03
1.098E-03 1.135E-03 1.464E-03 9.518E-04 1.245E-03 1.354E-03 6.956E-04 1.208E-03

```

```

1.171E-03 9.152E-04 8.054E-04 1.135E-03 1.318E-03 7.688E-04 1.098E-03 9.152E-04
8.054E-04 7.322E-04 8.786E-04 5.857E-04 5.491E-04 5.491E-04 6.589E-04 7.322E-04
5.491E-04 5.125E-04 5.857E-04 2.196E-04 3.295E-04 5.857E-04 6.223E-04 5.491E-04
4.027E-04 3.661E-04 3.295E-04 3.295E-04 1.830E-04 2.929E-04 1.464E-04 1.464E-04
1.464E-04 2.050E-04 2.196E-04 3.075E-04 2.343E-04 2.196E-04 2.196E-04 1.464E-04
1.904E-04 5.857E-05 8.786E-05 7.322E-05 1.171E-04 5.857E-05 8.786E-05 1.025E-04
5.857E-05 5.857E-05 4.393E-05 4.393E-05 1.464E-05 1.464E-05 1.464E-05 1.464E-05
1.464E-05 1.464E-05 2.196E-05 2.929E-05 2.929E-05 5.857E-05 1.464E-04 2.929E-05
5.857E-05 8.786E-05 5.857E-05 7.322E-05 1.025E-04 1.025E-04 4.393E-05 4.393E-05
1.318E-04 5.857E-05 4.393E-05 7.322E-05 2.929E-05 4.393E-05 7.322E-05 5.857E-05
7.322E-05 8.786E-05 4.393E-05 1.464E-04 1.025E-04 1.318E-04 1.611E-04 1.464E-04
1.171E-04 8.786E-05
Reg2      reg_2
1.000E+00      cm^2      0      0      3      1      1      0
9.965E-02 9.965E-02 9.965E-02 9.965E-02 9.965E-02 9.965E-02 1.026E-01 1.026E-01
1.026E-01 1.062E-01 1.062E-01 1.062E-01 1.062E-01 1.048E-01 1.048E-01 1.048E-01
1.055E-01 1.055E-01 1.055E-01 1.062E-01 1.062E-01 1.062E-01 1.055E-01 1.055E-01
1.055E-01 1.018E-01 1.018E-01 1.018E-01 1.018E-01 1.018E-01 1.018E-01 1.018E-01
9.965E-02 9.965E-02 9.965E-02 9.379E-02 9.379E-02 9.379E-02 9.086E-02 9.086E-02
9.086E-02 8.573E-02 8.573E-02 8.573E-02 8.573E-02 8.866E-02 8.866E-02 8.866E-02
8.646E-02 8.646E-02 8.646E-02 9.965E-02 9.965E-02 9.965E-02 1.018E-01 1.018E-01
1.018E-01 9.745E-02 9.745E-02 9.745E-02 9.892E-02 9.892E-02 9.892E-02 9.892E-02
1.004E-01 1.004E-01 1.004E-01 9.892E-02 9.892E-02 9.892E-02 1.018E-01 1.018E-01
1.018E-01 1.026E-01 1.026E-01 9.965E-02 1.018E-01 1.018E-01 9.672E-02 9.672E-02
9.745E-02 9.745E-02 9.745E-02 9.379E-02 9.379E-02 8.939E-02 8.939E-02 9.306E-02
9.379E-02 9.013E-02 9.013E-02 8.646E-02 8.720E-02 8.720E-02 8.500E-02 8.280E-02
7.767E-02 7.840E-02 7.987E-02 7.547E-02 7.547E-02 7.620E-02 7.620E-02 7.188E-02
6.998E-02 6.858E-02 6.624E-02 6.411E-02 6.485E-02 6.118E-02 5.964E-02 5.862E-02
5.789E-02 5.657E-02 5.715E-02 5.627E-02 5.290E-02 5.224E-02 4.961E-02 4.990E-02
4.814E-02 4.741E-02 4.799E-02 4.550E-02 4.330E-02 4.470E-02 4.448E-02 4.111E-02
3.840E-02 4.023E-02 3.883E-02 3.752E-02 3.356E-02 3.415E-02 3.517E-02 3.451E-02
3.305E-02 3.312E-02 3.305E-02 3.246E-02 3.012E-02 2.784E-02 2.682E-02 2.711E-02
2.543E-02 2.484E-02 2.396E-02 2.689E-02 2.308E-02 2.242E-02 2.323E-02 2.147E-02
2.030E-02 2.081E-02 1.898E-02 1.942E-02 1.795E-02 1.788E-02 1.737E-02 1.583E-02
1.641E-02 1.531E-02 1.619E-02 1.495E-02 1.524E-02 1.451E-02 1.363E-02 1.297E-02
1.341E-02 1.128E-02 1.312E-02 1.114E-02 1.040E-02 1.099E-02 9.672E-03 9.599E-03
9.159E-03 9.599E-03 8.207E-03 6.631E-03 7.291E-03 7.547E-03 6.411E-03 5.422E-03
6.155E-03 5.056E-03 4.286E-03 3.847E-03 4.103E-03 3.554E-03 3.664E-03 2.931E-03
2.674E-03 2.550E-03 1.978E-03 2.037E-03 2.008E-03 1.583E-03 1.583E-03 1.334E-03
9.965E-04 1.011E-03 8.646E-04 7.914E-04 5.129E-04 5.422E-04 4.983E-04 4.836E-04
3.224E-04 2.931E-04 3.077E-04 2.052E-04 1.759E-04 3.224E-04 2.784E-04 1.612E-04

```

```

1.612E-04 7.327E-05 2.784E-04 2.931E-04 1.172E-04 1.759E-04 2.052E-04 2.345E-04
1.026E-04 1.759E-04 2.345E-04 1.319E-04 2.198E-04 2.052E-04 2.931E-04 3.664E-04
2.198E-04 2.345E-04 2.345E-04 2.491E-04 2.052E-04 1.465E-04 2.491E-04 2.345E-04
3.664E-04 2.638E-04 3.517E-04 2.491E-04 4.250E-04 3.957E-04 3.371E-04 4.250E-04
4.396E-04 3.664E-04
Reg3      reg_3
1.000E+00      cm^2      0      0      3      1      1      0
1.586E-01 1.586E-01 1.586E-01 1.586E-01 1.586E-01 1.586E-01 1.608E-01 1.608E-01
1.608E-01 1.601E-01 1.601E-01 1.601E-01 1.601E-01 1.608E-01 1.608E-01 1.608E-01
1.637E-01 1.637E-01 1.637E-01 1.586E-01 1.586E-01 1.586E-01 1.564E-01 1.564E-01
1.564E-01 1.542E-01 1.542E-01 1.542E-01 1.542E-01 1.477E-01 1.477E-01 1.477E-01
1.404E-01 1.404E-01 1.404E-01 1.338E-01 1.338E-01 1.338E-01 1.250E-01 1.250E-01
1.250E-01 1.213E-01 1.213E-01 1.213E-01 1.213E-01 1.184E-01 1.184E-01 1.184E-01
1.170E-01 1.170E-01 1.170E-01 1.338E-01 1.338E-01 1.338E-01 1.192E-01 1.192E-01
1.192E-01 1.053E-01 1.053E-01 1.053E-01 9.065E-02 9.065E-02 9.065E-02 9.065E-02
8.918E-02 8.918E-02 8.918E-02 8.041E-02 8.041E-02 8.041E-02 7.676E-02 7.676E-02
7.676E-02 7.822E-02 7.822E-02 7.822E-02 8.041E-02 8.041E-02 7.968E-02 7.968E-02
7.895E-02 7.895E-02 7.895E-02 8.114E-02 8.114E-02 8.114E-02 8.114E-02 7.822E-02
7.822E-02 7.895E-02 7.895E-02 7.822E-02 8.041E-02 7.822E-02 7.968E-02 7.968E-02
8.187E-02 7.822E-02 7.822E-02 8.041E-02 8.114E-02 8.041E-02 7.968E-02 8.041E-02
8.041E-02 8.187E-02 7.968E-02 8.260E-02 8.334E-02 8.260E-02 8.041E-02 7.968E-02
8.260E-02 8.041E-02 8.334E-02 8.187E-02 8.041E-02 8.187E-02 8.260E-02 8.041E-02
8.187E-02 8.041E-02 8.260E-02 8.187E-02 7.822E-02 7.822E-02 7.968E-02 8.114E-02
8.041E-02 7.822E-02 8.041E-02 7.895E-02 7.676E-02 8.041E-02 7.968E-02 7.456E-02
7.603E-02 7.749E-02 7.529E-02 7.749E-02 7.749E-02 7.310E-02 7.456E-02 7.215E-02
7.529E-02 7.310E-02 7.310E-02 7.244E-02 7.676E-02 7.456E-02 7.142E-02 7.230E-02
7.310E-02 7.142E-02 7.456E-02 7.529E-02 7.456E-02 7.113E-02 7.310E-02 6.850E-02
6.930E-02 7.201E-02 6.974E-02 6.784E-02 7.310E-02 7.288E-02 7.193E-02 7.142E-02
7.310E-02 7.062E-02 7.054E-02 6.864E-02 7.237E-02 7.040E-02 6.499E-02 6.967E-02
6.828E-02 6.974E-02 6.667E-02 6.689E-02 6.740E-02 6.601E-02 6.382E-02 6.491E-02
6.104E-02 5.870E-02 5.855E-02 5.373E-02 5.358E-02 4.832E-02 4.890E-02 4.525E-02
4.123E-02 4.123E-02 3.831E-02 3.443E-02 3.246E-02 3.048E-02 2.661E-02 2.339E-02
2.193E-02 1.893E-02 1.747E-02 1.516E-02 1.411E-02 1.272E-02 1.121E-02 9.649E-03
8.801E-03 8.012E-03 5.892E-03 5.293E-03 4.795E-03 4.196E-03 3.757E-03 3.392E-03
3.187E-03 2.339E-03 2.792E-03 2.252E-03 1.769E-03 1.784E-03 1.769E-03 1.740E-03
1.330E-03 1.272E-03 1.389E-03 1.213E-03 1.170E-03 1.564E-03 1.404E-03 1.199E-03
9.796E-04 1.082E-03 1.097E-03 9.357E-04 1.097E-03 9.503E-04 1.053E-03 1.067E-03
1.418E-03 9.649E-04 1.287E-03 1.155E-03 1.345E-03 8.772E-04 1.608E-03 1.345E-03
1.637E-03 1.447E-03
Reg4      reg_4
1.000E+00      cm^2      0      0      3      1      1      0

```

0.000E+00							
0.000E+00							
0.000E+00							
0.000E+00							
0.000E+00							
0.000E+00							
0.000E+00							
0.000E+00							
0.000E+00							
0.000E+00							
0.000E+00							
0.000E+00	0.000E+00	0.000E+00	0.000E+00	1.462E-05	2.193E-05	2.924E-05	2.924E-05
1.462E-05	1.462E-05	8.772E-05	8.772E-05	2.485E-04	2.924E-04	7.749E-04	9.284E-03
2.763E-02	5.051E-02	8.041E-02	8.699E-02	8.187E-02	6.418E-02	5.285E-02	4.503E-02
3.969E-02	3.545E-02	3.100E-02	2.741E-02	2.398E-02	2.135E-02	1.937E-02	1.747E-02
1.630E-02	1.499E-02	1.323E-02	1.425E-02	1.257E-02	1.156E-02	1.192E-02	1.111E-02
1.184E-02	1.206E-02	1.199E-02	1.199E-02	1.265E-02	1.367E-02	1.367E-02	1.469E-02
1.542E-02	1.535E-02						

Bibliography

- [1] K. H. Beckurts, K. Wirtz, Neutron Physics, Springer-Verlag, 1964.
- [2] G. F. Knoll, Radiation detection and measurement, Wiley, 2010.
- [3] R. Murray, K. E. Holbert, Nuclear energy: An Introduction to the Concepts, Systems and Applications of Nuclear Processes, Elsevier, 2014.
- [4] ENDF, Evaluated Nuclear Data File, 2011.
- [5] C. Wagemans, The Nuclear Fission Process, CRC Press, 1991.
- [6] J. R. Lamarsh, et al., Introduction to Nuclear Reactor Theory, Addison-Wesley, 1966.
- [7] S. Glasstone, A. Sesonske, Nuclear Reactor Engineering, D. Van Nostrand Co., 1967.
- [8] W. Abson, et al., Boron trifluoride proportional counters, Proceedings IEEE, 1958.
- [9] I. O. Anderson, S. Malmskog, Investigation of the pulse height distribution of boron trifluoride proportional counters, International Nuclear Information System 84, 1962.
- [10] C. Birattari, et al., An extended range neutron rem counter, Nuclear Instruments and Methods A297, 1990.
- [11] A. Hanson, M. McKibben, A neutron detector having uniform sensitivity from 10 keV to 3 MeV, Physical Review 72, 1947.
- [12] L. East, R. Walton, The Los Alamos Neutron Science Center, Polyethylene moderated ^3He neutron detectors 72, 1969.

-
- [13] F. Sauli, GEM: A new concept for electron amplification in gas detectors, Nuclear Instruments and Methods A386, 1997.
- [14] S. Bachmann, et al., Performance of GEM detectors in high intensity particle beam, Nuclear Instruments and Methods A470, 2001.
- [15] M. Villa, et al., Progress on large area GEMs, Nuclear Instruments and Methods A628, 2011.
- [16] S. Bachmann, et al., Charge amplification and transfer processes in the gas electron multiplier, Nuclear Instruments and Methods A438, 1999.
- [17] J. Townsend, Electron in gases, Hutchinson, 1947.
- [18] F. Sauli, Principles of operation of multiwire proportional and drift chambers, CERN 77-09, 1997.
- [19] T. Zhao, et al., A study of electron drift velocity in Ar/CO₂ and Ar/CO₂/CF₄ gas mixtures, Nuclear Instruments and Methods A340, 1994.
- [20] W. Bonivento, et al., Development of the CARIOCA front-end chip for the LHCb muon detector, Nuclear Instruments and Methods A491, 2002.
- [21] B. Buonomo, et al., Applications in beam diagnostics with triple GEM detectors, Nuclear Instruments and Methods A617, 2010.
- [22] G. Corradi, et al., A novel High-Voltage System for a triple GEM detector, Nuclear Instruments and Methods A572, 2007.
- [23] A. Mitaroff, M. Silari, The CERN-EU high-energy Reference Field (CERF) facility for dosimetry at commercial flight altitudes and in space, Radiation Protection Dosimetry 102, 2002.
- [24] M. Pullia, et al., The National Center for Oncological Hadrontherapy in Italy (CNAO): Design and status, Conference AccApp2013, Bruges, Belgium.
- [25] E. Aza, et al., The triple GEM detector as beam monitor for relativistic hadron beams, Journal of Instrumentation 9 (2014) P06006.
- [26] E. Aza, et al., The December 2012 CERF run, Technical Report, CERN-DGS-2012-121-RP-TN, 2012.

-
- [27] F. L. Torre, et al., A new verification of the calibration factor of the CERF beam monitor, Technical Report, CERN-RP-2013-083-REPORTS-TN, 2013.
- [28] E. Aza, et al., Preliminary results of the Gas Electron Multiplier (GEM) as real-time beam monitor in hadron therapy Submitted to the International Journal of Particle Therapy, 2015.
- [29] C. Guerrero, et al., Performance of the neutron time-of-flight facility n_TOF at CERN, European Physical Journal A 49:27, 2013.
- [30] E. Aza, et al., The triple GEM detector as stray neutron monitor, Journal of Instrumentation 9 (2014) T11005.
- [31] A. Ferrari, et al., FLUKA: a multi-particle transport code, CERN-2005-10, INFN/TC05/11, SLAC-R-773, 2005.
- [32] T. T. Bohlen, et al., The FLUKA Code: Developments and Challenges for High Energy and Medical Applications, Nuclear Data Sheets 102, 2014.
- [33] A. Pietropaolo, et al., A new He-free thermal neutrons detector concept based on the GEM technology, Nuclear Instruments and Methods A729, 2013.
- [34] B. Esposito, et al., Design of a GEM-based detector for the measurement of fast neutrons, Nuclear Instruments and Methods A617, 2010.
- [35] G. Croci, et al., Measurements of γ -ray sensitivity of a GEM based detector using a coincidence technique, Journal of Instrumentation 8 (2013) P04006.
- [36] H. Vincke, et al., Simulation and measurements of the response of an air ionization chamber exposed to a mixed high-energy radiation field, Radiation Protection Dosimetry 116, 2005.
- [37] F. Murtas, Applications of triple GEM detectors beyond particle and nuclear physics, Journal of Instrumentation 9 (2014) C01058.
- [38] E. Aza, et al., Neutron Beam Profile Measurements with a Triple GEM for Thermal Neutrons at the CERN nTOF Facility, Proceedings IEEE, 2013.
- [39] E. Aza, et al., Neutron beam monitoring for time-of-flight facilities with gaseous detectors, Nuclear Instruments and Methods A806, 2016.

-
- [40] F. Murtas, et al., Triple GEM gas detectors as real time fast neutron beam monitors for spallation neutron sources, *Journal of Instrumentation* 7 (2014) P07021.
- [41] M. Martone, et al., The 14 MeV Frascati neutron generator, *Journal of Nuclear Materials B*, 1994.
- [42] S. Agostinelli, et al., GEANT4: a simulation toolkit, *Nuclear Instruments and Methods A506*, 2003.
- [43] C. Borcea, et al., Particle distributions, entering the vacuum tube, from an 80x80x60cm³ lead target, SL-Note-2000-029 EET 2006.
- [44] A. Tsinganis, Private communication, 2014.
- [45] G. Claps, et al., Performance test of triple GEM detectors at CERN nTOF facility, *Proceedings IEEE*, 2012.
- [46] D. Filges, K. Goldenbaum, *Handbook of spallation research*, Wiley, 2009.
- [47] ICRP, *Annals of the ICRP 37, Publication 103 (Users Edition)*, 2007.
- [48] ICRP, *Annals of the ICRP, Publication 74*, 1996.
- [49] H. Dinter, et al., Studies on the neutron field behind the shielding of proton accelerators Part II: Iron shielding, *Nuclear Instruments and Methods A368*, 1996.
- [50] R. Remetti, et al., Dose Equivalent Rate Evaluation for Nuclear Reactors Shielding Studies by Means of the Point Kernel Technique, *International Journal of Nuclear Energy Science and Engineering* 1, 2011.
- [51] O. Zeynali, et al., Study of Radiation Effects of Nuclear High Energy Particles on Electronic Circuits and Methods to Reduce Its Destructive Effects, *Journal of Modern Physics* 2, 2011.
- [52] R. L. Bramblett, et al., A new type of neutron spectrometer, *Nuclear Instruments and Methods* 9, 1960.
- [53] M. Cinausero, et al., A proton recoil telescope for neutron spectroscopy, *Journal of Physics* 41, 2006.

-
- [54] D. Sloan, J. C. Robertson, The efficiency of a recoil proton monitor, *Nuclear Instruments and Methods* A198, 1982.
- [55] M. Martinez, et al., Scintillating bolometers for fast neutron spectroscopy in rare events searches, *Journal of Physics Conference Series* 375, 2012.
- [56] P. Lisowski, K. Schoenberg, The Los Alamos Neutron Science Center, *Nuclear Instruments and Methods* A562, 2006.
- [57] C. Birattari, et al., A Bonner sphere spectrometer with extended response matrix, *Nuclear Instruments and Methods* A620, 2010.
- [58] A. Sutter, As-Raydetect-Gmbh, official distributor of Centronic for Switzerland, Private communication, 2011.
- [59] M. Caresana, et al., LUPIN, a new instrument for pulsed neutron fields, *Nuclear Instruments and Methods* A712, 2013.
- [60] E. Aza, et al., Instrument intercomparison in the pulsed neutron fields at the CERN HiRadMat facility, *Radiation Measurements* 61, 2014.
- [61] S. Barros, et al., Comparison of unfolding codes for neutron spectrometry with Bonner spheres, *Radiation Protection Dosimetry* 161, 2014.
- [62] M. Reginatto, P. Goldhagen, MAXED: a computer code for maximum entropy deconvolution of multisphere neutron spectrometer data, 1999.
- [63] E. Garcia-Dominguez, et al., Noniterative unfolding algorithm for neutron spectrum measurements with bonner spheres, *Transactions on Nuclear Science* 46, 1999.
- [64] R. Bedogni, et al., FRUIT: an operational tool for multisphere neutron spectrometry in workplaces, *Nuclear Instruments and Methods* A580, 2007.
- [65] M. Reginatto, The few-channel unfolding program in the UMG Package: MXD_FC33, GRV_FC33 and IQU_FC33 (UMG Package, Version 3.3.), 2004.
- [66] V. DeSmet, et al., Secondary neutrons inside a proton therapy facility: MCNPX simulations compared to measurements performed with a Bonner Sphere Spectrometer and neutron H*(10) monitors, Submitted to *Radiation Measurements* 2015.

-
- [67] M. D. Saint-Hubert, et al., Secondary neutron doses in a proton therapy centre, *Radiation Protection Dosimetry*, doi: 10.1093/rpd/nc0000 2015.
- [68] L. Jagerhofer, et al., A new method to calculate the response of the Wendi-2 rem counter using the FLUKA Monte Carlo code, *Nuclear Instruments and Methods A691*, 2012.
- [69] B. Burgkhardt, et al., The neutron fluence and $H^*(10)$ response of the new LB 6411 Remcounter, *Radiation Protection Dosimetry* 70, 1997.
- [70] D. Thomas, The system of radiation protection for neutrons: does it fit the purpose?, *Radiation Protection Dosimetry* 161, 2014.
- [71] X-5 Monte Carlo Team, MCNP - A General N-Particle Transport Code, Version 5, Volume I: Overview and Theory, LA-UR-03-1987, 2003.
- [72] D. Satoh, et al., Shielding study at the Fukui Prefectural Hospital Proton Therapy Center, *Journal of Nuclear Science and Technology* 49, 2012.
- [73] E. Aza, et al., The 2014 CERF runs, Technical Report, CERN-RP-2015-011-REPORTS-TN V2, 2015.
- [74] E. Dimovasili, M. Silari, Beam and reference field monitoring during the 2002 CERF runs, Technical Report, CERN-TIS-2002-RP-TN, 2002.
- [75] E. Dimovasili, et al., HANDI TEPC measurements during the 1999, 2000 and 2001 CERF runs, Technical Report, CERN-TIS-RP/TN/2002-020, 2002.
- [76] E. Aza, et al., A Bonner Sphere Spectrometer for pulsed fields, *Radiation Protection Dosimetry*, doi: 10.1093/rpd/ncv180 2015.
- [77] J. Barranco, S. Gilardoni, Simulation and optimization of beam losses during continuous transfer extraction at the CERN proton synchrotron, *Physical Review St Accelerators and Beams* 14 (2011) 030101.
- [78] R. Billen, C. Roderick, The LHC logging service: capturing, storing and using time-series data for the worlds largest scientific instrument, Technical Report, CERN-AB-Note-2006-046, 2006.
- [79] S. Damjanovic, et al., Shielding studies for the Route Goward / PS crossing, CERN-DGS-2011-065-RP-TN, 2011.

-
- [80] E. Aza, et al., Comparison of the performance of different instruments in the stray neutron field around the CERN Proton Synchrotron, *Radiation Protection Dosimetry* 161, 2014.
- [81] A. Mitaroff, Design, calibration and tests of an extended-range Bonner sphere spectrometer, Doctoral Thesis, CERN-THESIS-2002-029.
- [82] J. F. Ziegler, SRIM: The stopping and range of ions in matter, *Nuclear Instruments and Methods* B268, 2010.
- [83] D. S. McGregor, et al., Design consideration for thin coated semiconductor thermal neutron detectors, *Nuclear Instruments and Methods* A500, 2003.
- [84] S. Park, et al., Neutron detection with gem, *Transactions on Nuclear Science* 52, 2005.
- [85] M. Lener, Triple-GEM detectors for the innermost region of the muon apparatus at the LHCb experiment, Doctoral Thesis, 2005.
- [86] N. J. Zaluzec, Analytical Formulae for Calculation of X-Ray Detector Solid Angles in the Scanning and Scanning/Transmission Analytical Electron Microscope, *Microscopy and Microanalysis* 20, 2014.
- [87] <https://root.cern.ch/drupal/>.
- [88] B. D. Mellow, et al., Cadmium Toxicity and Treatment, *The Scientific World Journal* 2013,.
- [89] B. D. Mellow, et al., The replacement of cadmium as a thermal neutron filter, *Nuclear Instruments and Methods* A577, 2007.